

Study and Modeling of the Localized Nature of Top of the Line Corrosion

A dissertation presented to

the faculty of

The Russ College of Engineering and Technology of Ohio University

In partial fulfillment

of the requirements for the degree

Doctor of Philosophy

Marc Singer

August 2013

© 2013 Marc Singer. All Rights Reserved.

This dissertation titled  
Study and Modeling of the Localized Nature of Top of the Line Corrosion

by

MARC SINGER

has been approved for  
the department of Chemical and Biomolecular Engineering  
and the Russ College of Engineering and Technology by

Khairul Alam

Moss Professor of Mechanical Engineering

Dennis Irwin

Dean, Russ College of Engineering and Technology

## ABSTRACT

SINGER, MARC, Ph.D., August 2013, Chemical and Biomolecular Engineering

Study and Modeling of the Localized Nature of Top of the Line Corrosion (320 pp.)

Director of Dissertation: Khairul Alam

The occurrence of localized corrosion in Top of the Line Corrosion (TLC) was investigated both in sweet ( $\text{CO}_2$ -dominated) and sour ( $\text{H}_2\text{S}$ -dominated) environments. The focus of the work was to understand the influence of the environmental parameters on localized corrosion at the top of the line in order to develop a narrative of the mechanism.

The first part of this project presents the unique setup developed for the experimental work. Several large scale flow loops were used to perform the tests in order to recreate the field environments as closely as possible. The test section was designed using a carbon steel insert exposed to three different levels of cooling at the same time. This concept was quite successful in simulating realistic localized features. A series of long term exposure (one- to three-month) experiments was conducted to investigate the controlling parameters. The occurrence of localized corrosion could be very clearly correlated to the condensation rate, the gas temperature and the organic acid content. Important observations on the morphology of localized TLC features could be made, providing useful insight on the mechanisms involved.

The second part of the study attempted to link the presence or absence of a large droplet on the steel surface to the extent of corrosion occurring underneath it. However, this was not successful as no clear relationship could be established with certainty. Instead, the water condensation rate was thought to control the corrosion and the overall aggressiveness of the environment ( $\text{CO}_2$ , acetic acid).

Finally, a modeling approach was proposed for the prediction of the localized attack in a top of the line corrosion scenario. The method was based on the observations made during the experimental part of the work and presented a mechanism for the prediction of the onset and propagation of localized corrosion. The  $\text{FeCO}_3$  saturation level played a key role in defining the overall corrosiveness of the condensed water, while the condensation rate controlled the degree of which localized attack is sustainable.

## ACKNOWLEDGMENTS

I would like to express my appreciation to my advisor Dr. Khairul Alam, who always showed tremendous support and faith in me. I would also like to thank the faculty members, Dr. Valerie Young, Dr. Dina Lopez, Dr. Dusan Sormaz, Dr. Yoon-Seok Choi, Dr. Michael Prudich, Dr. Greg Van Patten and Dr. Lauren McMills for serving on my PhD committee and for providing invaluable guidance. I especially acknowledge Dr. Dusan Sormaz and Dr. Lauren McMills for agreeing to join the committee so late in the process.

I would like to thank Dr. Srdjan Nestic, who has been a true mentor for me all these years. It has been an honor to witness the amazing growth that the ICMT experienced under his leadership and I certainly owe much of my professional and academic development to his unwavering encouragements and his inspiring example.

My most sincere appreciation goes to my colleague (and soon to be Dr.) Bruce Brown, whose enduring friendship means so much to me and whose support made every day of this journey simply enjoyable.

I am also grateful to Dr. David Young who always followed my progress with sincere interest and care and from whom I benefited greatly.

Great thanks go to all the graduate students who were part of the TLC Joint Industry Project between 2006 and 2012, namely Dr. Ziru Zhang, Ms. Dezra Hinkson, Dr. Thunyaluk (Kod) Pojtanabuntoeng, Ms. Ussama Kaewpradap, and Mr. Najmiddin Yaakob. It has been a pleasure and an honor to work with them.

Special thanks also to my colleagues at the ICMT, namely Dr. Sonja Richter, Dr. Yoon Seok Choi, Dr. Brian Kinsella for their camaraderie and support. I also benefitted immensely from the outstanding quality of the current and former technical staff of the Institute: Mr. Al

Schubert, Mr. John Goettge, Mr. Danny Cain, Mr. Cody Shafer, Mr. Phil Bullington, Mr. Steve Upton, and Mr. Alexis Barxias.

Much of the credit for creating such a wonderful working atmosphere at the Institute goes to my fellow graduate and undergraduate students, visiting scholars, post-doctoral researchers, staff members with whom I have been so fortunate to cross path. Among them, I would like to especially acknowledge Mrs. Edie Chalfant and Mrs. Becky Gill.

I am very grateful to my parents Pierre and Nadine Singer, my brother Jerome Singer and my sister Anne Scali for making me feel that home was never too far.

Finally, I would never have made it anywhere without the love and unconditional support of my wife Emily, and the joy of having such a beautiful family.

## TABLE OF CONTENTS

	Page
Abstract.....	3
Acknowledgments.....	5
List of figures.....	13
List of tables.....	30
CHAPTER 1            Introduction: Top of the line corrosion – a field reality.....	32
1.1            Flow regime .....	33
1.2            Condensation process.....	36
1.3            Water chemistry of H <sub>2</sub> O/CO <sub>2</sub> /H <sub>2</sub> S system.....	39
1.3.1 <i>Basics</i> .....	39
1.3.2 <i>Special case of condensed water</i> .....	41
1.4            Corrosion process .....	42
1.5            Corrosion product layer .....	43
1.6            CO <sub>2</sub> top of the line corrosion field cases.....	45
1.7            H <sub>2</sub> S Top of the line corrosion field cases.....	49
1.8            TLC monitoring.....	52
1.9            Mitigation methods .....	53
CHAPTER 2            Gaps in the current understanding and research objectives.....	56
2.1            Gaps in the current understanding.....	56
2.2            Research objectives .....	58
2.3            Central hypothesis .....	58
2.4            Dissertation outline .....	59

CHAPTER 3	Development of experimental setups for the study of TLC .....	60
3.1	Objective .....	60
3.2	Literature review.....	60
3.2.1	<i>Small scale apparatus</i> .....	60
3.2.1.1	Glass cell .....	60
3.2.1.2	High-pressure equipment .....	66
3.2.2	<i>Large scale systems</i> .....	71
3.3	Original experimental setups used in this research work .....	73
3.3.1	<i>Large scale flow loop setup</i> .....	73
3.3.1.1	Liquid Phase Composition.....	75
3.3.1.2	Gas Phase Composition .....	76
3.3.1.3	Chemistry in the condensed water.....	76
3.3.1.4	Acetic Acid Concentration .....	76
3.3.1.5	Safety considerations.....	77
3.3.2	<i>Standard test section</i> .....	77
3.3.3	<i>Challenges related to the experimental design</i> .....	80
3.3.4	<i>Test section focused on localized corrosion</i> .....	81
3.3.4.1	Experimental setup and procedure .....	81
3.3.4.2	Weight loss sample in flat slab .....	82
3.3.4.3	Carbon steel insert in flat slab .....	83
3.3.4.4	External cooling setup .....	84
3.3.5	<i>Localized Corrosion Characterization</i> .....	86
3.3.6	<i>Materials Characterization</i> .....	89

CHAPTER 4	Experimental study of uniform and localized TLC.....	93
4.1	Objective.....	93
4.2	Literature review.....	93
4.2.1	<i>Experimental work on CO<sub>2</sub> top of the line corrosion.....</i>	<i>93</i>
4.2.2	<i>Experimental work on H<sub>2</sub>S top of the line corrosion.....</i>	<i>97</i>
4.3	Parameteric study performed in flow loop using the standard test section.....	102
4.3.1	<i>Test matrix.....</i>	<i>102</i>
4.3.2	<i>Experimental results.....</i>	<i>105</i>
4.3.2.1	Influence of the CO <sub>2</sub> partial pressure .....	105
4.3.2.2	Influence of gas velocity .....	110
4.3.2.3	Influence of the concentration of undissociated acetic acid.....	114
4.3.2.4	Influence of the condensation rate .....	117
4.3.2.5	Influence of the gas temperature .....	120
4.3.2.6	Influence of the partial pressure of H <sub>2</sub> S.....	123
4.3.2.7	Combined effect of WCR and acetic acid concentration .....	128
4.3.2.8	Combined effect of pH <sub>2</sub> S and the acetic acid concentration.....	133
4.3.3	<i>Summary.....</i>	<i>141</i>
4.4	Localized sweet TLC study in large scale flow loop using the steel insert.....	146
4.4.1	<i>Test matrix.....</i>	<i>146</i>
4.4.2	<i>Experimental results.....</i>	<i>147</i>
4.4.2.1	Influence of the gas temperature and the water condensation rate....	147
4.4.2.1.1	TEST #1 - T <sub>gas</sub> =62°C .....	147
4.4.2.1.2	TEST #2 - T <sub>gas</sub> = 42°C.....	163

		10
4.4.2.1.3	TEST #3 - $T_{\text{gas}}=25^{\circ}\text{C}$ .....	174
4.4.2.2	Test #4 - Influence of the presence of acetic acid .....	186
4.4.3	<i>Summary</i> .....	195
CHAPTER 5	Direct observation of the condensation process .....	202
5.1	Objective .....	202
5.2	Indirect indication of the presence of droplets of condensed water .....	202
5.3	Experimental setup .....	204
5.4	Example A: In-situ observation of the condensation process .....	206
5.5	Example B: In-situ observation of the condensation process .....	209
5.6	Artificial water trap .....	212
5.7	Summary .....	214
CHAPTER 6	Characteristics of localized features at the top of the line .....	216
6.1	Objective .....	216
6.2	Methodology.....	216
6.3	Analysis of localized feature characteristics .....	217
6.3.1	<i>Overall view</i> .....	217
6.3.2	<i>SEM analysis of the corrosion product layer</i> .....	218
6.3.3	<i>Cross sectional analysis</i> .....	220
6.4	General comments on properties of the $\text{FeCO}_3$ layer.....	223
6.4.1	<i>Initiation of localized corrosion</i> .....	223
6.4.2	<i>Localized corrosion growth</i> .....	224
6.4.3	<i>Localized corrosion termination/sustainability</i> .....	225
6.5	Summary .....	226

CHAPTER 7	Descriptive model of localized corrosion at the top of the line.....	227
7.1	Objective.....	227
7.2	Literature review.....	227
7.2.1	<i>Water condensation rate (WCR) prediction</i> .....	227
7.2.1.1	Average WCR calculations considering water dropout .....	227
7.2.1.2	Local WCR calculations considering dropwise condensation theory ....	228
7.2.2	<i>Corrosion mechanisms under dewing conditions</i> .....	231
7.2.2.1	Empirical and semi empirical modeling of top of the line corrosion.....	231
7.2.2.2	Mechanistic modeling of top of the line corrosion .....	234
7.2.2.3	Modeling of localized corrosion .....	241
7.3	Descriptive model of localized TLC .....	244
7.3.1	<i>Summary of experimental observations</i> .....	244
7.3.2	<i>Model basis</i> .....	246
7.3.3	<i>Model overall narrative</i> .....	250
7.3.4	<i>Localized TLC model development</i> .....	251
7.3.4.1	Step 1 – Initial uniform corrosion .....	252
7.3.4.2	Step 2 – Formation and breakdown of the FeCO <sub>3</sub> layer .....	254
7.3.4.3	Step 3 – Determination of the sustainability of localized corrosion ....	257
7.3.4.4	Step 4 – Localized corrosion propagation.....	261
7.3.5	<i>Model validation</i> .....	261
7.3.6	<i>Model context and limitations</i> .....	264
7.4	Summary.....	266
CHAPTER 8	Conclusions and recommendations for future development.....	267

References .....	270
APPENDIX A          Momentum balance for flow regime prediction.....	285
A.1          Momentum balance and determination of liquid holdup.....	285
A.2          Transition between stratified and non-stratified .....	289
A.3          Transition between stratified-smooth and stratified-wavy.....	290
APPENDIX B          Simulation of flow disturbance created by test section geometry .....	292
B.1          Introduction .....	292
B.2          Objectives .....	295
B.3          Problem simulation (mesh creation) .....	296
B.4          Simulation results .....	298
B.5          Conclusions .....	300
APPENDIX C          Considerations on steel microstructure characteristics.....	308
C.1          Objectives .....	308
C.2          Methodology.....	308
C.3          Results analysis .....	309
C.3.1 <i>General Appearance of Corrosion Attack</i> .....	309
C.3.2 <i>Microstructural Analysis of Steel Samples</i> .....	309
C.4          Summary .....	311
APPENDIX D          Heat balance derivation for dropwise condensation.....	312
APPENDIX E          Description of the FREECORP model .....	317

## LIST OF FIGURES

	Page
Figure 1: Flow regime encountered in gas-liquid two-phase ion horizontal pipe (reproduced and adapted from [1] – License number 3134411241350) .....	35
Figure 2: Flow regime map generated for a mixture for air / water system VSL: Superficial liquid velocity and VSG: Superficial gas velocity P=1.013bar, T=25°C, D=6", Inclination=0° (Reproduced from [4]) .....	36
Figure 3: Example of a pressure/temperature diagram representing the phase equilibrium for water .....	37
Figure 4: Representation of offshore oil and gas production.....	38
Figure 5: Schematic representation of the locations along the pipeline affected by TLC (Reproduced from [36] - © NACE international 1999) .....	46
Figure 6: Schematic representation of zones where TLC was experienced (Reproduced from [36] - © NACE international 1999) .....	47
Figure 7: Typical ILI results for TLC – Most of the corrosion features are measured at the inlet of the line (Reproduced from [44] - © NACE international 2012) .....	48
Figure 8: Situation where “cold spot” corrosion can occur (Adapted from [46] - © NACE international 2010).....	49
Figure 9: Corrosion in the upper part of the pipe (Reproduced from [49] - © NACE international 1963) .....	50
Figure 10: Cross-sectional diagram of the pipe failure (Reproduced from [50] - © NACE international 1987).....	51

Figure 11: Representation of spray-pigging inside a flowline (Reproduced from [43] - © NACE international 2003).....	54
Figure 12: Typical TLC failures in CO <sub>2</sub> dominated environment (Reproduced from [38] - © NACE international 2006).....	56
Figure 13: TLC experimental device involving a cooled steel tube (Reproduced from [60] - © NACE international 2000).....	61
Figure 14: TLC experimental device focused on the composition of the condensate (Reproduced from [9] - © NACE international 2008) .....	62
Figure 15: Cooled finger probe concept (Reproduced from [62] - © NACE international 2012) .	63
Figure 16: Volatile inhibitor testing equipment (Reproduced from [56] - © NACE international 2010) .....	64
Figure 17: Experimental setup using Electrical Resistance (ER) probe (bottom) and water condensation process on the lid (top) - (Reproduced from [56] - © NACE international 2010) .....	65
Figure 18: Experimental setup designed for the observation of condensation (Reproduced from [63] - © NACE international 2011) .....	66
Figure 19: Autoclave setup designed by Olsen (Reproduced from [64] - © NACE international 1991) .....	67
Figure 20: Horizontal cooled tube concept (Reproduced from [62] - © NACE international 2012) .....	67
Figure 21: Wet gas autoclave design proposed by Zhang (Reproduced from [65] - © NACE international 2009).....	68

Figure 22: Quartz crystal microbalance design proposed by Jovancicevic (Reproduced from [67] - © NACE international 2012) .....	69
Figure 23: 20L autoclave setup (left) and details of the sample holder (right) .....	70
Figure 24: Small scale flow loop (top) and test section (bottom) proposed by Olsen (reproduced from [64] - © NACE international 1991) .....	71
Figure 25: Large scale flow loop proposed by Andersen and Dugstad (reproduced from [69] - © NACE international 2007).....	72
Figure 26: Test section proposed by Andersen and Nyborg (reproduced from [69] and [68] - © NACE international 2007 & 2009) .....	72
Figure 27: Schematic of the TLC flow loop #1 30 m long, Stainless Steel 316L, Maximum gas velocity: 17 m/s.....	74
Figure 28: Schematic of the TLC flow loop #2 20 m long, Stainless Steel 316L, Maximum gas velocity: 11 m/s.....	74
Figure 29: Schematic of the H <sub>2</sub> S flow loop (reproduced from [73] - © NACE international 2002) .....	75
Figure 30: Typical TLC test section equipped with condensed water collector (bottom left).....	78
Figure 31: Schematic view of the test section showing how corrosion samples are flush mounted inside the flow loop.....	78
Figure 32: a) Weight loss samples with Teflon coating at the back and the side and b) Sample holder configuration .....	79
Figure 33: View of the edge mismatch involved in using a flat sample in a 4" ID pipe .....	80
Figure 34: Initial flat slab test section .....	82
Figure 35: Stainless steel with weight loss probe ports (top view) .....	82

Figure 36: Stainless steel with weight loss probe ports (left) and view of the edge mismatch involved in using a flat sample in a flat slab (right).....	83
Figure 37: Design of the carbon steel insert in stainless steel slab (a) and b)) and pictures of the stainless steel slab (c) and d)) .....	83
Figure 38: Flat slab cooling setup .....	85
Figure 39: Stainless steel flat slab equipped with carbon steel insert and aluminum heat exchanger, a) with or b) without thermal insulation .....	85
Figure 40: Schematic representation of pitting corrosion.....	86
Figure 41: Schematic representation of mesa attack .....	87
Figure 42: Determination of the depth of localized corrosion features Free HAc= 1000 ppm and condensation rate= 1 mL/m <sup>2</sup> /s (P <sub>T</sub> : 3 bars, V <sub>g</sub> = 5 m/s, pCO <sub>2</sub> = 2 bars, T <sub>g</sub> : 70°C).....	88
Figure 43: Evaluation of percentage of surface area affected by localized corrosion Free HAc= 1000 ppm and condensation rate= 1 mL/m <sup>2</sup> /s (PT: 3 bars, V <sub>g</sub> = 5 m/s, pCO <sub>2</sub> = 2 bars, T <sub>g</sub> : 70°C) .....	89
Figure 44: Microstructure of the X65 carbon steel a) longitudinal cut, b) transversal cut.....	90
Figure 45: Optical analysis - General microstructure of the steel grade used for the “flat slab” experiments .....	92
Figure 46: Corrosion regimes in CO <sub>2</sub> /H <sub>2</sub> S corrosion (reproduced from Pots [92] - © NACE international 2002).....	98
Figure 47: Corrosion product formation as a function of temperature and H <sub>2</sub> S (Reproduced from [94] - © NACE international 2002) .....	99
Figure 48: General corrosion – Effect of the pCO <sub>2</sub> T <sub>g</sub> =70°C, [HAc] <sub>free</sub> =0ppm, V <sub>g</sub> =5m/s, Condensation rate=0.25 mL/m <sup>2</sup> /s.....	106

Figure 49: Surface analysis of corrosion product / $p\text{CO}_2 = 2$ bars ( $P_T: 3$ bars, $V_g = 5$ m/s, Free HAC: 0 ppm, $T_g: 70^\circ\text{C}$ , condensation rate= $0.25$ mL/m <sup>2</sup> /s, Exposure time: 21 days).....	106
Figure 50: Surface analysis of corrosion product / $p\text{CO}_2 = 0.13$ bar ( $P_T: 3$ bars, $V_g = 5$ m/s, Free HAC: 0 ppm, $T_g: 70^\circ\text{C}$ , condensation rate= $0.25$ mL/m <sup>2</sup> /s) .....	107
Figure 51: Surface analysis of corrosion product / $p\text{CO}_2 = 2$ bars ( $P_T: 3$ bars, $V_g = 5$ m/s, Free HAC: 0 ppm, $T_g: 70^\circ\text{C}$ , condensation rate= $0.25$ mL/m <sup>2</sup> /s) .....	108
Figure 52: Surface analysis with corrosion product / $p\text{CO}_2 = 7$ bars ( $P_T: 7.3$ bars, $V_g = 5$ m/s, Free HAC: 0 ppm, $T_g: 70^\circ\text{C}$ , condensation rate= $0.25$ mL/m <sup>2</sup> /s) Exposure time: 21 days .....	109
Figure 53: Localized corrosion - Effect of the $p\text{CO}_2$ $T_g = 70^\circ\text{C}$ , $[\text{HAC}]_{\text{free}} = 0$ ppm, $V_g = 5$ m/s, Condensation rate= $0.25$ mL/m <sup>2</sup> /s, Exposure time: 21 days .....	110
Figure 54: View of the weight loss sample at the beginning of test, taken via a port installed at the bottom of the line .....	111
Figure 55: Surface analysis with corrosion product / $V_g = 10$ m/s ( $P_T: 3$ bars, $p\text{CO}_2: 2$ bars, Free HAC: 0 ppm, $T_g: 70^\circ\text{C}$ , condensation rate= $0.25$ mL/m <sup>2</sup> /s) .....	113
Figure 56: General corrosion - Effect of the free HAC concentration $p\text{CO}_2 = 3$ bars, $T_g = 70^\circ\text{C}$ , Condensation rate= $0.25$ mL/m <sup>2</sup> /s, $V_g = 5$ m/s .....	114
Figure 57: Surface analysis with corrosion product / Free HAC= 1000 ppm ( $P_T: 3$ bars, $V_g = 5$ m/s, $p\text{CO}_2 = 2$ bars, $T_g: 70^\circ\text{C}$ , condensation rate= $0.25$ mL/m <sup>2</sup> /s).....	116
Figure 58: Localized corrosion - Effect of the free HAC concentration $p\text{CO}_2 = 3$ bars, $T_g = 70^\circ\text{C}$ , Condensation rate= $0.25$ mL/m <sup>2</sup> /s, $V_g = 5$ m/s, Exposure time: 21 days.....	117
Figure 59: General corrosion – Effect of the condensation rate $p\text{CO}_2 = 3$ bars, $T_g = 70^\circ\text{C}$ , $[\text{HAC}]_{\text{free}} = 0$ ppm, $V_g = 5$ m/s.....	118

Figure 60: Surface analysis without corrosion product ( $P_T$ : 3 bars, $V_g$ = 5 m/s , $p_{CO_2}$ = 2 bars, $T_g$ : 70°C, Free HAC= 0 ppm, Water condensation rate= 1 mL/m <sup>2</sup> /s) .....	119
Figure 61: Localized corrosion - Effect of the condensation rate $p_{CO_2}$ =3 bars, $T_g$ =70°C, $[HAC]_{free}$ =0 ppm, $V_g$ =5 m/s, Exposure time: 21 days .....	120
Figure 62: General corrosion – Effect of the gas temperature $p_{CO_2}$ =3bars, $[HAC]_{free}$ =0 ppm, $V_g$ =5 m/s, Condensation rate=0.25 mL/m <sup>2</sup> /s.....	121
Figure 63: Surface analysis with corrosion product / $T_g$ : 40°C (left) and $T_g$ : 80°C (right) ( $P_T$ : 3 bars, $V_g$ = 5 m/s, $p_{CO_2}$ = 2 bars, Free HAC: 0 ppm, condensation rate= 0.25 mL/m <sup>2</sup> /s) Exposure time: 21 days .....	122
Figure 64: Localized corrosion - Effect of the gas temperature $p_{CO_2}$ =3 bars, $[HAC]_{free}$ =0 ppm, $V_g$ = 5 m/s, Condensation rate=0.25 mL/m <sup>2</sup> /s, Exposure time: 21 days .....	123
Figure 65: Influence of the partial pressure of H <sub>2</sub> S Evolution of the general corrosion rate with the partial pressure of H <sub>2</sub> S ( $P_T$ : 3 bars, $p_{CO_2}$ : 2 bars, Free HAC: 0 ppm, $T_g$ : 70°C, WCR: 0.25 ml/m <sup>2</sup> /s, $V_g$ : 5 m/s .....	124
Figure 66: Localized corrosion – Influence of the H <sub>2</sub> S partial pressure $P_T$ : 3 bars, $p_{CO_2}$ : 2 bars, Free HAC: 0 ppm, $T_g$ : 70°C, WCR: 0.25 ml/m <sup>2</sup> /s, $V_g$ : 5 m/s, Exposure time: 21 days.....	124
Figure 67: Test 4 – CO <sub>2</sub> environment with traces of H <sub>2</sub> S – CO <sub>2</sub> /H <sub>2</sub> S: 500 ( $p_{CO_2}$ : 2 bars, $p_{H_2S}$ : 0.004 bar, No Free HAC, $T_g$ : 70°C, WCR: 0.25 ml/m <sup>2</sup> /s, $V_g$ : 5 m/s, Exposure time: 3 weeks) .....	126
Figure 68: Test 6 – CO <sub>2</sub> environment with H <sub>2</sub> S – CO <sub>2</sub> /H <sub>2</sub> S: 15 ( $p_{CO_2}$ : 2 bars, $p_{H_2S}$ : 0.13 bar, No Free HAC, $T_g$ : 70°C, WCR: 0.25 ml/m <sup>2</sup> /s, $V_g$ : 5 m/s, Exposure time: 3 weeks).....	127
Figure 69: General corrosion – Effect of HAC/Condensation rate $p_{CO_2}$ =3 bars, $T_g$ =70°C, $V_g$ =5m/s Set 1: Fixed $[HAC]_{free}$ = 100 ppm and varying Condensation rate = 0.05, 0.25 and 1 mL/m <sup>2</sup> /s .....	129

- Figure 70: Localized corrosion - Effect of HAc/Condensation rate  $p_{CO_2}=3$  bars,  $T_g=70^\circ C$ ,  $V_g=5$  m/s,  
Exposure time: 21 days Set 1: Fixed  $[HAc]_{free} = 100$  ppm and varying Condensation rate =  
0.05, 0.25 and 1 mL/m<sup>2</sup>/s..... 129
- Figure 71: General corrosion - Effect of HAc/Condensation rate  $p_{CO_2}=3$  bars,  $T_g=70^\circ C$ ,  $V_g=5$  m/s,  
Set 2: Fixed  $[HAc]_{free} = 1000$  ppm and varying Condensation rate = 0.05, 0.25 and 1  
mL/m<sup>2</sup>/s..... 130
- Figure 72: Localized corrosion - Effect of HAc/Condensation rate  $p_{CO_2}=3$  bars,  $T_g=70^\circ C$ ,  $V_g=5$  m/s,  
Exposure time: 21 days Set 2: Fixed  $[HAc]_{free} = 1000$  ppm and varying Condensation rate =  
0.05, 0.25 and 1 mL/m<sup>2</sup>/s..... 130
- Figure 73: General corrosion – Effect of HAc/Condensation rate  $p_{CO_2}=3$  bars,  $T_g=70^\circ C$ ,  $V_g=5$  m/s  
Set 3: Fixed Condensation rate = 0.05 mL/m<sup>2</sup>/s and varying  $[HAc]_{free} = 0, 100, 1000$  ppm 131
- Figure 74: Localized corrosion - Effect of HAc/Condensation rate  $p_{CO_2}=3$  bars,  $T_g=70^\circ C$ ,  $V_g=5$  m/s,  
Exposure time: 21 days Set 3: Fixed Condensation rate = 0.05 mL/m<sup>2</sup>/s and varying  
 $[HAc]_{free} = 0, 100, 1000$  ppm..... 131
- Figure 75: General corrosion – Effect of HAc/Condensation rate  $p_{CO_2}=3$  bars,  $T_g=70^\circ C$ ,  $V_g=5$  m/s  
Set 4: Fixed Condensation rate = 1 mL/m<sup>2</sup>/s and varying  $[HAc]_{free} = 0, 100, 1000$  ppm .... 132
- Figure 76: Localized corrosion - Effect of HAc/Condensation rate  $p_{CO_2}=3$  bars,  $T_g=70^\circ C$ ,  $V_g=5$  m/s,  
Exposure time: 21 days Set 4: Fixed Condensation rate = 1 mL/m<sup>2</sup>/s and varying  $[HAc]_{free} =$   
0, 100, 1000 ppm ..... 132
- Figure 77: Surface analysis without corrosion product Free HAc= 1000 ppm and condensation  
rate= 0.05 mL/m<sup>2</sup>/s (PT: 3 bars,  $V_g= 5$  m/s,  $p_{CO_2}= 2$  bars,  $T_g: 70^\circ C$ ) ..... 133

- Figure 78: Combined effect of the partial pressure of H<sub>2</sub>S and the concentration of free HAc  
Evolution of the general corrosion rate over time (P<sub>T</sub>: 3 bars, pCO<sub>2</sub>: 2 bars, pH<sub>2</sub>S: 0.004 bar,  
T<sub>g</sub>: 70°C, WCR: 0.25 ml/m<sup>2</sup>/s, V<sub>g</sub>: 5 m/s) ..... 135
- Figure 79: Localized corrosion – Influence of the free HAc concentration in CO<sub>2</sub>/H<sub>2</sub>S environment  
(P<sub>T</sub>: 3 bars, pCO<sub>2</sub>: 2 bars, pH<sub>2</sub>S: 0.004 bar, T<sub>g</sub>: 70°C, WCR: 0.25 ml/m<sup>2</sup>/s, V<sub>g</sub>: 5 m/s, Exposure  
time: 21 days)..... 135
- Figure 80: Combined effect of the partial pressure of H<sub>2</sub>S and the concentration of free HAc  
Evolution of the general corrosion rate over time (P<sub>T</sub>: 3 bars, pCO<sub>2</sub>: 2 bars, pH<sub>2</sub>S: 0.13 bar,  
T<sub>g</sub>: 70°C, WCR: 0.25 ml/m<sup>2</sup>/s, V<sub>g</sub>: 5 m/s) ..... 136
- Figure 81: Combined effect of the partial pressure of H<sub>2</sub>S and the concentration of free HAc  
Evolution of the general corrosion rate over time (P<sub>T</sub>: 3 bars, pCO<sub>2</sub>: 2 bars, Free HAc: 100  
ppm, T<sub>g</sub>: 70°C, WCR: 0.25 ml/m<sup>2</sup>/s, V<sub>g</sub>: 5 m/s) ..... 136
- Figure 82: Combined effect of the partial pressure of H<sub>2</sub>S and the concentration of free HAc  
Evolution of the general corrosion rate over time (P<sub>T</sub>: 3 bars, pCO<sub>2</sub>: 2 bars, Free HAc: 1000  
ppm, T<sub>g</sub>: 70°C, WCR: 0.25 ml/m<sup>2</sup>/s, V<sub>g</sub>: 5 m/s) ..... 137
- Figure 83: Localized corrosion – Influence of the free HAc concentration in CO<sub>2</sub>/H<sub>2</sub>S environment  
(P<sub>T</sub>: 3 bars, pCO<sub>2</sub>: 2 bars, Free HAc: 1000ppm, T<sub>g</sub>: 70°C, V<sub>g</sub>: 5 m/s, WCR: 0.25 ml/m<sup>2</sup>/s,  
Exposure time: 21 days)..... 137
- Figure 84: Test 7 – CO<sub>2</sub> environment with traces of H<sub>2</sub>S and acetic acid – CO<sub>2</sub>/H<sub>2</sub>S: 500 (pCO<sub>2</sub>: 2  
bars, pH<sub>2</sub>S: 4 mbar, Free HAc: 100 ppm, T<sub>g</sub>: 70°C, WCR: 0.25 ml/m<sup>2</sup>/s, V<sub>g</sub>: 5 m/s, Exp. time: 3  
weeks) ..... 138

Figure 85: Test 8 – CO <sub>2</sub> environment with traces of H <sub>2</sub> S and acetic acid – CO <sub>2</sub> /H <sub>2</sub> S: 500 (pCO <sub>2</sub> : 2 bars, pH <sub>2</sub> S: 4 mbar, Free HAC: 1000 ppm, T <sub>g</sub> : 70°C, WCR: 0.25 ml/m <sup>2</sup> /s, V <sub>g</sub> : 5 m/s, Exp. time: 3 weeks) .....	139
Figure 86: Test 9 – CO <sub>2</sub> environment with H <sub>2</sub> S and acetic acid – CO <sub>2</sub> /H <sub>2</sub> S: 15 (pCO <sub>2</sub> : 2 bars, pH <sub>2</sub> S: 0.13 bar, Free HAC: 1000 ppm, T <sub>g</sub> : 70°C, WCR: 0.25 ml/m <sup>2</sup> /s, V <sub>g</sub> : 5 m/s, Exp. time: 3 weeks) .....	140
Figure 87 : Test #1 - C1018(I) insert – High condensation (0.76-0.95 mL/m <sup>2</sup> /s) Analysis of the steel surface before cleaning of the corrosion product layer .....	149
Figure 88: SEM/EDS analysis of the corrosion product layer Medium condensation rate section (0.36-0.47 ml/m <sup>2</sup> /s).....	150
Figure 89: Pourbaix Diagram for Fe/H <sub>2</sub> O/CO <sub>2</sub> system at different temperature (40 and 70°C) [98] - Potential vs SHE - Area of interest is highlighted in red .....	151
Figure 90: Test #1 - Steel surface after removal of the corrosion product layer.....	152
Figure 91: Test #1 – C1018(I) insert – Surface profile analysis Upstream section - Low condensation (0.12-0.15 mL/m <sup>2</sup> /s) .....	154
Figure 92: Test #1 – C1018(I) insert – Surface profile analysis Upstream section - Medium condensation (0.36-0.47 mL/m <sup>2</sup> /s) .....	155
Figure 93: Test #1 – C1018(I) insert – Surface profile analysis .....	156
Figure 94: Test #1 - 3D profile of the bare steel surface High condensation rate section (0.76-0.95 ml/m <sup>2</sup> /s) .....	157
Figure 95: Test #1 - Feature depth distribution over the entire scanned steel surface .....	160
Figure 96: Test #1: Influence of the condensation rate on the localized corrosion rate.....	161

Figure 97: Test #1: Influence of the condensation rate and the exposure time on the pit/mesa depth .....	162
Figure 98: Test #1: Influence of the condensation rate on the percentage of the steel surface area affected by localized corrosion .....	163
Figure 99: Test #2 - Steel surface before removal of the corrosion product layer The flow direction is from left to right.....	165
Figure 100: Test #2 – SEM/EDX analysis Cooled section - High condensation (0.23 ml/m <sup>2</sup> /s)....	166
Figure 101: Test #2 – X65 insert - Steel surface before removal of the corrosion product layer The flow direction is from left to right.....	167
Figure 102: Test #2 – X65 insert – Surface profile analysis Upstream section - Low condensation rate: 0.1 ml/m <sup>2</sup> /s.....	168
Figure 103: Test #2 – X65 insert – Surface profile analysis Middle section - Medium condensation rate: 0.15 ml/m <sup>2</sup> /s.....	169
Figure 104: Test #2 – X65 insert – Surface profile analysis Downstream section – High condensation rate: 0.23 ml/m <sup>2</sup> /s.....	170
Figure 105: Test #2 - Feature depth distribution over the entire scanned steel surface .....	172
Figure 106: Test #2 - X65 Weight loss sample Influence of the condensation rate on the localized and average corrosion rate and pictures of the samples before and after the removal of the corrosion product layer.....	174
Figure 107: Test #3 - MEG Cooling system .....	175
Figure 108: Test #3 - Steel surface before removal of the corrosion product layer The flow direction is from left to right.....	176

Figure 109: Test #3 – SEM/EDX analysis Upstream section - Low condensation (0.038 ml/m <sup>2</sup> /s) .....	177
Figure 110: Pourbaix Diagram for Fe/H <sub>2</sub> O/CO <sub>2</sub> system Potential vs SHE - Area of interest in highlighted in red .....	177
Figure 111: Test #3 - Steel surface before removal of the corrosion product layer Upstream section - Low condensation (0.038 ml/m <sup>2</sup> /s) .....	178
Figure 112: Test #3 – X65 insert – Surface profile analysis Upstream section - Low condensation (0.038 ml/m <sup>2</sup> /s) .....	179
Figure 113: Test #3 – X65 insert – Surface profile analysis Middle section - Medium condensation (0.059 ml/m <sup>2</sup> /s) .....	180
Figure 114: Test #3 – X65 insert – Surface profile analysis Cooled section - High condensation (0.101 ml/m <sup>2</sup> /s) .....	181
Figure 115: Test #3 - Feature depth distribution over the entire scanned steel surface .....	183
Figure 116: Test #3 - X65 insert - Influence of the condensation rate on the pit/mesa depth ...	184
Figure 117: Test #3 - X65 Weight loss sample Influence of the condensation rate on the localized and average corrosion rate and pictures of the samples with before the removal of the corrosion product.....	185
Figure 118: Test #4 - C1018(III) insert - Steel surface before removal of the corrosion product layer -The flow direction is from left to right.....	187
Figure 119: Test #4 – SEM/EDX analysis Middle section – Medium condensation (0.4 ml/m <sup>2</sup> /s) .....	188
Figure 120: Test #4 - C1018(III) insert - Steel surface before removal of the corrosion product layer - The flow direction is from left to right.....	189

Figure 121: Test #4 – C1018(III) insert – Surface profile analysis Upstream section - Low condensation rate: 0.2 mL/m <sup>2</sup> /s .....	190
Figure 122: Test #4 – C1018(III) insert – Surface profile analysis Middle section - Medium condensation rate: 0.4 mL/m <sup>2</sup> /s .....	191
Figure 123: Test #4 – C1018(III) insert – Surface profile analysis Downstream section – High condensation rate: 0.7 mL/m <sup>2</sup> /s .....	192
Figure 124: Test #4 - Feature depth distribution over the entire scanned steel surface .....	194
Figure 125: Test #4 - Comparison between short and long term experiments Influence of the condensation rate on the pit/mesa depth .....	195
Figure 126: Influence of the acetic acid concentration and condensation rate .....	196
Figure 127: Influence of the acetic acid concentration and the water condensation rate Summary of results .....	198
Figure 128: Effect of the gas temperature and the WCR on the localized corrosion rate .....	200
Figure 129: Influence of the gas temperature and the water condensation rate Summary of results .....	201
Figure 130: Indication of the presence of droplets or of the artificial accumulation of condensed water (edge effect) at the same location on the surface of a sample Droplets of condensed water can be trapped on the side the flat sample since it cannot be perfectly flushed with the curved pipe surface (X65 samples before (left) and after (right) removal of the FeCO <sub>3</sub> layer) .....	203
Figure 131: In-situ video camera for live observation of corrosion phenomena .....	204
Figure 132: Test section equipped with video camera (left) – Observation of the condensation process on a weight loss sample (right) .....	205

Figure 133: Localized corrosion test – Condensation process A droplet of condensed water forms always at the same location .....	206
Figure 134: Localized corrosion test – Condensation process – Falling droplet cycle.....	207
Figure 135: Surface analysis of the surface wetted by the droplet.....	208
Figure 136: Surface profile of the surface wetted by the droplet Weight loss samples after the removal of the corrosion product layer .....	209
Figure 137: X65 WL sample – Observation of the condensation process .....	210
Figure 138: X65 WL sample – Exposure time 99 days .....	211
Figure 139 : Test #4 – Artificial indentations created on the steel insert before the beginning of the test. ....	212
Figure 140: Test #4 - C1018(III) insert – Morphology of the artificial indentation after the end of the experiment.....	213
Figure 141: Weight loss sample at the end of the test.....	217
Figure 142: XRD analysis identifying the presence of $\text{FeCO}_3$ .....	218
Figure 143: EDS analysis of the corrosion product layer and associated breakdowns .....	219
Figure 144: Cross section analysis – Morphology of large localized features .....	220
Figure 145: Cross section analysis – $\text{FeCO}_3$ coverage on the side of the localized feature .....	221
Figure 146: Cross section analysis – $\text{Fe}_3\text{C}$ coverage on the side of the localized feature.....	222
Figure 147: Cross section analysis - EDS Line scan (along the red line).....	223
Figure 148: Localized corrosion initiation $\text{FeCO}_3$ layer initial coverage after 2 days of exposure .....	224
Figure 149: Localized corrosion features growth underneath $\text{FeCO}_3$ layer $T=70^\circ\text{C}$ , WL X65, HAc=0 ppm, WCR= $1 \text{ mL/m}^2/\text{s}$ , Exposure time= 21 days.....	225

Figure 150: FeCO <sub>3</sub> top layer collapsing T=70°C, WL X65, HAc=1000 ppm, WCR= 1 ml/m <sup>2</sup> /s, Exposure time= 21 days .....	225
Figure 151: FeCO <sub>3</sub> layer regaining coverage on the metal surface T=70°C, WL X65, HAc=1000 ppm, WCR= 1 ml/m <sup>2</sup> /s , Exposure time= 21 days .....	226
Figure 152: Transport, source and sink of Fe <sup>2+</sup> under a thin film of condensed water during TLC (Reproduced from [75] - © NACE international 2003) .....	235
Figure 153: The simplification from a 3D (droplet) to 1D (liquid film) approach reproduced from (Reproduced from [83] - © NACE international 2007) .....	238
Figure 154: Schematic of the corrosion calculations in a growing droplet .....	240
Figure 155: Mechanism for initiation and growth of mesa attack (Reproduced from [116] - © NACE international 1998).....	242
Figure 156: Mechanism for initiation and growth of mesa attack (Reproduced from [118] - © NACE international 2004).....	243
Figure 157: Schematic representation of the galvanic corrosion approach.....	247
Figure 158: Fe <sup>2+</sup> concentration and pH at different FeCO <sub>3</sub> saturation levels and different temperature - T=25°C, pCO <sub>2</sub> =3 bars.....	248
Figure 159: Fe <sup>2+</sup> concentration and pH at different FeCO <sub>3</sub> saturation levels and different temperature - T=70°C, pCO <sub>2</sub> =3 bars.....	248
Figure 160: Schematic representation of the localized condensation approach .....	249
Figure 161: Initial steps of uniform corrosion on “film-free” steel surface T <sub>steel</sub> =35°C, WCR=1 ml/m <sup>2</sup> /s, pCO <sub>2</sub> =3 bars, SS <sub>FeCO<sub>3</sub></sub> max=10 100% of the steel surface is corroded uniformly – No localized corrosion .....	253

Figure 162: Formation of a uniform FeCO <sub>3</sub> layer after short term exposure T <sub>gas</sub> =70°C, WCR=0.25 ml/m <sup>2</sup> /s, pCO <sub>2</sub> =8 bars, Undissociated HAC=0 ppm Exposure time: 2 days – No Localized corrosion .....	255
Figure 163: Schematic representation of the initiation step of localized corrosion at the top of the line .....	255
Figure 164: Unsustainable localized corrosion T <sub>steel</sub> =35°C, WCR=0.05 ml/m <sup>2</sup> /s, pCO <sub>2</sub> =3 bars, SS <sub>FeCO<sub>3</sub></sub> max=10, A <sub>Localized</sub> =4% Localized corrosion cannot not be sustained on 50% of the surface area .....	258
Figure 165: Unsustainable localized corrosion T <sub>steel</sub> =35°C, WCR=0.05 ml/m <sup>2</sup> /s, pCO <sub>2</sub> =3 bars, SS <sub>FeCO<sub>3</sub></sub> max=10, A <sub>Localized</sub> =3% 3% of the steel surface can sustain localized corrosion at rate of 1 mm/year.....	259
Figure 166: Sustainable localized corrosion T <sub>steel</sub> =35°C, WCR=0.5 ml/m <sup>2</sup> /s, pCO <sub>2</sub> =3 bars, SS <sub>FeCO<sub>3</sub></sub> max=10, A <sub>Localized</sub> =35% 35% of the steel surface can be corroded locally at a rate of 1 mm/year.....	260
Figure 167: Sustainable uniform corrosion T <sub>steel</sub> =35°C, WCR=1.4 ml/m <sup>2</sup> /s, pCO <sub>2</sub> =3 bars, SS <sub>FeCO<sub>3</sub></sub> max=10, A <sub>Localized</sub> =100% 100% of the steel surface can sustain a corrosion of 1 mm/year.	260
Figure 168: Model validation / Comparison between experimental data and model predictions SS <sub>FeCO<sub>3</sub></sub> max=10.....	262
Figure 169: Model validation / Comparison between experimental data and model predictions SS <sub>FeCO<sub>3</sub></sub> max=10.....	263
Figure 170: Model validation / Comparison between experimental data and model predictions SS <sub>FeCO<sub>3</sub></sub> max=10 at T <sub>gas</sub> =60°C, SS <sub>FeCO<sub>3</sub></sub> max=26 at T <sub>gas</sub> =42°C and SS <sub>FeCO<sub>3</sub></sub> max=53 at T <sub>gas</sub> =25°C	264
Figure 171: Narrative of localized TLC - (Adapted from [118] - © NACE international 2004).....	266

Figure 172: Schematic of the cross section of a pipe in gas-liquid two-phase flow ( $A_G$ : area covered by gas, $A_L$ : area covered by liquid, $S_G$ : wetted length of the gas phase, $S_L$ : wetted length of the liquid phase, $S_i$ : the boundary length at gas-liquid interface, $h_L$ : liquid holdup) .....	285
Figure 173: 4" ID stainless steel pipe with top part removed .....	293
Figure 174: Difference in pipe curvature between 4" and a 30" ID pipes .....	293
Figure 175: Schematic representation of the Flat Stainless steel Section .....	294
Figure 176: Frontal and cross sectional view of the Flat Stainless steel Section FSS .....	294
Figure 177: Cross section representation of the stainless steel section .....	294
Figure 178: Picture of the actual stainless steel section .....	295
Figure 179: Inside of the pipe – View of the leading edge of the slab .....	295
Figure 180: 3D approach – Mesh of slab (entire view and close-up on the slab) .....	297
Figure 181: 3D approach – Velocity magnitude in m/s (mostly velocity I the direction of the flow) – $V_G$ : 5 m/s Selection of view planes .....	301
Figure 182: 3D approach – Velocity magnitude in m/s (mostly velocity I the direction of the flow) – $V_G$ : 5 m/s Selection of view planes .....	302
Figure 183: 3D approach – Velocity magnitude in m/s (mostly velocity I the direction of the flow) – $V_G$ : 5 m/s Selection of view planes – Details on the slab section .....	303
Figure 184: 3D approach – Velocity magnitude in m/s (mostly velocity I the direction of the flow) – $V_G$ : 5 m/s Longitudinal plane - The flow direction is from left to right .....	304
Figure 185: 3D approach – Turbulence intensity (non dimensional ratio of velocities) – $V_G$ : 5 m/s Longitudinal plane - The flow direction is from left to right .....	305
Figure 186: 3D approach – Velocity magnitude in m/s (mostly velocity I the direction of the flow) – $V_G$ : 10 m/s Longitudinal plane - The flow direction is from left to right .....	306

Figure 187: 3D approach – Turbulence intensity (non dimensional ratio of velocities) – $V_G$ : 10 m/s Longitudinal plane - The flow direction is from left to right.....	307
Figure 188: Optical analysis - General microstructure and general appearance of corrosion attack at the bottom of a shallow pit observed in steel sample from Baseline Test #1 (C1018(I)) .....	310
Figure 189: Optical analysis - General microstructure and general appearance of corrosion attack at the bottom of a shallow pit observed in steel sample from Test #4 (C1018(III)) .....	311
Figure 190: Optical analysis - General microstructure and general appearance of corrosion attack at the bottom of a shallow pit observed in steel sample from Test #2 (X65).....	311
Figure 191: Temperature gradient for a single droplet (Reproduced from [83] - © NACE international 2007).....	313

## LIST OF TABLES

	Page
Table 1: Chemical analysis of the cylindrical carbon steel samples used in the experiments.....	90
Table 2: Hardness (HRB) results of the X65 steel .....	90
Table 3: Chemical composition (wt.pct.) of steel samples used in the experiments C1018 steel insert (I): Baseline Test #1; (III): Test #4.....	91
Table 4: Chemical composition (wt.pct.) of steel samples used in the experiments X65 steel insert used for Test #2 and for Test #3. ....	91
Table 5: Baseline conditions for the parametric study* .....	103
Table 6: Range of variables used for the parametric study .....	104
Table 7: Wall temperature.....	104
Table 8: Summary of general and localized corrosion results – Sweet TLC series .....	144
Table 9: Summary of general and localized corrosion results – Sour TLC series.....	145
Table 10: Localized condensation/corrosion study - Test matrix .....	146
Table 11: Test #1 – Test conditions .....	148
Table 12 : Test #1 – Localized corrosion rate analysis .....	158
Table 13: Test #2 –Test conditions .....	164
Table 14 : Test #2 – Localized corrosion rate analysis .....	171
Table 15: Test #3 - Test conditions .....	175
Table 16 : Test #3 – Localized corrosion rate analysis .....	182
Table 17: Test #4 - Test conditions .....	186
Table 18 : Test #4 – Localized corrosion rate analysis .....	193
Table 19: Test #4 - Corrosion analysis on the artificial holes.....	214

Table 20: TLC feature characteristics study - Test conditions .....	216
---	-----

## CHAPTER 1 INTRODUCTION: TOP OF THE LINE CORROSION – A FIELD REALITY

Since the drilling and completion of the first oil well, the oil and gas industry has had to battle many types of corrosion, some more serious than others. Top of the line corrosion (TLC) is one of these types and probably one of the most recent to be discovered, as it was first identified only in the 1990s. At that time, it was regarded as a curiosity more than a real problem. However, top of the line corrosion has been progressively recognized as a major cause of pipeline failure all over the world and has become the focus of intense research relating to its mechanism, prevention and prediction.

The transportation of fluid is a critical step for the oil and gas industry. When the fluid comes directly from the oil well, it is usually unprocessed and consists multiple phases, *i.e.*, a mixture of oil, solids, gas and water (as brine). The presence of water can lead to considerable corrosion problems on the internal walls of the pipelines, though the use of corrosion inhibitors dissolved in the oil or water phase can usually provide some protection if it is applied effectively. The phenomena of interest in this study are related to the transportation of gas containing condensable liquids (“wet gas”) and, more precisely, the corrosion issues that occur when significant heat exchange is present between the pipelines and the surroundings (frozen land, deep-sea water, etc.). The unprocessed water and hydrocarbon vapor flowing through the pipe have the potential to condense particular components on the cold walls, one of them being water, forming a thin film and/or droplets of liquid. The condensed water can contain corrosive species such as organic acids and dissolved corrosive gases (e.g. carbon dioxide or hydrogen sulfide). Typical carbon steels can corrode rapidly under these conditions, which could lead to a loss of pipeline integrity and potential failure. Consequences exceed loss of production. The use of standard corrosion inhibitors to combat TLC is usually inefficient since the inhibitors

themselves are non-volatile and typically do not provide any protection to the top of the pipeline, at least in stratified flow regime.

Top of the line corrosion is consequently a complex phenomenon for which several processes interact:

- **Fluid mechanics:** Knowing the location of the gas and liquid phases on the cross section of the pipe is the first step in determining whether TLC is an issue.
- **Heat and mass transfer:** TLC is the consequence of water vapor condensation on the pipe wall, which is driven by a gradient of temperature across the pipe wall.
- **Chemistry:** Corrosive gases dissolve in the condensed water and generate a number of species, some of them acidic, which can react to form corrosion products.
- **Electrochemistry:** The acidity of the condensed water drives the corrosion process.

The present chapter gives an in-depth description of the main mechanisms involved in TLC, covering all the processes listed above, and also draws comparisons with reported field experience.

### 1.1 Flow regime

The issue of TLC occurs only when specific flow conditions are met. Probably the most important one is the flow regime. The transportation of fluids coming from the well involves a mixture of gas (containing water vapor, hydrocarbon vapors, carbon dioxide, and hydrogen sulfide), liquid hydrocarbon and water. At the temperatures and pressures encountered in flowline conditions, the presence of liquid water in contact with the pipe steel is responsible for corrosion. As mentioned earlier, the injection of corrosion inhibitor, often water soluble, does provide effective protection against metal loss. Consequently, any parts of the pipe surface wetted - even intermittently - by the inhibited water, should benefit from some level of

protection. Some flow conditions lead to this kind of scenario while some others do not. The most common type of flow encountered in the transport of unprocessed hydrocarbon fluids is gas-oil-water three-phase flow (oil here meaning liquid hydrocarbons). Some fields may generate little or no liquid hydrocarbons but they all produce non-condensable gas (light hydrocarbons, CO<sub>2</sub>, etc.) and water vapor (saturated water vapor in most cases). When no liquid hydrocarbon is produced, the flow type is described as gas-water two-phase flow.

Within gas-oil-water three-phase flow or gas-liquid two-phase flow, three major flow regimes may be encountered. Their characteristics and corresponding flow conditions are described below:

- **Stratified flow (wavy or smooth):** At low gas and liquid flow rates, the gas and liquid phases are clearly segregated and the gas-liquid interface is smooth. With increased liquid and gas velocity, waves can be initiated at the gas-liquid interface.
- **Intermittent flow (slug or plug):** At higher liquid velocity, the crests of the waves can reach the top of the pipe, and a liquid connection (slug) between the top and the bottom of the line is formed.
- **Annular flow:** When gas velocity increases but liquid velocity is kept low, droplets of liquid are atomized and transported to the upper pipe wall surface, forming a liquid film covering the whole circumference of the pipe, with the gas flowing in the core and the majority of liquid flowing at the bottom.

These main flow regimes encountered in two-phase horizontal flow are described in Figure 1. In an inclined or vertical pipeline, only the intermittent and annular flow regimes can occur.

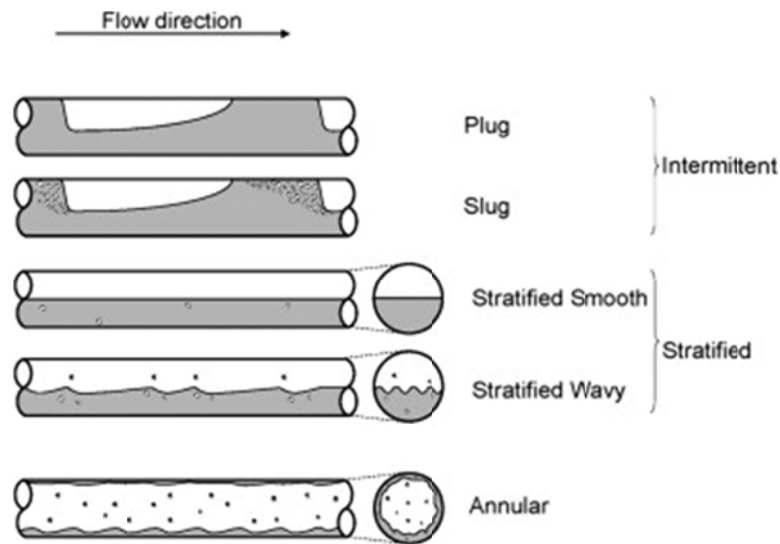


Figure 1: Flow regime encountered in gas-liquid two-phase in horizontal pipe (reproduced and adapted from [1] – License number 3134411241350)

Only one of these flow regimes (stratified flow) leads to TLC issues. In the case of slug or annular flow, the liquid phase (water or oil), which can be inhibited, is at least intermittently in contact with the pipe surface.

It is therefore important to be able to predict under which conditions stratified flow will be encountered along the length of a pipeline. The most widely accepted mechanism for the transition between stratified and slug/annular flow is the wave-mixing mechanism developed by Milne-Thomson et al. [2] and, later, Taitel et al. [3].

The basics of flow modeling calculations are shown in 0 and a flow map (Figure 2) can be generated using this methodology. The model developed for the determination of the flow regime transitions in intermittent flow (with annular and dispersed bubble) is not described in this study.

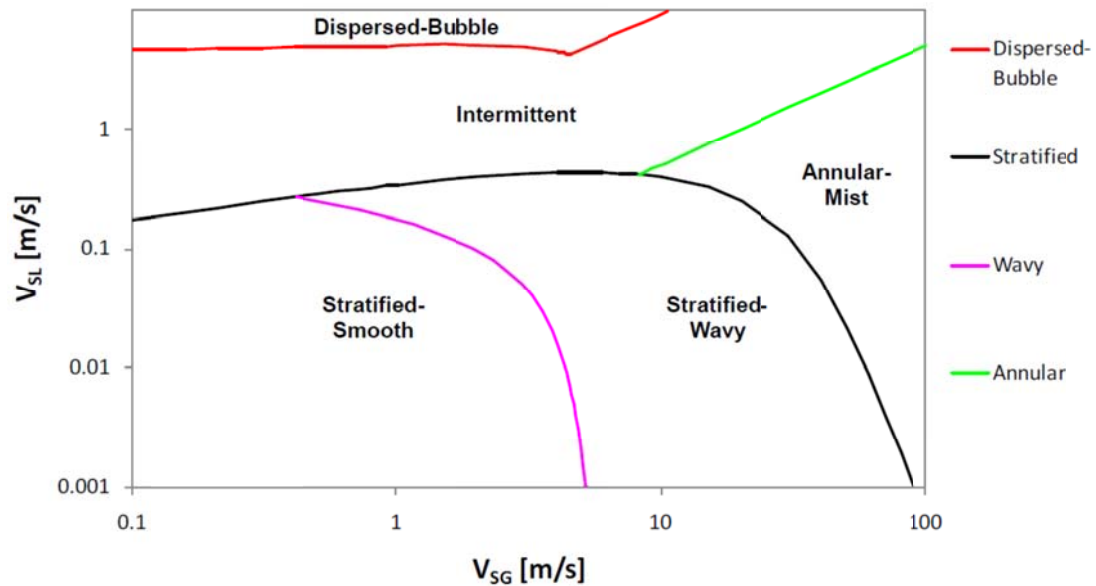


Figure 2: Flow regime map generated for a mixture for air / water system  
 VSL: Superficial liquid velocity and VSG: Superficial gas velocity  
 P=1.013bar, T=25°C, D=6", Inclination=0° (Reproduced from [4])

In terms of TLC, the area of risk is below the "stratified" line (black line in Figure 2), where the gas and liquid flow rates are low enough that the water vapor can condense freely on the upper pipe steel surface, while the bulk liquid water phase, which can be inhibited, stays at the bottom of the line.

## 1.2 Condensation process

Liquid water, as brine, is always present in the well together with a variety of hydrocarbons. Considering the many thousands of years it took for the fluids to accumulate, water vapor can be assumed to be in equilibrium with the liquid water. This is also true for a number of hydrocarbons, although the lighter ones (methane, ethane, etc.) are always in a superheated state. As the fluids are extracted from the well through production tubing and flowlines, the pressure and temperature decrease. A decrease in pressure tends to move the equilibrium towards the super-heated zone (leading to more evaporation of the liquid water)

while a decrease in temperature leads to the formation of water by condensation of the vapor phase, as shown in Figure 3.

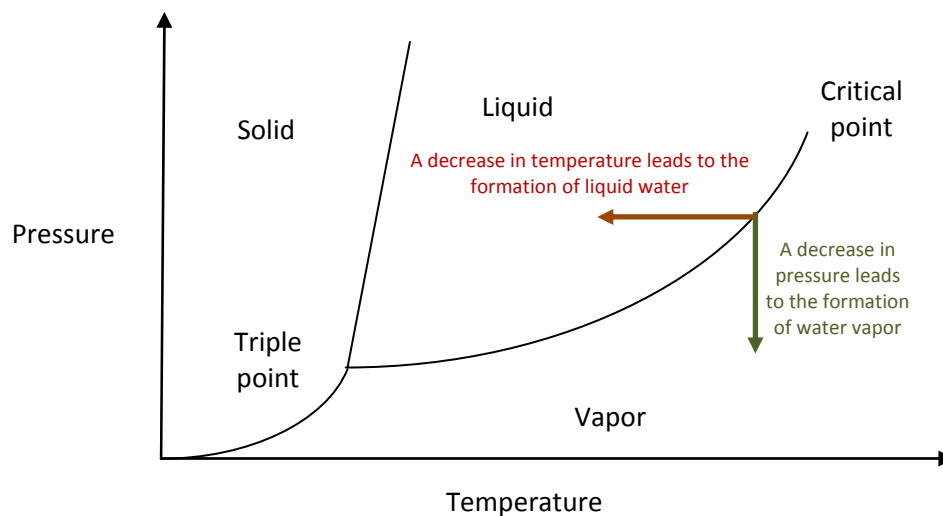


Figure 3: Example of a pressure/temperature diagram representing the phase equilibrium for water

These two changes in conditions “work” in opposite directions but, practically speaking, the drop in temperature always has a much greater effect. Consequently, the water vapor should always remain at saturation as long as the produced fluids are not artificially separated. Gas and liquid treatment will effectively remove the water from the produced fluids but this complex process is only typically done at the production facilities.

A simple representation of a typical off-shore oil and gas transport system is shown in Figure 4. Since particular segments of the transmission infrastructure involve vertical tubing, from the reservoir to the subsea wells, the flow regime is never stratified and no TLC should be expected. However, once the fluid enters the flowlines, *i.e.*, the sections of pipe between the wells, the platform and the onshore facilities, stratified flow can be expected, depending on the line topography. Under these conditions, there is no reason to believe that any inhibited water

present at the bottom of the line could reach the top of the pipe, and TLC can therefore occur in an un-mitigated environment.

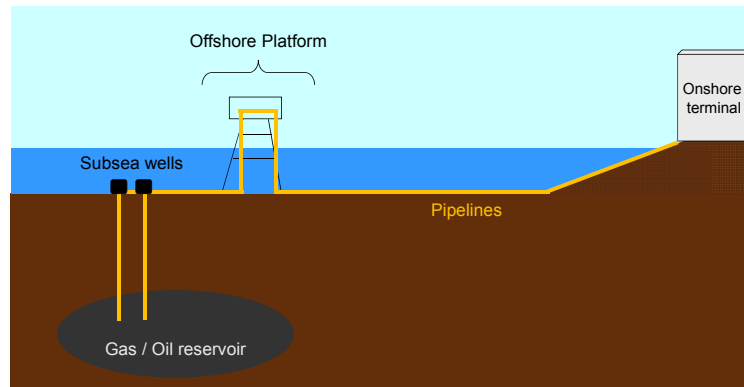


Figure 4: Representation of offshore oil and gas production

The top part of the pipeline will corrode if liquid water comes into contact with the steel surface. This is why a significant amount of water vapor condensation is required for there to be any significant amount of corrosion. In practical terms, the main factor affecting the amount of water that can condense is the gas temperature; the hotter the fluid is, the higher is the saturated water vapor pressure. However, other parameters do influence the process. The rate of water condensation is dependent on not just the amount of water vapor carried in the gas phase but also on the gradient of temperature with respect to the outside environment. Thermal insulation or burial of the pipeline is particularly important, as it will limit the heat transfer between the pipeline and the outside environment and consequently limit the rate of water condensation. Finally, the nature of the outside environment also plays a role, as more heat can be “extracted” from the produced fluid if the pipe is in contact with flowing water (river or maritime current) as opposed to air or soil.

In summary, several key factors can be identified in assessing whether a pipeline will suffer from significant water condensation:

- The water vapor pressure of the produced fluid
- The gradient of temperature between the produced fluid and the outside environment
- The nature of the outside environment (air, sea or river)
- The extent of thermal insulation or pipeline burial

A detailed discussion of modeling approaches developed to determine the rate of condensation is presented in Chapter 7.2.1.

### 1.3 Water chemistry of H<sub>2</sub>O/CO<sub>2</sub>/H<sub>2</sub>S system

#### 1.3.1 Basics

Understanding the water chemistry is a necessary step in assessing the severity of a corrosion attack. The basic principles of the H<sub>2</sub>O/CO<sub>2</sub>/H<sub>2</sub>S system are presented below, with a special focus on condensed water. It should be noted that parts of this section are taken directly from previous publications from the author of this dissertation [5].

The different chemical and electrochemical reactions involved in CO<sub>2</sub> corrosion are described below:

- Water dissociation 
$$H_2O_{(l)} \rightleftharpoons H_{(aq)}^+ + OH_{(aq)}^- \quad \text{Eq (1-1)}$$
- Carbon dioxide dissolution 
$$CO_{2(g)} \rightleftharpoons CO_{2(aq)} \quad \text{Eq (1-2)}$$
- Carbon dioxide hydration (slowest step) 
$$CO_{2(aq)} + H_2O_{(l)} \rightleftharpoons H_2CO_{3(aq)} \quad \text{Eq (1-3)}$$
- Carbonic acid dissociation 
$$H_2CO_{3(aq)} \rightleftharpoons H_{(aq)}^+ + HCO_{3(aq)}^- \quad \text{Eq (1-4)}$$
- Bicarbonate ion dissociation 
$$HCO_{3(aq)}^- \rightleftharpoons H_{(aq)}^+ + CO_{3(aq)}^{2-} \quad \text{Eq (1-5)}$$

Organic acids are also often present in produced fluids. The most common and abundant among them is acetic acid [6], a weak acid whose dissociation is expressed below:



In addition, as more and more field conditions involve the presence of large quantities of H<sub>2</sub>S, the prediction of sour corrosion appears today as one of the most pressing matters in the oil and gas industry [7]. The understanding of H<sub>2</sub>S corrosion mechanisms lags significantly and majorly behind that of CO<sub>2</sub>, even though much effort has already been made in this direction [8]. Although H<sub>2</sub>S gas is about three times more soluble in water than CO<sub>2</sub> gas (at 25°C,  $K_{sol}^{H_2S} = 0.1$  mol/L/bar and  $K_{sol}^{CO_2} = 0.03$  mol/L/bar), the acidity constant for H<sub>2</sub>S is about four times lower than for carbonic acid (at 25°C,  $K_a^{H_2S} = 9.3 \cdot 10^{-8}$  mol/L and  $K_a^{H_2CO_3} = 4.6 \cdot 10^{-7}$  mol/L). Hence, the effect of H<sub>2</sub>S gas on decreasing the solution pH is approximately the same as for CO<sub>2</sub> gas. The different chemical and electrochemical reactions involved in H<sub>2</sub>S corrosion are described below:



In oil and gas production scenarios, the water phase may be formed by condensation of water vapor, or due to the presence of formation water. In the latter case, the water contains significant amounts of salts (chloride, sodium and calcium ions to cite the most common species). The concentration of these salts can be measured if a liquid sample is taken, since they stay in solution. This is not the case for carbonic and sulfide species, which leave the water

phase when the sample is depressurized. The *ex-situ* measurement of pH is consequently of limited value. The most reliable method for evaluating the *in-situ* pH is to measure species concentrations and to back-calculate the pH of the water under realistic temperature and CO<sub>2</sub>/H<sub>2</sub>S pressures. This can be performed by solving the electro-neutrality equation (Eq (1-10)), considering the sum of the cations and anions concentrations as well as the iron concentration are known. All the other terms can be expressed as a function of the hydrogen ions concentration:

$$\sum_i x [Cation_i^{x+}] + 2[Fe^{2+}] + [H^+] = [OH^-] + [H_2CO_3^-] + 2[CO_3^{2-}] + [HS^-] + 2[S^{2-}] + [CH_3COO^-] + \sum_i y [Anion_i^{y-}] \quad \text{Eq (1-10)}$$

In the field, typical CO<sub>2</sub> contents range from 0.1 to 10 mol% (although much higher concentrations have been reported). In terms of H<sub>2</sub>S, gas contents ranging from 5 to 5000 ppm are also common. Considering that the production pressures and temperatures in flowlines typically range from 30 to 200 bars and from 5 to 100°C, respectively, the pH of condensed water should vary between 3 and 4.5 [9]. However the presence of formation water [10] and the injection of a strong base (a common corrosion mitigation method) result in significantly higher in-situ pH (practically between 6 and 8).

### 1.3.2 Special case of condensed water

The only difference between the chemical composition of the water at the bottom of the line (brine) and the water at the top is the mineral content, which is nil in freshly condensed water. In addition, any base injected in-line as part of a corrosion mitigation method would typically have no effect at the top of the line. Consequently, the electro-neutrality equation for condensed water becomes:

$$[H^+] = [OH^-] + [H_2CO_3^-] + 2[CO_3^{2-}] + [HS^-] + 2[S^{2-}] + [CH_3COO^-] \quad \text{Eq (1-11)}$$

Determining the pH of the condensed water requires knowing the partial pressure of acetic acid, in addition to the CO<sub>2</sub> and H<sub>2</sub>S content:

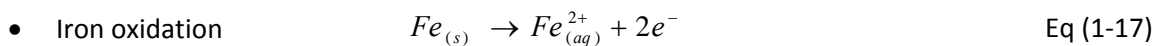
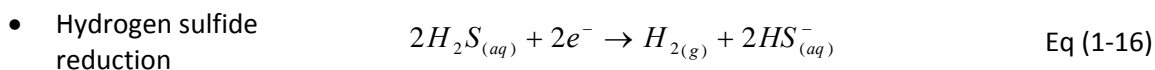
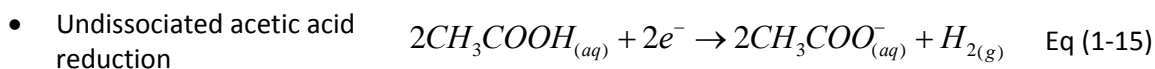
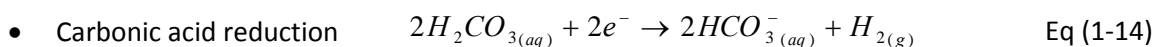
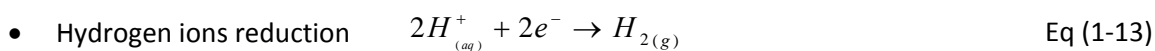


The typical pH value of freshly condensed water is consequently quite low and varies between 3 and 4. However, as the corrosion process takes place, iron ions are released in solution as acidity is consumed, which rapidly increases the pH; especially when the rate of condensed water renewal is low.

#### 1.4 Corrosion process

CO<sub>2</sub> corrosion has been extensively studied by many different investigators [11-24]. Consequently, the main corrosion mechanisms for this system are now well defined and have been incorporated into prediction models [25,26].

The main cathodic and anodic reactions involved are listed below:



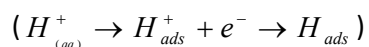
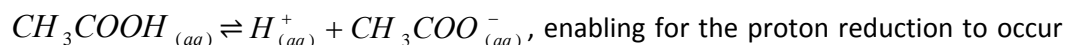
It should be noted that the acetic acid and, to some degree, the carbonic acid direct reduction reactions are currently subject to debate regarding whether or not they actually occur to any significant degree in the environment considered. It is understood that the presence of

acetic acid leads to a considerable increase in the corrosion rate [6, 18]. However, two main pathways have been presented in order to explain this effect:

1. Direct reduction - The acid is directly reduced at the metal surface



2. The buffering effect – The weak acid present close to the metal surface first dissociates

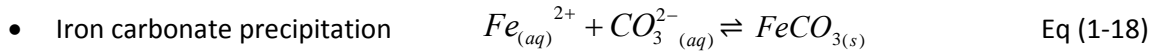


Following the pathway of direct reduction, the concentration of acetic acid is directly linked to the corrosion rate, as more acid leads to a higher steel dissolution rate. Considering the buffering effect, the acetic acid only acts as a provider of hydrogen ions and the corrosion rate will increase until it eventually falls under charge transfer control. Distinguishing between the two pathways is not an easy task, but recent work seems to favor the buffering effect over the direct reduction [19, 20]. Although it is too early to conclude, the same behavior can be expected for the carbonic acid reduction.

In terms of the hydrogen reduction, the direct reduction at the metal surface has been clearly observed through a number of experimental studies [21, 22].

### 1.5 Corrosion product layer

As a direct product of the dissolution of steel, the concentration of  $Fe^{2+}$  ions can increase in solution depending on the flow conditions. In a top of the line scenario, the  $Fe^{2+}$  concentration can quickly reach a relatively high level, especially if the rate of water condensation is slow. In  $CO_2/H_2S/H_2O$  systems, two main families of corrosion product can form: iron carbonate ( $FeCO_3$ ) and iron sulfide ( $Fe_xS_y$ ).



The choice of the expression of the equilibrium constant  $K_{sp,FeCO_3}$  governing the iron carbonate precipitation/dissolution is of importance, as many empirical equations exist. Recent work proposed by Sun [27] suggests using the following equation derived from the work of Greenberg [28] and Silva [29]:

$$\log K_{sp,FeCO_3} = -59.3498 - 0.041377 \times T_k - \frac{2.1963}{T_k} + 24.5724 \times \log(T_k) + 2.518 \times I^{0.5} - 0.657 \times I \quad \text{Eq (1-19)}$$

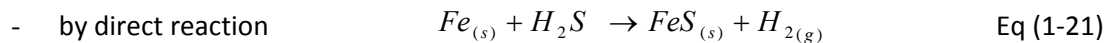
with:  $K_{sp, FeCO_3}$ : Solubility constant for iron carbonate ( $\text{mol}^2/\text{l}^2$ )

$T_k$ : Temperature (K)

$I$ : Ionic strength (mol/l)

The influence of acetic acid on the  $FeCO_3$  film characteristics and formation is not well understood and no widely accepted theory has emerged [12-14].

- Iron sulfide formation



The chemical reactions proposed above are the most widely accepted [27] reactions describing sulfide chemistry in aqueous solution. Other authors [30-32] have proposed different pathways for FeS formation and dissolution. An example is the so called “direct” reaction:  $Fe_{(s)} + H_2S \rightarrow FeS_{(s)} + H_2$  where it is assumed that iron dissolution does not occur; rather, a fast oxidation of solid iron transforms it directly into solid iron sulfide attached to the steel

surface. The mechanism of this reaction is still under investigation, including the role of various species in the formation of the different types of iron sulfide compounds.

The uncertainty related to the expressions for the equilibrium constants involved in H<sub>2</sub>S aqueous chemistry is much more acute than with CO<sub>2</sub> aqueous chemistry and it is therefore necessary to state precisely what has been used in this work. Sun [27] postulated the following equations were the most reliable:

$$K_{H_2S} = 10^{-\left(634.27 + 0.2709 T_K - 0.11132 \times 10^{-3} T_K^2 - \frac{16719}{T_K} - 261.9 \log T_K\right)} \quad \text{from Suleimenov [33]} \quad \text{Eq (1-22)}$$

$$K_1 = 10^{\frac{782.43 + 0.361 T_K - 1.6722 \times 10^{-4} T_K^2 - \frac{20565.7315}{T_K} - 142.741 \ln T_K}{}} \quad \text{from Suleimenov [34]} \quad \text{Eq (1-23)}$$

$$K_{sp,mck} = 10^{\frac{2848.779}{T_k} - 6.347 + \log(K_1)} \quad \text{from Benning [35]} \quad \text{Eq (1-24)}$$

with:  $K_{H_2S}$ : Solubility constant of hydrogen sulfide (mol/l/bar)

$K_1$ : Dissociation constant of hydrogen sulfide (mol/l)

$K_{sp,mck}$ : Solubility limit of mackinawite (mol/l)

$T_k$ : Temperature (K)

Sun [27] also stated that there was not yet a reliable expression for the second dissociation constant  $K_2$  and that the use of this constant to calculate the solubility limit should be avoided altogether.

## 1.6 CO<sub>2</sub> top of the line corrosion field cases

A number of field cases attributed to TLC have been reported over the years, most of them encountered in sweet (CO<sub>2</sub> dominated) environments. Gunaltun, who is one of the first authors to identify TLC as a major field issue, describes in great detail a case of CO<sub>2</sub> TLC that occurred in an onshore pipeline in Indonesia [36]. An extensive description of the field

parameters as well as a thorough interpretation of the underlying causes of corrosion was presented. In line inspection (ILI) tools were used to identify three locations along the flowline which suffered from extensive internal corrosion on the upper side of the pipe (Figure 5).

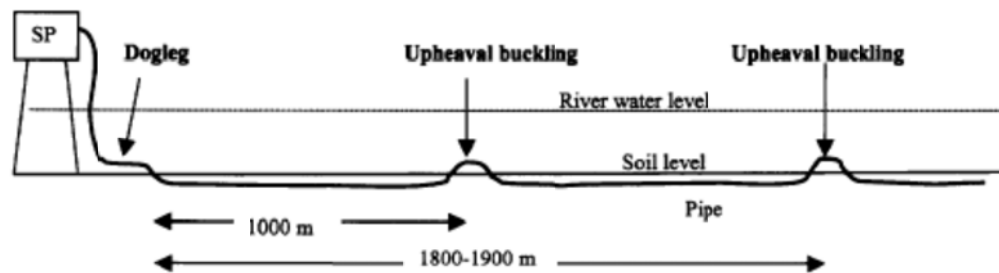


Figure 5: Schematic representation of the locations along the pipeline affected by TLC (Reproduced from [36] - © NACE international 1999)

These three zones corresponded to locations where the pipe was crossing a river delta, where it was alternately buried and in contact with the flowing water. The  $\text{CO}_2$  content in this line was 4.7mol%, for a total pressure of 90 bars, and the inlet temperature was about 80°C. Considering that the river water was at 25°C on average, this situation led to high local heat exchange with the surrounding environment and consequently high water condensation rates.

Further analysis completed in 2000 by the same author [37] showed that the presence of large quantities of acetic acid in the production water accelerated the corrosion rate. Gunaltun added more insight into the TLC mechanisms by defining three main zones in the pipeline (Figure 6):

- **The bottom of the line:** At this location, the corrosion can be lowered by the use of inhibitors.

- **The top of the line:** The water vapor condenses and forms droplets attached to the pipe wall. A protective iron carbonate layer can be formed in certain cases (in CO<sub>2</sub>-dominated environments), but inhibitors cannot reach the top of the pipe and are not effective. Localized corrosion is the predominant form of corrosion.
- **The side of the pipe:** Due to gravity, the condensed water flows on the sidewall and drains to the bottom. Although the corrosion is also uniform, there is no guarantee that inhibitors could access this location and provide any protection.

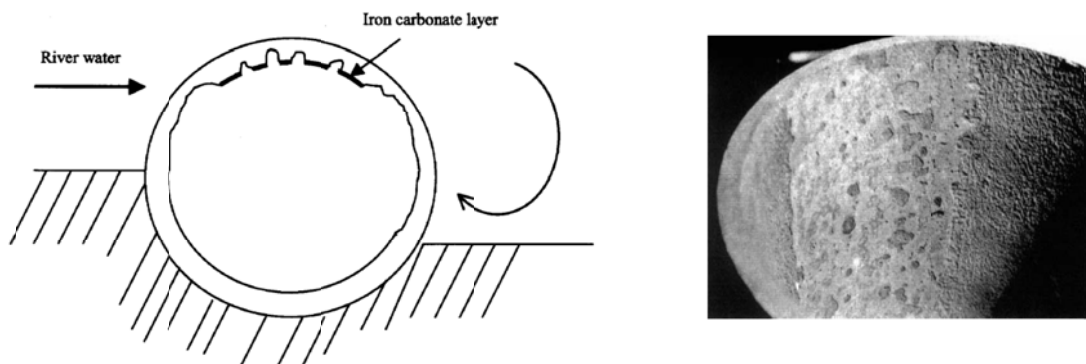


Figure 6: Schematic representation of zones where TLC was experienced  
(Reproduced from [36] - © NACE international 1999)

The condensation rate was identified as a controlling parameter in TLC. The concept of critical condensation, below which TLC was considered to be manageable, was introduced as an engineering tool. This threshold value was presented as a helpful design tool but could not be expected to be valid under every condition. It was set at 0.25 mL/m<sup>2</sup>/s, considering that the condensation would happen on the upper half of the pipe only. If large quantities of organic acid are present (above 2500 ppm of acetate containing species), this critical threshold [38] is reduced to 0.025 mL/m<sup>2</sup>/s. Similar observations were made on four separate flowlines located

in Europe [39] and the influence of organic acid was also reinforced. TLC is now a definitive concern for the industry as a whole [40].

A large set of results of a field pipeline inspection was presented for a network of offshore pipelines off the coast of Thailand [41 - 45], in a field containing high levels of CO<sub>2</sub> (23mol% on average). The pipelines, ranging from 14" to 22" internal diameter, were operated in stratified flow and were only naturally buried on approximately one third of their surface (the pipes were sitting on the sea bed). Considering that the inlet fluid temperature could reach 90°C, very high heat exchange with the sea water occurred (on average at 18°C). Since the fluid would rapidly cool to ambient, severe water condensation only occurred on the first 500 meters of line. TLC was identified as a serious issue leading to potential de-rating of the pipe or replacement of entire sections. Features as deep as 30-60% of the original wall thickness were measured by different types of ILI. The deepest features were located in the first 240 meters of line, corresponding to the zone of high water condensation rate (Figure 7).

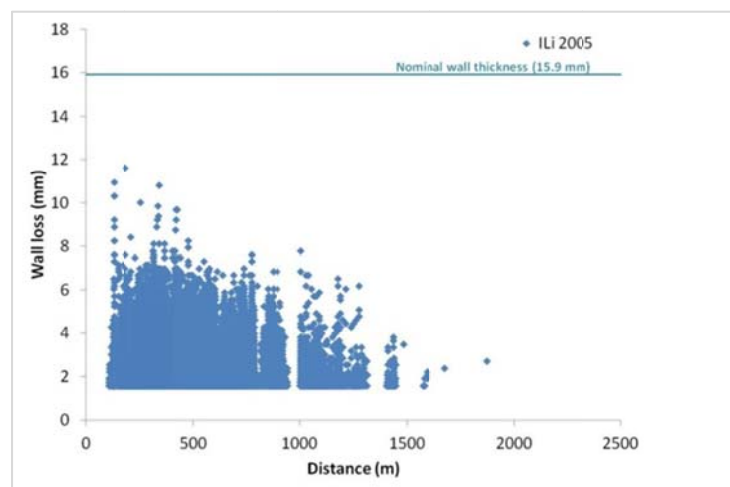


Figure 7: Typical ILI results for TLC – Most of the corrosion features are measured at the inlet of the line (Reproduced from [44] - © NACE international 2012)

Kaewpradap [44] proposed a method to use these data to estimate the remaining life of the pipeline. The notion of TLC stabilization was also introduced as consecutive ILI seemed to show that the number and size of the corroded features did not seem to increase with time. However, this observation was based only on highly inaccurate ILI measurements and was therefore uncertain. Nevertheless, valuable information was presented about operating practices and monitoring techniques used in the field to prevent top of the line corrosion.

Several more recent publications related to the same field were published in 2010 [46, 47]. The notion of “cold spot” corrosion was introduced, described as a worst-case TLC scenario. This situation occurred when the pipe thermal insulation had to be removed to accommodate the installation of sacrificial anodes, commonly used for external corrosion. This led to very high local condensation rates, dramatic overall rates of corrosion and, ultimately to pipeline failure (Figure 8).

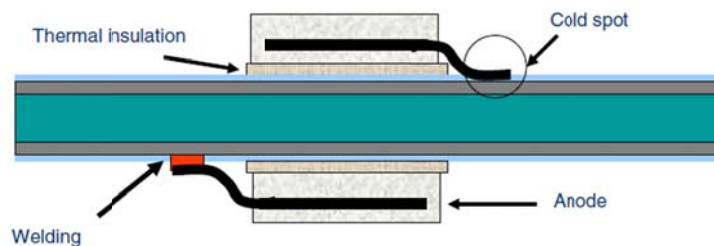


Figure 8: Situation where “cold spot” corrosion can occur  
(Adapted from [46] - © NACE international 2010)

### 1.7 H<sub>2</sub>S Top of the line corrosion field cases

There are only a handful of well-documented sour TLC field failures described in the literature [48].

The first ever reported TLC case was from a sour gas field in France, in 1963 [49]. A serious corrosion issue (Figure 9) was discovered on the top part of a horizontal, buried 6" pipeline transporting a mixture of light hydrocarbons and inhibited water under stratified flow.



Figure 9: Corrosion in the upper part of the pipe  
(Reproduced from [49] - © NACE international 1963)

The gas composition was 9% CO<sub>2</sub> and 15% H<sub>2</sub>S and the fluid temperature was between 35°C and 50°C. Under these conditions, the water condensation rate should have been extremely low. The corrosion issue was identified as TLC and was mitigated by increasing the gas flow rate in order to switch from stratified to annular flow regime.

Another case was also reported from a field in Canada [50, 51]: a 6" pipe made of API 5LX52 carrying produced gas (5.9 % of CO<sub>2</sub> and 0.3% of H<sub>2</sub>S) at an operating pressure of 68 bars. The pipe was split open at the 4 o'clock position (Figure 10) in a straight longitudinal line for the entire length of a pipe section. In the failed section, wall loss was measured up to 64% of the original nominal wall thickness. The corrosion mechanism was identified as TLC due to the condensation of water vapor in presence of acid gases and in the absence of hydrocarbon condensate.

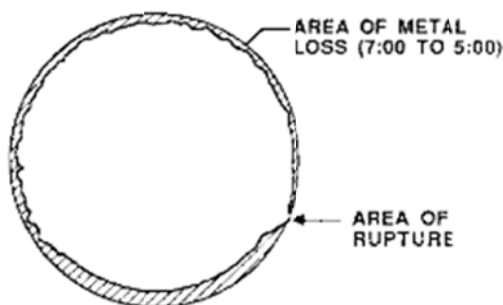


Figure 10: Cross-sectional diagram of the pipe failure  
(Reproduced from [50] - © NACE international 1987)

A third case was reported in North Dakota [52], again with low inlet temperatures (below 40°C) and stratified flow regime. The gas contained 2.6 mole % CO<sub>2</sub> and 16.4 mole % H<sub>2</sub>S at total pressure around 500 psi. The flow line (10" ID) was pigged every 5 days. The failure occurred on the top of the line, in a segment immediately following an elevation drop.

A more recently reported pipe failure [53] involved a 6" ID onshore pipeline transporting wet gas at 5.45% CO<sub>2</sub> and 2800 ppm H<sub>2</sub>S at the time of the rupture. The fluid temperature was again quite low (15°C), which should have led to low water condensation rates. The line ruptured after 8.5 years of operation with extensive reported wall loss (60 to 85%) on the upper part of the pipe. It is important to mention that methanol injection was often used in these cases for methane hydrate control and that it has been determined to be a contributing factor. Due to its high solubility in methanol, oxygen was thought to be introduced in quantities significant enough to impact H<sub>2</sub>S corrosion and lead to the formation of elemental sulfur.

Cases where TLC was not detected are also valuable. Two 8" ID wet gas flow lines (a few kilometers long) transporting sour gas (although contents are not specified in the publication) with respective inlet and outlet pressures at 116 bars and 107 bars did not suffer from TLC [37].

Inlet temperatures are reported at 63°C and 74°C with corresponding outlet temperatures at 29°C and 41°C. These lines have been in operation for 12 years and ultrasonic scanning showed no sign of TLC.

Bonis [54] listed the main findings of a review of intelligent pigging operations performed on offshore and onshore wet sour gas pipelines. The production conditions ranged from 80 to 40°C inlet temperature, 50 to 20°C outlet temperature, 2 to 17% H<sub>2</sub>S, 3 to 10 % CO<sub>2</sub> and 2-3 to 10 m/s. No indication of serious TLC was ever detected.

### 1.8 TLC monitoring

Several methods are used in the field in order to monitor corrosion.

The most commonly used, but also the most expensive, are called In Line Inspections (ILI) and involve monitoring devices mounted on pipeline inspection gauges (also called pigs). This method often requires considerable shut-down or slow-down of the production rate, and consequent loss of revenue. Two main techniques are used [38, 42, 44]:

- Magnetic flux leakage (MFL), which detects pipeline defects through the magnetization of the ferrous metal,
- Ultrasonic Testing (UT), which is based on measuring the ultrasonic signal propagated through the pipe wall.

Other much less expensive methods involve the use of Electrical Resistance (ER) or Weight Loss (WL) probes installed at specific locations in order to monitor the corrosion. However, the relevance of the results is highly dependent on the location of the measurements, which can only marginally represent pipeline conditions [55].

## 1.9 Mitigation methods

Effective mitigation of TLC is a difficult and often costly process. The most common method used in pipelines to control corrosion involves the continuous injection of chemical corrosion inhibitor into the produced fluid. This method is efficient where the inhibitor can remain in contact with the steel surface. However, in a TLC scenario (*i.e.* stratified flow), there is no means for the inhibitor present in the bulk liquid phase at the bottom of the line to reach the top of the pipe since the inhibitor is generally non-volatile and does not condense at the top of the pipe. Continuous injection of inhibitor is consequently ineffective for TLC control, unless the chemical has some volatile properties and can evaporate and then condense together with the water at the top of the line. The development and use of Volatile Corrosion Inhibitor (VCI) for field application is on-going and some limited success has been obtained [55]. However, finding the chemical formulation which will retain sufficient inhibitive properties (usually held by long chain molecules) while presenting superior volatility (more common for smaller molecules) has proven to be a challenge [56].

Another common inhibitor application is through batch treatment: a plug of fluid containing high content of inhibitor is circulated through the pipeline system between two pipeline inspection gauges (also called pigs). Another similar method involves the use of specially-designed spraying device [42], as shown in Figure 11.

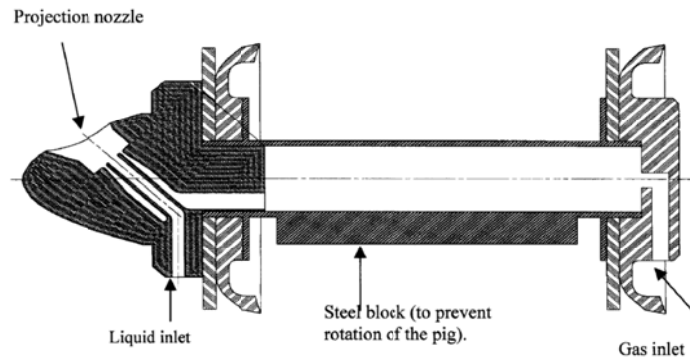


Figure 11: Representation of spray-pigging inside a flowline  
(Reproduced from [43] - © NACE international 2003)

This technique can effectively control TLC since it provides a means for the inhibitor to reach the top of the line provided that:

- The line is pig-able (most lines are not equipped with a pig launcher and receiver) .
- The batch treatment frequency is sufficient to maintain inhibitor coverage.
- The batch treatment is applied according to plan (since “pigging” leads to a decrease in production flow rate and consequently revenue, batch treatment schedules are often not respected).

More specific to TLC itself, an additional way to minimize corrosion is to decrease the water condensation rate on the pipe wall by minimizing the temperature difference between the gas and the pipe. This is typically done by applying an external coating (such as polypropylene or concrete) on the pipeline before it is laid down. However, applying insulation layers can be rather costly on long pipe sections. In addition, TLC issues are often discovered after the fact. TLC mattresses have been developed and used in the field in order to address this issue because they can locally decrease the water condensation rate [57, 58]. However, this method is only effective for short pipelines: as the heat exchange with the outside environment

is decreased, the produced fluid remains warmer and the water vapor could condense if the additional thermal insulation is discontinued.

Finally, replacing certain sections of the carbon steel flowlines by Corrosion Resistance Alloy (CRA) offers definitive protection against TLC. The section can be especially designed to enhance cooling and force most of the water vapor to condense on these sections [59]. However, this solution is only economically viable on short pipelines, and severe corrosion issues do exist at the transition between CRA and carbon steel lines.

## CHAPTER 2 GAPS IN THE CURRENT UNDERSTANDING AND RESEARCH OBJECTIVES

### 2.1 Gaps in the current understanding

TLC is inherently a localized process. Pipe failures occur in specific areas along the line and the corrosion is not usually extended to large sections. This localized aspect is often related to situations where high condensation rates occur, *i.e.* where the gradient of temperature between the produced fluid and the outside environment is large. In sweet environments ( $\text{CO}_2$ -dominated), the corrosion process is often characterized as a mesa attack: the steel is not uniformly corroded but the pits are usually wide, often flat-bottomed and bare of any layers, surrounded by areas with intact corrosion product layers (Figure 12).



Figure 12: Typical TLC failures in  $\text{CO}_2$  dominated environment  
(Reproduced from [38] - © NACE international 2006)

By comparison, the mode of the corrosion attack in a sour ( $\text{H}_2\text{S}$ -dominated) system is largely speculative, as both uniform and pitting corrosion have been encountered. The

mechanism of uniform H<sub>2</sub>S corrosion is subject to ongoing research [115] and is not well understood; research on sour localized corrosion has not been significantly reported in the literature. Consequently, the focus of this research work is put on failure mechanisms (localized corrosion) in CO<sub>2</sub> dominated systems.

Although more and more work is being performed on the modeling of top of the line corrosion (CHAPTER 7.2), the localized nature of TLC is still not well understood. The corrosion features observed in the field can be so large that the corrosion process is often referred to as “localized uniform corrosion” instead of a purely “localized corrosion”. The unique TLC scenario where droplets of condensed water appear and are renewed continuously at the metal surface must play a crucial role. It is likely that the condensation process initiates and promotes the localized corrosion at the top of the line by challenging the protectiveness of the iron carbonate layer.

There is a clear need to develop a better understanding of the mechanisms of sour and sweet localized corrosion in order to provide more accurate predictions of the likelihood of occurrence and the severity of the attack. This would have direct implications in pipeline design and operation. To achieve this goal, it is also important to develop the right experimental tools. No laboratory set up can perfectly represent the conditions in the field. While pure corrosion issues have been successfully simulated in small scale set-ups, the flow conditions relative to a 30” ID pipeline are not easily reproducible.

While several different experimental setups have been used with some success at the Institute for Corrosion and Multiphase Technology (ICMT) at Ohio University and elsewhere, it is believed that significant improvements can be made in the way TLC is simulated.

## 2.2 Research objectives

As mentioned above, since the present understanding of the localized nature of top of the line corrosion is limited, more work needs to be done to identify the controlling mechanisms.

The objectives of the current project are stated as follows:

1. Devise new experimental setups and procedures, which can realistically simulate typical top of the line corrosion (in terms of flow, geometry, corrosive environment, condensation regime) as it is observed in the oil & gas field.
2. Investigate the effect of different influencing parameters on top of the line corrosion (both uniform and localized rates), including:
  - Effect of the flow velocity and condensation pattern
  - Effect of the condensation rate
  - Effect of the gas temperature
  - Effect of the concentration of corrosive species (CO<sub>2</sub>, acetic acid, H<sub>2</sub>S)
3. Implement various methods to qualitatively and quantitatively characterize the interaction between condensation pattern and corrosion attack and to define the localized nature of top of the line corrosion processes.
4. Based on the experimental data, propose a new modeling approach for the prediction of the localized attack in a top of the line corrosion scenario.

## 2.3 Central hypothesis

The main hypothesis is developed around the notion that, at least in sweet environment, the water condensation rate (WCR) is the key parameter controlling the protectiveness (or lack thereof) of the corrosion product layer at the top of the line. It governs the change in water chemistry in the condensed water and dictates whether localized corrosion

can be initiated and sustained. The rate of localized corrosion is, in turn, controlled by other environmental parameters, such as the temperature and the content of corrosive gases. The presence of the droplet of condensed water on the steel surface is also a key parameter in defining where localized corrosion will occur.

## 2.4 Dissertation outline

CHAPTER 3 presents the efforts developed for the manufacture of an experimental test setup capable of reproducing a realistic TLC scenario. It discusses the drawbacks and advantages of existing apparatuses and describes the main characteristics of the design eventually selected for this study.

The experimental results are then presented in detail in CHAPTER 4, focusing on the influence of the controlling environmental parameters on the occurrence of localized corrosion.

The effect of the water condensation rate is clearly identified and is further studied in CHAPTER 5, which takes a deeper look at the interaction between the presence of droplets of condensed water and the extent of corrosion.

The morphology of typical localized TLC features, encountered in sweet environments, is investigated in detail in CHAPTER 6, showing the presence of different corrosion product layers and providing clues about the pit growth process.

Finally, the main observations gathered so far are summarized in CHAPTER 7, and a narrative for the occurrence of localized TLC is proposed and converted into a physical model. Simulation results are compared with experimental results, and the pros and cons of the approach are discussed.

CHAPTER 8 presents the concluding remarks and the path forward.

## CHAPTER 3 DEVELOPMENT OF EXPERIMENTAL SETUPS FOR THE STUDY OF TLC

### 3.1 Objective

The main objective of this chapter is to devise new experimental setup and procedures that can simulate realistically typical top of the line corrosion (in terms of flow, geometry, corrosive environment, condensation regime) as it is observed in the oil & gas field.

### 3.2 Literature review

Over the last 25 years, a number of researchers have proposed a variety of TLC-oriented experimental devices, geared towards the study of some aspects of TLC. The equipment designed in the present study was inspired by some of the devices. They are categorized into two main groups: small scale setups (glass cell, autoclave, small scale flow loop) or large scale flow systems.

#### 3.2.1 *Small scale apparatus*

##### 3.2.1.1 *Glass cell*

The development of glass cell setups for corrosion study holds many advantages as it involves very versatile and low cost systems. Safety concerns related to high pressure and temperature setups are also avoided. However, linkage between experimental results and field reality is often more difficult to make.

In 2000, Pots et al. [60] developed an apparatus comprised of a carbon steel tube mounted on a heat exchanger and inserted inside an atmospheric chamber containing wet CO<sub>2</sub> (saturated water vapor and CO<sub>2</sub> gas). The water vapor would condense on the cooled steel tube at a rate controlled by the cooling water flow rate (Figure 13). The condensed water was also collected in a container underneath, enabling the measurement of the condensation rate and the sampling of the condensed water for chemical analysis. Although the pressure rating of the

device was atmospheric, a wide range of gas temperatures and water condensation rates could be achieved (30-70°C and 0.1 to 1.5 mL/m<sup>2</sup>/s, respectively). Rates of corrosion were measured by evaluating the difference in mass of the tube before and after the test (weight loss method) and by visual observation of the steel surface. The main disadvantage of this system is that the corrosion process occurred on the outside diameter of the relatively small tube (only a few mm internal diameter), affecting the retention time of the condensed water and creating areas of non-homogeneous corrosion. Nevertheless, this setup enabled the collection of condensed water for pH and iron ion concentration analysis (although it can be argued that the composition of the condensed water may have been altered by re-evaporation).

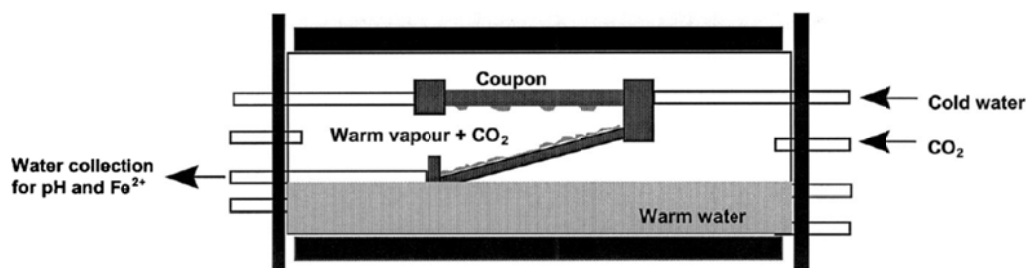


Figure 13: TLC experimental device involving a cooled steel tube  
(Reproduced from [60] - © NACE international 2000)

In 2008, Hinkson et al. [9] published the results of a study focused on the composition of the condensed water. A glass cell setup was constructed utilizing a heated container that would generate water vapor, which would then condense when passing through a heat exchanger. Using this sort of configuration, samples could be collected in vials for subsequent chemical analysis, such as their pH and Fe<sup>2+</sup> ion concentration (Figure 14). This system was later upgraded by inserting a carbon tube (coated on its outside) inside the heat exchanger in order to perform TLC experiments. The corrosion rate was measured by weight loss method only.

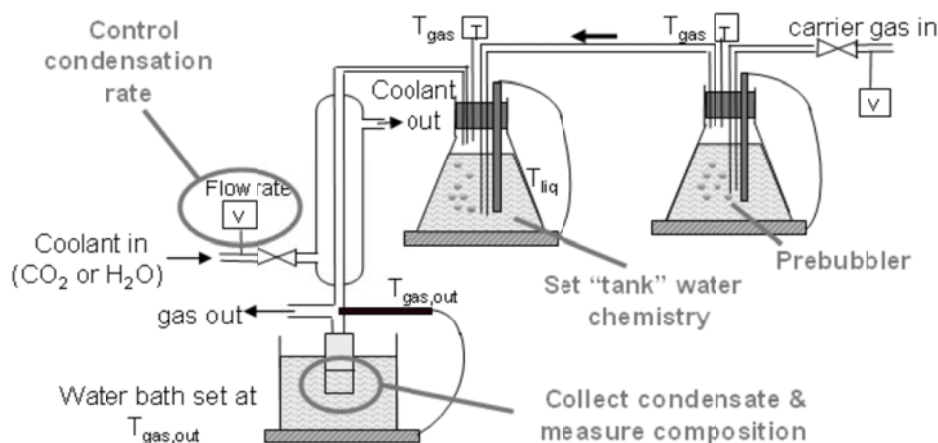


Figure 14: TLC experimental device focused on the composition of the condensate (Reproduced from [9] - © NACE international 2008)

Cough et al. [61] and Oehler et al. [62] developed a very similar experimental design involving a sample holder mounted with carbon steel pins exposed to the corrosive vapor phase (Figure 15). The sample holder was externally cooled in order to force water condensation onto the pins, which dripped and was collected in a condensed liquid container. The pins could also be used for Linear Polarization Resistance (LPR) measurements. However, readings could not be made unless the electrodes (working, reference and counter) were fully immersed in the electrolyte, which is not the case in the vapor phase (as only a thin and poorly conductive liquid film covers the metal surface). Consequently, they were intermittently lowered into the condensed water reservoir for direct corrosion readings. It is important to mention that accurate LPR readings require a strong electrolyte in order to minimize the solution resistance, which is not the case for condensed water. Although this setup presented many advantages (notably, two methods for corrosion measurements), the specific design of the metal samples (vertical pins) and the intermittent reading of corrosion in the condensed water reservoir cannot accurately represent the influence of environmental parameters such as condensation rate and

temperature. This setup has been used primarily for the evaluation of the efficiency of inhibitors. It is well-adapted for this because it only requires a black and white answer -- either full protection or active corrosion.

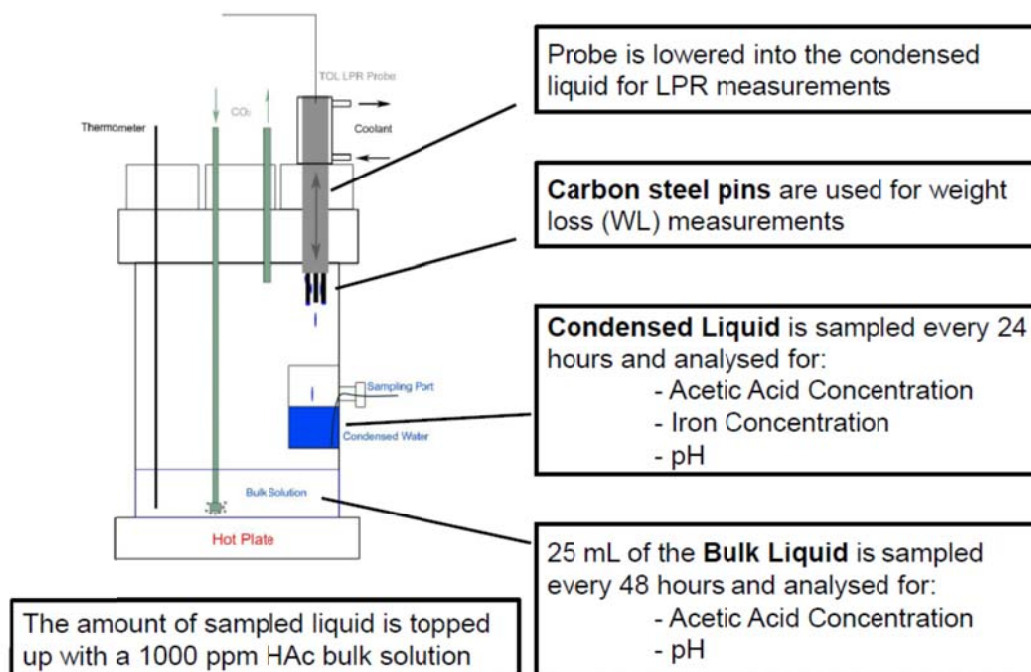


Figure 15: Cooled finger probe concept  
(Reproduced from [62] - © NACE international 2012)

Gunaltun et al. [56] published another comprehensive effort at evaluating the efficiency of inhibitors using a variety of experimental setups. One of these innovative setups consists of a heated reactor generating the water vapor and a “condensation cell”, where electrochemical measurements are performed (Figure 16). These two main elements were connected in a loop enabling control of condensation rate, temperature and water chemistry as well as online corrosion measurements using an LPR setup. This rather complex setup obviously presented many advantages, especially since the chemistry of the condensed water in contact with the

sensing element (LPR probe) could be measured (pH and  $\text{Fe}^{2+}$  concentration). However, the condensed water accumulated on top of the electrodes, which were facing up instead of down. The true effect of condensed water renewal was altered by this specific setup. In addition, LPR measurements are not believed to give very accurate results in condensed water due to the poor quality of the electrolyte.

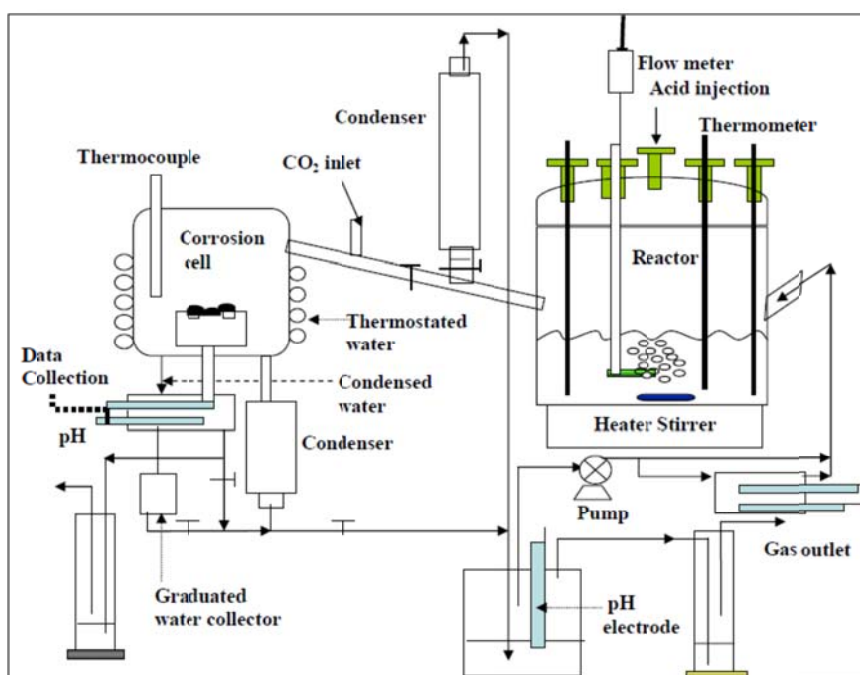


Figure 16: Volatile inhibitor testing equipment  
(Reproduced from [56] - © NACE international 2010)

Another experimental glass cell design proposed by Gunaltun et al. [56] involved a unique glass cell used for vapor generation and online corrosion measurement with a weight loss steel sample and Electrical Resistance (ER) probe (Figure 17). The ER technique is more appropriate for the study of TLC since it does not require a good electrolyte and a reference/counter electrode setup. However, full coverage of the sensing element is still

essential for accurate measurement of the corrosion rate. The ER and WL probes were flush mounted to the bottom side of the lid facing down and the condensation process was observed using a borescope (Figure 16). This specific setup is quite representative of a real case of TLC. However, the condensed water accumulating on the surface of the corrosion sample could not be collected for analysis, which represents a drawback.

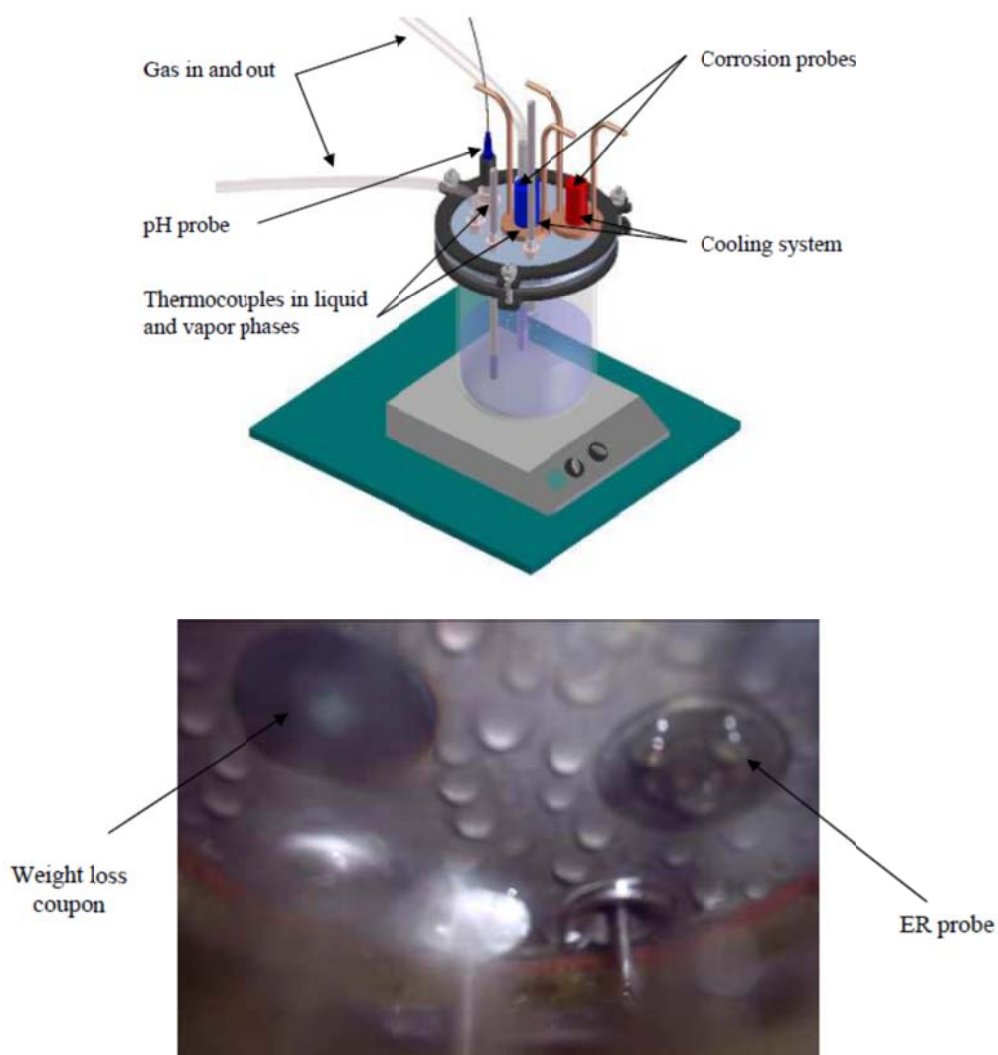


Figure 17: Experimental setup using Electrical Resistance (ER) probe (bottom) and water condensation process on the lid (top) - (Reproduced from [56] - © NACE international 2010)

Pojtanabuntoeng et al. [63] proposed a similar setup equipped with a borescope and a WL sample for corrosion measurement. However, the cooling setup involved the innovative use of a thermoelectric “Peltier” device, enabling better control of the local condensation rate on the steel sample (Figure 18). Using this setup, the temperature of the corroding sample (“coupon”) could be closely monitored.

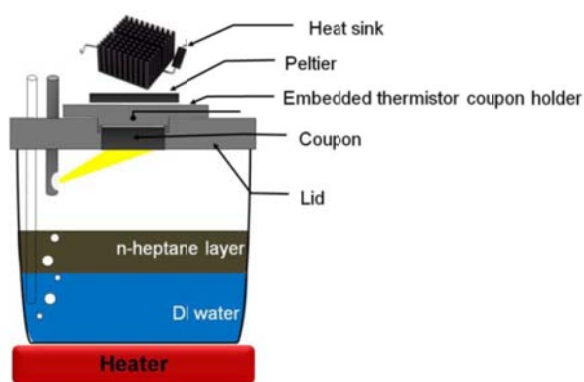


Figure 18: Experimental setup designed for the observation of condensation (Reproduced from [63] - © NACE international 2011)

### 3.2.1.2 High-pressure equipment

High-pressure systems obviously hold a high safety risk, but they also represent a positive step in the direction of making experimental setups which are more representative of field environments. As early as in 1991, Olsen proposed the first high-pressure autoclave especially designed for the study of TLC [64]. The lid of the autoclave was cooled with water and clamped with WL flushed samples (Figure 19). The partial pressure of CO<sub>2</sub> could be raised up to 5 bars.

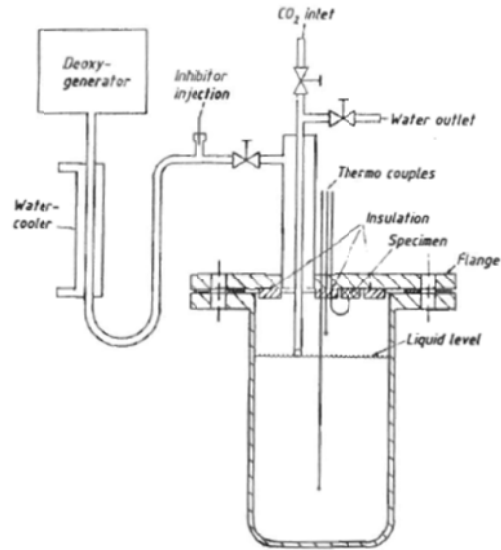


Figure 19: Autoclave setup designed by Olsen  
(Reproduced from [64] - © NACE international 1991)

Another setup proposed by Oehler et al. [62] involved an inhibited coolant flowing through a  $\frac{1}{4}$ " steel tubing located inside an autoclave rated at 20 bars (Figure 20).

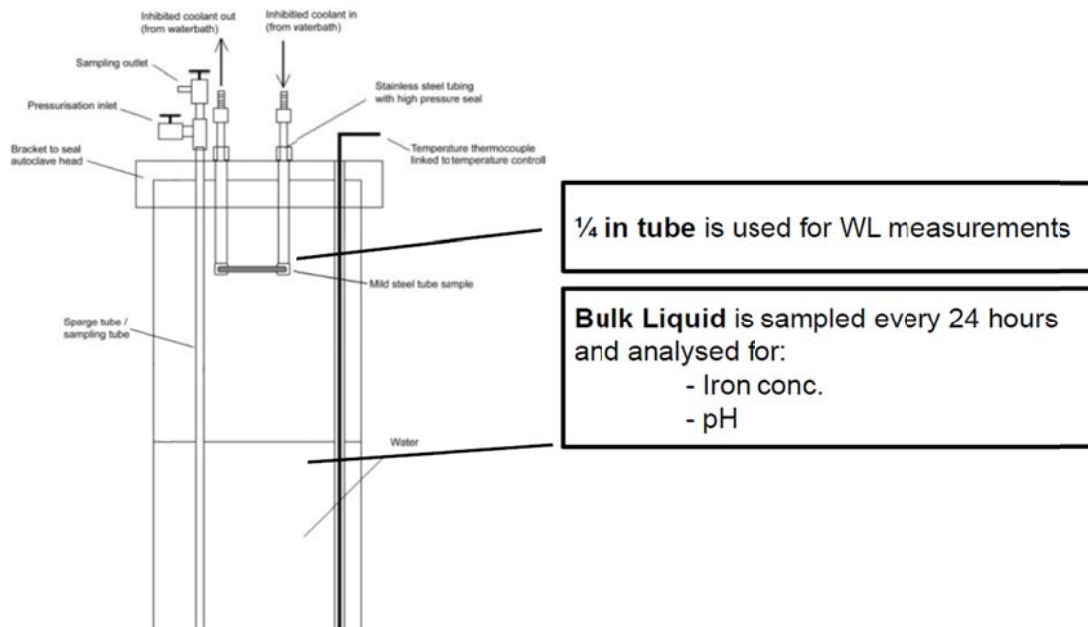


Figure 20: Horizontal cooled tube concept  
(Reproduced from [62] - © NACE international 2012)

The concept was similar to the approach developed by Pots et al. [60] and held similar advantages and inconveniences (sample morphology). The water condensation rate could also be evaluated by calculating the heat loss through the coolant liquid.

Zhang et al. [65] and Qin et al. [66] presented in two separate studies an original setup which combined external cooling of the steel samples as well as rotation of the specimen. The samples were “arc shaped” (108 mm diameter and 14 mm width) and mounted around the rotating shaft. Consequently, vapor condensation occurred on the sides of the specimen with a thin film or with droplets of condensed water sliding to the bottom of the autoclave (Figure 21).

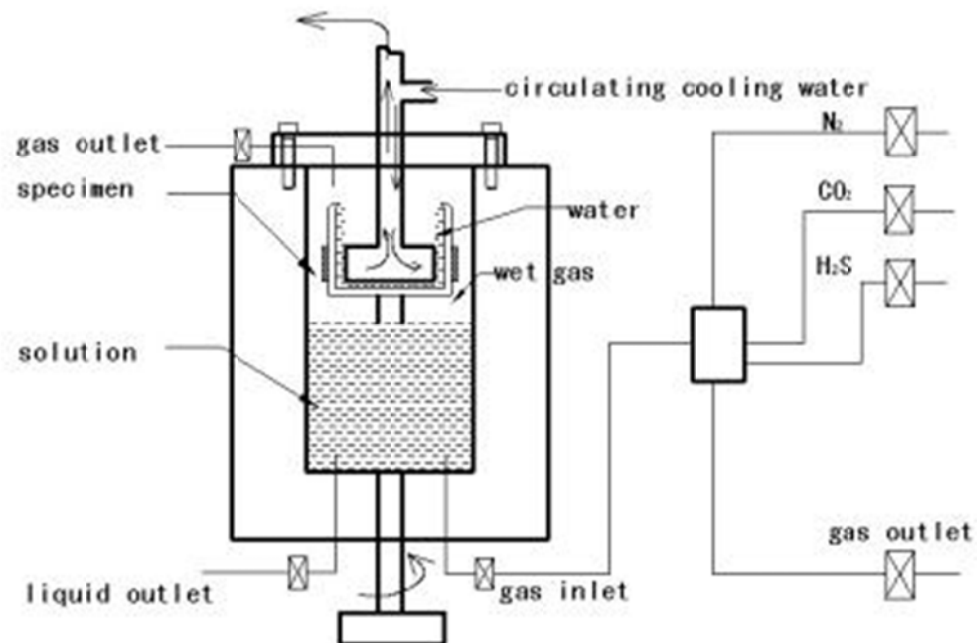


Figure 21: Wet gas autoclave design proposed by Zhang  
(Reproduced from [65] - © NACE international 2009)

A rather innovative setup was proposed by Jovancicevic et al. [67]. It involved the use of a Quartz Crystal Microbalance (QCM), a device in which the change in mass of a thin film

deposited on a quartz crystal resonator is determined by measuring its change in frequency. The QCM can accurately measure very small rates of iron dissolution (if the deposited film is made of iron) and can, in theory, be adapted to measure the rate of water evaporation on the surface of the sensing element. A small autoclave was adapted to include a QCM for evaluation of the efficiency of corrosion inhibitors (Figure 22). Although the results are promising, many technical challenges still exist in adapting this very specialized device to simulate representative conditions.

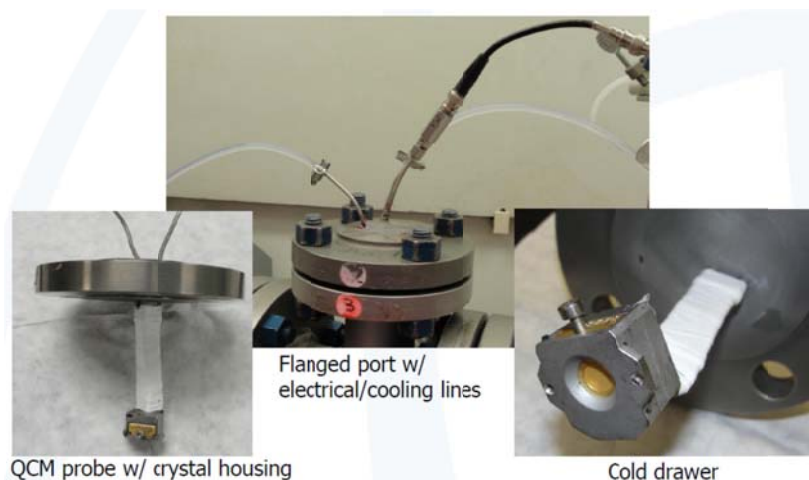


Figure 22: Quartz crystal microbalance design proposed by Jovancicevic  
(Reproduced from [67] - © NACE international 2012)

Another high-pressure setup was presented in 2011 by Singer et al. [48]. The 20L autoclave made of alloy C-276 (UNS N10276) was specially manufactured to enable corrosion measurements under condensing conditions. The top lid of the autoclave was equipped with an internal cooling system and a sample holder plate (Figure 23). The design of the sample holder enabled the study of the effect of the condensation rate in one single test. This was done by

“hanging” some of the steel samples in the gas phase but a distance (15 cm) away from the cooled plate.

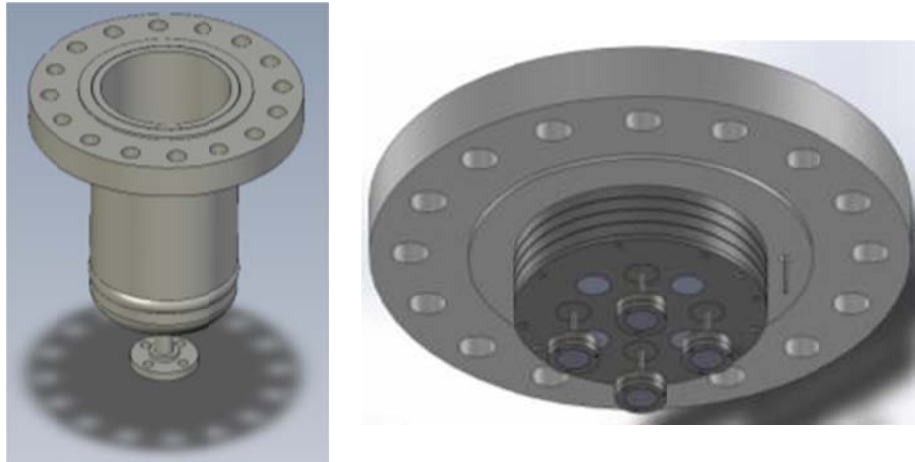


Figure 23: 20L autoclave setup (left) and details of the sample holder (right)

The first attempt to add more representative flow conditions to a high-pressure/temperature setup was performed in 1991 by Olsen et al. [64]. The flow loop consisted of a gas booster connected to a reservoir and a set of 16 mm stainless steel tubing systems (Figure 24). The gas flow rate could reach 5 m/s while the pressure of CO<sub>2</sub> was reported at 5 bars. The corrosion rate was measured on a 5cm long carbon steel tubing specimen using a radioactive technique (scintillation detectors measuring the loss in activity -- *i.e.* metal loss -- of neutron-activated specimens) capable of differentiating top and bottom of the line corrosion.

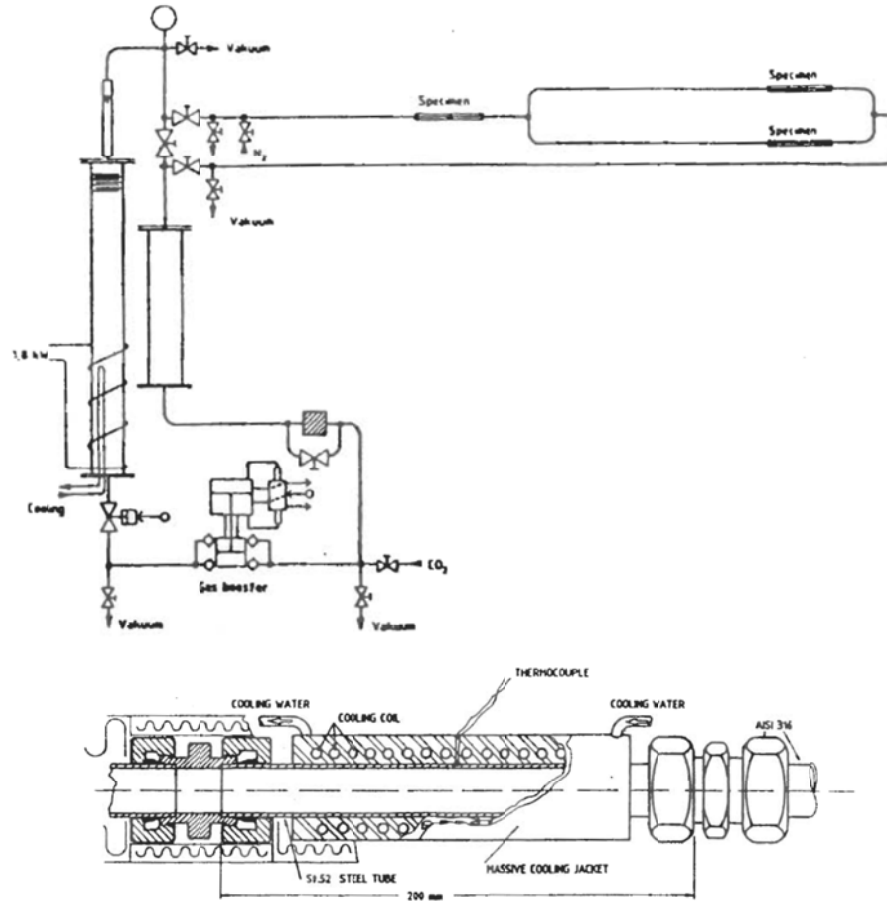


Figure 24: Small scale flow loop (top) and test section (bottom) proposed by Olsen (reproduced from [64] - © NACE international 1991)

### 3.2.2 Large scale systems

Although expensive to run and less versatile than smaller setups, high-pressure/temperature large scale flow loops do represent the next step towards simulating real field situations.

In 2007, Andersen et al. [68] and later Nyborg et al. [69] proposed a system enabling the circulation of the gas phase from a high-pressure reservoir to a low-pressure reservoir, containing the bulk liquid phase. A liquid pump/ejector setup ensured proper mixing between the phases, such that the vapor phase was always in equilibrium with the bulk liquid phase. Only

the gas phase circulated through the 55 mm ID piping. Several carbon steel pipes, from 1.8 to 5m in length, could be inserted in the flow loop and exposed to the moist gas (Figure 25).

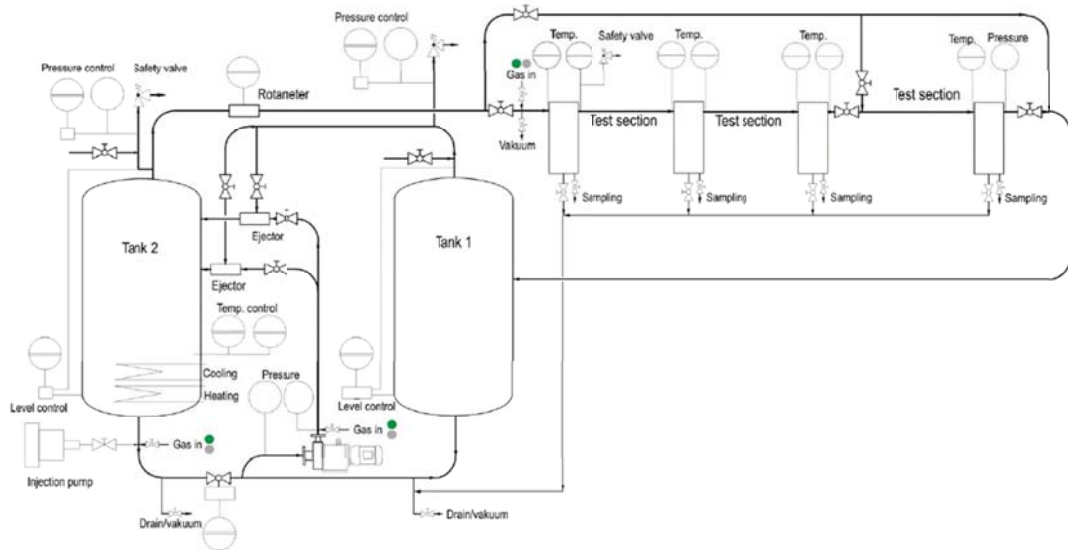


Figure 25: Large scale flow loop proposed by Andersen and Dugstad (reproduced from [69] - © NACE international 2007)

The bottom inner area of the pipes (about 20% of the entire surface area) was painted with corrosion resistance coating in order to differentiate between top and bottom of the line corrosion. Water condensation was achieved by circulating water through cooling coils mounted on the outside of the pipe (Figure 26).

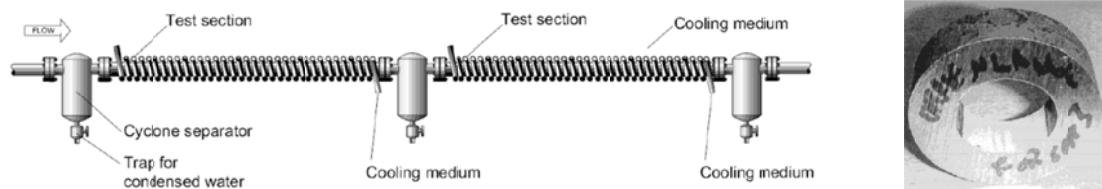


Figure 26: Test section proposed by Andersen and Nyborg (reproduced from [69] and [68] - © NACE international 2007 & 2009)

The rate of condensation was controlled by the flow rate of cooling water. A condensed water collector placed downstream of the test section enabled the measurement of the condensation rate as well as important chemical parameters (pH, iron, acetic acid concentration). Visual inspection of the test pipes before and after the experiment as well as continuous iron content monitoring were used for corrosion measurement.

### 3.3 Original experimental setups used in this research work

The large scale flow loops which have been developed for the purpose of the current research work are described in detail in the following sections. Part of the content of this chapter is taken directly from some of the author's previous publications [70, 71, 72].

#### 3.3.1 *Large scale flow loop setup*

The experiments presented throughout this study were carried out in three similar high-temperature, high-pressure, 4" ID (0.1 m internal diameter) flow loops, all located in the laboratory of the Institute for Corrosion and Multiphase Technology (ICMT) at Ohio University. While one of these loops (H<sub>2</sub>S flow loop) was dedicated to experimental work in sour environments and required dedicated operating and safety procedures, the other two (TLC flow loop #1 and 2) were utilized for sweet (CO<sub>2</sub>) corrosion studies. These three setups were needed to accommodate the number of experiments to be performed. These flow loops are all comprised of the same main components: a large tank (1000L) holding the bulk liquid phase, a gas blower (and in some cases a liquid pump), and a system of 4"ID (0.1 m internal diameter) stainless steel pipes forming a loop. Each of these systems is about 30 meters in total length. Various monitoring devices (pressure gauge, thermometers, gas flow meter, liquid sampling device) are installed along the pipe system. Several test sections, where the actual corrosion measurements are performed, are located along the pipe system. A detailed description of the



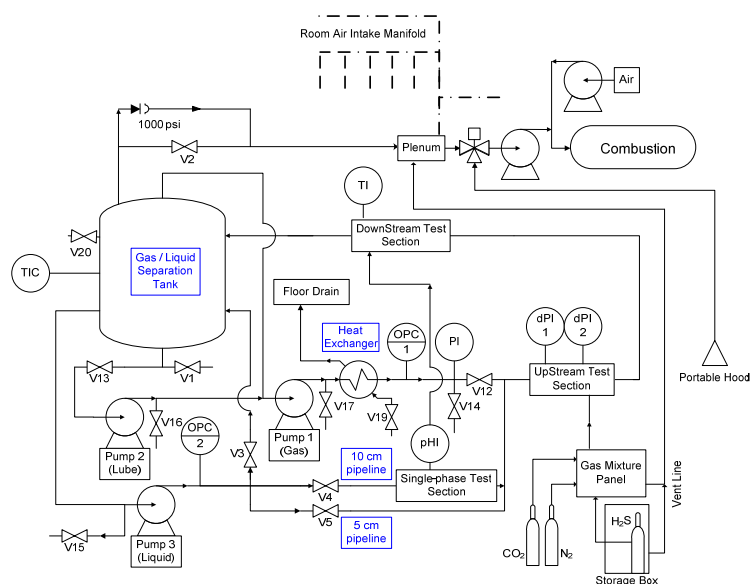


Figure 29: Schematic of the H<sub>2</sub>S flow loop  
(reproduced from [73] - © NACE international 2002)

### 3.3.1.1 Liquid Phase Composition

The liquid phase was made up exclusively of de-ionized water containing in some cases acetic acid; no salt was added. However, dissolved ferrous iron Fe<sup>2+</sup> build-up occurred throughout the test due to the corrosion process on the carbon steel samples. The main liquid phase in the tank was heated to the required temperature, according to the test matrix, using immersion heaters. The vapor phase, containing water, acetic acid vapor, CO<sub>2</sub> and N<sub>2</sub>, was circulated through the pipe and no liquid from the tank was carried over. pH in the bulk liquid phase (tank) was regularly monitored in the main liquid storage tank, and liquid samples were also taken. Although the pH in the main tank could vary between tests from 3.5 to 4.8 depending on the conditions, there is no direct influence on the liquid composition at the top of the line, which was always pure condensed water. In fact, the pH in the main tank had to be considered only when evaluating the concentration of free acetic acid which, being a weak acid, dissociates in aqueous environments.

### 3.3.1.2 Gas Phase Composition

In almost all of the experiments, the gas phase was comprised of a mixture of CO<sub>2</sub> and N<sub>2</sub> (2 bars of CO<sub>2</sub> and 0.7 bars of N<sub>2</sub>, with 0.3 bars of water vapor) for a total pressure of 3 bars. For the H<sub>2</sub>S environment, the required amount of H<sub>2</sub>S was introduced in pure gas form at the beginning of the test and checked regularly using a piston pump and low range standard detection tubes. The trace amounts of H<sub>2</sub>S introduced in the loop were consumed fairly rapidly by the corrosion process and the H<sub>2</sub>S partial pressure had to be adjusted almost every day to maintain an accuracy of ±20%.

### 3.3.1.3 Chemistry in the condensed water

There is no easy way to measure the evolution of the pH in the condensed water at the top of the line. Initially, the fresh condensed liquid has a relatively low pH, as it is pure water saturated with CO<sub>2</sub>. Calculations have shown that the pH can initially be as low as 3.0 to 3.5. However, as the corrosion process proceeds, the iron concentration in the condensed water droplet rises quickly. Depending on the water condensation rate, FeCO<sub>3</sub> saturation can also be rapidly met inside the droplet.

### 3.3.1.4 Acetic Acid Concentration

The acetic acid (HAc) concentration was adjusted by adding a calculated amount of de-oxygenated pure HAc into the tank. The acid would then dissociate to form acetate (Ac<sup>-</sup>) and hydrogen ions (H<sup>+</sup>). The remaining amount of undissociated acetic acid (which depends on the pH) could evaporate and would consequently control the concentration of total acetic acid present in the condensed liquid at the top of the line. A comprehensive study on the thermodynamics of water/HAc/liquid vapor equilibrium was published by Hinkson [9] in 2007. This study shows that, within the range of parameters tested in the present study, the

concentration of total acetate-containing species in the condensed water should be very similar to or slightly lower than the concentration of undissociated acetic acid present at the bottom of the line. It is not possible to provide a constant concentration of undissociated acetic acid in the condensed water, as this depends on the pH of the droplets, which fluctuates considerably during the condensation process due to the release of  $\text{Fe}^{2+}$  ions in solution. A gradient of concentration also exists between the outer envelope of the droplets (liquid/vapor interface) and the steel surface. For clarity purposes, the concentration of acetic acid referred to in the following is the one in the liquid phase at the bottom of the line (tank water).

#### *3.3.1.5 Safety considerations*

The main safety concern identified with the flow loop experiments in  $\text{CO}_2$  environment is high pressure. The loop itself is designed to handle 600 psi (40 bars) of total pressure. Operational and emergency procedures are developed in order to avoid any mishandling of the instrumentation (heater, gas blower, liquid pump) and to ensure the proper maintenance of the facility.

For the flow loop tests in sour environments, the toxicity of  $\text{H}_2\text{S}$  was an additional safety concerns. The flow loop is housed in the ICMT  $\text{H}_2\text{S}$  facilities which are fully equipped to ensure the safety of operations. Operational, emergency procedures and job safety analysis were performed on the equipment, and the personnel conducting the research were properly trained to operate in  $\text{H}_2\text{S}$  environments and in the use of self-contained breathing apparatus.

#### *3.3.2 Standard test section*

Specially-designed test sections enabled the insertion of cylindrical weight loss samples made of carbon steel inside the flow system. The condensation conditions were simulated using cooling coils wrapped around the pipe. The rate of water condensation was measured by

collecting the condensed water downstream of the test section, using a 2" ID bottom port connected to a graduated water trap. The test section, showing four top and four bottom ports, as well as the condensed water collection device, is presented in Figure 30. A schematic of a typical test section showing the position of corrosion probes is displayed in Figure 31.



Figure 30: Typical TLC test section equipped with condensed water collector (bottom left)

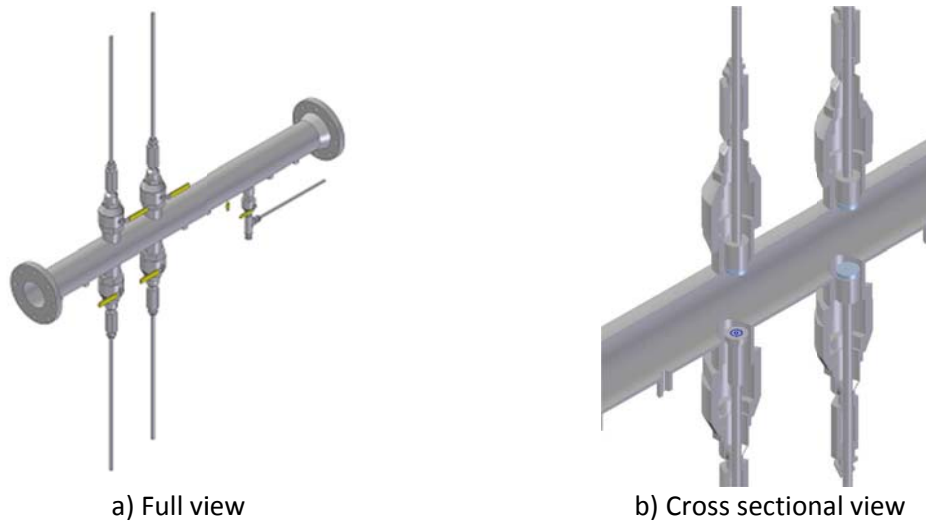


Figure 31: Schematic view of the test section showing how corrosion samples are flush mounted inside the flow loop

The weight loss samples were inserted into the corrosion environment as soon as the system had reached steady state. The corrosion rates were measured with weight loss samples made of API X65 carbon steel. The cylindrical samples (0.76 cm internal diameter, 3.17 cm external diameter and 0.5 cm thickness) were polished using isopropanol as a coolant with silicon carbide abrasive papers up to 600 grit. After this preparation, they were covered with liquid Teflon on the outer edges and bottom, leaving an exposed area of 7.44 cm<sup>2</sup> on top. Following four to six hours of curing at ambient conditions, the samples were held at 200°C in an oven for four hours. The uncovered steel surface was then re-polished with 600 grit silicon carbide paper wetted with isopropanol, cleaned, dried, and weighed. The samples were then flush mounted on the internal pipe wall of the loop using a specially designed probe holder (Figure 32).

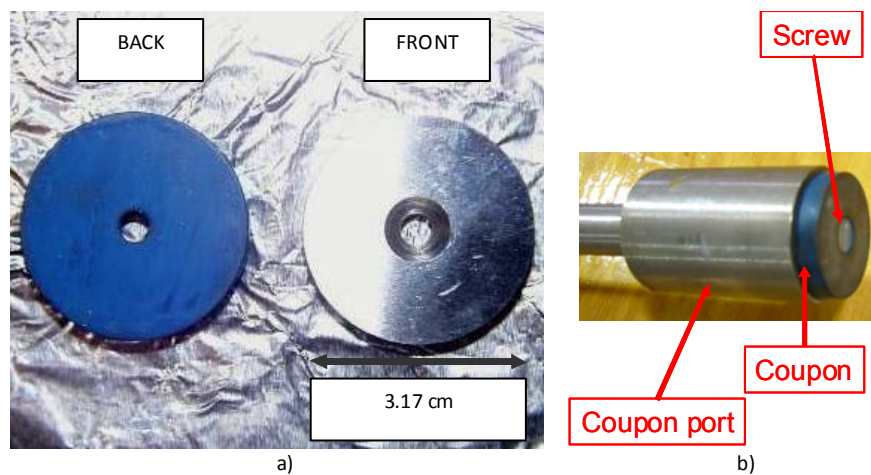


Figure 32: a) Weight loss samples with Teflon coating at the back and the side and b) Sample holder configuration

Therefore, only one face of each sample was in direct contact with the corrosive environment. The exposure time was between 2 and 21 days in all experiments. Upon removal

from the loop, the sample surface was flushed with isopropanol to facilitate dehydration and then photographs of the surface were taken. The weight of the sample after each test was registered, and the ASTM G1 standard cleaning procedure [74] was followed to remove the corrosion products and to determine the corrosion rate by weight loss. Some samples were preserved for corrosion product evaluation by scanning electron microscopy (SEM), energy dispersive X-ray spectroscopy (EDS), X-ray diffraction (XRD) or cross-section analysis.

### 3.3.3 Challenges related to the experimental design

No laboratory set up can perfectly represent the conditions in the field. While pure corrosion issues have been successfully simulated in small scale set-ups, the flow conditions relative to a 30" ID pipeline are not easily reproducible. Top of the line corrosion is as much a flow regime and heat transfer issue as it is a corrosion issue. TLC occurs only in stratified flow, but the way that the condensation process occurs at the top of the line (forming a thin flowing liquid film, or a bigger stagnant droplet) is of prime importance. Using flat weight loss samples flush mounted to a cylindrical 4" ID pipe creates conditions leading to preferential condensation and areas where the condensed liquid is trapped artificially (Figure 33).

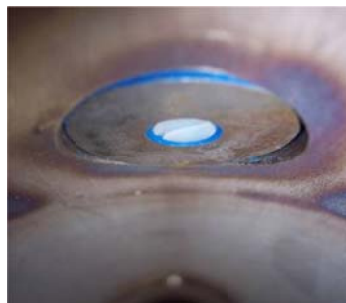


Figure 33: View of the edge mismatch involved in using a flat sample in a 4" ID pipe

On the other hand, using long carbon steel spool pieces is a better representation of the field conditions but it is inconvenient and more costly. In addition, the condensation process happening at the top of a 30" ID pipeline cannot be reproduced perfectly by a 4" ID spool piece because the wall curvature is different, leading to unrealistic wetting properties (smaller droplet size, shorter droplet residence time, etc.). This artifact rendered the study of some experimental parameters, namely the water condensation rate, difficult. Improvement of the experimental setup was warranted, which is the focus of the next section.

#### *3.3.4 Test section focused on localized corrosion*

This section focuses on the design and development of a new test section aimed at:

- Minimizing the artificial accumulation of condensed water on the steel sample and,
- Enabling the proper experimental study of the effect of the condensation rate.

##### *3.3.4.1 Experimental setup and procedure*

The solution was to use a new design involving a steel insert installed on a flat slab. This "flat slab" concept design aims at eliminating the unwanted edge effect by using a large piece of carbon steel as a corrosion sample. It also correctly simulates the large pipe curvature of a 30" ID (0.76 m internal diameter) pipeline -- a size commonly encountered in oil and gas fields -- which is much closer to a flat surface than the 4" ID pipe is. A portion of a pipe section was especially manufactured in order to enable the insertion of a thick flat stainless steel slab about 1m long (Figure 34). The stainless steel slab and the pipe were sealed together using a thermally resistant silicon resin. On top of the stainless steel slab lays an aluminum slab containing a cooling system that enabled the control of the condensation rate. A computational fluid dynamics study was completed in order to characterize the flow characteristics around the slab (APPENDIX B).



Figure 34: Initial flat slab test section

#### 3.3.4.2 *Weight loss sample in flat slab*

Using pipeline steel samples flushed to a stainless steel flat slab represented a compromise between the two previous designs (Figure 35 and Figure 36). Only the carbon steel samples would undergo corrosion, since the slab itself was made of stainless steel. It enabled the collection of corrosion rates and the analysis of the steel surface of the samples. At the same time, unwanted edge effects encountered in the weight loss sample in 4" ID pipe design were minimized but not completely resolved, as the samples were still not perfectly flushed with the slab surface (Figure 36).



Figure 35: Stainless steel with weight loss probe ports (top view)



Figure 36: Stainless steel with weight loss probe ports (left) and view of the edge mismatch involved in using a flat sample in a flat slab (right)

#### 3.3.4.3 Carbon steel insert in flat slab

In order to improve the accuracy of the simulation (and especially the effect of hydrodynamics), a new design was developed for the test section. It involved a flat sleeve of carbon steel inserted into a stainless steel slab as shown in Figure 37.

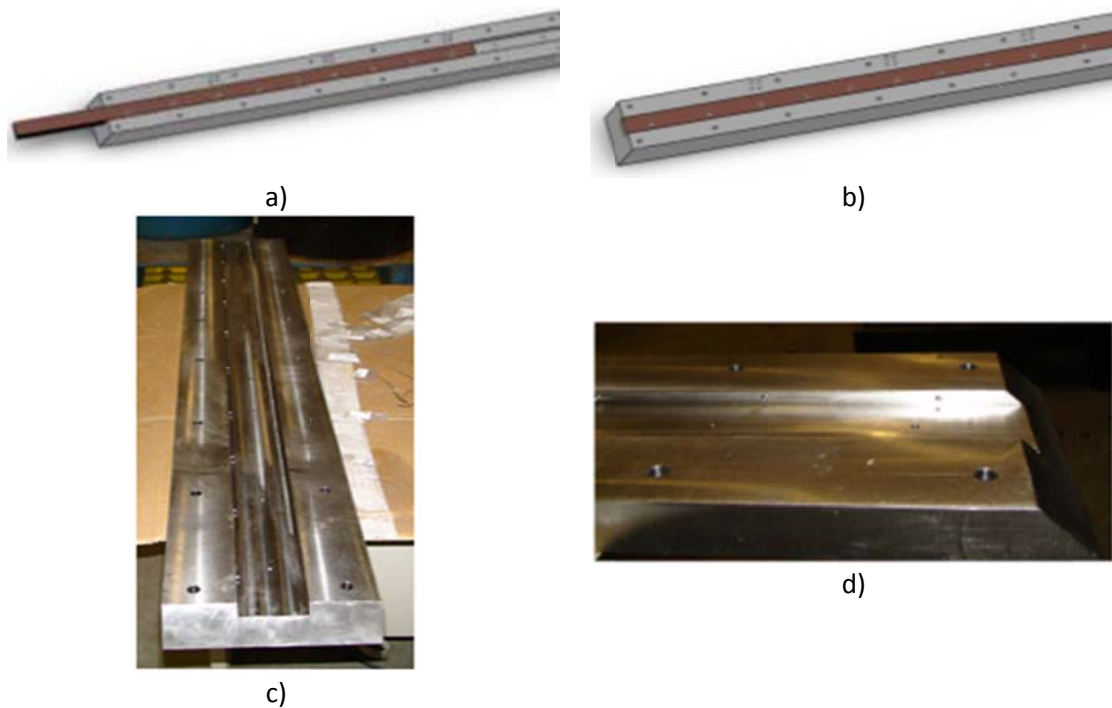


Figure 37: Design of the carbon steel insert in stainless steel slab (a) and b)) and pictures of the stainless steel slab (c) and d))

This final setup had the advantages of exposing a large carbon steel surface to the corrosive environment, more accurately simulating the curvature of a 20" or 30" ID (0.5 or 0.76 m internal diameter) pipe used in the field, and limiting the edge effects to a minimum. The steel sample was also small enough that surface analysis could be performed later on.

One limitation was that the insert had to be installed before the test conditions were set (pressure, temperature) and that the insert could be removed only when the test was completed. Improvements in the experimental procedure were implemented in order to optimize the duration of the insert installation and removal.

#### *3.3.4.4 External cooling setup*

Vapor phase condensation on the internal pipe wall was achieved by artificially cooling specific segments of the loop (test sections) using coils wrapped around the pipe. Tap water was circulated through the coils, and the flow rate was adjusted in order to reach the required amount of cooling. The condensation rate was measured either using a water trap downstream of the test section (similar setup as in Figure 30) or by measuring the difference in temperature between the gas and the pipe wall's inner surface using a model developed by Zhang et al. [83].

For the localized condensation/corrosion study involving the carbon steel insert in a stainless steel flat slab, three 20 cm long zones with different cooling areas were created (Figure 38): A well-insulated section {1}, a section not insulated but not subject to forced external cooling {2}, and a section subject to high external cooling {3}.

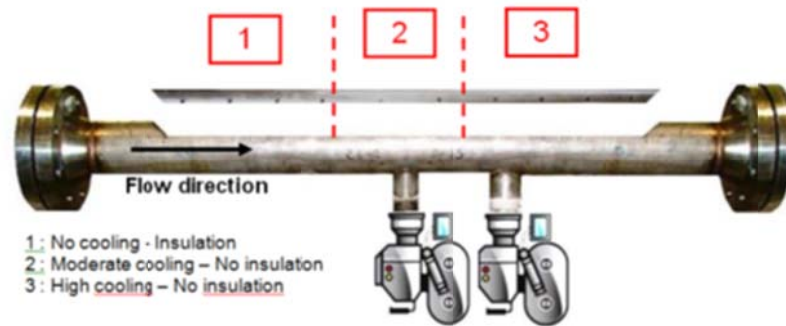
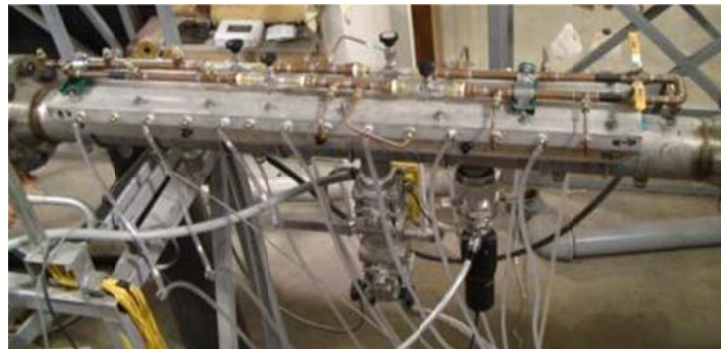
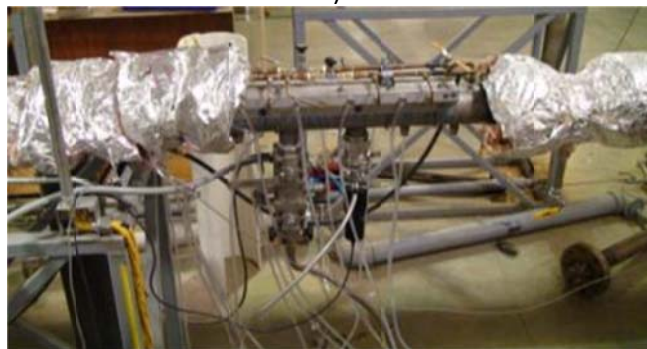


Figure 38: Flat slab cooling setup

A set of thermistors embedded in the stainless steel component was used to monitor the steel temperature and compute the condensation rate on each section. Pictures of the actual setup are shown in Figure 39.



a)



b)

Figure 39: Stainless steel flat slab equipped with carbon steel insert and aluminum heat exchanger, a) with or b) without thermal insulation

### 3.3.5 Localized Corrosion Characterization

Information on the occurrence and extent of localized corrosion was collected for each test performed using a 3D surface profilometer. It is, therefore, important to clearly define the parameters measured as follows.

Pitting corrosion: Generally, pits are deep and narrow, and either hemispherical or cup-shaped. When pitting corrosion happens, a part of the material surface undergoes rapid attack while most of the adjacent surface remains unaffected. As described in Figure 40, the criteria used to define pitting corrosion are displayed below.

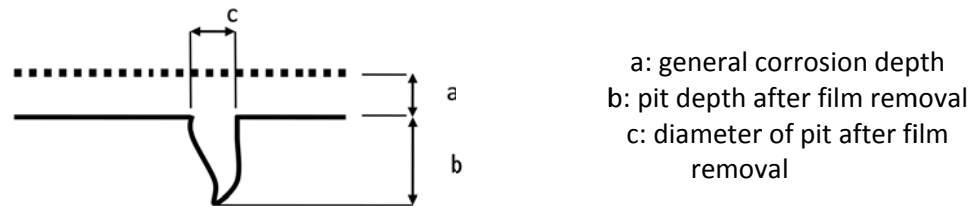


Figure 40: Schematic representation of pitting corrosion

- the pit depth is 5 times bigger than the general corrosion depth ( $b \geq 5a$ ),
- the diameter of pit after film removal is smaller than the pit depth ( $c \leq b$ ).

Mesa attack: Mesa attack is characterized by a wide and often flat-bottomed local attack without protective corrosion film, surrounded by areas with intact corrosion product layers (Figure 41). Generally, mesa attack starts as several small pits growing beneath the porous corrosion product layer. These pits can then continue to grow beneath the corrosion layer until its top is torn away by the mechanical forces of flow. Growth of the pits continues by corrosion both laterally and in depth; then the original corrosion film is removed stepwise by the

flow. Several such pits can be initiated during a short period of time and grow together into a wide, flat-bottomed mesa attack feature. A galvanic effect between the film-free corroding metal in the bottom of the mesa attack feature and the film-covered steel outside can increase the corrosion rate in the mesa attack area.

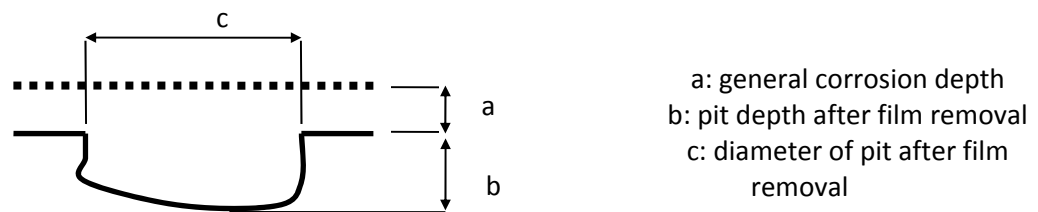


Figure 41: Schematic representation of mesa attack

As described in Figure 41, the criteria used for mesa attack are:

- the mesa attack depth is 5 times bigger than general corrosion depth ( $b \geq 5a$ ),
- the diameter of mesa is bigger than pit depth ( $c \geq b$ ).

Percentage of sample surface affected by localized corrosion: Since weight loss steel carbon samples are used in this study, it was found that the percentage of the sample surface affected by localized corrosion (pitting and mesa attack together) constitutes an indication of the likelihood of its occurrence.

An example of the analysis performed on each steel sample is shown in Figure 42 and Figure 43. The results of a line profile (depth of features along selected line) are shown together with the data used to determine the percentage of the steel surface area affected by localized corrosion. Rates of localized corrosion are calculated by dividing the feature depth (average or maximum pit depth) by the exposure time, and are given in mm/year.

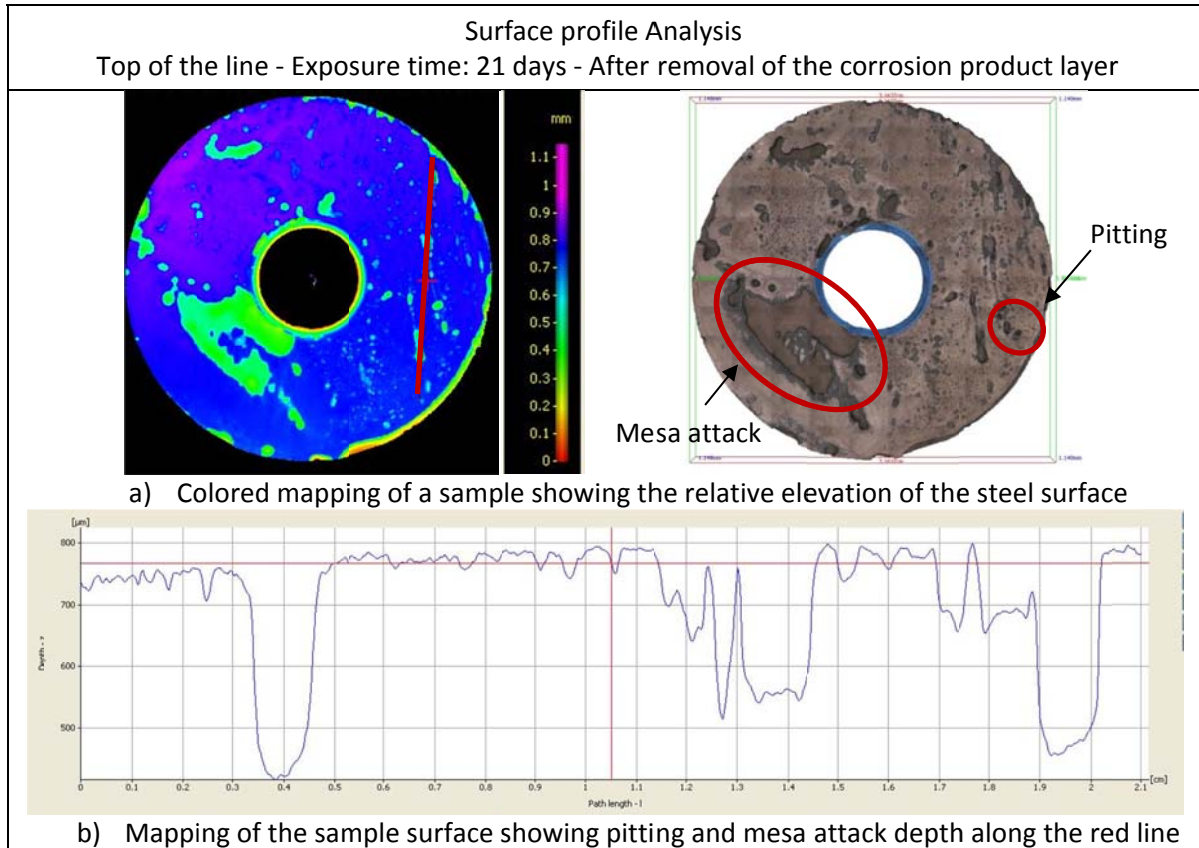


Figure 42: Determination of the depth of localized corrosion features

Free HAC= 1000 ppm and condensation rate= 1 mL/m<sup>2</sup>/s

(P<sub>T</sub>: 3 bars, V<sub>g</sub>= 5 m/s, pCO<sub>2</sub>= 2 bars, T<sub>g</sub>: 70°C)

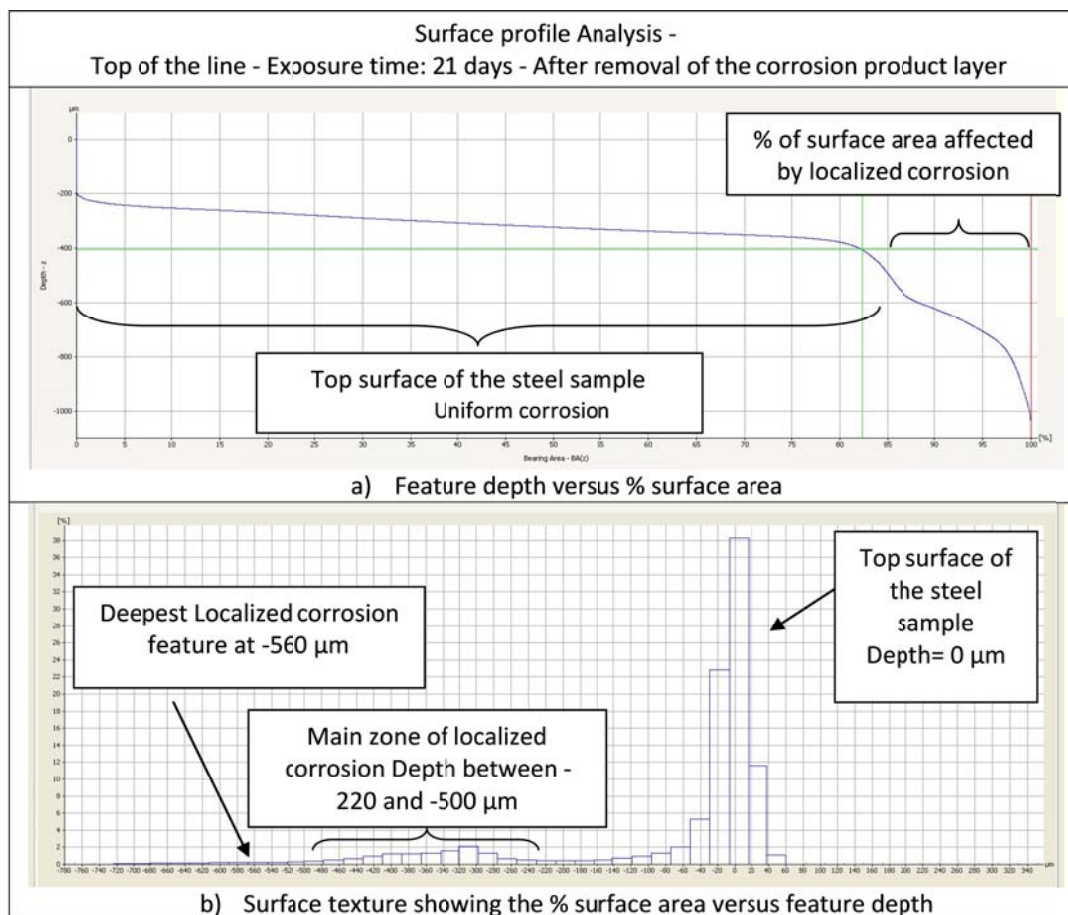


Figure 43: Evaluation of percentage of surface area affected by localized corrosion  
Free HAc= 1000 ppm and condensation rate= 1 mL/m<sup>2</sup>/s  
(PT: 3 bars, Vg= 5 m/s, pCO<sub>2</sub>= 2 bars, Tg: 70°C)

### 3.3.6 Materials Characterization

All of the corrosion samples were made of carbon steel types commonly encountered in the oil and gas industry. Most of the experiments were conducted using American Petroleum Institute (API) X65 steel samples from a single source: a field pipe line (33 cm outside diameter pipe section, 3.8 inch thickness). The chemical analysis of this X65 steel, its microstructure (quenched and tempered), and its hardness characteristics are presented in Table 1, Figure 44 and Table 2.

Table 1: Chemical analysis of the cylindrical carbon steel samples used in the experiments

Element	X65 Composition (%)	API 5L X65 Standard (%)
C	0.13	< 0.26
Mn	1.16	<1.40
P	0.009	< 0.03
S	0.009	< 0.03

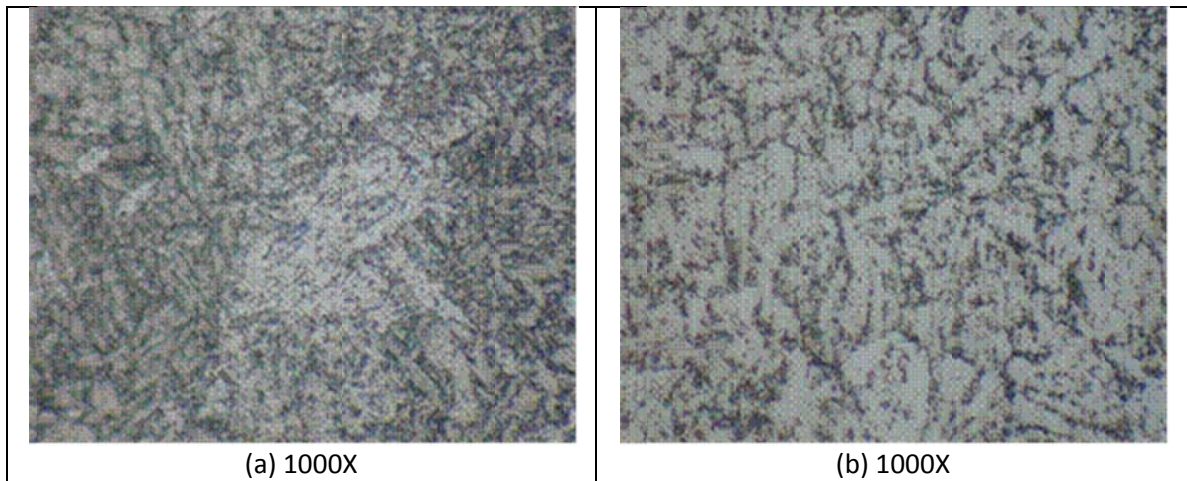
Figure 44: Microstructure of the X65 carbon steel  
a) longitudinal cut, b) transversal cut

Table 2: Hardness (HRB) results of the X65 steel

	X65 longitudinal cut	X65 transversal cut
Average	90.7 kgf	64.8 kgf
Approx. Tensile Strength	90,000 psi for 90.7 kgf HRB	56,000 psi for 65.7 kgf HRB
Tensile requirements	77,000psi (min)	77,000psi (min)
Yield Strength	65,000psi (min)	65,000psi (min)

The carbon steel inserts used in the “flat slab” test section concept were obtained from three different batches of C1018 carbon steel. The chemical composition analysis, showing very similar composition within the specification of C1018, is shown in Table 3.

Table 3: Chemical composition (wt.pct.) of steel samples used in the experiments  
C1018 steel insert (I): Baseline Test #1; (III): Test #4

<u>ELEMENT</u>	<u>REQUIREMENTS</u>		<u>(I)</u>	<u>(III)</u>
	<u>MIN</u>	<u>MAX</u>		
C	0.15	0.20	0.19%	0.19%
Cr			0.069%	0.070%
Cu			0.021%	0.022%
Mn	0.60	0.90	0.74%	0.75%
Mo			0.024%	0.024%
Ni			0.110%	0.116%
P		0.030	0.017%	0.018%
S		0.050	0.014%	0.016%
Si			0.012%	0.012%

Later on, a 20" ID (0.5 m internal diameter) API X65 section of pipe was obtained and all new steel inserts were made from this source. The chemical composition analysis of this new API X65 steel is shown in Table 4.

Table 4: Chemical composition (wt.pct.) of steel samples used in the experiments  
X65 steel insert used for Test #2 and for Test #3.

<u>ELEMENT</u>	<u>REQUIREMENTS</u>		<u>ACTUAL</u>
	<u>MIN</u>	<u>MAX</u>	
C	0.10	0.16	0.14%
Mn	1.10	1.40	1.39%
P		0.040	0.008%
S		0.050	0.008%
Si			0.36%

Figure 45 presents the microstructure of the different grades of steel used for the inserts. All three samples present a ferritic-pearlitic microstructure, consisting of a mixture of ferrite (white constituent) and pearlite colonies (black constituent). However, the steel samples present differences in microstructure as it relates to the volume fraction, colony size and colony density of the pearlite constituent. The steel sample from C1018 (I) contains the lowest volume

fraction of pearlite out of all the characterized C1018 samples. Additionally, fewer pearlite colonies are present in this sample and they are also smaller as compared to C1018(III). The volume fraction of pearlite and the pearlite colony size in the sample C1018(III) seem to be larger than those in the sample from the baseline C1018 (I). The X65 steel also presents a ferritic-pearlitic microstructure. However, the grain size of this steel is much smaller than those of the three C1018 samples. Additionally, the pearlite colonies have a higher density and are much smaller in size. An analysis of the corrosion behavior of all the grades of steel used for the “flat slab” test section design is shown in APPENDIX C.

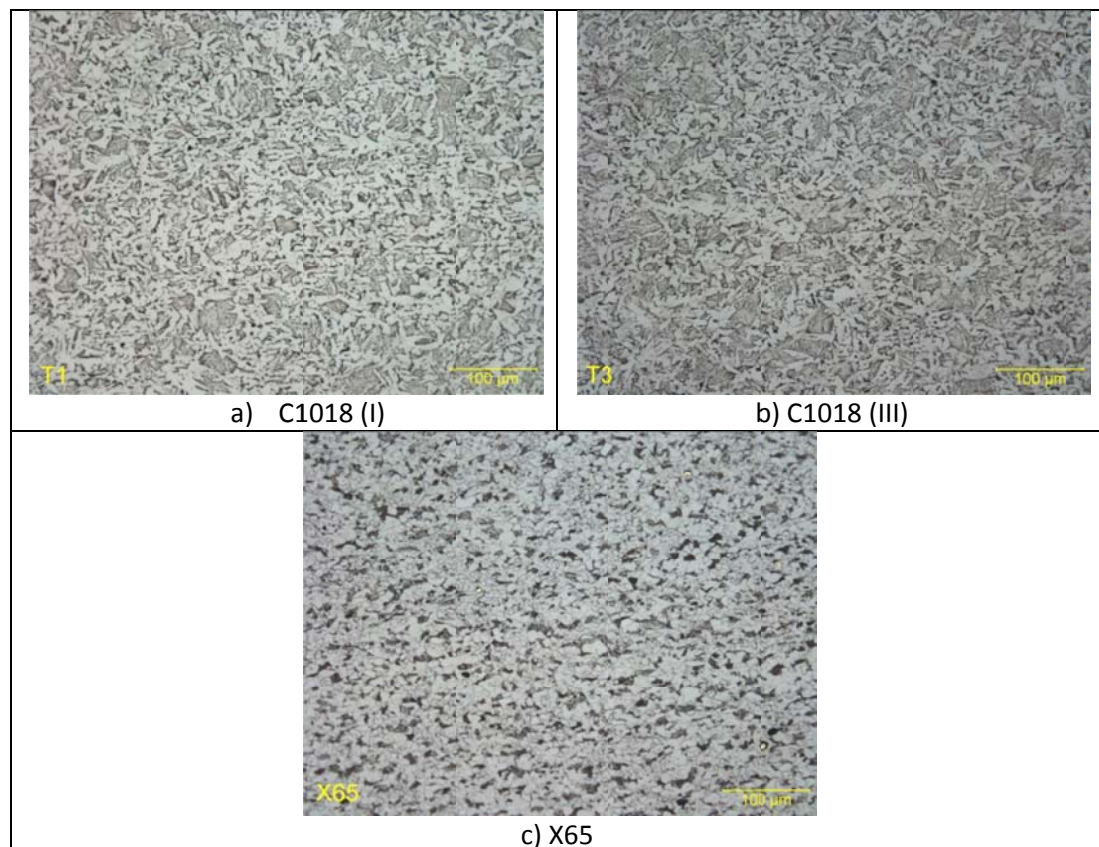


Figure 45: Optical analysis - General microstructure of the steel grade used for the “flat slab” experiments

## CHAPTER 4 EXPERIMENTAL STUDY OF UNIFORM AND LOCALIZED TLC

### 4.1 Objective

The primary objective of this chapter is to investigate the effect of different influencing parameters on top of the line corrosion (both uniform and localized rates), which include:

- Effect of flow velocity and condensation pattern
- Effect of the condensation rate
- Effect of the temperature
- Effect of the concentration of corrosive species ( $\text{CO}_2$ , acetic acid,  $\text{H}_2\text{S}$ )

### 4.2 Literature review

The present chapter presents a review of the laboratory work related to TLC published over the years. Authors have frequently proposed a modeling approach to represent the mechanism observed. These models are described in detail in Section 7.2.2. It should be noted that parts of this section are taken directly from previously published works by the author of this dissertation [71, 72].

#### 4.2.1 *Experimental work on $\text{CO}_2$ top of the line corrosion*

In the past twenty years, TLC has been the subject of intensive research. Olsen et al. [64] conducted a systematic experimental study on parameters influencing TLC in sweet conditions. The formation of a protective  $\text{FeCO}_3$  corrosion product layer was suggested to play a key role (Section 1.5). The precipitation of  $\text{FeCO}_3$  only occurs when the saturation level is above the value of one. High levels of super-saturation in  $\text{FeCO}_3$  could lead to very dense and protective  $\text{FeCO}_3$ , as was the case at a high temperature ( $70^\circ\text{C}$ ) and a low condensation rate. The authors also found that the competition between the rate of iron dissolution (*i.e.*, the increase of  $\text{Fe}^{2+}$  ions in the aqueous phase) and the water condensation rate controlled the extent of  $\text{FeCO}_3$  film

formation. At a high condensation rate, the saturation in  $\text{FeCO}_3$  is more difficult to obtain due to the rate of fresh water renewal.

In 2000, Pots et al. [60] conducted a series of experiments aimed at highlighting the competition between the scale formation rate linked to the iron dissolution and the condensation rate. Pots developed a corrosion prediction model for TLC based on the calculation of the concentration of iron at saturation under film-forming conditions. The author emphasized the importance of correctly evaluating the condensation rate in order to accurately predict the corrosion rate.

In 2002, Vitse et al. [75-77] completed a thorough experimental and theoretical study on TLC caused by carbon dioxide. Condensation and corrosion experiments were conducted in a large-scale 4" ID flow loop, which represented a significant improvement on what had been done before. This setup was later upgraded and improved for the purpose of the present study. Vitse was able to link high gas temperatures to larger condensation rates and consequently to corrosion rates at the top of the line. However, Vitse observed that the formation of  $\text{FeCO}_3$  was favored by high fluid temperature and could lead to a decrease in the corrosion rate. The experiments also explored the effect of the gas velocity and partial pressure of  $\text{CO}_2$  on TLC, which play an important role in the water condensation rate and corrosion rate, respectively. However, the experiments conducted by Vitse were all of relatively short duration (2-4 days) and consequently could not capture the full extent of the corrosion, especially in terms of localized corrosion, which often requires weeks of exposure. Nevertheless, Vitse's corrosion model constituted a considerable breakthrough in the understanding of the mechanisms involved in TLC.

Several experimental studies [70-80, 68] have been published on the effect of different parameters such as acetic acid, Mono-Ethylene-Glycol (MEG) or pH control. However, these experiments also had a relatively short exposure time and offered only limited data in terms of localized corrosion. MEG is commonly used in gas fields in order to prevent the formation of methane gas hydrate (a solid ice structure which can obstruct the flow). The presence of a large quantity of MEG (typically 50 to 70 wt%) decreases the water vapor pressure, which effectively inhibits hydrate formation. It also decreases the water condensation since the amount of water vapor is lower. pH control (a method consisting of injecting a base in order to control the bulk aqueous pH) was shown to have no real effect on TLC other than limiting the concentration of undissociated acetic acid in the bulk liquid phase available for evaporation. The presence of acetic acid was found to greatly affect TLC and mild steel corrosion in general [81].

Okafor et al. [82] proposed through his experimental study a mechanism for corrosion under liquid droplets containing acetic acid. Okafor linked the initiation of localized corrosion with the presence of protected and non-protected regions under drop-wise condensation. He assumed the formation of a galvanic cell between the film-free regions, with those the regions covered by a  $\text{FeCO}_3$  film. It was the first attempt to differentiate general and localized corrosion at the top of the line.

Strong advances in TLC research were published in 2007. Zhang et al. [83] published the first fully mechanistic approach in TLC modeling, covering the three main processes involved in top of the line corrosion phenomena: dropwise condensation, chemistry in the condensed water and corrosion at the steel surface. Zhang's approach represents one of the most advanced attempts to model the mechanisms involved in TLC to date. It takes into account the most important parameters in  $\text{CO}_2$  TLC: condensation rate, gas temperature,  $\text{CO}_2$  partial pressure, gas

velocity and acetic acid concentration. Zhang actively participated in the collection of some of the experimental data shown in the present study, and these data were used to validate his model.

Singer [71] published the results of this experimental parametric study of sweet TLC ( $\text{CO}_2$  dominated) performed in 4"ID flow loops. This study summarized the effect of the most influencing parameters on which the severity of the corrosion attack depends: the condensation rate, the gas temperature, the gas flow rate, the  $\text{CO}_2$  partial pressure and the presence of organic acid. Information about both uniform and localized corrosion was collected through this series of long-term experiments (3 weeks long). The experimental results (in addition to some unedited data) are presented in Section 4.3, where the main findings are discussed in detail.

In 2011, Rotimi [84] conducted a series of long-term experiments (up to 6 weeks of exposure) in an autoclave especially designed for TLC study. The effect of water condensation and temperature was evaluated under different partial pressures of  $\text{CO}_2$ . The author reported that the uniform corrosion decreased as the temperature increased, due to the formation of a more protective  $\text{FeCO}_3$  layer. However, no information was reported on localized corrosion although this type of corrosion was expected to play a big role in these conditions.

Since then, several experimental studies have been published on the characteristics of the water condensation at the top of the line [9] and on the possible role of hydrocarbon condensate [42]. It was found that the condensation of light hydrocarbons could not prevent liquid water from reaching the hydrophilic steel surface.

Even though much progress has been made over the years in the understanding of TLC mechanisms, none of the models proposed thus far tackles the occurrence and prediction of localized corrosion. The first experimental study focusing on this aspect linked to TLC

phenomena was published by Amri [85, 86], in an effort to relate pit growth and environmental conditions. A conceptual model of pit propagation and growth was proposed, although more validation work is clearly needed since the experimental work was not performed in a setup designed to simulate a representative environment.

#### 4.2.2 *Experimental work on H<sub>2</sub>S top of the line corrosion*

Although sour corrosion in general is one of the most important issues for the Oil & Gas industry, very little experimental work has been dedicated to sour TLC. However, most of the findings valid for bottom of the line corrosion are also true in a TLC scenario.

Some valuable experimental work has been conducted recently in order to determine the effect of small amounts of H<sub>2</sub>S on the CO<sub>2</sub> corrosion of carbon steel [87-90]. It has been shown that small amounts of H<sub>2</sub>S lead to a rapid and significant reduction of the CO<sub>2</sub> corrosion rate. The reduction of the corrosion rate is usually associated with the formation of a corrosion product layer on the metal surface, even if the bulk conditions for supersaturation of FeCO<sub>3</sub> or FeS are not met. In the case of H<sub>2</sub>S, the analysis of the layer usually shows the presence of a very thin mackinawite film. It has been reported that the formation of mackinawite on mild steel is a very fast, direct surface reaction leading to a solid, adherent mackinawite layer [90-91]. Depending on various environmental factors, different thermodynamically stable types of FeS can be formed. In some cases FeS film can be non-protective and result in localized attack. For example, the formed layer can develop internal stresses which can lead to film fracture, initiating an environment for potential localized attack. Generally, three regimes in CO<sub>2</sub>/H<sub>2</sub>S systems have been classified based on the concentration of H<sub>2</sub>S [92], as shown in Figure 46. A ratio of pCO<sub>2</sub>/pH<sub>2</sub>S of 500 has been proposed to define the transition. Nevertheless, the mixed CO<sub>2</sub>/H<sub>2</sub>S zone has been reported to begin at a much smaller ratio than the one displayed in the

graph [89]. Smith [93] recently performed a comprehensive analysis of the validity of this ratio and pointed out it was extremely sensitive to the quality of the thermodynamic data used, and that it should not be used as an “engineering tool”. Instead, efforts should be made on predicting the occurrence of FeS and FeCO<sub>3</sub>.

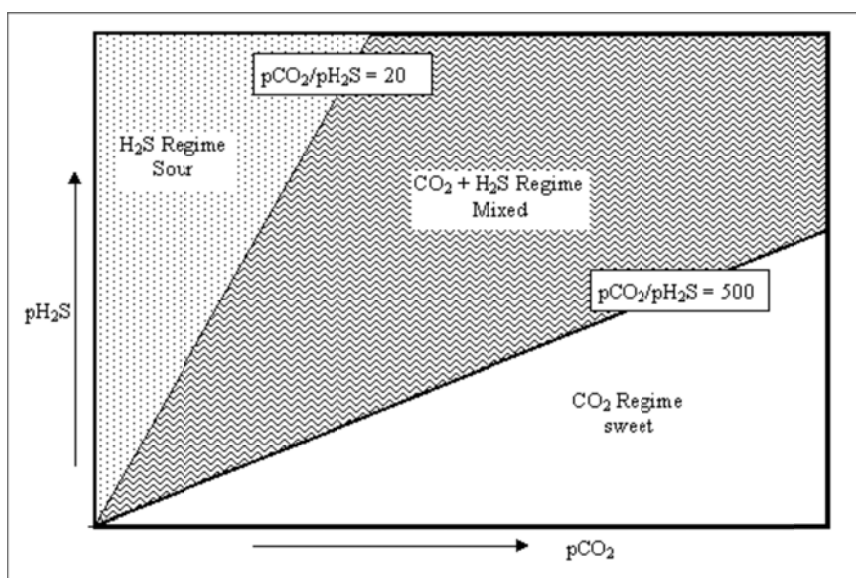


Figure 46: Corrosion regimes in CO<sub>2</sub>/H<sub>2</sub>S corrosion (reproduced from Pots [92] - © NACE international 2002)

The chemistry of iron sulfide formation is very complex, and the corrosion product characteristics and morphology can change with test conditions and time. This can lead to very different corrosiveness scenarios. Smith [94] reported that there are four main forms of iron sulfide commonly found in the field: mackinawite, pyrrhotite, cubic FeS and pyrite.

- Mackinawite is a metastable form of FeS that forms in the presence of small amounts of H<sub>2</sub>S.
- Pyrrhotite is believed to be more thermodynamically stable than mackinawite because the pyrrhotite formation kinetics are much slower than those of mackinawite and it has been reported to form from mackinawite.

- Cubic FeS is the least stable of the three FeS phases and is consequently favored by high saturation levels (*i.e.* high concentration of  $\text{Fe}^{2+}$  ions) and low temperatures (between 35 and 50°C).
- The formation of pyrite is associated with high  $\text{H}_2\text{S}$  partial pressure and is believed to require elemental sulfur.

The corrosion product map related to the formation of these three types of FeS film is shown in Figure 47.

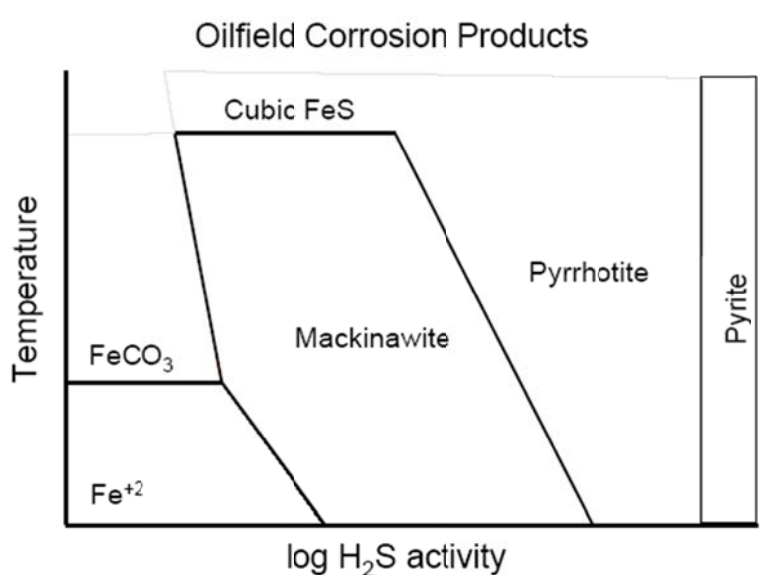


Figure 47: Corrosion product formation as a function of temperature and  $\text{H}_2\text{S}$   
(Reproduced from [94] - © NACE international 2002)

The influence of organic acids on the relative protectiveness of iron sulfide films adds another unknown to the problem since there is, to date, only one published paper on that subject [95].

As mentioned earlier, sour TLC has been the subject of focused research only recently. It is fair to say that even “standard” (bottom of the line) sour corrosion is not very well understood [8], making any attempt to understand sour TLC rather unclear.

Camacho [96] presented a series of short-term (2 to 4 days long) experiments carried out in a 4”ID flow loop. The tests were performed at 3 bars total pressure, at 70°C and at a gas velocity of 5m/s ensuring stratified flow. The condensation was kept constant at 0.25 mL/m<sup>2</sup>/s. The presence of small quantities of H<sub>2</sub>S (up to 0.13 bar) led to a strong decrease in the general corrosion rate compared to its pure CO<sub>2</sub> counterpart. The corrosion was strictly uniform and did not seem to be greatly affected by the range of CO<sub>2</sub>/H<sub>2</sub>S ratio tested. An FeS layer was always found to be the predominant corrosion product present on the carbon steel surface. As is customary in top of the line corrosion testing, the short duration of the experiment made it difficult to extrapolate laboratory corrosion rates to field reality.

Nyborg [69] presented a series of experiments in a 2”ID flow loop using carbon steel tubes as corrosion samples. The tests were conducted at 25°C, with 0.02 bar of H<sub>2</sub>S and 10 bars of CO<sub>2</sub> with 300 ppm of acetic acid. The experiments lasted for more than 30 days at very low condensation rates (lower than 0.006 mL/m<sup>2</sup>/s). The corrosion rate was very stable during the entire test duration. A porous and fluffy FeS film was found on top of a more protective FeCO<sub>3</sub> layer covering the metal surface. It was proposed that dissolved H<sub>2</sub>S acted as a “sink for ferrous ions” by promptly forming an un-protective FeS layer and enabling the corrosion to continue, albeit at a low rate (0.1 mm/year).

Pugh [97] performed experiments in an autoclave equipped with top of the line corrosion capabilities. The aim was to simulate specific field conditions where TLC was observed. The tests were conducted at 25 and 55°C and at condensation rates of 0.002 and 0.1 ml/m<sup>2</sup>/s

respectively. The gas phase consisted of 2.4% CO<sub>2</sub> and 1.0% H<sub>2</sub>S and the tests were performed over a 6 to 10 weeks period. The results showed that the corrosion rate was higher at a lower temperature and lower condensation rate (25°C and 0.002 ml/m<sup>2</sup>/s) than at a higher temperature and higher condensation rate (55°C and 0.1 ml/m<sup>2</sup>/s). In both cases, a mackinawite film formed on the metal surface but had different characteristics depending on the temperature; at 25°C, the film was fluffy, porous, crystalline with 500 nm grains and unprotective; at 55°C, the film was denser, crystalline with 10 microns grains and protective. The presence of organic acid increased the general corrosion rate and promoted localized corrosion, especially where the FeS film was protective.

Singer [72], the author of this dissertation, continued Camacho's work [96] and conducted a parametric study in a 4" ID flow loop. The partial pressure of H<sub>2</sub>S (up to 0.13 bar) and the acid acetic concentration (up to 1000 ppm) were studied in a series of 21-day experiments. In the presence of H<sub>2</sub>S, the presence of acetic acid seemed to affect the integrity of the FeS film and trigger the occurrence of localized corrosion initiation. The experimental results are shown in details in section 4.3.

Singer [48] published another set of experiments, this time performed in a specially designed autoclave for experiments performed under high H<sub>2</sub>S and CO<sub>2</sub> partial pressures (4 and 10 bars, respectively). Mackinawite, cubic FeS and troilite were identified as components of the corrosion product layer, which seemed to be comprised of two distinct layers: a thin and dense inner layer and a porous and thick outer layer. It was also shown that higher uniform corrosion rates could be expected at lower gas temperatures and that the water condensation rate had little effect on the corrosion results.

Although no firm conclusion can be made at this stage, some important characteristics of sour TLC have been proposed:

- Sour TLC does not seem to be as serious or as common as sweet,
- The condensation rate may not be the main controlling parameter, as it is in sweet TLC,
- The severity of the attack seems to depend on the type and protectiveness of the iron sulfide film formed at the condensed water/steel interface,
- Gas temperature could consequently be a key factor, as it directly affects the phase identity and characteristics of the formed iron sulfide.

#### 4.3 Parametric study performed in flow loop using the standard test section

The experimental work presented in this section was performed using the large scale flow loops described in Chapter 3.3. The “standard” test section, consisting of a 4" ID pipe section equipped with several corrosion ports and presented in chapter 3.3.2 was used for this part, both for sweet and sour experiments. As mentioned in section 3.3.3, the design of this test section contained some flaws, creating artificial accumulation of condensed water on the side of the steel samples due to the difference in curvature between the flat samples and the curved pipe. These flaws notwithstanding, the author believes that the key effects of each influential parameter were successfully determined, but advises that the numerical values of corrosion rates should be employed with caution as they are probably conservative estimates. It should be noted that parts of this section are taken directly from previously published publications from the author of this dissertation [71, 72].

##### 4.3.1 Test matrix

A useful approach towards understanding any mechanism is to select a baseline condition and to vary one parameter at a time. That is what has been done throughout the work

presented here. In addition, some tests have focused on the study of interacting effects between parameters. This approach gives a better insight into the relative weight of each parameter and helps in identifying specific areas of interest where the current understanding remains limited.

The most important parameters were identified as follows: the gas velocity, the undissociated acetic acid concentration, the water condensation rate, the CO<sub>2</sub> partial pressure, the H<sub>2</sub>S partial pressure and the gas temperature. In addition, two interacting effects are investigated: condensation rate / acetic acid and H<sub>2</sub>S partial pressure / Acetic acid.

Table 5 presents the experimental conditions of the baseline test. Each series of tests proposes a variation of a single parameter around the baseline conditions.

Table 5: Baseline conditions for the parametric study\*

Parameters	Baseline conditions
<i>Absolute pressure (bar) **</i>	3
<i>pCO<sub>2</sub> (bar)</i>	2
<i>Gas temperature (°C)</i>	70
<i>Condensation rate (mL/m<sup>2</sup>/s)</i>	0.25
<i>Gas velocity (m/s)</i>	5
<i>pH<sub>2</sub>S (bar)</i>	0
<i>Free HAc concentration in the tank (ppm)</i>	0
Steel type	API X65
Liquid phase composition	DI water
pH (tank)	4.5
Test duration (weeks)	3

\*Only the value of the parameters in italics are varied in this study

\*\* Nitrogen is used as a makeup gas

Table 6 shows the range of values by which each parameter is varied.

Table 6: Range of variables used for the parametric study

Parameters	Range		
	Min	Medium	Max
pCO <sub>2</sub> (bar)	0.13	2	8
pH <sub>2</sub> S (bar)	0.004 (or 0)	0.07	0.13
Gas temperature (°C)	40	70	90
Condensation rate (mL/m <sup>2</sup> /s)	0.05	0.25	1
Gas velocity (m/s)	5	10	15
Free HAc concentration in tank (ppm)	0	100	1000

During the experiment, some water accumulated at the bottom of the line due to the water condensation forming a small liquid stream. The flow regime was observed through a high pressure transparent window and was always stratified.

Another important aspect is the wall temperature at the top of the line where the corrosion reaction takes place. This wall temperature is dependent on the gas temperature, the condensation rate and, to a lesser extent, the total pressure and the gas velocity. The corresponding values encountered in this experimental study are shown in Table 7. These values are calculated using an approach developed by Zhang [83] which shows very good agreement with experimental measurements.

Table 7: Wall temperature

Gas temperature (°C)	Condensation rate (mL/m <sup>2</sup> /s)	Total pressure (bar)	Wall temperature (°C)
70	0.03	3	69.8
70	0.25	3	68.2
70	1	3	63.2
40	0.25	3	33.5
70	0.25	0.13	68.3
70	0.25	8.3	67.8

### 4.3.2 Experimental results

This section presents the corrosion rate results obtained for each of the tests performed. Two types of information are displayed: the evolution of the average (uniform) corrosion rate with time and the occurrence of localized corrosion. The average (uniform) corrosion rate is calculated using the weight loss of a sample and the time of exposure. It gives an average corrosion rate over the entire period of exposure. The localized corrosion graphs present corrosion rates that are due to pitting or mesa attack and indicate the percentage of the surface area of the sample affected by localized corrosion (pitting or mesa). The corresponding values are obtained by performing a surface analysis on each sample with a 3D surface profilometer. As localized corrosion is always more noticeable after longer exposure time, only the data obtained with the "21 days" samples are presented.

The corrosion rate results are displayed in a series of graphs from Figure 48 to Figure 76. Error bars represent the minimum and the maximum values obtained, and the number of samples (*i.e.*, the number of repeated measurements) is displayed on each graph.

#### 4.3.2.1 Influence of the CO<sub>2</sub> partial pressure

In general, the higher the partial pressure of CO<sub>2</sub>, the higher the uniform corrosion will be, as shown in Figure 48. At 2 bars partial pressure of CO<sub>2</sub>, a declining trend of the corrosion attack with time is clearly visible and is due to the formation of a protective FeCO<sub>3</sub> film on the surface of the sample (Figure 49). In this section, the corrosion product layers are characterized mostly through EDS analysis and study of the crystals morphology, methods which are not sufficient to identify the product phase (FeCO<sub>3</sub> for example). However, experimental work described later in this document (Figure 142) supports the phases reported in this section. In

addition, the corrosion product identification was corroborated by analysis of Pourbaix diagrams (Figure 89).

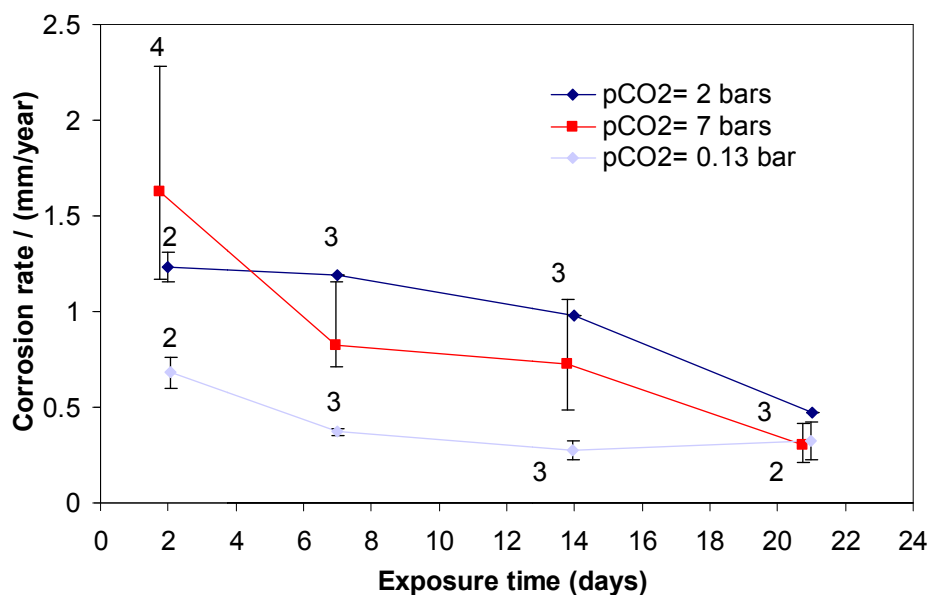


Figure 48: General corrosion – Effect of the pCO<sub>2</sub>  
 $T_g=70^\circ\text{C}$ ,  $[\text{HAc}]_{\text{free}}=0\text{ppm}$ ,  $V_g=5\text{m/s}$ , Condensation rate= $0.25\text{ mL/m}^2/\text{s}$

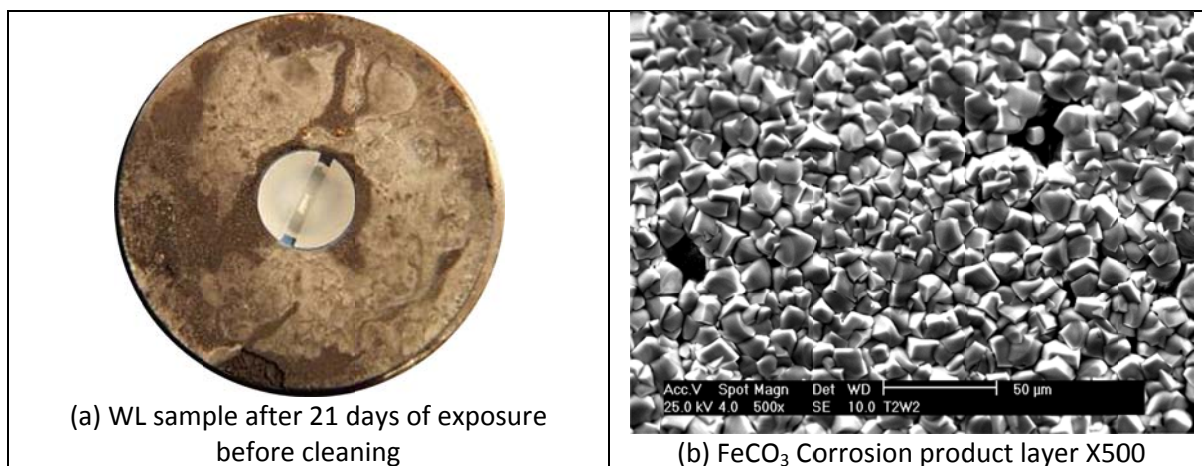


Figure 49: Surface analysis of corrosion product / pCO<sub>2</sub>= 2 bars  
 (PT: 3 bars,  $V_g= 5\text{ m/s}$ , Free HAc: 0 ppm,  $T_g: 70^\circ\text{C}$ , condensation rate=  $0.25\text{ mL/m}^2/\text{s}$ ,  
 Exposure time: 21 days)

At lower partial pressure of  $\text{CO}_2$  (0.13 bar), the conditions of  $\text{FeCO}_3$  supersaturation seem to be more difficult to reach, and the protective film does not form uniformly over the entire steel surface (Figure 50), leading to a low but constant corrosion rate over time (around 0.4 mm/year). At higher partial pressure of  $\text{CO}_2$ , the corrosion attack is initially more aggressive but the uniform corrosion rate decreases with time to reach 0.3 mm/year after 21 days of testing. Since all the conditions of  $\text{FeCO}_3$  supersaturation (high  $\text{Fe}^{2+}$  and  $\text{CO}_3^{2-}$  concentration) can easily be met, a dense and protective layer should form on the metal surface.

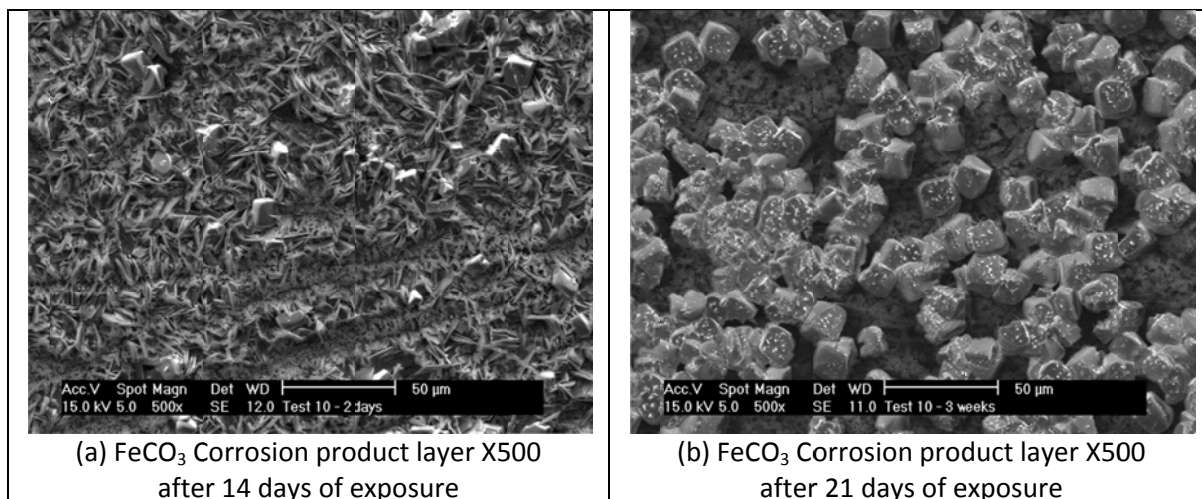


Figure 50: Surface analysis of corrosion product /  $p\text{CO}_2 = 0.13$  bar  
(PT: 3 bars,  $V_g = 5$  m/s, Free HAC: 0 ppm,  $T_g = 70^\circ\text{C}$ , condensation rate =  $0.25 \text{ mL/m}^2/\text{s}$ )

However, local breakdowns in an otherwise rather uniform coverage of tightly packed crystals are seen, like in Figure 51 which presents an example of this situation, obtained with 2 bars of  $\text{CO}_2$ . Inside these breakdowns, the corrosion product is identified by EDS as iron carbide with elements of the steel microstructure appearing (traces of Mo, Cr, Mn in Figure 51 d)).

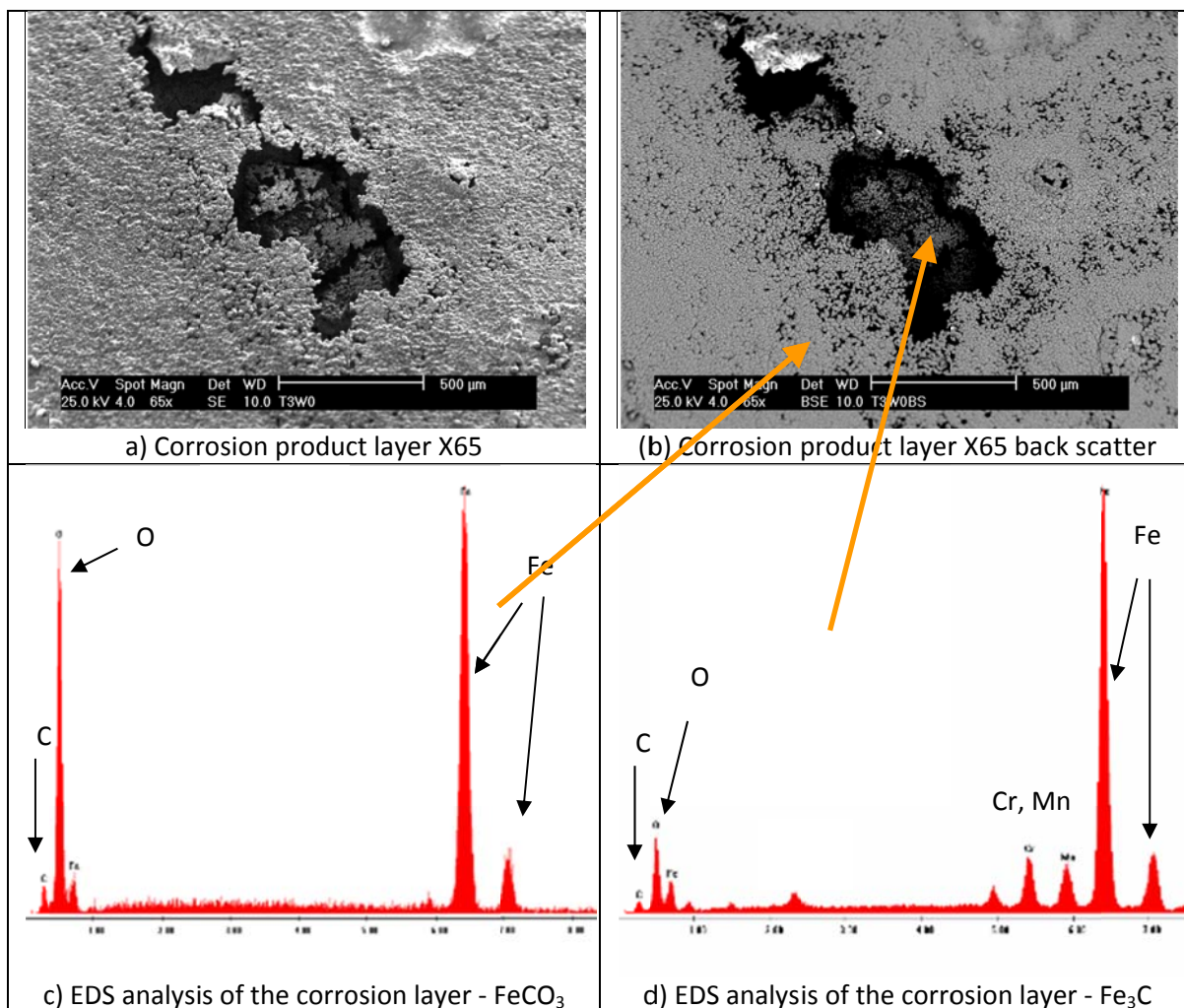


Figure 51: Surface analysis of corrosion product /  $p\text{CO}_2=2$  bars  
 ( $P_T$ : 3 bars,  $V_g=5$  m/s, Free HAc: 0 ppm,  $T_g=70^\circ\text{C}$ , condensation rate=  $0.25$  mL/m<sup>2</sup>/s)

This layer does not offer protection against corrosion and deep localized features are always encountered at these locations (Figure 52). Pitting corrosion was observed at partial pressures of 2 and 7 bars, and it was stronger at 7 bars partial pressure of  $\text{CO}_2$ . Both pitting corrosion (narrow features) and mesa attack (wide features) are encountered on the metal surface, as it is the case for all experiments performed in sweet environments. It is suspected that pits grow in depth and in width and tend to combine with each other, forming large features, which are then qualified as mesa attack.

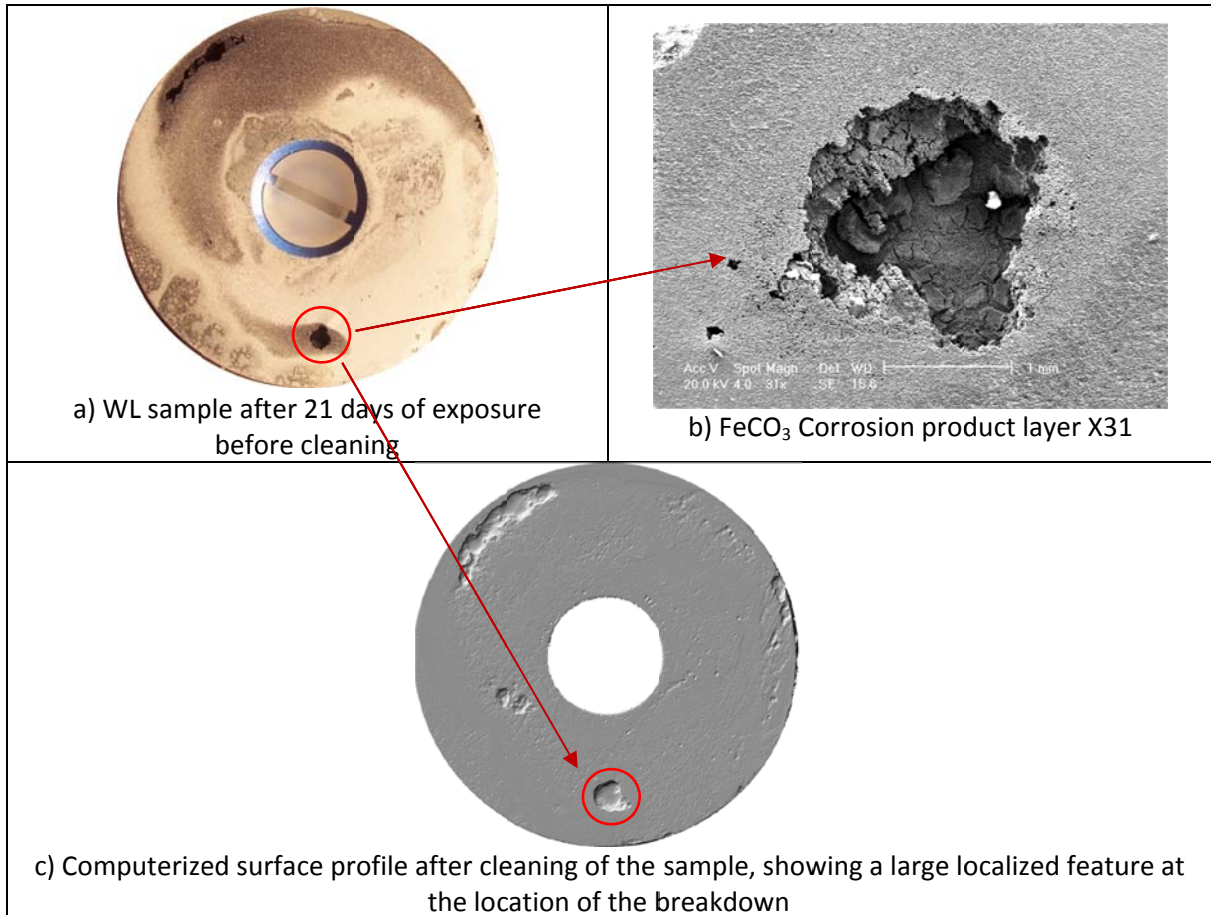


Figure 52: Surface analysis with corrosion product /  $p\text{CO}_2= 7$  bars  
 (PT: 7.3 bars,  $V_g= 5$  m/s, Free HAc: 0 ppm,  $T_g: 70^\circ\text{C}$ , condensation rate= $0.25$  mL/m<sup>2</sup>/s)  
 Exposure time: 21 days

The data presented in Figure 53 represent the extent of localized corrosion measured for each sample. The average pitting rate, average mesa rate and average uniform corrosion rates refers to the left axis with a unit in mm/year, while the percentage of the surface affected by localized corrosion refers to the right axis with a unit in %. The figure shows that pitting and mesa attack rates increase with increasing  $\text{CO}_2$  partial pressure. Weaker pitting was observed at 0.13 bar partial pressure. In the case of  $\text{CO}_2$  top of the line corrosion, the occurrence of localized corrosion is strongly linked with the presence of a protective  $\text{FeCO}_3$  layer, which undergoes some breakdown due to higher local corrosiveness. The change in corrosiveness of the

condensed liquid is due to the condensation process itself, which sees droplets of liquid nucleate grow and eventually fall because of gravitational forces. During this process, the chemistry in the droplet undergoes a significant increase in pH and in  $\text{Fe}^{2+}$  concentration, which favors scale formation. Once the droplet reaches its maximum size and falls, a new droplet will form with lower pH and more aggressive corrosiveness. The cycle is believed to challenge the protectiveness of the  $\text{FeCO}_3$  layer and lead to localized corrosion. Higher partial pressures of  $\text{CO}_2$  render the condensed water more corrosive (*i.e.*, higher localized corrosion rates are encountered). However, the percentage of surface area affected by localized corrosion remains mostly unaffected by the  $\text{CO}_2$  partial pressure (Figure 53).

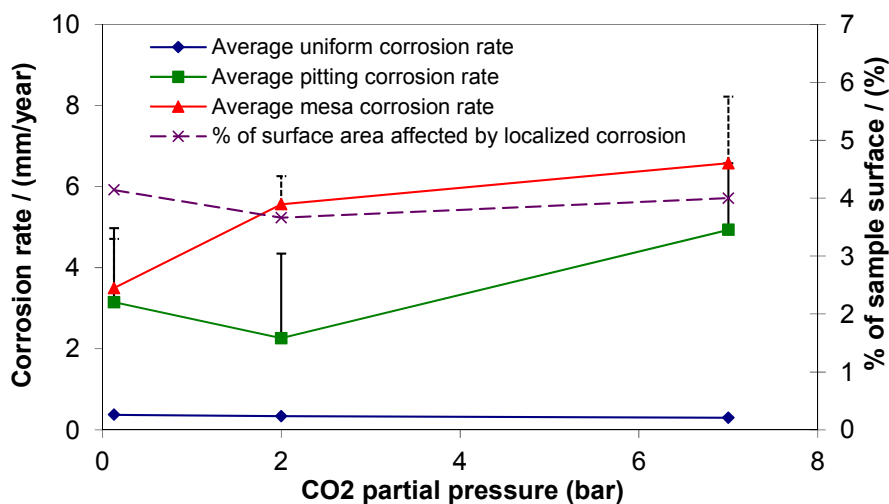


Figure 53: Localized corrosion - Effect of the  $\text{pCO}_2$

$T_g=70^\circ\text{C}$ ,  $[\text{HAc}]_{\text{free}}=0\text{ppm}$ ,  $V_g=5\text{m/s}$ , Condensation rate= $0.25\text{ mL/m}^2/\text{s}$ , Exposure time: 21 days

#### 4.3.2.2 Influence of gas velocity

The most visible influence of gas velocity appears to be on the condensation regime which, in return, affects the way the corrosion process occurs. At low gas velocity (usually below

5 m/s for the present experiments), the vapor condenses by forming stagnant droplets at the top of the pipe (Figure 54).

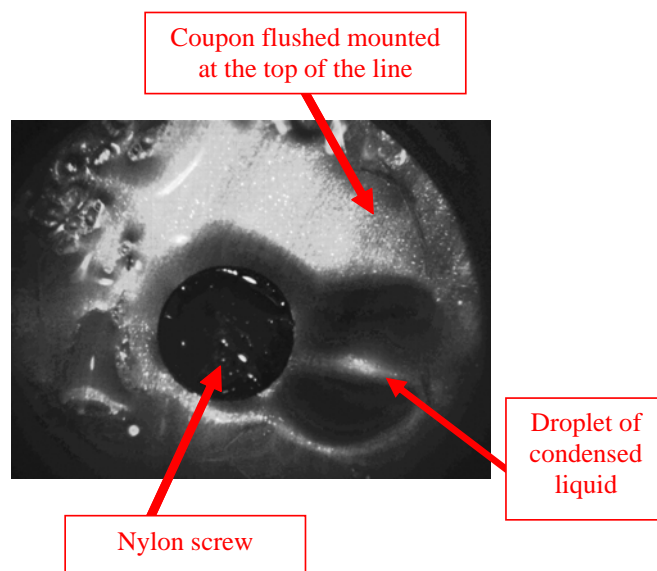


Figure 54: View of the weight loss sample at the beginning of test, taken via a port installed at the bottom of the line

In these stagnant droplets, the  $\text{FeCO}_3$  supersaturation can be very high, enabling the formation of a dense protective layer. As the gas velocity increases, the condensation regime switches gradually from stagnant to sliding droplet. In the sliding droplet mode, the droplets of condensed liquid flow along the top of the pipe and eventually slide to the bottom. The sliding droplets are not generally in contact with the carbon steel long enough to create an  $\text{FeCO}_3$  layer (as opposed to the stagnant droplet condensation regime). Instead, the droplets upstream of the sample slide on the stainless steel part of the pipe and reach the sample without containing any product of corrosion. Considering this very aggressive corrosiveness, a thick but non-protective  $\text{Fe}_3\text{C}$  film only forms on the liquid pathways that the sliding droplets create. It leads to the formation of two different types of film at the top of the line: protective  $\text{FeCO}_3$  on most of

the sample area and non-protective  $\text{Fe}_3\text{C}$  on the preferential liquid pathways. Figure 55 clearly shows these preferential liquid pathways at a gas velocity of 10 m/s, as highlighted in blue in Figure 55 a). The weight loss method does not differentiate between the types of film and gives an average corrosion rate across the entire surface of the samples. It is possible to correct the space average corrosion rate by evaluating the percentage of surface coverage of both types of film on the sample surface. However, this process can lead to a high margin of error and does not bring any valuable additional information. Under the  $\text{Fe}_3\text{C}$  layer (Figure 55 d) and f)), the average corrosion rate can be as high as 10 mm/year. Under the parts of the samples covered by a  $\text{FeCO}_3$  layer (Figure 55 c) and e)), the situation resembles a more typical TLC scenario with a much lower uniform corrosion rate and with some visible localized corrosion features; whereas the corrosion under  $\text{Fe}_3\text{C}$  is usually uniform. There was no clear influence of the gas velocity on the extent of the localized corrosion, only on the condensation regime as discussed above. The space average corrosion rate results do not appear in this dissertation as they do not help in clarifying this particular phenomenon. There was no visible effect of the gas velocity on the top of the line corrosion (uniform and localized corrosion) except for the change in condensation regime discussed earlier.

Visual observations made during the experiment showed that the condensation regime starts to change from stagnant droplet to sliding droplet at a gas velocity around 10 m/s (rivulets of liquid form on the sample surface) for a total pressure of 3 bars. Since then, a more comprehensive effort to understand and predict the transition zone between stagnant and sliding droplets has been made. A model developed by Zhang [83] was presented in 2006 and constitutes a good predictive tool for this kind of scenario.

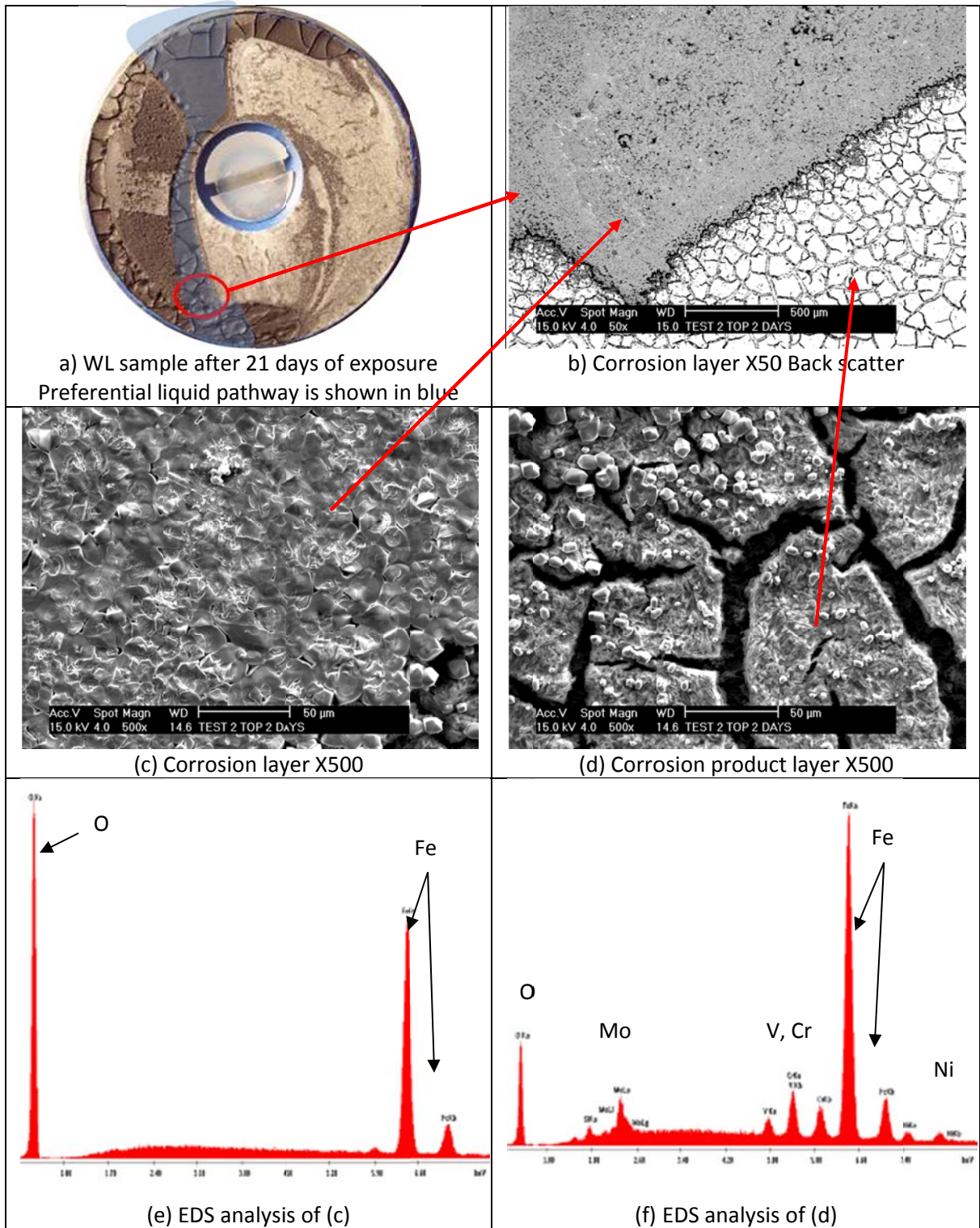


Figure 55: Surface analysis with corrosion product /  $v_g=10\text{m/s}$   
 ( $P_T$ : 3 bars,  $p\text{CO}_2$ : 2 bars, Free HAC: 0 ppm,  $T_g$ :  $70^\circ\text{C}$ , condensation rate= $0.25\text{ mL/m}^2/\text{s}$ )

In summary, once the condensation regime switches from stagnant to sliding droplet, parts of the sample at the top of the line start to be heavily corroded at a rate similar to that at the bottom of the line. However, the flow regime is not yet annular (which happens in our experimental conditions at around 20 m/s), as the droplets flowing at the top are still exclusively made of pure condensed water saturated with CO<sub>2</sub>. Additional issues related to droplet transport from the bottom to the top of the line may be expected at high gas velocity. However, no inquiry was made into this phenomenon during the study.

#### 4.3.2.3 Influence of the concentration of undissociated acetic acid

The presence of 100 ppm of free acetic acid in the liquid phase of the tank does not seem to have a strong impact on the average corrosion rate (Figure 56), as the corrosion rate is almost identical between the two conditions.

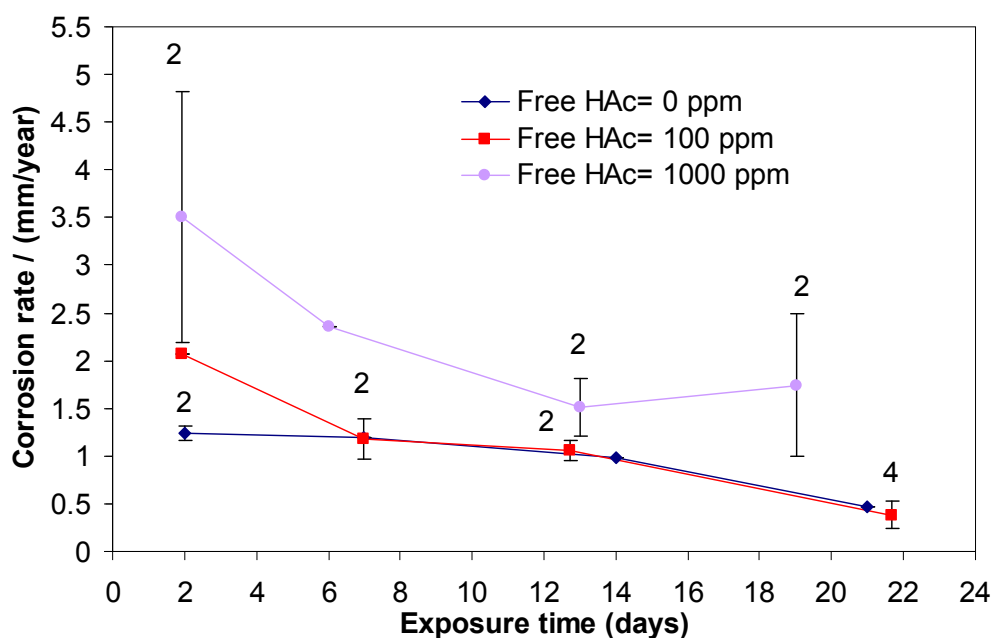


Figure 56: General corrosion - Effect of the free HAC concentration  
 $p\text{CO}_2=3\text{bars}$ ,  $T_g=70^\circ\text{C}$ , Condensation rate= $0.25\text{ mL/m}^2/\text{s}$ ,  $V_g=5\text{m/s}$

The contribution to the overall cathodic reaction of such a small amount seems to be minimal. However, as the free acetic acid concentration is increased to 1000 ppm, the average corrosion rate increases significantly compared to lower concentrations. Furthermore, the uniform corrosion rate does not decrease significantly with time and is still at around 2 mm/year after the first week of exposure. The presence of acetic acid strongly promotes the occurrence of pitting corrosion proportionate to the amount of acid in the solution (Figure 58).

With 1000 ppm of free acetic acid, the pitting and mesa attack rates are between 7.5 and 11 mm/year after 3 weeks of exposure. These rates are almost double the ones encountered for the baseline case (no acetic acid) or with 100 ppm of acetic acid. The percentage of surface area affected by localized corrosion jumps to 14% in the presence of 1000 ppm of acetic acid, while it is around 4% with 0 or 100 ppm. Once again, the presence of a corrosion product layer offering protection at least on some parts of the steel surface, together with a local change in chemistry and pH (due to the continuous renewal of condensed droplets), are believed to be responsible for the occurrence of localized corrosion. Figure 57 a) and b) present images of the steel surface before removal of the corrosion product layer and illustrates the previous statement with apparent protection on most of the surface encountered together with massive localized attack. Acetic acid, being a volatile weak acid, increases the corrosiveness of the condensed water and challenges the integrity of the layer. Once again, although the layer is identified as  $\text{FeCO}_3$  and seems to be mostly made of tightly packed crystals (Figure 57 c) and e)), numerous breakdowns are encountered which correspond to the location of the pits. Inside these breakdowns,  $\text{Fe}_3\text{C}$  is identified as the main corrosion product (Figure 57 d) and f)).

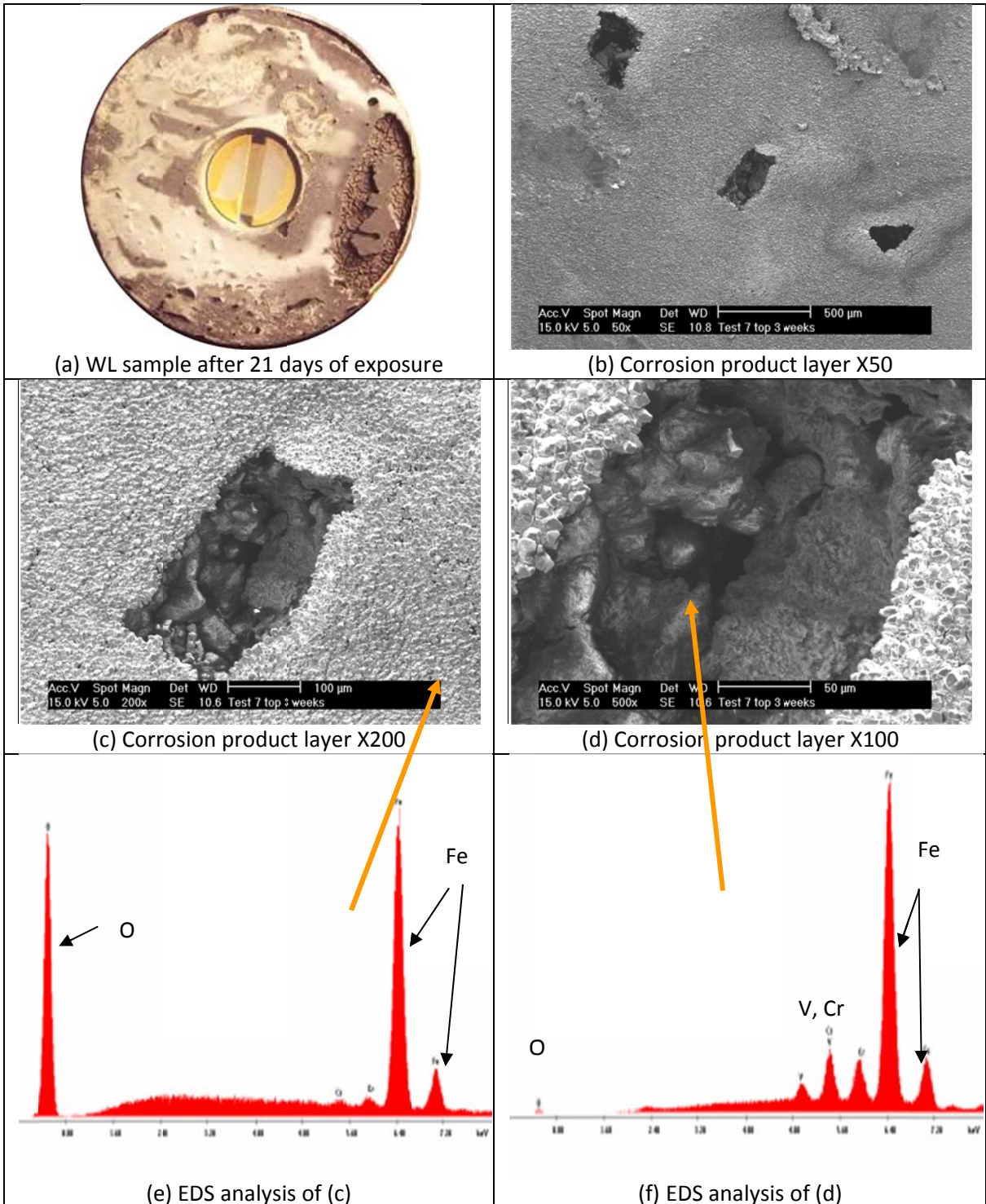


Figure 57: Surface analysis with corrosion product / Free HAc= 1000 ppm  
 (P<sub>T</sub>: 3 bars, V<sub>g</sub>= 5 m/s, pCO<sub>2</sub>= 2 bars, T<sub>g</sub>: 70°C, condensation rate= 0.25 mL/m<sup>2</sup>/s)

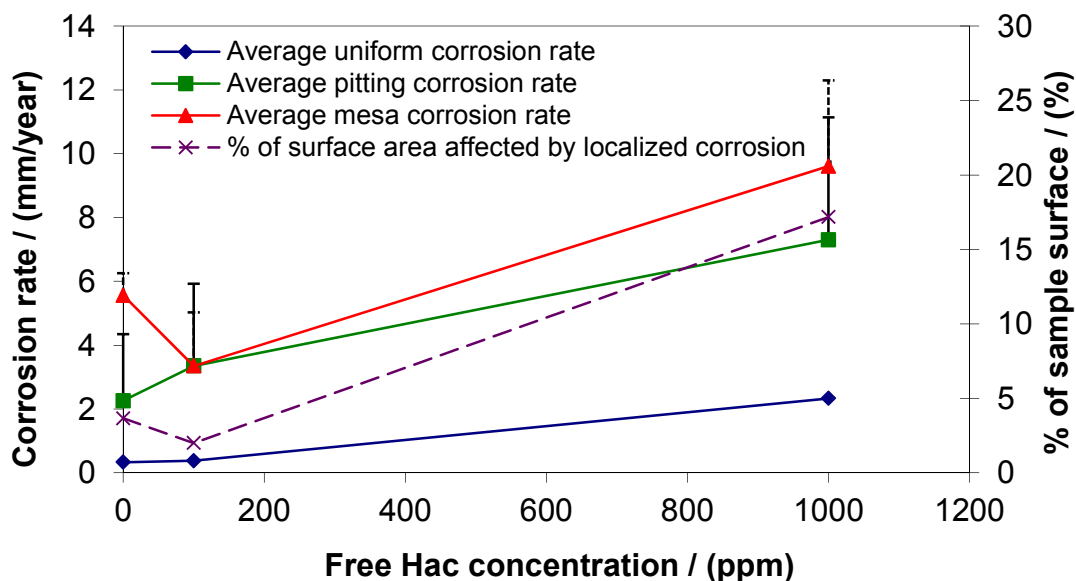


Figure 58: Localized corrosion - Effect of the free HAc concentration  
 $p\text{CO}_2=3\text{bars}$ ,  $T_g=70^\circ\text{C}$ , Condensation rate= $0.25\text{ mL/m}^2/\text{s}$ ,  $V_g=5\text{m/s}$ , Exposure time: 21 days

#### 4.3.2.4 Influence of the condensation rate

The average corrosion rate is expected to be lowest at the lowest condensation rate (Figure 59) because the rate of renewal of condensed droplets is faster at higher condensation rates. The saturation of  $\text{FeCO}_3$  is easier to achieve when droplets of liquid remain attached to the metal surface for a longer time. Nevertheless, the effect of the water condensation rate was not always clear in the conditions tested. The final average corrosion rate is about twice as high at  $1\text{ mL/m}^2/\text{s}$  compared to  $0.03\text{ mL/m}^2/\text{s}$ , but the overall trend (uniform corrosion rate decreasing with time) is rather similar in all cases (especially at 1 and  $0.25\text{ mL/m}^2/\text{s}$ ). A stronger contrast was expected, since a higher condensation rate is usually synonymous with a higher general corrosion rate. The lack of stronger influence on the average corrosion rate is thought to be due to the specific design of the sample holder. As mentioned previously, using flat weight loss samples flush mounted to a cylindrical 4" ID pipe leads to areas on the samples where

condensed water is artificially “trapped”, which could have diminished the effect of the water condensation rate and led to an overestimation of the corrosion rate.

The influence of the condensation is much stronger on the localized attack as both pitting rate and surface coverage by localized attack increase significantly when the condensation rate increases from 0.05 to 1 mL/m<sup>2</sup>/s (Figure 61). The effect is even more pronounced on the surface coverage by localized attack which increases from 2% at 0.05 mL/m<sup>2</sup>/s to 14% at 1 mL/m<sup>2</sup>/s. Figure 60 shows one of the weight loss samples exposed for 21 days to the baseline environment and a condensation rate of 1 mL/m<sup>2</sup>/s. The corrosion product layer has been removed and the steel surface presents numerous localized corrosion features. Mesa attack seems to be predominant in this case with wide pits easily identifiable.

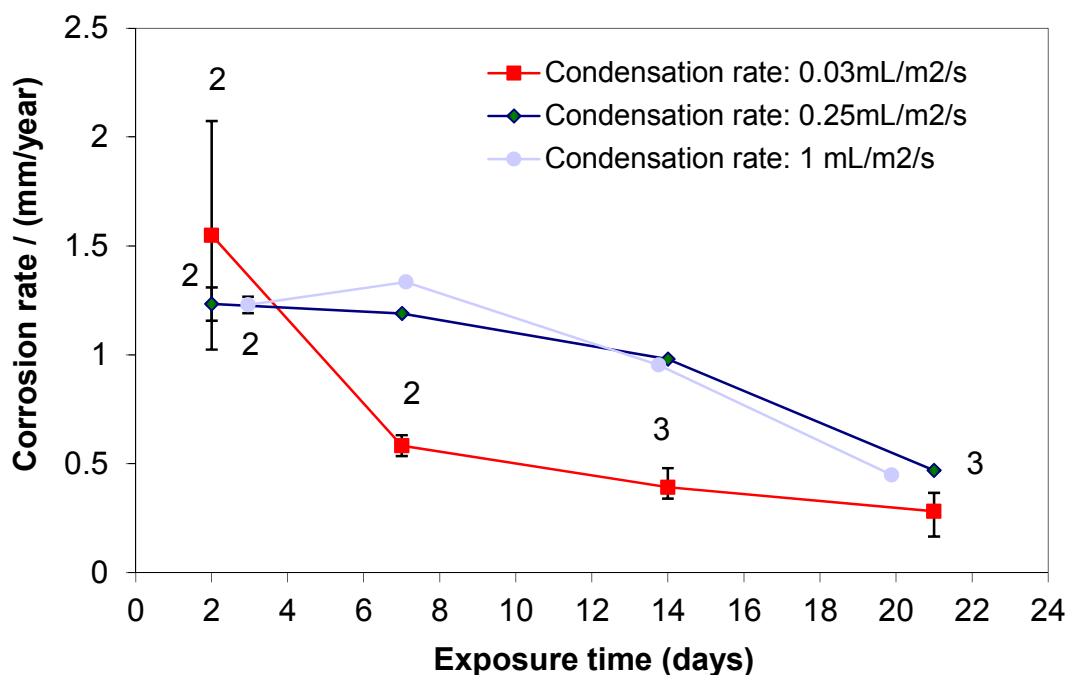


Figure 59: General corrosion – Effect of the condensation rate  
 $p\text{CO}_2=3\text{bars}$ ,  $T_g=70^\circ\text{C}$ ,  $[\text{HAc}]_{\text{free}}=0\text{ppm}$ ,  $V_g=5\text{m/s}$

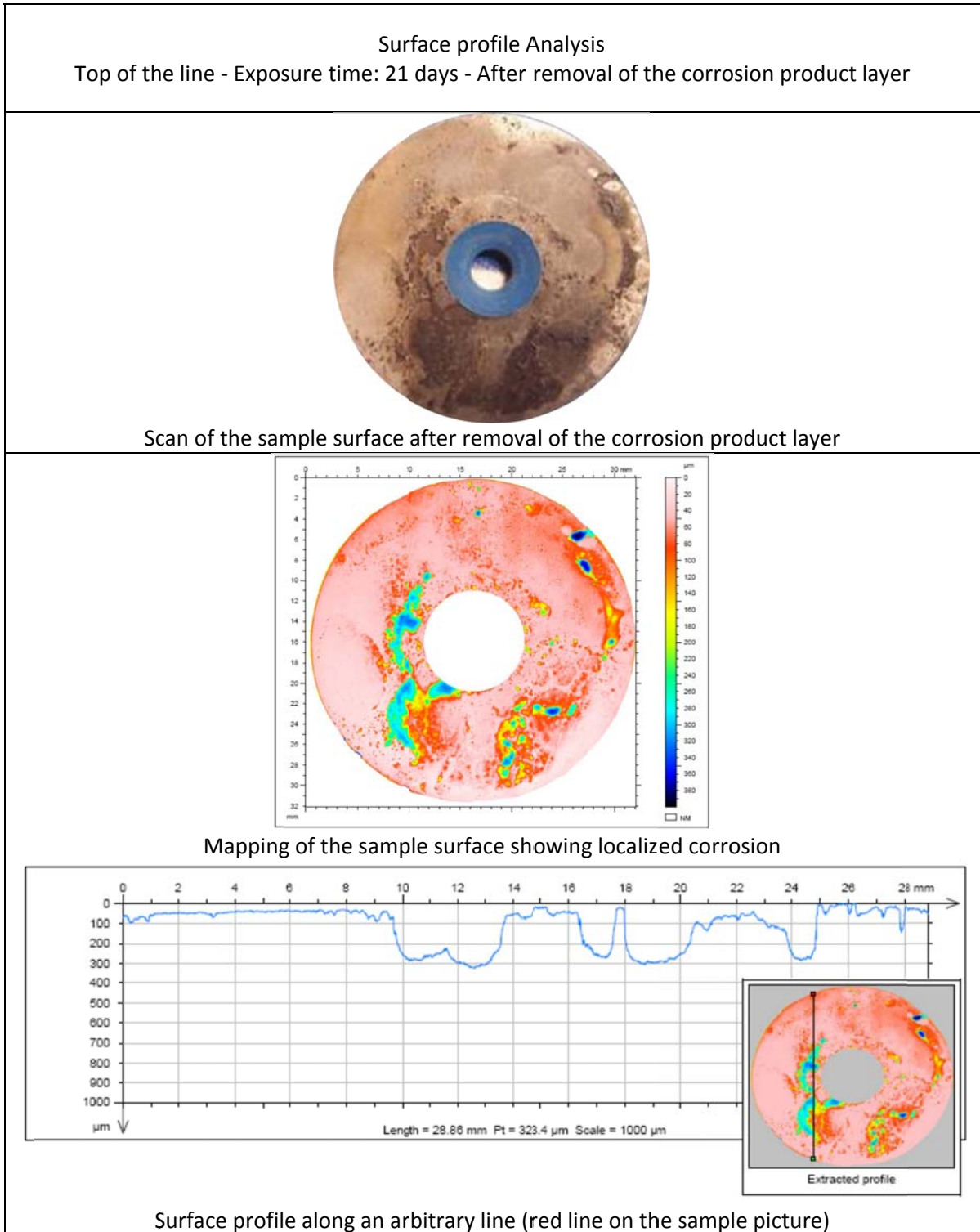


Figure 60: Surface analysis without corrosion product

( $P_T$ : 3 bars,  $V_g$ = 5 m/s,  $p_{CO_2}$ = 2 bars,  $T_g$ : 70°C, Free HAc= 0 ppm, Water condensation rate= 1 mL/m<sup>2</sup>/s)

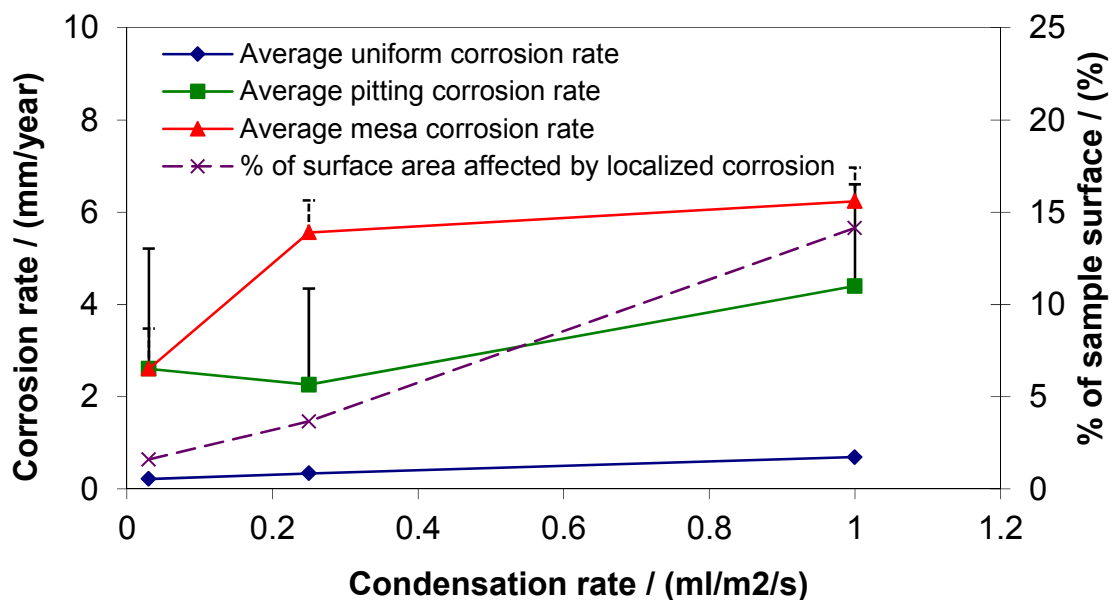


Figure 61: Localized corrosion - Effect of the condensation rate  
 $p\text{CO}_2=3$  bars,  $T_g=70^\circ\text{C}$ ,  $[\text{HAc}]_{\text{free}}=0$  ppm,  $V_g=5$  m/s, Exposure time: 21 days

#### 4.3.2.5 Influence of the gas temperature

Since the corrosion reactions respond to temperature according to Arrhenius type laws, the average corrosion rate decreases as the gas temperature decreases (Figure 62). This is usually true if there is no protective layer forming at the surface of the steel (low pH). The situation is, however, more complicated at the top of the line, as the presence of a protective layer plays a role as well.

In the first days of testing, the corrosion rate is higher at  $70^\circ\text{C}$  or  $80^\circ\text{C}$  compared to  $40^\circ\text{C}$  with average uniform corrosion rates at 1.2 and 0.5 mm/year, respectively. However, as time goes by, the corrosion rate measured at  $70^\circ\text{C}$  decreases strongly. In contrast, at  $40^\circ\text{C}$ , the corrosion rate starts at a low value (0.5 mm/year) but remains almost constant throughout the test. This is explained by the properties of the film forming at the surface of the steel: a dense

and protective  $\text{FeCO}_3$  layer at  $70^\circ\text{C}$  and a more porous and less-protective  $\text{FeCO}_3$  layer at  $40^\circ\text{C}$  (Figure 63). The same reasoning applies for the test at  $85^\circ\text{C}$ , where it starts at the highest value (above 1.5 mm/year) and significantly decreases with time to reach 0.5 mm/year after 17 days. The corrosion product film is expected to be denser and more protective at a higher temperature since the kinetics of  $\text{FeCO}_3$  precipitation are faster, thus favoring the precipitation of larger numbers of smaller crystals which pack more densely on the surface.

Moreover, at the top of the line, there was no sign of localized corrosion at  $40^\circ\text{C}$  or  $85^\circ\text{C}$  while there was strong evidence of pitting at  $70^\circ\text{C}$  (Figure 64). It is clear that the properties of the corrosion product film (rate of formation, density, integrity) are strongly linked to the occurrence of localized corrosion.

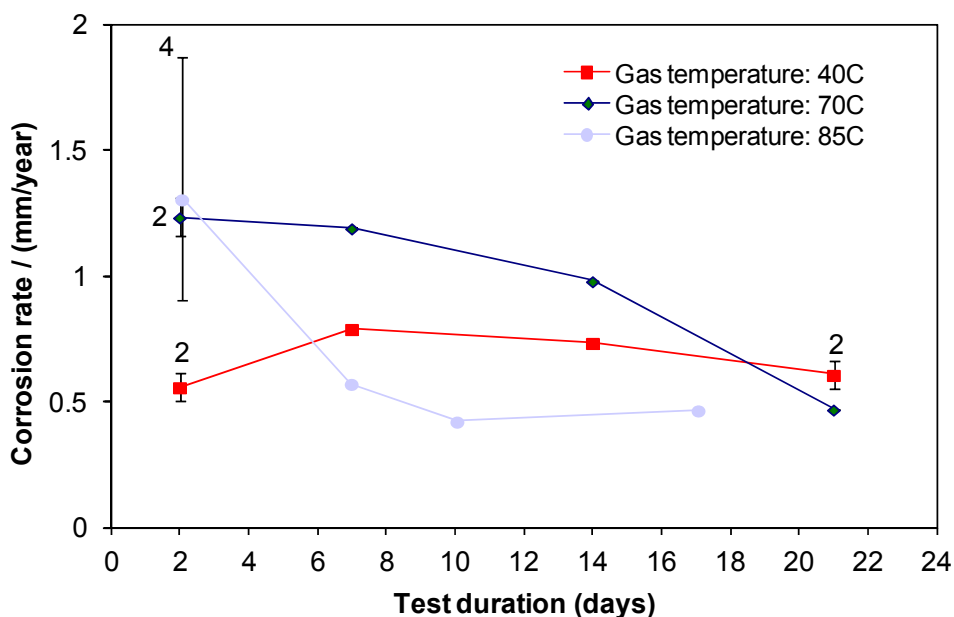


Figure 62: General corrosion – Effect of the gas temperature  
 $p\text{CO}_2=3\text{bars}$ ,  $[\text{HAc}]_{\text{free}}=0\text{ ppm}$ ,  $V_g=5\text{ m/s}$ , Condensation rate= $0.25\text{ mL/m}^2/\text{s}$

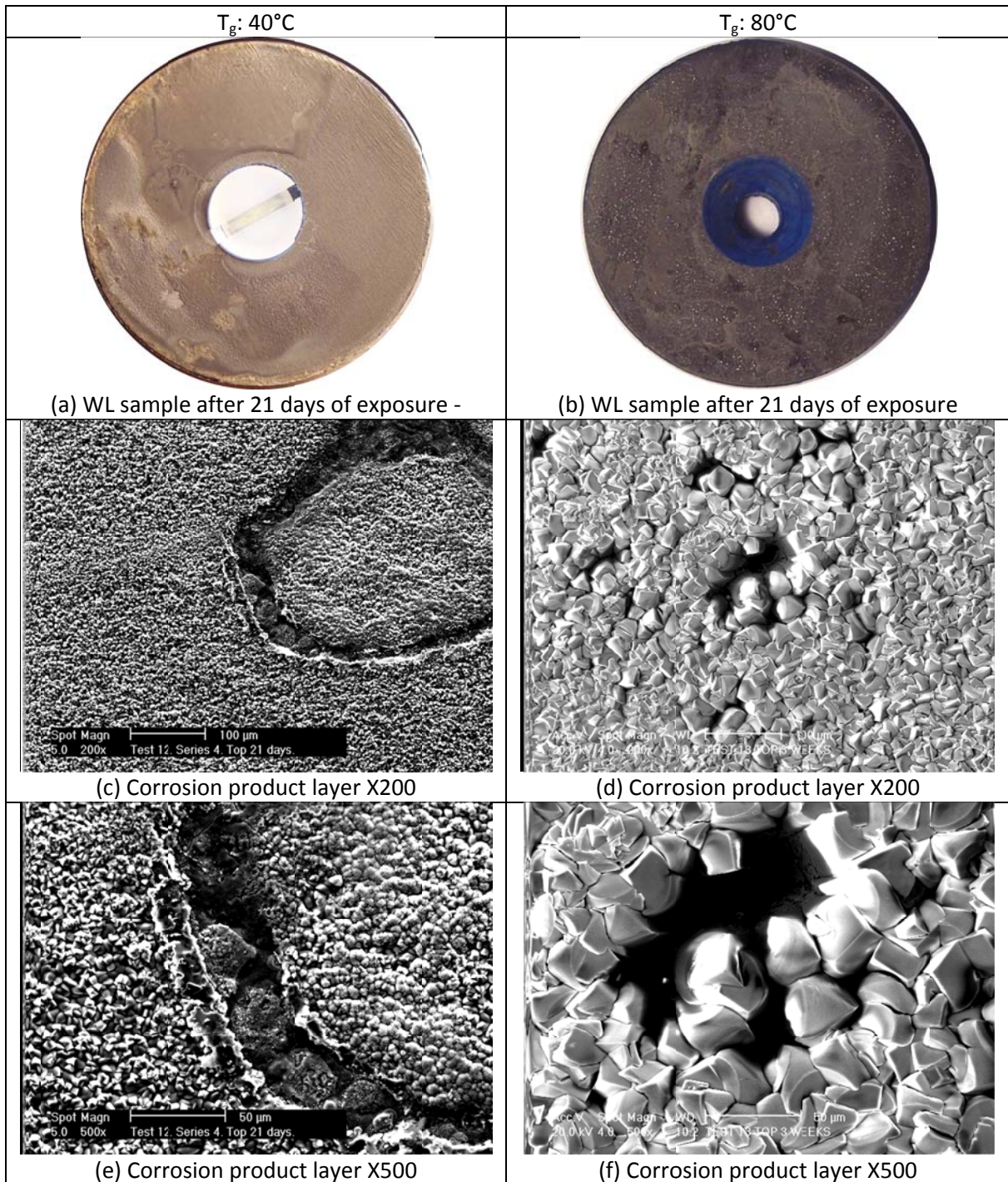


Figure 63: Surface analysis with corrosion product / T<sub>g</sub>: 40°C (left) and T<sub>g</sub>: 80°C (right)  
(P<sub>T</sub>: 3 bars, V<sub>g</sub>= 5 m/s, pCO<sub>2</sub>= 2 bars, Free HAC: 0 ppm, condensation rate= 0.25 mL/m<sup>2</sup>/s)  
Exposure time: 21 days

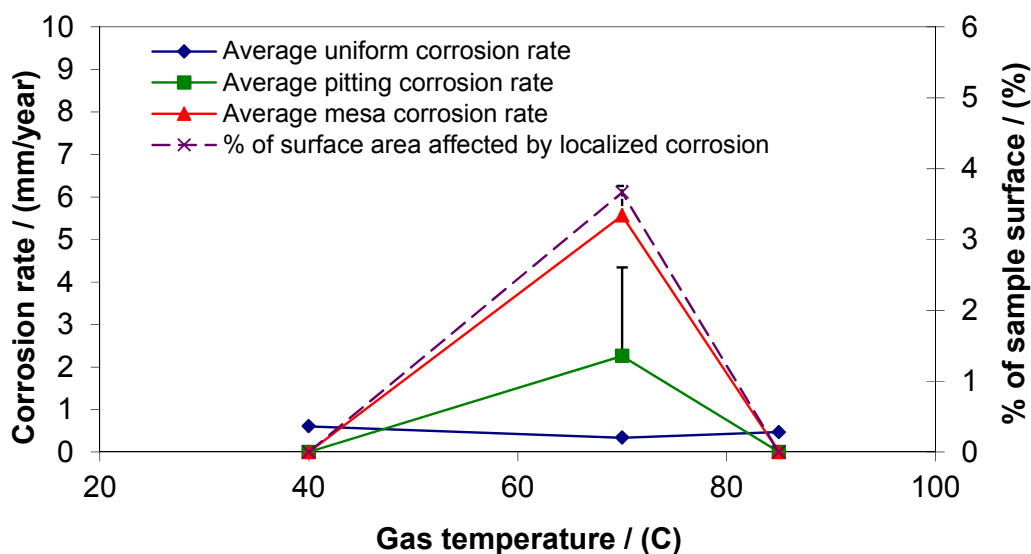


Figure 64: Localized corrosion - Effect of the gas temperature  
 $p\text{CO}_2=3$  bars,  $[\text{HAC}]_{\text{free}}=0$  ppm,  $V_g=5$  m/s, Condensation rate= $0.25$  mL/m<sup>2</sup>/s,  
 Exposure time: 21 days

#### 4.3.2.6 Influence of the partial pressure of H<sub>2</sub>S

Figure 65 and Figure 66 present information about general and localized corrosion in environments containing H<sub>2</sub>S but no acetic acid. The presence of trace amounts of H<sub>2</sub>S ( $p\text{H}_2\text{S}=0.004$  bar,  $\text{CO}_2/\text{H}_2\text{S}$  ratio: 500) clearly decreases the corrosion rate compared to a pure CO<sub>2</sub> environment. This is generally explained by the formation of a very protective film of iron sulfide on the surface of the metal. It is expected that further addition of H<sub>2</sub>S (partial pressure of H<sub>2</sub>S up to 0.13 bar,  $\text{CO}_2/\text{H}_2\text{S}$  ratio: 15) should cause a gradual increase in the corrosion rate. This is not obviously the case at the top of the line where it is difficult to identify a distinct trend. The additional cathodic reaction may compete with an increase in protectiveness of the iron sulfide film. It seems, however, that the corrosion decreases rapidly in the first 15 days and then reverses this tendency and increases slightly. One of the main differences with a pure CO<sub>2</sub> environment is that the corrosion process does not seem to slow down considerably, even if the

severity of the attack is lower. No localized corrosion (pitting or mesa attack) was observed at the top of the line in the conditions tested.

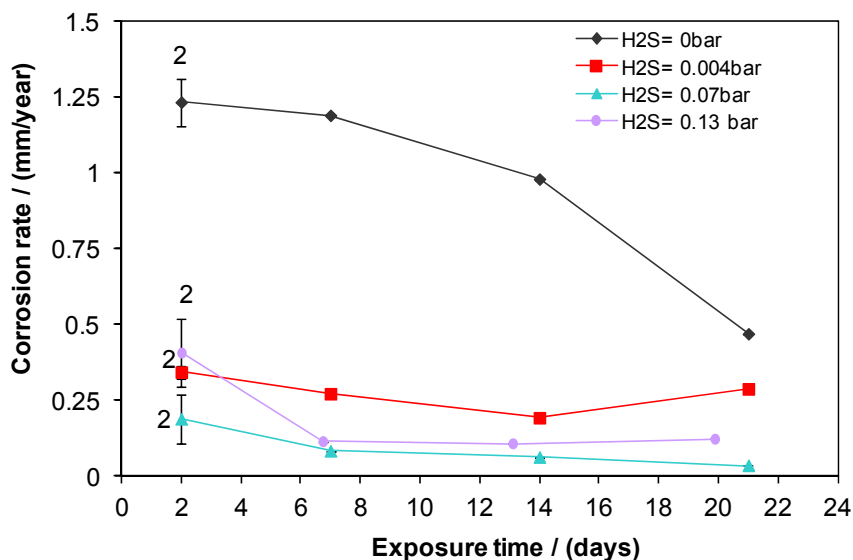


Figure 65: Influence of the partial pressure of H<sub>2</sub>S  
Evolution of the general corrosion rate with the partial pressure of H<sub>2</sub>S  
(P<sub>T</sub>: 3 bars, pCO<sub>2</sub>: 2 bars, Free HAc: 0 ppm, T<sub>g</sub>: 70°C, WCR: 0.25 ml/m<sup>2</sup>/s, V<sub>g</sub>: 5 m/s)

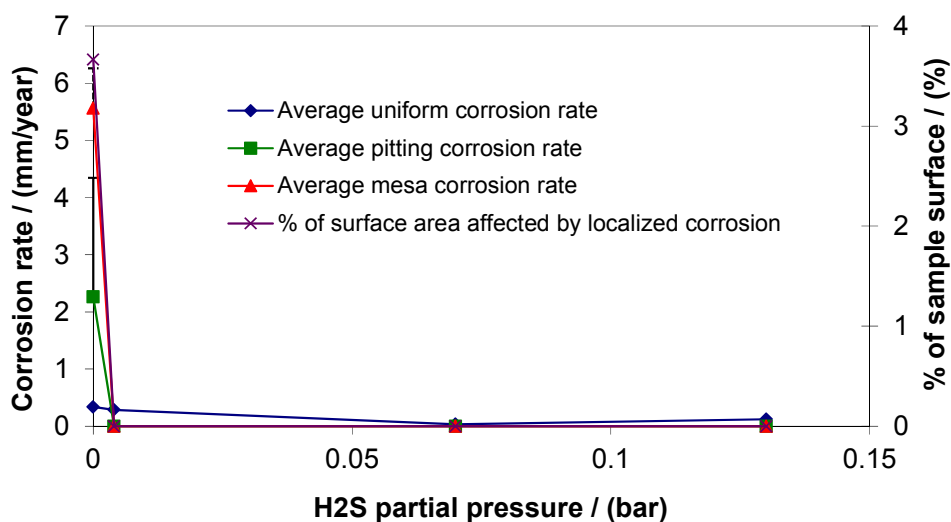


Figure 66: Localized corrosion – Influence of the H<sub>2</sub>S partial pressure  
P<sub>T</sub>: 3 bars, pCO<sub>2</sub>: 2 bars, Free HAc: 0 ppm, T<sub>g</sub>: 70°C, WCR: 0.25 ml/m<sup>2</sup>/s, V<sub>g</sub>: 5 m/s,  
Exposure time: 21 days

SEM and EDS analysis of the corrosion layer formed in CO<sub>2</sub>/H<sub>2</sub>S environments without acetic acid are shown in Figure 67 (pH<sub>2</sub>S= 0.004 bar, CO<sub>2</sub>/H<sub>2</sub>S ratio: 500) and Figure 68 (pH<sub>2</sub>S= 0.13 bar, CO<sub>2</sub>/H<sub>2</sub>S ratio: 15). In all cases, even though the tests were performed with 2 bars of CO<sub>2</sub>, no FeCO<sub>3</sub> crystals could be clearly identified (although their presence cannot be ruled out). Instead, a mostly macroscopically amorphous corrosion product layer covers the specimen surface. The layer does not always appear to be homogeneous, especially at higher H<sub>2</sub>S partial pressures where large parts of the product layer seem to have peeled off during the corrosion process. In addition, peculiar features (which show obvious crystalline structure) were observed but could not be clearly identified, as EDS analysis always shows peaks of similar intensity for iron (Fe) and sulfur (S). In all cases, the steel was uniformly corroded and no localized corrosion could be observed even after 21 days of exposure to the corrosive environment.

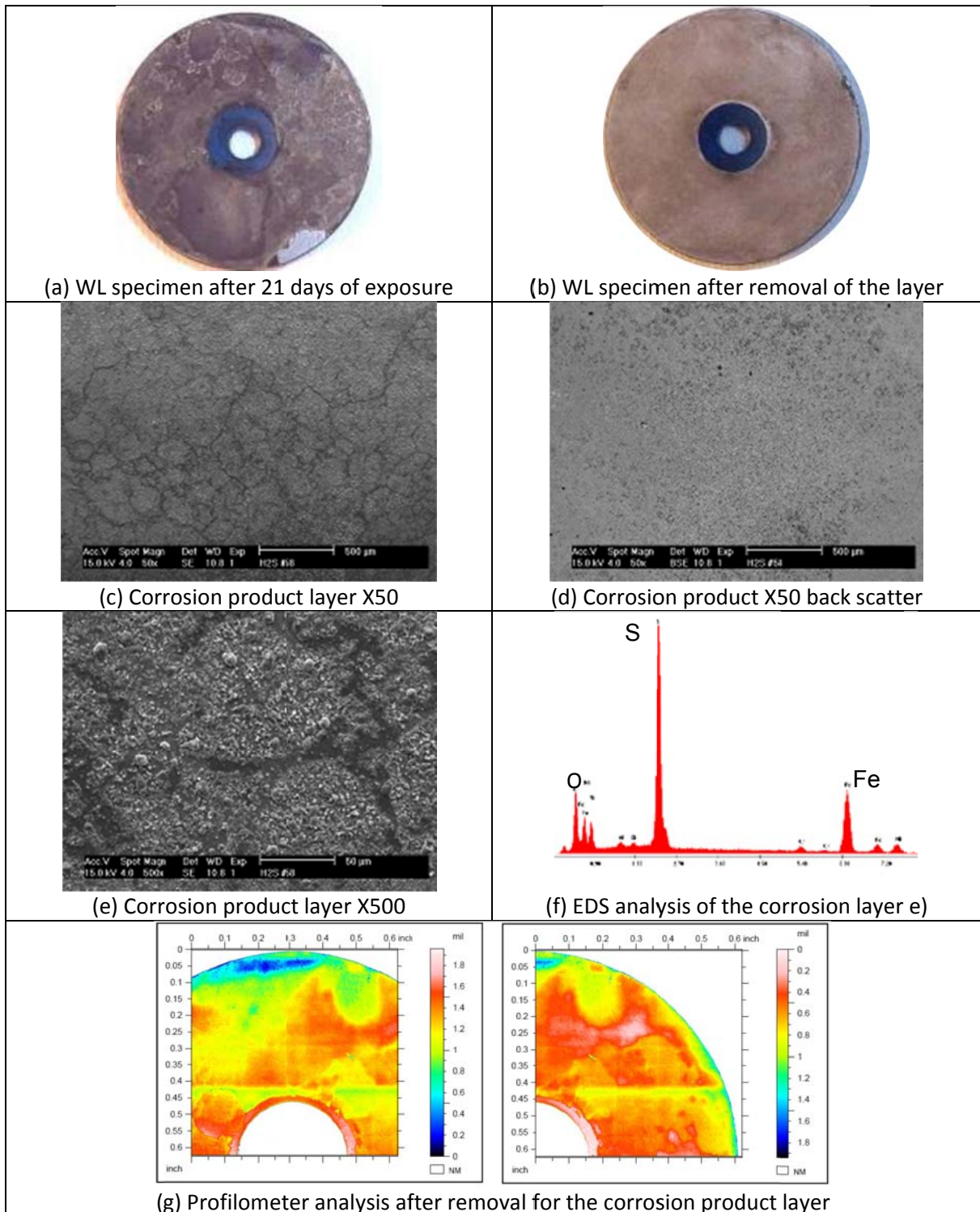


Figure 67: Test 4 – CO<sub>2</sub> environment with traces of H<sub>2</sub>S – CO<sub>2</sub>/H<sub>2</sub>S: 500 (pCO<sub>2</sub>: 2 bars, pH<sub>2</sub>S: 0.004 bar, No Free HAc, T<sub>g</sub>: 70°C, WCR: 0.25 ml/m<sup>2</sup>/s, V<sub>g</sub>: 5 m/s, Exposure time: 3 weeks)

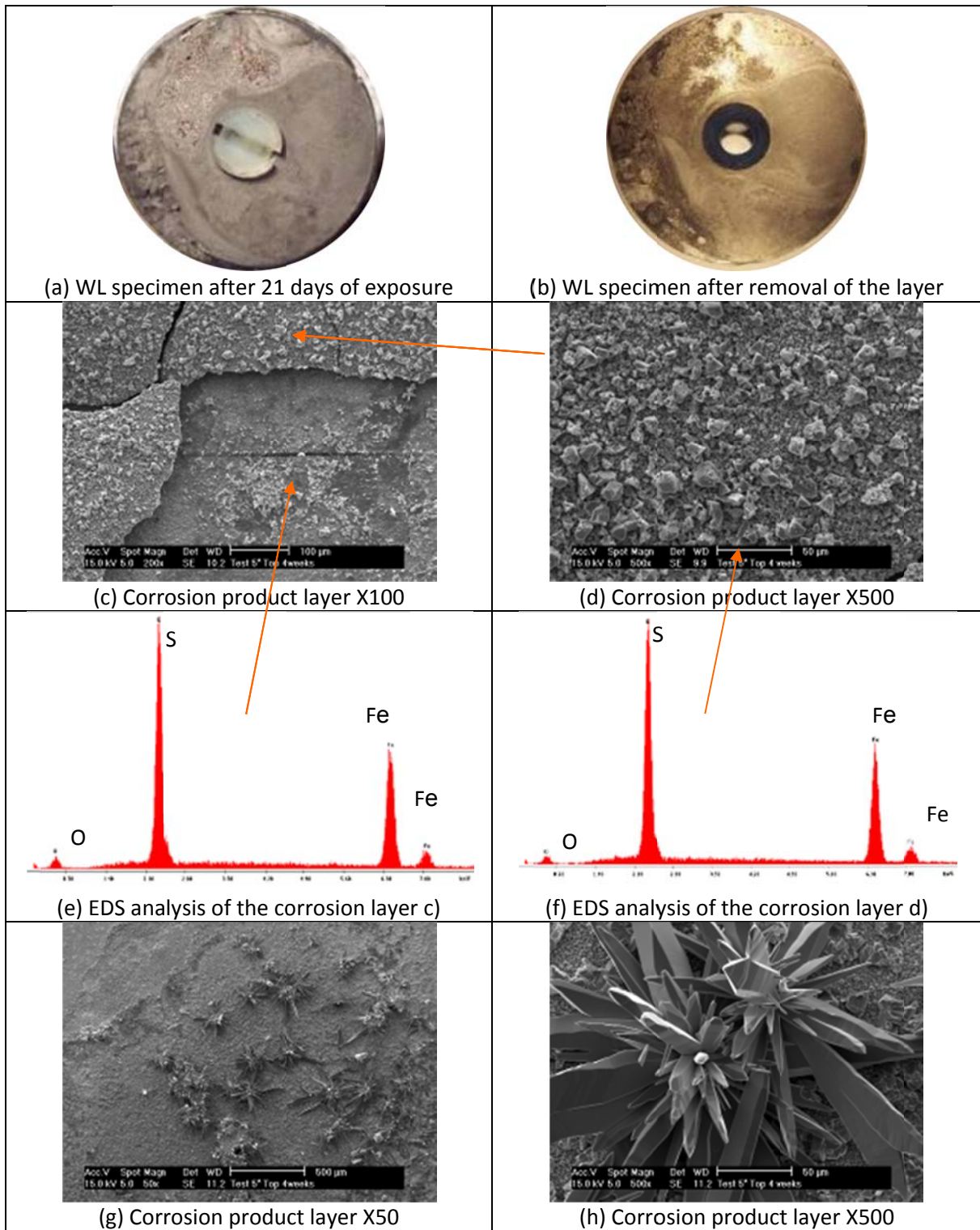


Figure 68: Test 6 – CO<sub>2</sub> environment with H<sub>2</sub>S – CO<sub>2</sub>/H<sub>2</sub>S: 15  
 (pCO<sub>2</sub>: 2 bars, pH<sub>2</sub>S: 0.13 bar, No Free HAc, T<sub>g</sub>: 70°C, WCR: 0.25 ml/m<sup>2</sup>/s, V<sub>g</sub>: 5 m/s, Exposure time: 3 weeks)

#### 4.3.2.7 Combined effect of WCR and acetic acid concentration

For clarity, the results are presented in four sets of graphs isolating one parameter each time:

- Set 1: Fixed undissociated acetic acid concentration of 100 ppm and varying condensation rate of 0.03, 0.25 and 1 mL/m<sup>2</sup>/s
- Set 2: Fixed undissociated acetic acid concentration of 1000 ppm and varying condensation rate of 0.03, 0.25 and 1 mL/m<sup>2</sup>/s
- Set 3: Fixed condensation rate of 0.05 mL/m<sup>2</sup>/s and varying undissociated acetic acid concentration of 0, 100, 1000 ppm
- Set 4: Fixed condensation rate of 1 mL/m<sup>2</sup>/s and varying undissociated acetic acid concentration of 0, 100, 1000 ppm

The graphs related to each set are presented in Figure 69 to Figure 76. The clearest observation is that the higher the concentration of free acetic acid and the condensation rate are, the higher the risk for localized corrosion. Even if the condensation rate is low (0.05 mL/m<sup>2</sup>/s), 1000 ppm of free HAc will lead to high uniform corrosion rate and severe localized attack (Figure 77). The opposite is also true for the condensation rate, but to a slightly lesser extent. The notion of a critical condensation rate threshold below which no TLC is expected (or where the TLC rate is acceptable) is not validated by these results. The condensation is clearly a factor influencing the uniform corrosion and localized corrosion rate but cannot be extracted alone and used as a design tool. The extent of TLC is rather the result of complex interactions between all the parameters presented in this paper, and any comprehensive mitigation method would require a good understanding of the mechanisms involved.

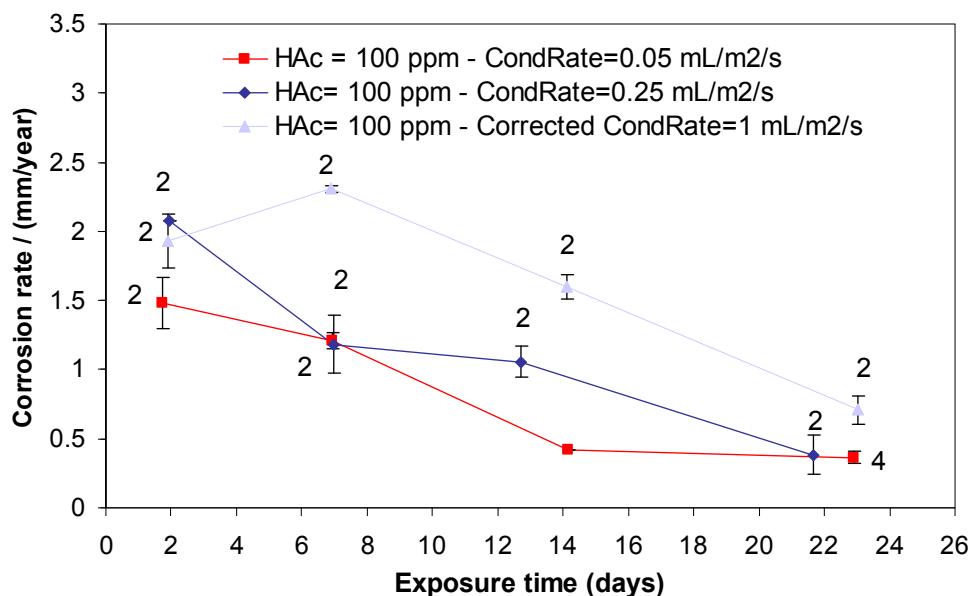


Figure 69: General corrosion – Effect of HAC/Condensation rate  
 $p\text{CO}_2=3$  bars,  $T_g=70^\circ\text{C}$ ,  $V_g=5\text{m/s}$   
 Set 1: Fixed  $[\text{HAC}]_{\text{free}} = 100$  ppm and  
 varying Condensation rate = 0.05, 0.25 and 1 mL/m<sup>2</sup>/s

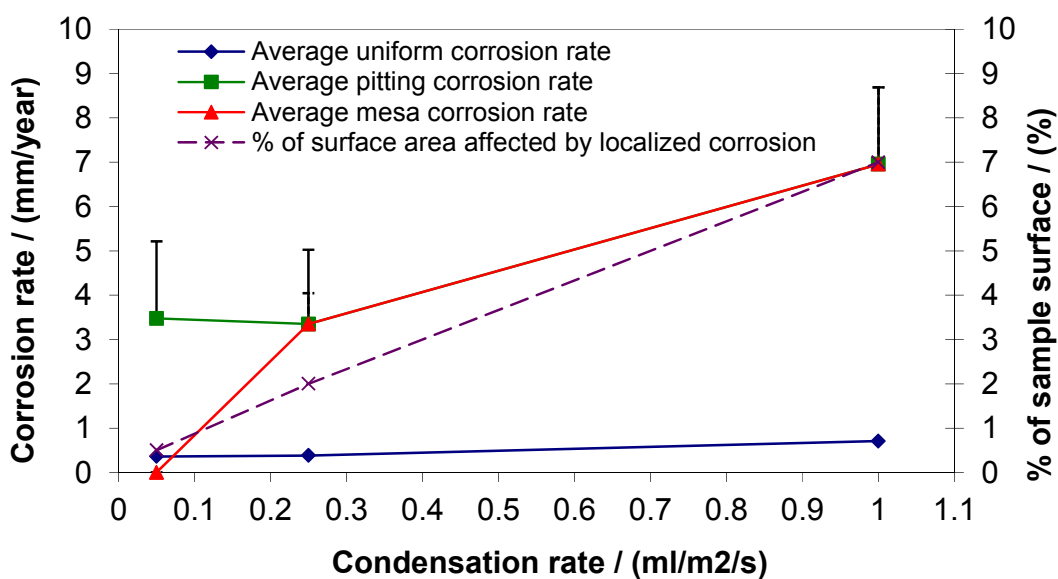


Figure 70: Localized corrosion - Effect of HAC/Condensation rate  
 $p\text{CO}_2=3$  bars,  $T_g=70^\circ\text{C}$ ,  $V_g=5\text{m/s}$ , Exposure time: 21 days  
 Set 1: Fixed  $[\text{HAC}]_{\text{free}} = 100$  ppm and  
 varying Condensation rate = 0.05, 0.25 and 1 mL/m<sup>2</sup>/s

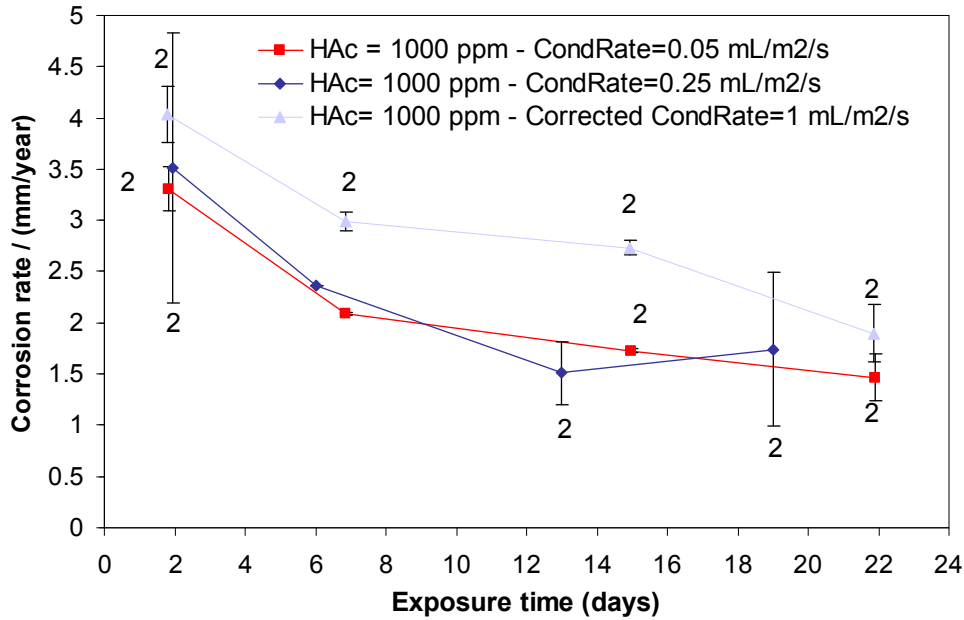


Figure 71: General corrosion - Effect of HAC/Condensation rate  
 $pCO_2=3$  bars,  $T_g=70^\circ C$ ,  $V_g=5m/s$ ,  
 Set 2: Fixed  $[HAc]_{free} = 1000$  ppm and  
 varying Condensation rate = 0.05, 0.25 and 1 mL/m<sup>2</sup>/s

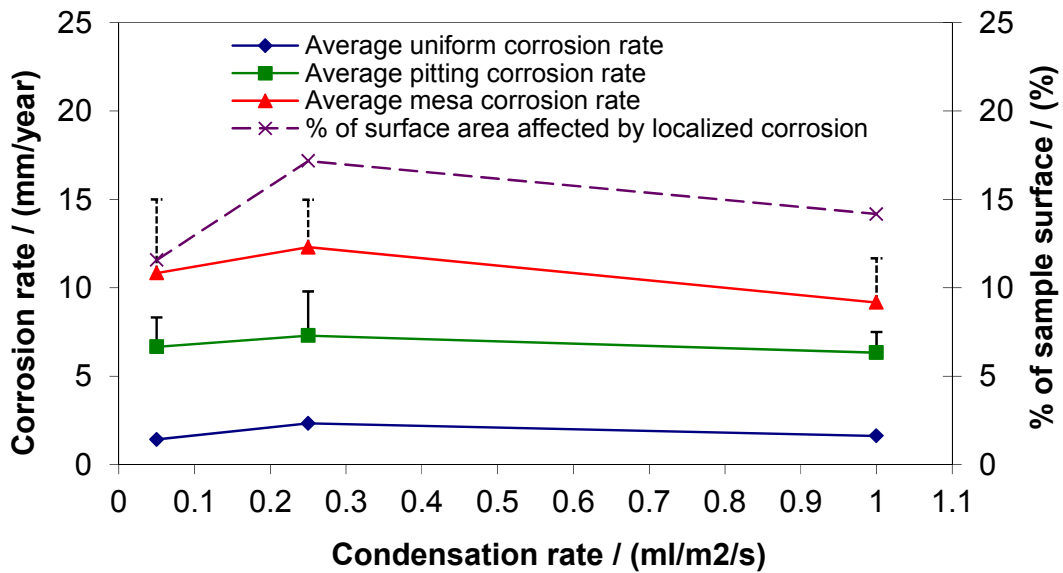


Figure 72: Localized corrosion - Effect of HAC/Condensation rate  
 $pCO_2=3$  bars,  $T_g=70^\circ C$ ,  $V_g=5m/s$ , Exposure time: 21 days  
 Set 2: Fixed  $[HAc]_{free} = 1000$  ppm and  
 varying Condensation rate = 0.05, 0.25 and 1 mL/m<sup>2</sup>/s

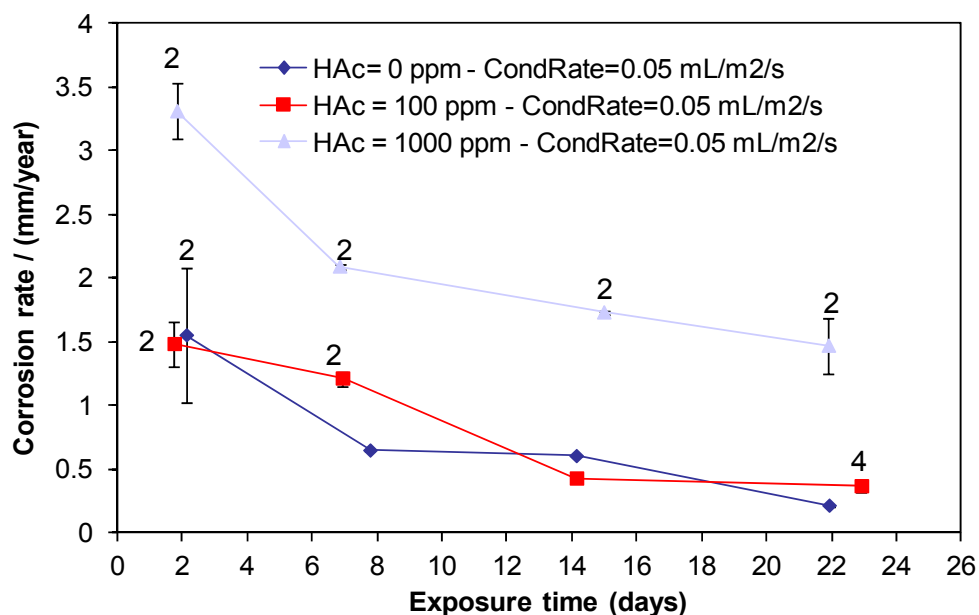


Figure 73: General corrosion – Effect of HAC/Condensation rate  
 $p\text{CO}_2=3$  bars,  $T_g=70^\circ\text{C}$ ,  $V_g=5\text{m/s}$   
 Set 3: Fixed Condensation rate =  $0.05\text{ mL/m}^2/\text{s}$  and  
 varying  $[\text{HAc}]_{\text{free}} = 0, 100, 1000$  ppm

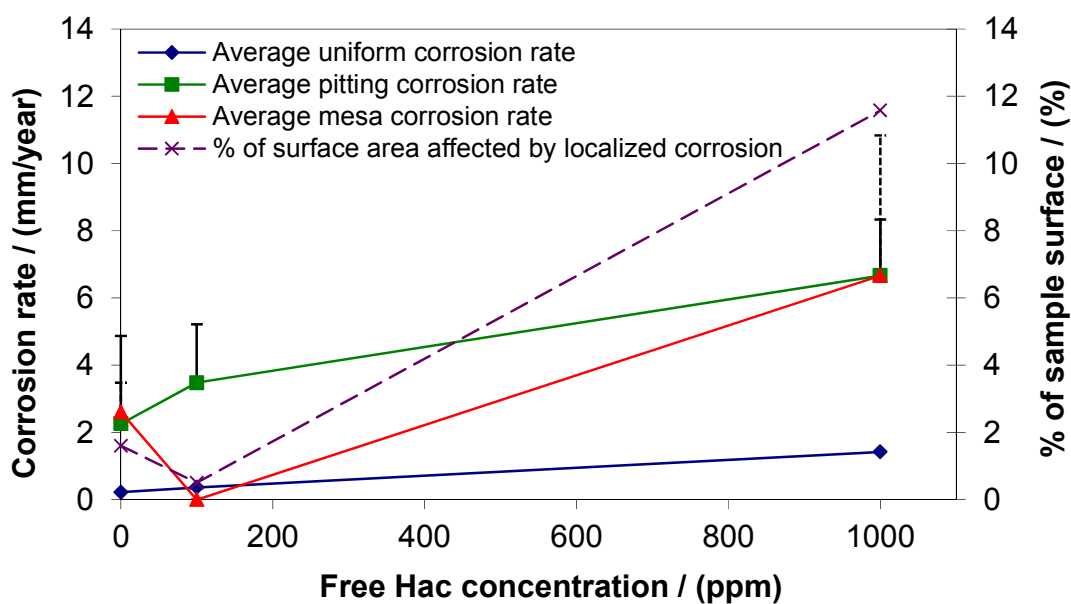


Figure 74: Localized corrosion - Effect of HAC/Condensation rate  
 $p\text{CO}_2=3$ bars,  $T_g=70^\circ\text{C}$ ,  $V_g=5\text{m/s}$ , Exposure time: 21 days  
 Set 3: Fixed Condensation rate =  $0.05\text{ mL/m}^2/\text{s}$  and  
 varying  $[\text{HAc}]_{\text{free}} = 0, 100, 1000$  ppm

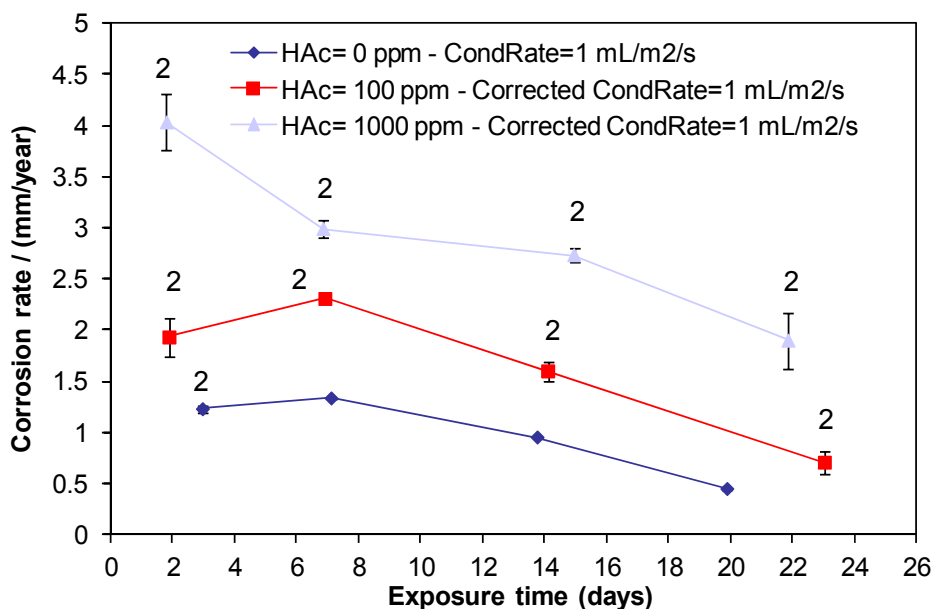


Figure 75: General corrosion – Effect of HAc/Condensation rate  
 $pCO_2=3$  bars,  $T_g=70^\circ C$ ,  $V_g=5m/s$   
 Set 4: Fixed Condensation rate =  $1 mL/m^2/s$  and  
 varying  $[HAc]_{free} = 0, 100, 1000$  ppm

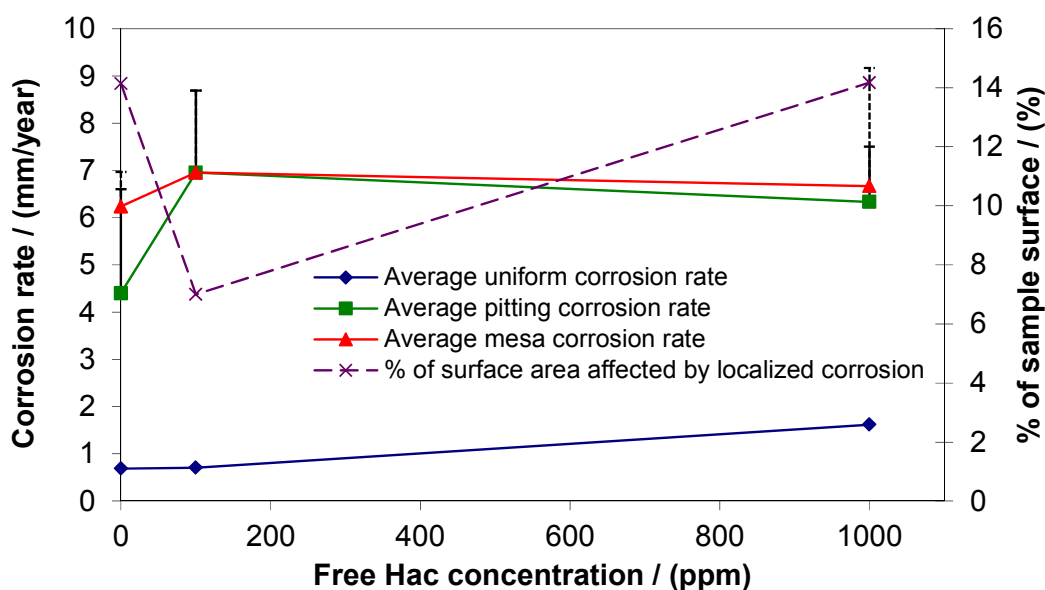


Figure 76: Localized corrosion - Effect of HAc/Condensation rate  
 $pCO_2=3$  bars,  $T_g=70^\circ C$ ,  $V_g=5m/s$ , Exposure time: 21 days  
 Set 4: Fixed Condensation rate =  $1 mL/m^2/s$  and  
 varying  $[HAc]_{free} = 0, 100, 1000$  ppm

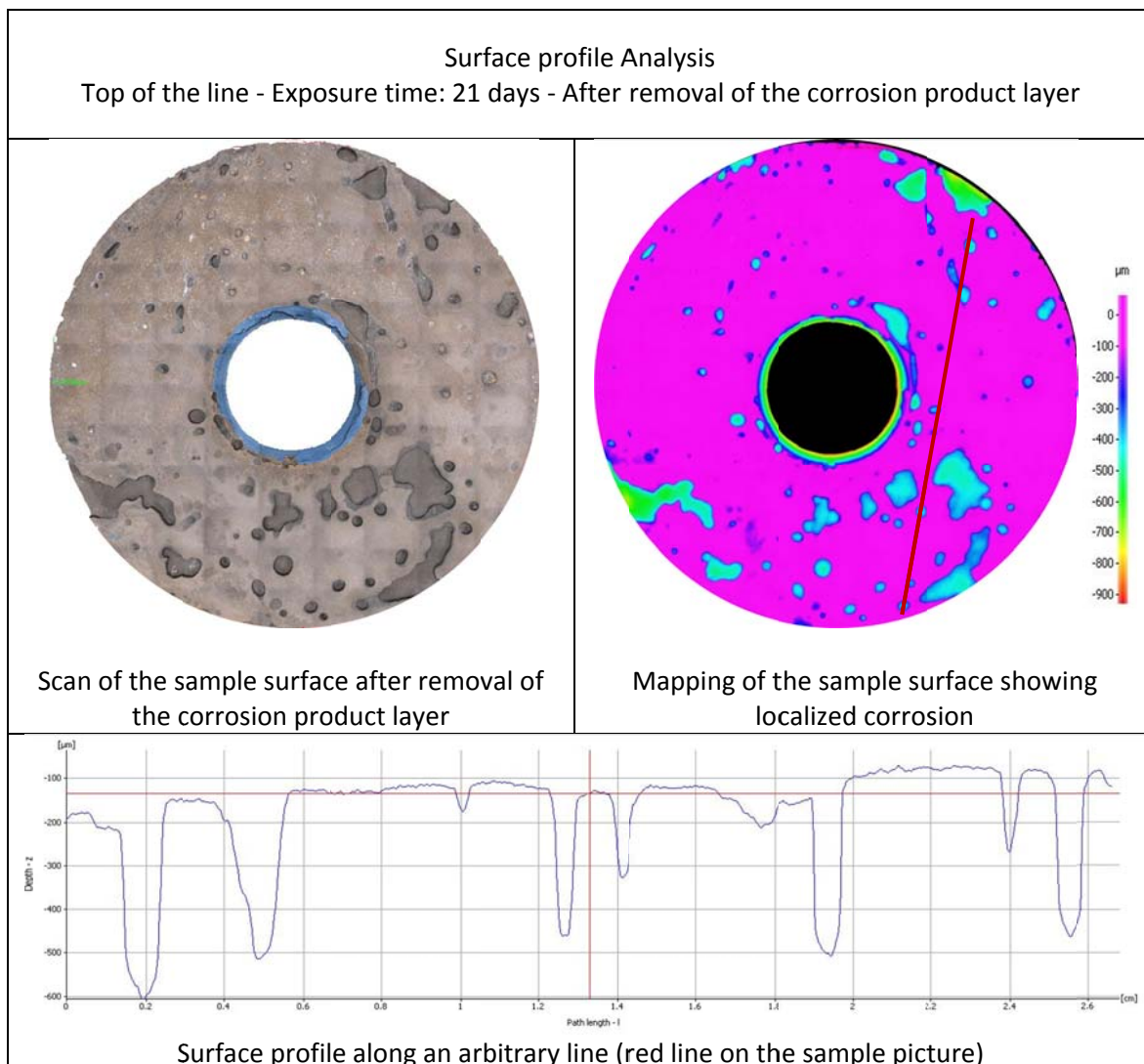


Figure 77: Surface analysis without corrosion product  
Free HAc= 1000 ppm and condensation rate= 0.05 mL/m<sup>2</sup>/s  
(PT: 3 bars, Vg= 5 m/s, pCO<sub>2</sub>= 2 bars, Tg: 70°C)

#### 4.3.2.8 Combined effect of pH<sub>2</sub>S and the acetic acid concentration

The influence of acetic acid on H<sub>2</sub>S TLC is shown in Figure 78 to Figure 83. As in a CO<sub>2</sub>/H<sub>2</sub>S environment, the TLC rates remained more or less constant during the entire duration of the test. While 100 ppm of free acetic acid seems to have little effect, the corrosion rate

jumps from 0.3 to 1.8 mm/year with 0.004 bar of H<sub>2</sub>S when 1000 ppm of the weak acid is present. It is interesting to note that, with traces of H<sub>2</sub>S (pH<sub>2</sub>S=0.004 bar, CO<sub>2</sub>/H<sub>2</sub>S ratio: 500), the average top of the line corrosion rate after 21 days of exposure is similar to the one obtained in pure CO<sub>2</sub> environment when a significant amount of free acetic acid is present (Figure 82). Further increases in H<sub>2</sub>S partial pressure (0.13 bar of H<sub>2</sub>S, CO<sub>2</sub>/H<sub>2</sub>S ratio: 15) seem to reverse this tendency and offer better protection against top of the line corrosion. The average corrosion rate after 3 weeks of exposure is still three to four times higher with 1000 ppm of acetic acid than without.

In the presence of acetic acid, some localized corrosion was observed, but only in the form of small pits. The percentage area affected by pitting corrosion is usually very limited (unlike in a pure CO<sub>2</sub> environment) and pitting rates do not exceed 4 mm/year, which barely qualifies the corrosion as pitting in accordance with the definition presented in section 3.3.5.

The surface analysis associated with the influence of acetic acid on CO<sub>2</sub>/H<sub>2</sub>S top of the line corrosion is shown in Figure 84 to Figure 86. The corrosion product layer at the top of the line is made of FeS, as is usually the case at the top of the line in H<sub>2</sub>S environments. In all cases, the film looks fairly uniform, quite porous and easily wiped off the surface of the specimen. The film is also, in most cases, cracked; this cracking is believed to take place over time owing to internal mechanical stresses. The corrosion process was then able to continue under the film. FeCO<sub>3</sub> crystals were observed in these cracks. There is no clear difference in the EDS analysis (identification of the film composition) performed for the tests with or without acetic acid. The surface looks evenly corroded except for a few isolated pits, especially at higher concentrations of acetic acid. Once again, the extent of localized corrosion seems to be negligible, with maximum pitting rates close to average corrosion rates.

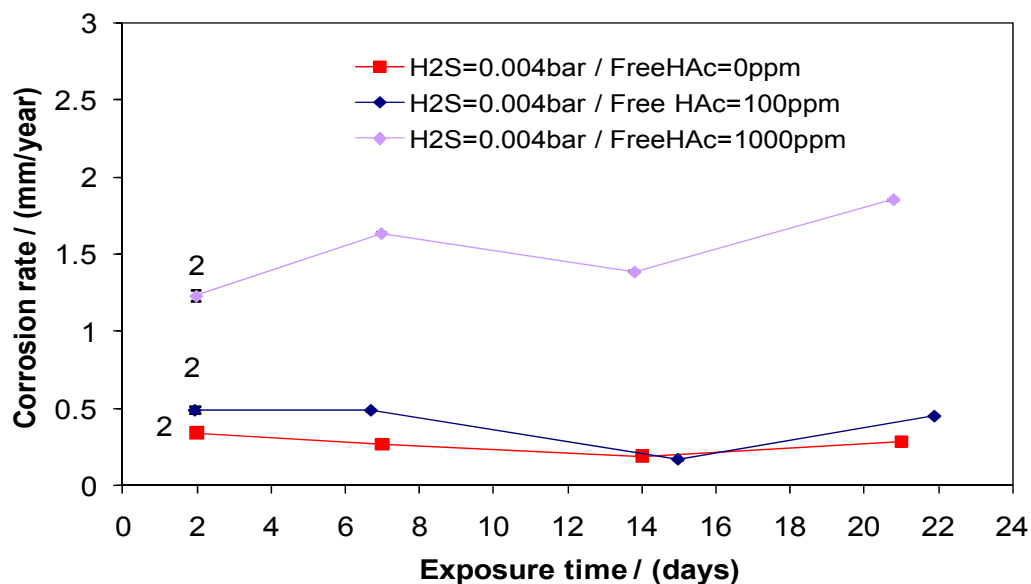


Figure 78: Combined effect of the partial pressure of H<sub>2</sub>S and the concentration of free HAc  
Evolution of the general corrosion rate over time  
(P<sub>T</sub>: 3 bars, pCO<sub>2</sub>: 2 bars, pH<sub>2</sub>S: 0.004 bar, T<sub>g</sub>: 70°C, WCR: 0.25 ml/m<sup>2</sup>/s, V<sub>g</sub>: 5 m/s)

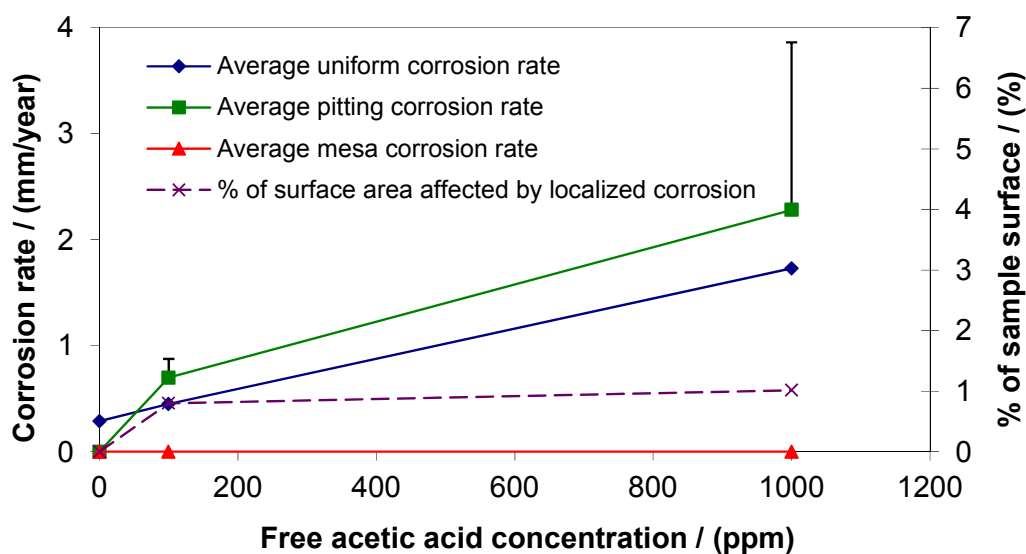


Figure 79: Localized corrosion – Influence of the free HAc concentration in CO<sub>2</sub>/H<sub>2</sub>S environment  
(P<sub>T</sub>: 3 bars, pCO<sub>2</sub>: 2 bars, pH<sub>2</sub>S: 0.004 bar, T<sub>g</sub>: 70°C, WCR: 0.25 ml/m<sup>2</sup>/s, V<sub>g</sub>: 5 m/s,  
Exposure time: 21 days)

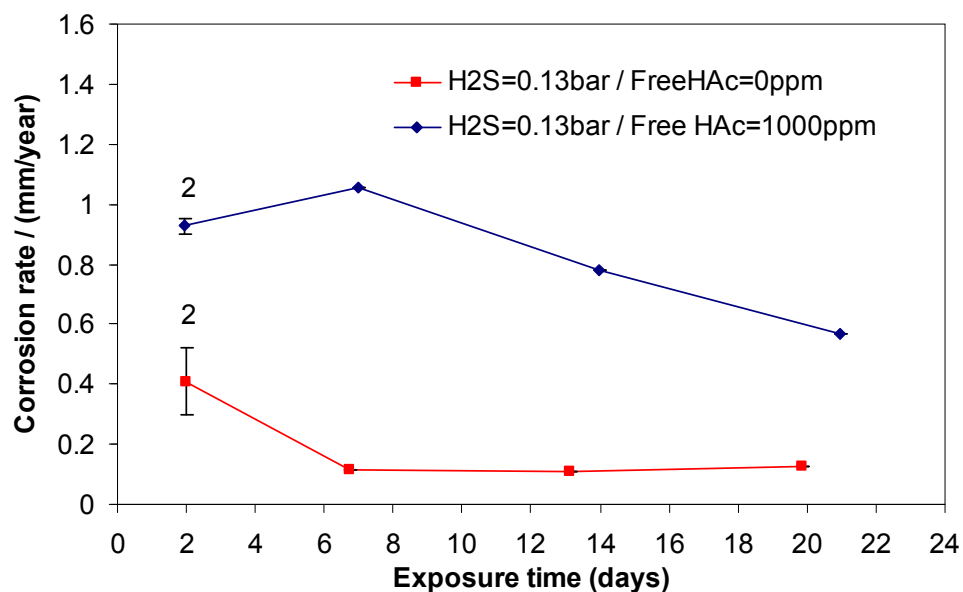


Figure 80: Combined effect of the partial pressure of H<sub>2</sub>S and the concentration of free HAC  
 Evolution of the general corrosion rate over time  
 (P<sub>T</sub>: 3 bars, pCO<sub>2</sub>: 2 bars, pH<sub>2</sub>S: 0.13 bar, T<sub>g</sub>: 70°C, WCR: 0.25 ml/m<sup>2</sup>/s, V<sub>g</sub>: 5 m/s)

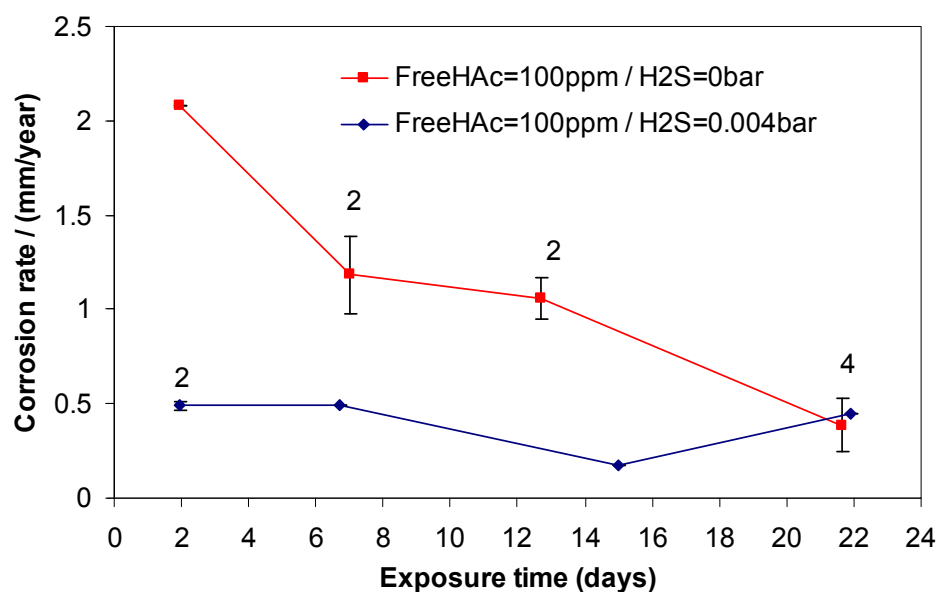


Figure 81: Combined effect of the partial pressure of H<sub>2</sub>S and the concentration of free HAC  
 Evolution of the general corrosion rate over time  
 (P<sub>T</sub>: 3 bars, pCO<sub>2</sub>: 2 bars, Free HAC: 100 ppm, T<sub>g</sub>: 70°C, WCR: 0.25 ml/m<sup>2</sup>/s, V<sub>g</sub>: 5 m/s)

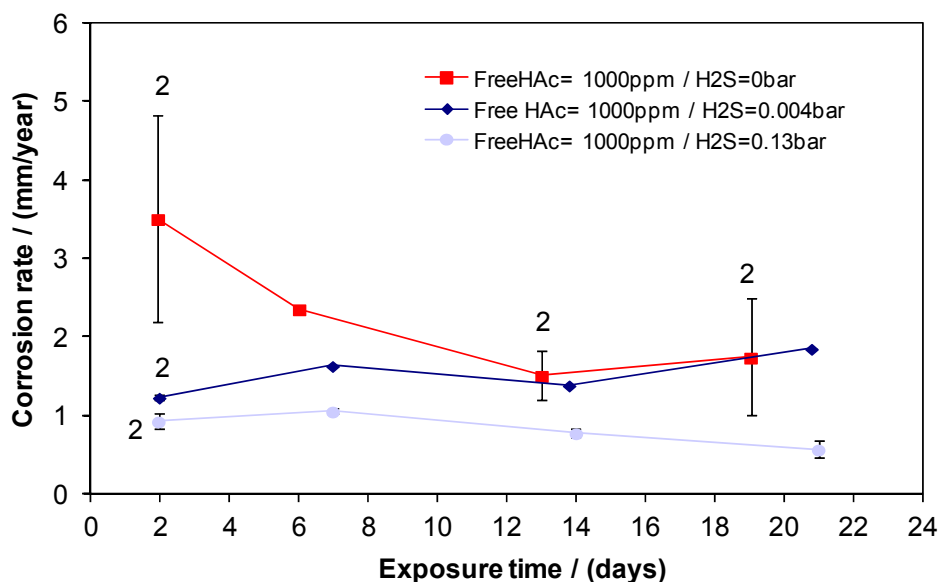


Figure 82: Combined effect of the partial pressure of H<sub>2</sub>S and the concentration of free HAc  
Evolution of the general corrosion rate over time  
(P<sub>T</sub>: 3 bars, pCO<sub>2</sub>: 2 bars, Free HAc: 1000 ppm, T<sub>g</sub>: 70°C, WCR: 0.25 ml/m<sup>2</sup>/s, V<sub>g</sub>: 5 m/s)

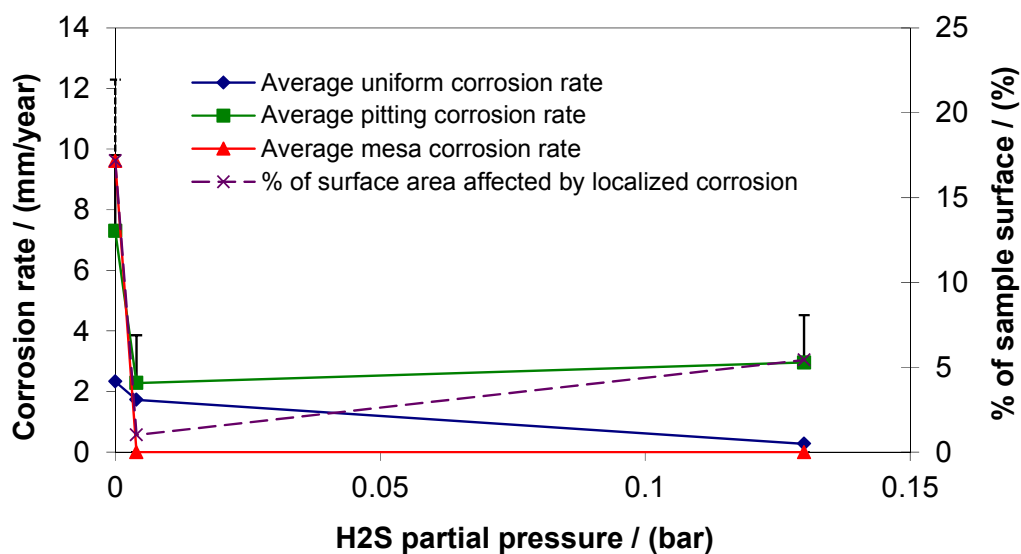


Figure 83: Localized corrosion – Influence of the free HAc concentration in CO<sub>2</sub>/H<sub>2</sub>S environment  
(P<sub>T</sub>: 3 bars, pCO<sub>2</sub>: 2 bars, Free HAc: 1000ppm, T<sub>g</sub>: 70°C, V<sub>g</sub>: 5 m/s, WCR: 0.25 ml/m<sup>2</sup>/s, Exposure time: 21 days)

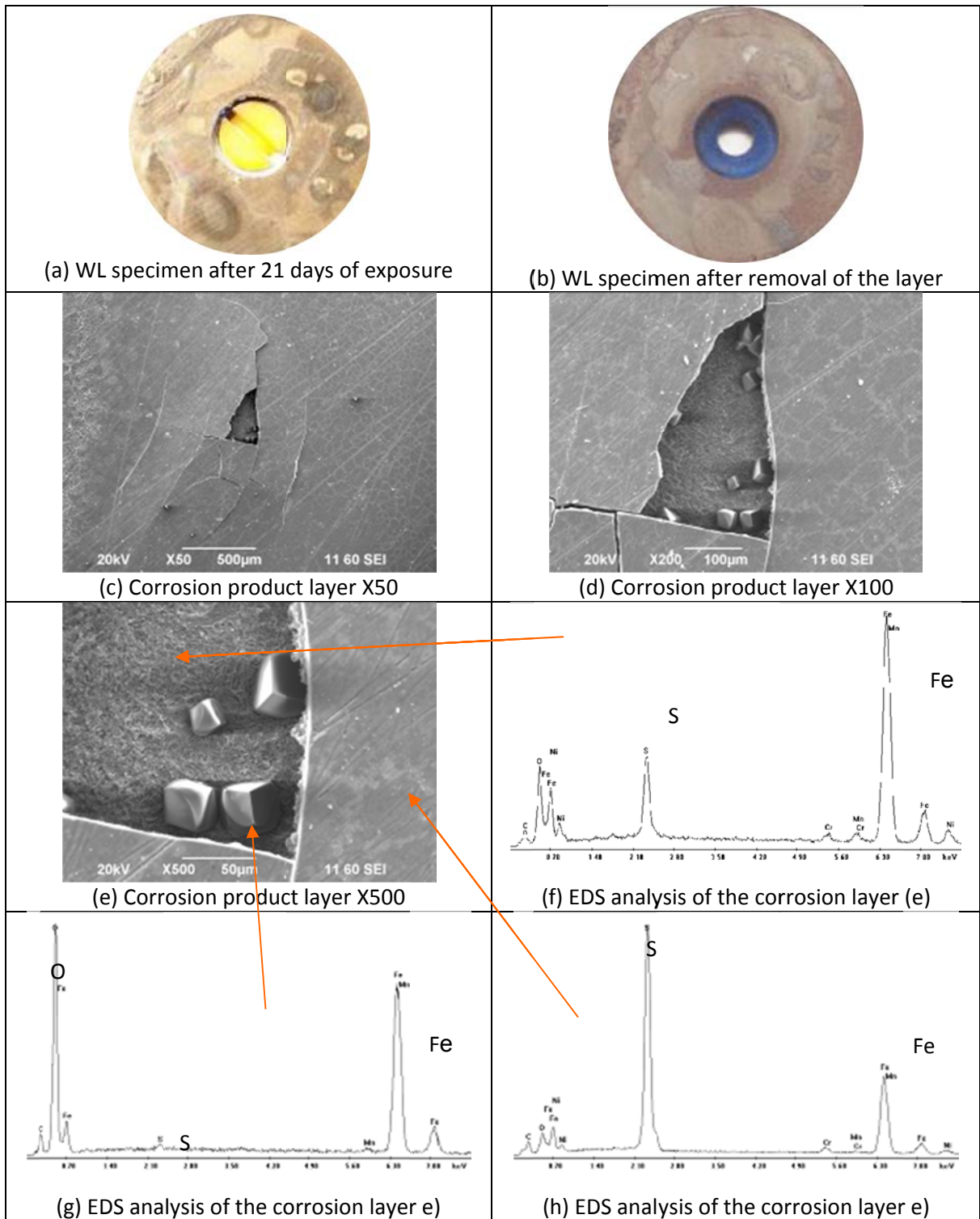


Figure 84: Test 7 – CO<sub>2</sub> environment with traces of H<sub>2</sub>S and acetic acid – CO<sub>2</sub>/H<sub>2</sub>S: 500 (pCO<sub>2</sub>: 2 bars, pH<sub>2</sub>S: 4 mbar, Free HAc: 100 ppm, T<sub>g</sub>: 70°C, WCR: 0.25 ml/m<sup>2</sup>/s, V<sub>g</sub>: 5 m/s, Exp. time: 3 weeks)

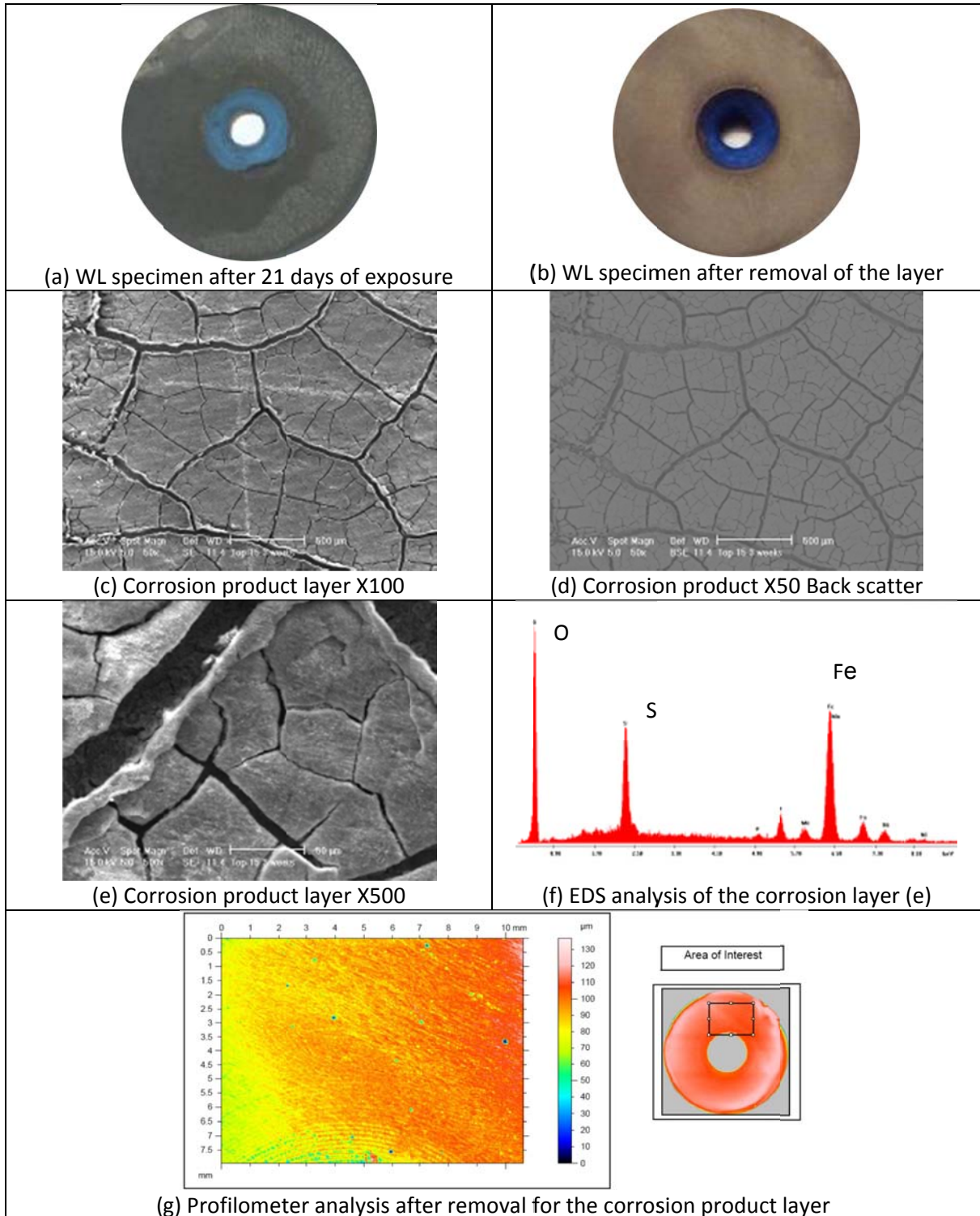


Figure 85: Test 8 – CO<sub>2</sub> environment with traces of H<sub>2</sub>S and acetic acid – CO<sub>2</sub>/H<sub>2</sub>S: 500 (pCO<sub>2</sub>: 2 bars, pH<sub>2</sub>S: 4 mbar, Free HAc: 1000 ppm, T<sub>g</sub>: 70°C, WCR: 0.25 ml/m<sup>2</sup>/s, V<sub>g</sub>: 5 m/s, Exp. time: 3 weeks)

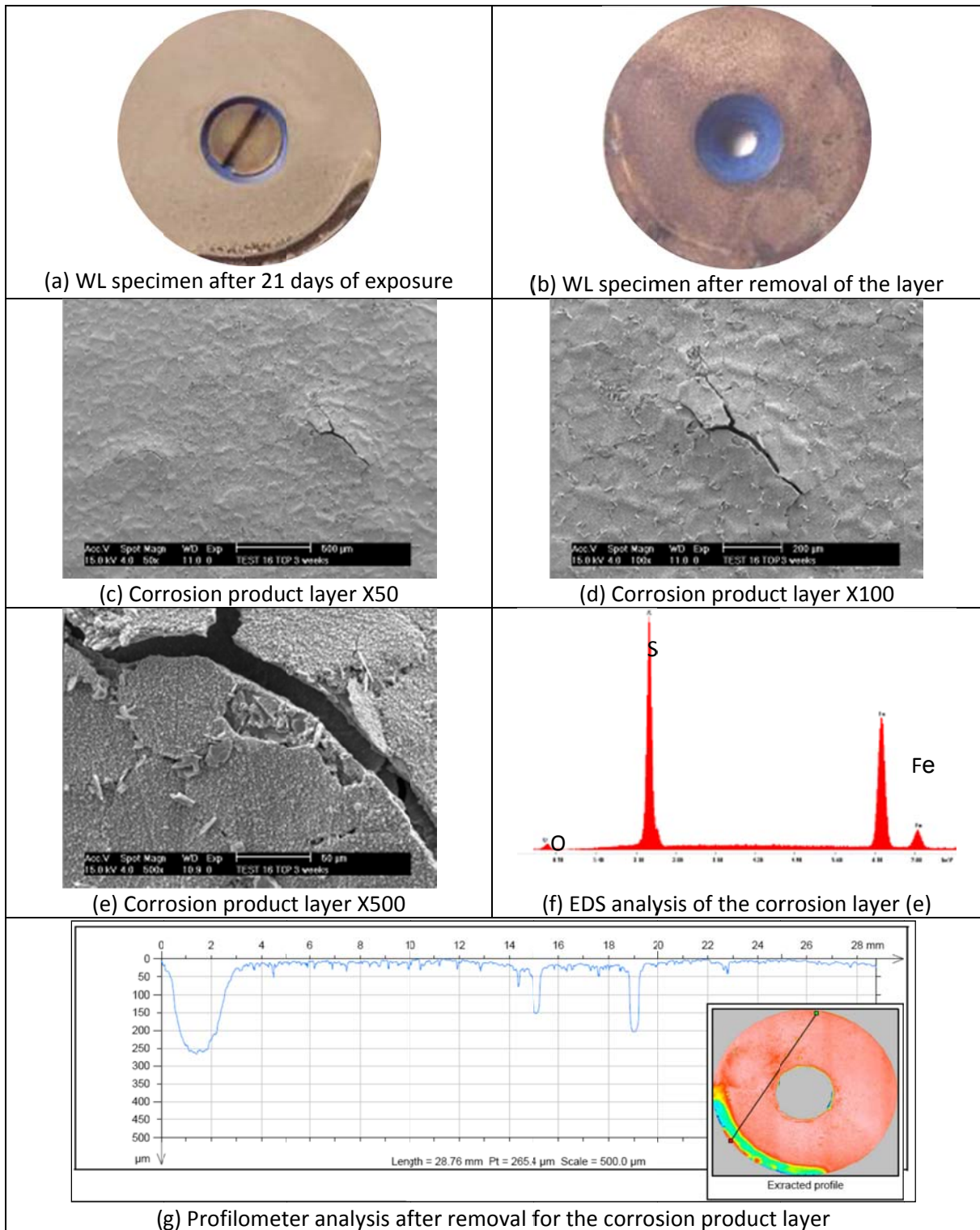


Figure 86: Test 9 – CO<sub>2</sub> environment with H<sub>2</sub>S and acetic acid – CO<sub>2</sub>/H<sub>2</sub>S: 15 (pCO<sub>2</sub>: 2 bars, pH<sub>2</sub>S: 0.13 bar, Free HAC: 1000 ppm, T<sub>g</sub>: 70°C, WCR: 0.25 ml/m<sup>2</sup>/s, V<sub>g</sub>: 5 m/s, Exp. time: 3 weeks)

### 4.3.3 Summary

The present experimental study performed in large scale flow loops, the results of which are summarized in Table 8 and Table 9, highlights some important characteristics of sweet and sour top of the line corrosion. TLC is a phenomenon that occurs only in stratified flow, although two distinct condensation regimes are encountered: stagnant droplet condensation at low gas velocity and sliding droplet condensation at higher gas velocity. The water vapor condenses at the top of the line in the form of small water droplets, which follow a specific cycle: growth to reach a critical size, falling to the bottom of the pipe due to gravity forces or sliding along the pipeline, and renewal governed by the rate of condensation. It is also clear that TLC mechanisms in sweet and sour corrosion are different. The summary of the experimental results is consequently divided in two main parts: TLC in sweet environment and TLC in sour environment.

- TLC in sweet environment

The initial average corrosion rates are normally quite high but often decrease with time to relatively low average values. This decrease is an indication of the precipitation on the metal surface of a corrosion product layer made of  $\text{FeCO}_3$ . This layer can provide some protection but is also intrinsically linked to the initiation and propagation of localized corrosion. Two to three weeks of exposure time are consequently necessary to catch these tendencies, as shorter experiments may lead to unrealistically high general corrosion rates and may miss the occurrence of localized corrosion altogether. In terms of general corrosion, a more aggressive environment (high partial pressure of  $\text{CO}_2$ , higher temperature, higher acetic acid content) logically leads to higher initial corrosion rates. As the corrosion process occurs and iron ions are released in solution, the water droplets can reach saturation in  $\text{FeCO}_3$ . How quickly this saturation is reached depends upon the temperature: experiments performed at lower gas

temperatures (<40°C) lead to little to no FeCO<sub>3</sub> precipitation, and a lower but uniform and relatively constant corrosion rate over time is observed. Higher gas temperatures (above 80°C) seem to lead to a more rapid formation of the FeCO<sub>3</sub> layer. The saturation level with respect to FeCO<sub>3</sub> also strongly depends on the water condensation, which continuously provides fresh and acidic condensed water. The cycle of droplet renewal greatly affects the chemistry in the condensed water (pH, FeCO<sub>3</sub> saturation level) and challenges the protectiveness of the FeCO<sub>3</sub>, which seems to be substantially weakened by high acidity (provided in part by CO<sub>2</sub> but especially acetic acid). Higher water condensation rates also prevent the formation of a stable corrosion product layer and strongly affect the extent of localized corrosion. Small pits are generally observed at the initial stages of the corrosion process and seem to grow together into wide, flat-bottomed mesa attack features, which can affect rather large parts of the steel sample surface area. Very high localized corrosion rates, often reaching 10-12 mm/year, are measured in the presence of 1000 mg/L of acetic acid or at water condensation of 1 mL/m<sup>2</sup>/s. Under certain conditions, localized corrosion can be limited, such as at low condensation rates (<0.05 mL/m<sup>2</sup>/s), but only with little or no acetic acid present. In all conditions tested, the presence of a large concentration of acetic acid always leads to tremendous localized corrosion rates, however low the water condensation rate might be. The extent of top of the line corrosion is definitively the result of complex interactions amongst all of these parameters. Threshold values, often used as engineering guidelines in the industry, should be used with caution, and a solid understanding of the mechanisms involved is a prerequisite for the development of effective TLC inhibition programs.

- TLC in sour environment

In the presence of H<sub>2</sub>S, the average corrosion rate at the top and the bottom of the line starts at a low value and remains relatively constant over time.

The presence of trace amounts of H<sub>2</sub>S reduces the initial average corrosion rate compared to a pure CO<sub>2</sub> environment. There is no clear influence of further additions of H<sub>2</sub>S (up to 0.13 bar) on the average corrosion rate. No localized corrosion was observed in the presence of H<sub>2</sub>S (up to 0.13 bar), considering an exposure time of 21 days.

The presence of acetic acid seems to affect the integrity of the FeS film and also to strongly influence the general corrosion rate. The acetic acid seems to trigger the occurrence of localized corrosion in the form of small pits. The maximum pitting rate measured falls close to the average corrosion rate and is therefore considered to be mechanistically identical.

Table 8: Summary of general and localized corrosion results – Sweet TLC series

Investigating	Acetic acid			WCR			pCO <sub>2</sub>		Gas temp.		Acetic acid / WCR		
General experimental conditions													
Gas temperature (°C)	70	70	70	70	70	70	70	<b>40</b>	<b>85</b>	70	70	70	70
Gas velocity (m/s)	5												
pCO <sub>2</sub> (bar)	2	2	2	2	2	<b>0.13</b>	<b>7</b>	2	2	2	2	2	2
pH <sub>2</sub> S (bar)	0												
Free HAc in the tank (ppm)	<b>0</b>	<b>100</b>	<b>1000</b>	0	0	0	0	0	0	<b>100</b>	<b>100</b>	<b>1000</b>	<b>1000</b>
Condensation rate (ml/m <sup>2</sup> /s)	0.25			<b>0.05</b>	<b>1</b>	0.25	0.25	0.25	0.25	<b>0.05</b>	<b>1</b>	<b>0.05</b>	<b>1</b>
Style type	X65												
General corrosion over the entire sample surface area													
Corrosion rate (mm/year)	0.34	0.38	2.33	0.22	0.69	0.37	0.3	0.61	0.47	0.36	0.71	1.42	1.62
Pitting corrosion													
Average pitting rate (mm/year)	2.3	3.35	7.3	2.61	4.4	3.15	4.93	0	0	3.47	6.95	6.67	6.33
Max pitting rate (mm/year)	4.35	5.02	9.8	5.21	6.6	4.98	6.58	0	0	5.21	8.69	8.33	7.5
Mesa Attack													
Average mesa rate (mm/year)	5.6	3.35	9.61	2.61	6.24	3.5	6.57	0	0	0	7	6.67	6.67
Max mesa attack (mm/year)	6.3	5.02	12.3	3.56	6.6	4.72	8.22	0	0	0	8.7	10.8	9.16
Percentage of sample surface area affected by localized corrosion (Mesa + Pitting)													
% of surface area	3.7	2	17.2	1.6	14.1	4.1	4	0	0	0.5	7	11.6	14.2

Table 9: Summary of general and localized corrosion results – Sour TLC series

Investigating	H2S partial pressure				H2S partial pressure/ Acetic acid		
General experimental conditions							
Gas temperature (°C)	70	70	70	70	70	70	70
Gas velocity (m/s)	5	5	5	5	5	5	5
pCO <sub>2</sub> (bar)	2	2	2	2	2	2	2
pH <sub>2</sub> S (bar)	<b>0</b>	<b>0.004</b>	<b>0.07</b>	<b>0.13</b>	<b>0.004</b>	<b>0.07</b>	<b>0.13</b>
Free HAc in the tank (ppm)	0	0	0	0	<b>100</b>	<b>1000</b>	<b>1000</b>
Condensation rate (ml/m <sup>2</sup> /s)	0.25	0.25	0.25	0.25	0.25	0.25	0.25
Style type	X65	X65	X65	X65	X65	X65	X65
General corrosion over the entire sample surface area							
Corrosion rate (mm/year)	0.34	0.29	0.04	0.12	0.45	1.73	0.28
Pitting corrosion							
Average pitting rate (mm/year)	2.26	0	0	0	0.7	2.28	2.96
Max pitting rate (mm/year)	4.34	0	0	0	0.87	3.86	4.52
Mesa Attack							
Average mesa rate (mm/year)	5.56	0	0	0	0	0	0
Max mesa attack (mm/year)	6.26	0	0	0	0	0	0
Percentage of sample surface area affected by localized corrosion (Mesa + Pitting)							
% of surface area	3.6	0	0	0	0.8	1.01	5.43

#### 4.4 Localized sweet TLC study in large scale flow loop using the steel insert

The parametric study presented in section 4.3 raised a few unresolved aspects of TLC, especially related to the effect of the water condensation rate. In order to answer the remaining questions, a new test section design was implemented. This new design, labeled “flat slab concept” (described in details in Chapter 3.3.4), aims at eliminating the artificial edge effect issue encountered in the previous design. The following chapter presents a summary of the work performed to date.

##### 4.4.1 Test matrix

The test matrix below (Table 10) was selected in order to investigate the effect of the water condensation using an experimental setup designed to simulate the field environment more realistically.

Table 10: Localized condensation/corrosion study - Test matrix

Common parameters:

Test duration: 3 months

Steel type: C1018(I), (II), (III) and APIX65

Corrosion measurement method: Weight loss sample and carbon steel insert

Condensation regime: Sliding droplet mode

Gas velocity: 2.5 m/s -  $p_{CO_2}$ = 2.7 bars -  $p_{H_2S}$ = 0 bar -  $P_T$ = 3 bars

Test #	1	2	3	4
Investigating	Gas temperature			CO <sub>2</sub> /HAc
Steel type	C1018(I)	X65	X65	C1018(III)
T <sub>g</sub> (°C)	<b>65</b>	<b>45</b>	<b>25</b>	65
Undissociated HAc (ppm)	0	0	0	<b>1000</b>
Low WCR (mL/m <sup>2</sup> /s)	0.13	0.1	0.04	0.2
Medium WCR (mL/m <sup>2</sup> /s)	0.41	0.14	0.06	0.4
High WCR (mL/m <sup>2</sup> /s)	0.9	0.22	0.1	0.7

Due to safety restrictions linked to the use of the special test section, the experimental study was limited to sweet environments (CO<sub>2</sub> only). Three different condensation rates were reproduced on the surface of the steel insert during each test.

#### 4.4.2 *Experimental results*

This chapter presents a summary of the most relevant experimental work performed with the new “flat slab” concept. It is divided into two main parts: the effect of the gas temperature (section 4.4.2.1) or the presence of acetic acid (section 4.4.2.2).

##### 4.4.2.1 *Influence of the gas temperature and the water condensation rate*

###### 4.4.2.1.1 *TEST #1 - $T_{gas}=62^{\circ}C$*

###### 4.4.2.1.1.1 *Experimental conditions*

The experimental conditions of this baseline test are summarized in Table 11. The slab was divided into three parts:

- The upstream part of the flat slab was well insulated with a condensation rate calculated between 0.12 and 0.15 mL/m<sup>2</sup>/s.
- The middle part of the slab was neither insulated nor artificially cooled to produce a condensation rate between 0.37 and 0.46 mL/m<sup>2</sup>/s.
- The downstream part of the slab was cooled with a condensation rate estimated between 0.76 and 0.95 mL/m<sup>2</sup>/s.

This way, the same piece of carbon steel is exposed to low, medium and high condensation rates for an extended period of time.

Table 11: Test #1 – Test conditions

Parameter	Value / range
Steel type	C1018(l)
Gas temperature	62°C
Total pressure	3bars
pCO <sub>2</sub>	2.7 bars
Free HAc concentration	0 ppm
Gas velocity	2-3 m/s
Low condensation rate (upstream section)	Between 0.12 and 0.15 mL/m <sup>2</sup> /s T <sub>wall</sub> : 56-59°C
Medium condensation rate (middle section)	Between 0.37 and 0.46 mL/m <sup>2</sup> /s T <sub>wall</sub> : 52-54°C
High condensation rate (Downstream section)	Between 0.76 and 0.95 mL/m <sup>2</sup> /s T <sub>wall</sub> : 38-40°C
Exposure time	93 days

#### 4.4.2.1.1.2 Surface analysis

##### 4.4.2.1.1.2.1 Overview of the corrosion product layer characteristics

As shown in Figure 87 a), the part of the C1018 insert exposed to a low condensation rate (0.12-0.15 mL/m<sup>2</sup>/s) did not seem to be highly corroded (*i.e.*, the corrosion product layer was still fairly intact). The part of the insert exposed to a high condensation rate (0.76-0.95 mL/m<sup>2</sup>/s) in Figure 87 c) seemed much more affected by corrosion. Numerous breakdowns in the layer (which is usually related to extensive localized corrosion) could be observed, especially on the section exposed to higher water condensation rates. The yellow/orange color found on part of the steel sample is a sign of the presence of iron oxide (most likely ferric oxide) which is thought to have formed after the end of the experiment as the slab assembly was removed from the loop. Operational procedures often require a few minutes before the steel insert, wetted by droplets of condensed water saturated with species generated due to corrosion processes, can be accessed and dried. In this elapsed time, the steel is exposed to air. During the experiment

itself, great care is given to maintain the level of oxygen in the bulk liquid phase below 20 ppb so as not to interfere with the corrosion process.

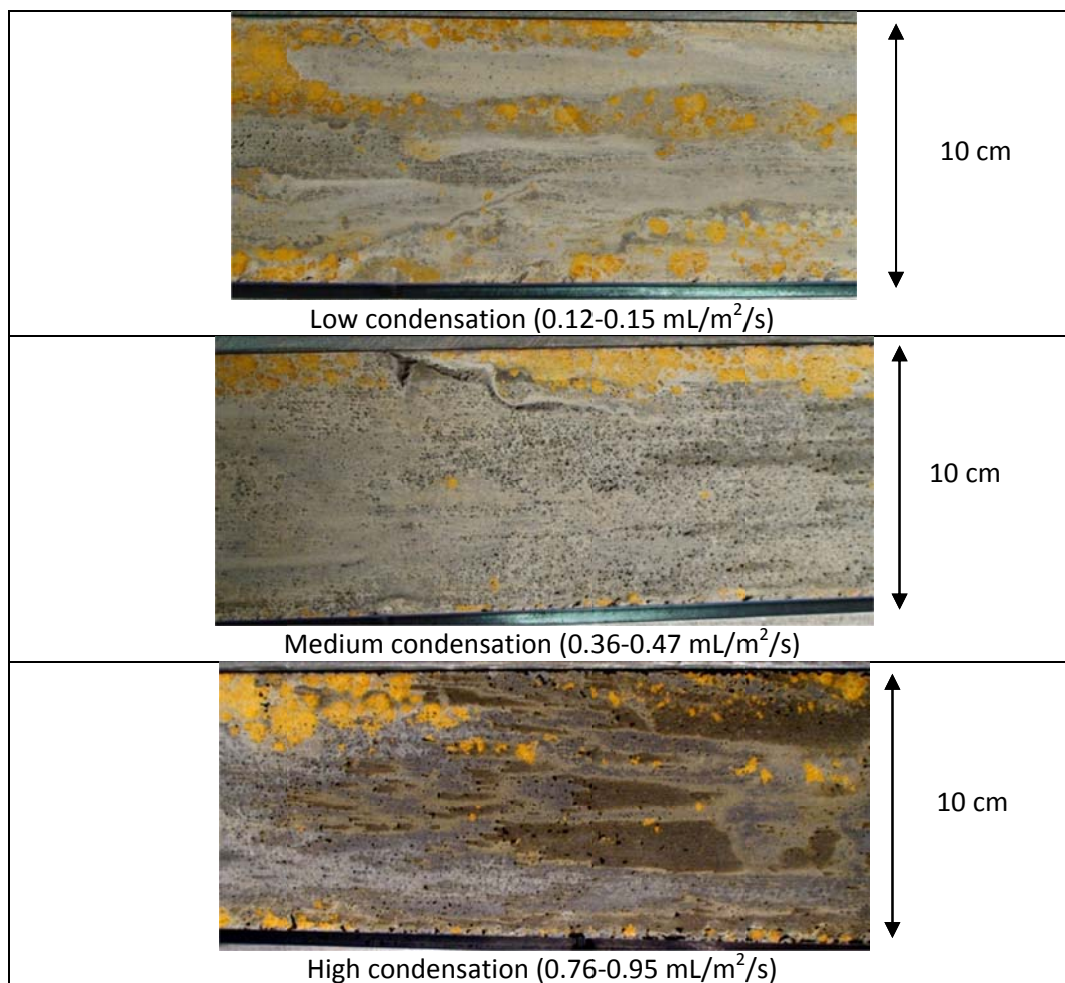


Figure 87 : Test #1 - C1018(l) insert – High condensation (0.76-0.95 mL/m<sup>2</sup>/s)  
Analysis of the steel surface before cleaning of the corrosion product layer

#### 4.4.2.1.1.2.2 SEM/EDS analysis of the corrosion product layer

Figure 88 presents the SEM/EDS analysis of the corrosion product layer commonly found on the surface of the steel insert. No significant difference of the type and composition of the layer was observed with regard to the change in water condensation rates. Although no X-

ray diffraction analysis was performed on the surface of the steel insert, the corrosion product layer is believed to be a mixture of iron carbonate and iron oxide. Once again, the iron oxide (most likely ferric oxide  $\text{Fe}_2\text{O}_3$ ) must have formed during the removal of the slab assembly at the end of experiment, since no oxygen was present in the loop during the experiment. Some crystals of  $\text{FeCO}_3$  could be seen underneath the ferric oxide layer (Figure 88 d)).

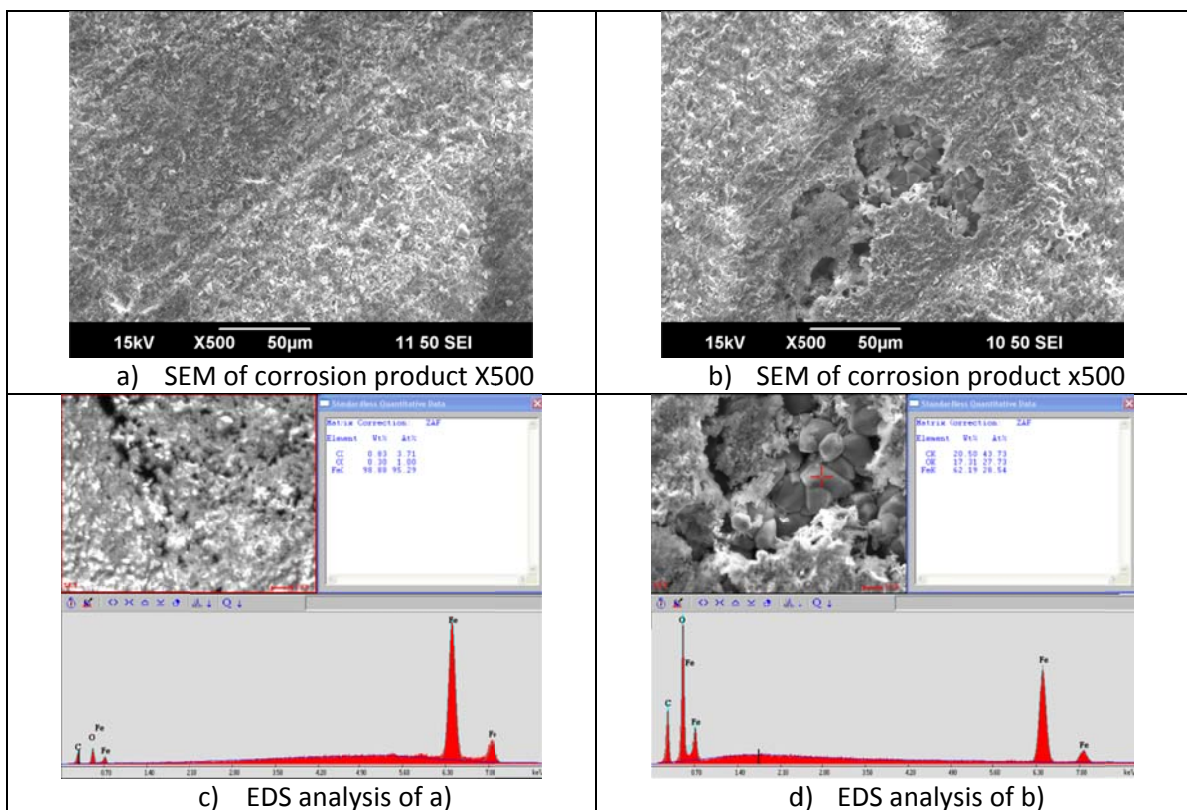


Figure 88: SEM/EDS analysis of the corrosion product layer  
Medium condensation rate section ( $0.36\text{-}0.47\text{ ml/m}^2/\text{s}$ )

Figure 89 shows the E-pH Pourbaix diagrams for the  $\text{Fe}/\text{CO}_2/\text{H}_2\text{O}$  system at different temperatures corresponding to the steel temperature experienced by the steel insert under the different water condensation rates. These graphs were obtained from the work developed by Tanupabrunsun [98]. It clearly shows that in the area of interest for this study (pH between 3

and 7, temperature between 20 and 70°C and potential vs. saturated hydrogen electrode between [SHE] -0.4 and -0.6 V), no corrosion product other than  $\text{FeCO}_3$  and  $\text{Fe}^{2+}$  ions is thermodynamically stable. Ferric oxide ( $\text{Fe}_2\text{O}_3$ ) requires higher potential and pH to form and magnetite ( $\text{Fe}_3\text{O}_4$ ) appears at a much higher temperature [98].

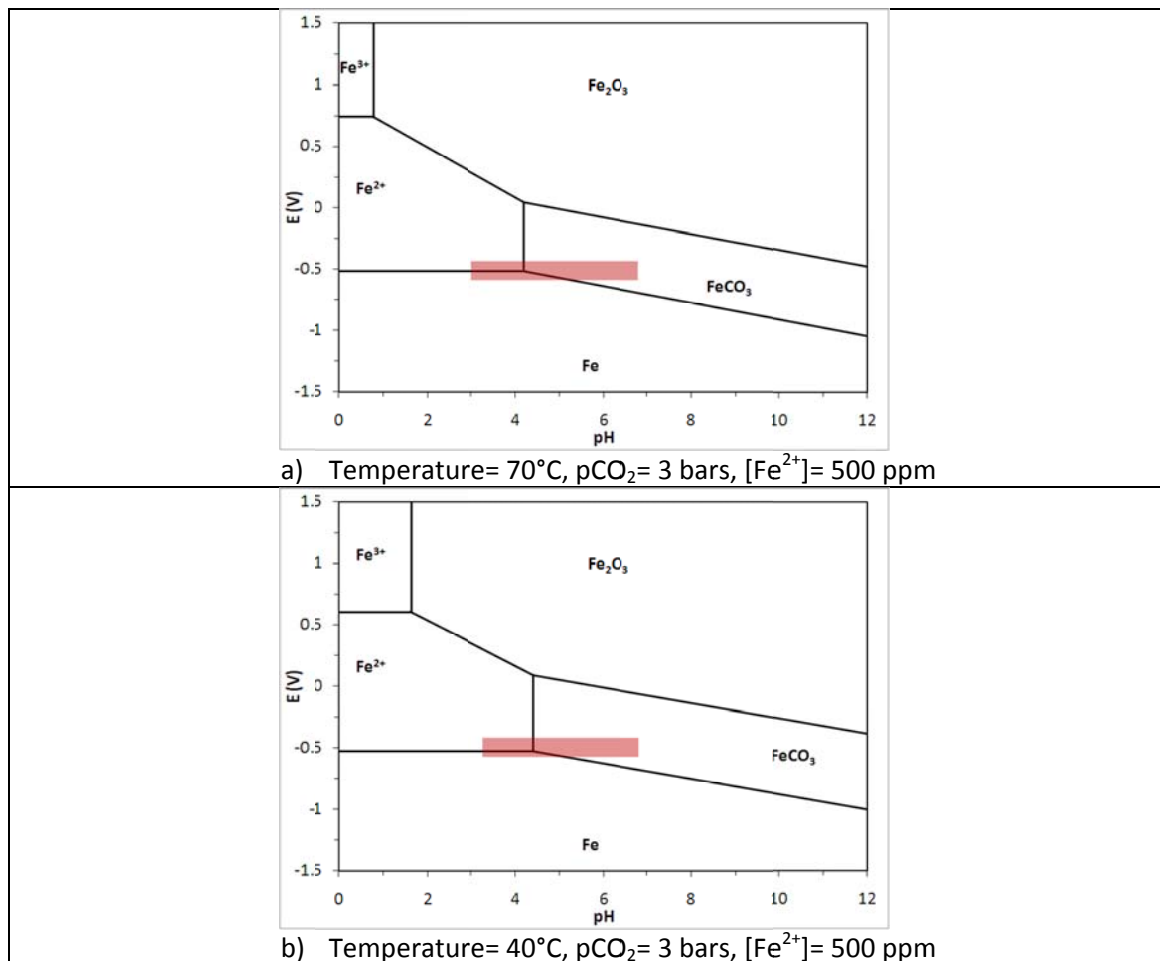


Figure 89: Pourbaix Diagram for Fe/H<sub>2</sub>O/CO<sub>2</sub> system at different temperature (40 and 70°C) [98]  
- Potential vs SHE - Area of interest is highlighted in red

#### 4.4.2.1.1.2.3 3D surface profile of bare steel (after removal of the corrosion product layer)

These initial observations were confirmed with the surface analysis on the bare steel shown in Figure 90 (once the corrosion product layer was removed by chemical means).

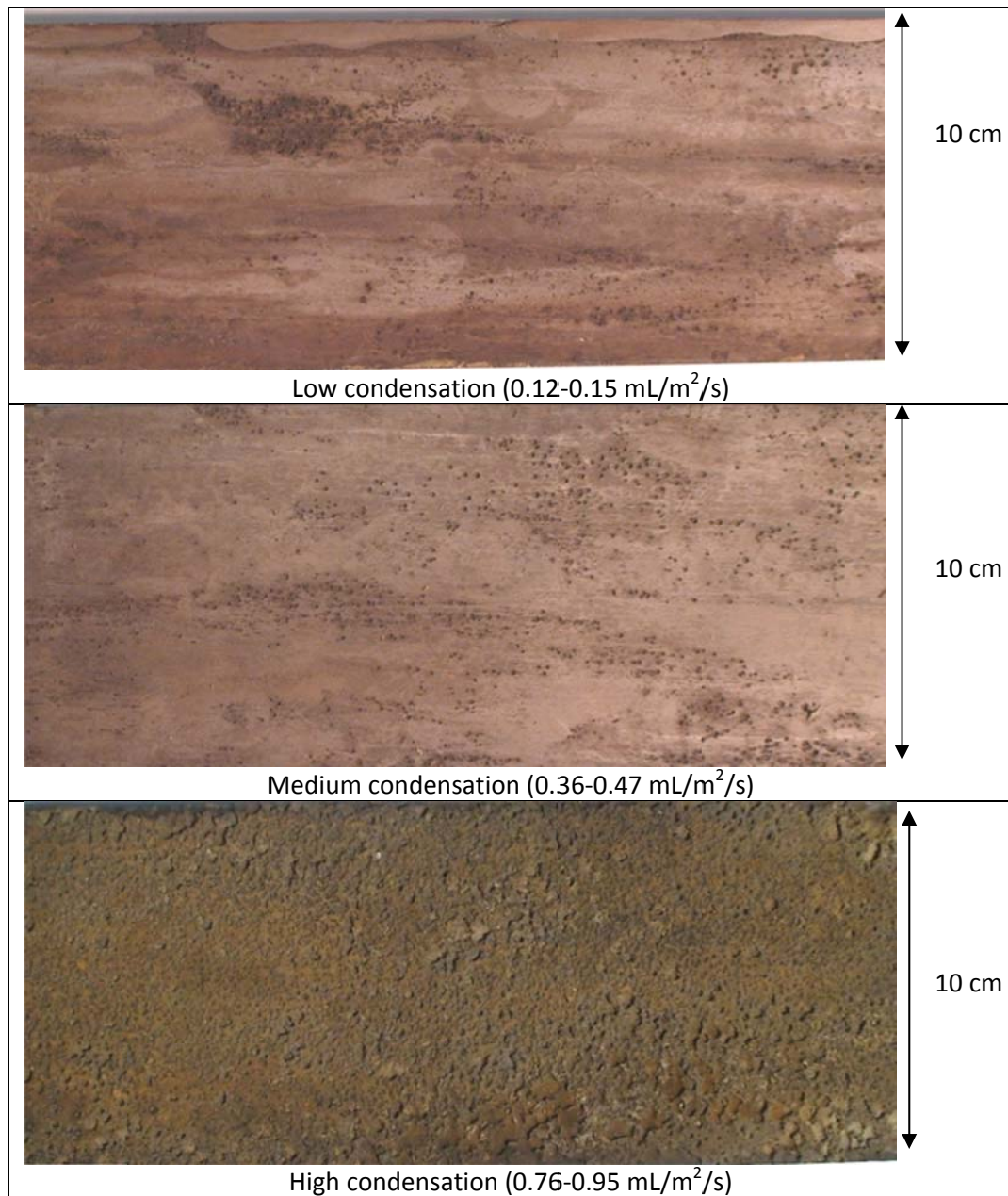


Figure 90: Test #1 - Steel surface after removal of the corrosion product layer

The section of the insert exposed to a low condensation rate did present some pitting corrosion but the pits were fairly isolated. In the middle section exposed to a medium condensation rate, the pitting density increased. The pits seemed to coalesce in the section

exposed to a high condensation rate which also showed severe mesa attack (localized corrosion with flat bottom features). The relationship between condensation rate and localized corrosion is, therefore, clearly demonstrated in this experiment.

Average, minimum and maximum localized corrosion rates were extracted from the 3D profile analysis, and the results are displayed below in Figure 91, Figure 92 and Figure 93. It is important to mention that, due to the limitation of the instrument, only small areas of the insert (1.5 cm by 2 cm) could be analyzed at once. These selected areas are thought to be representative.

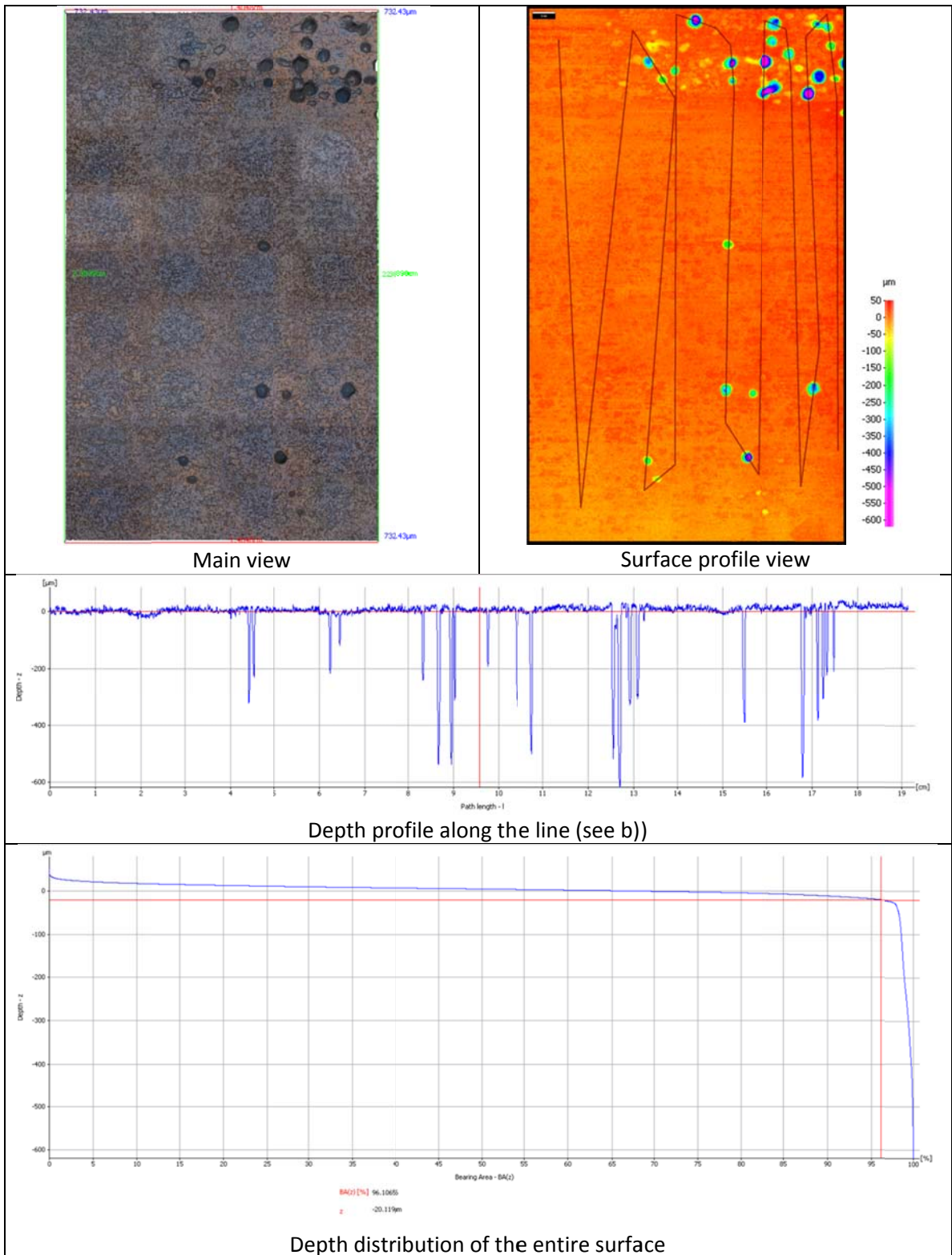


Figure 91: Test #1 – C1018(I) insert – Surface profile analysis  
Upstream section - Low condensation (0.12-0.15 mL/m<sup>2</sup>/s)

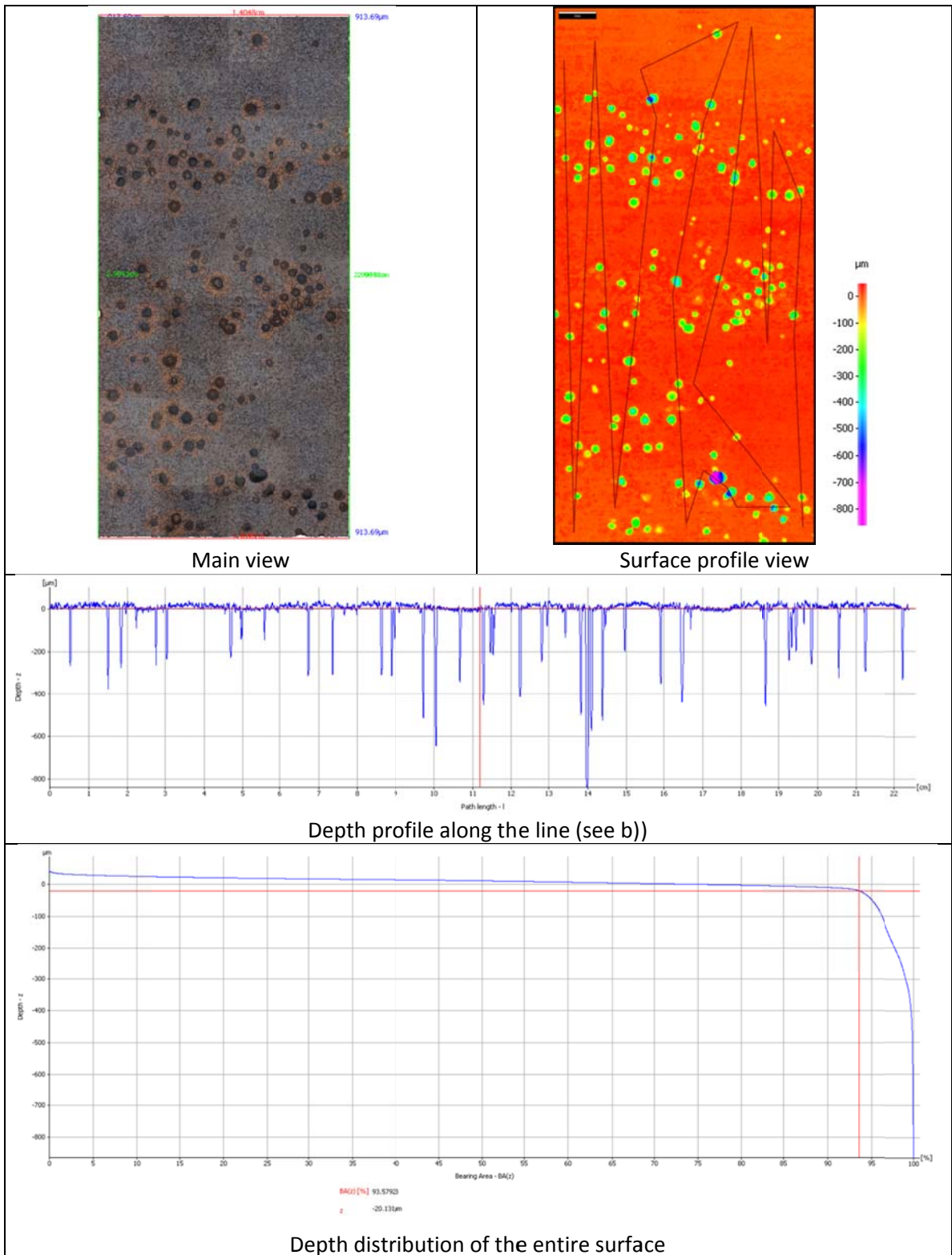


Figure 92: Test #1 – C1018(I) insert – Surface profile analysis  
Upstream section - Medium condensation (0.36-0.47 mL/m<sup>2</sup>/s)

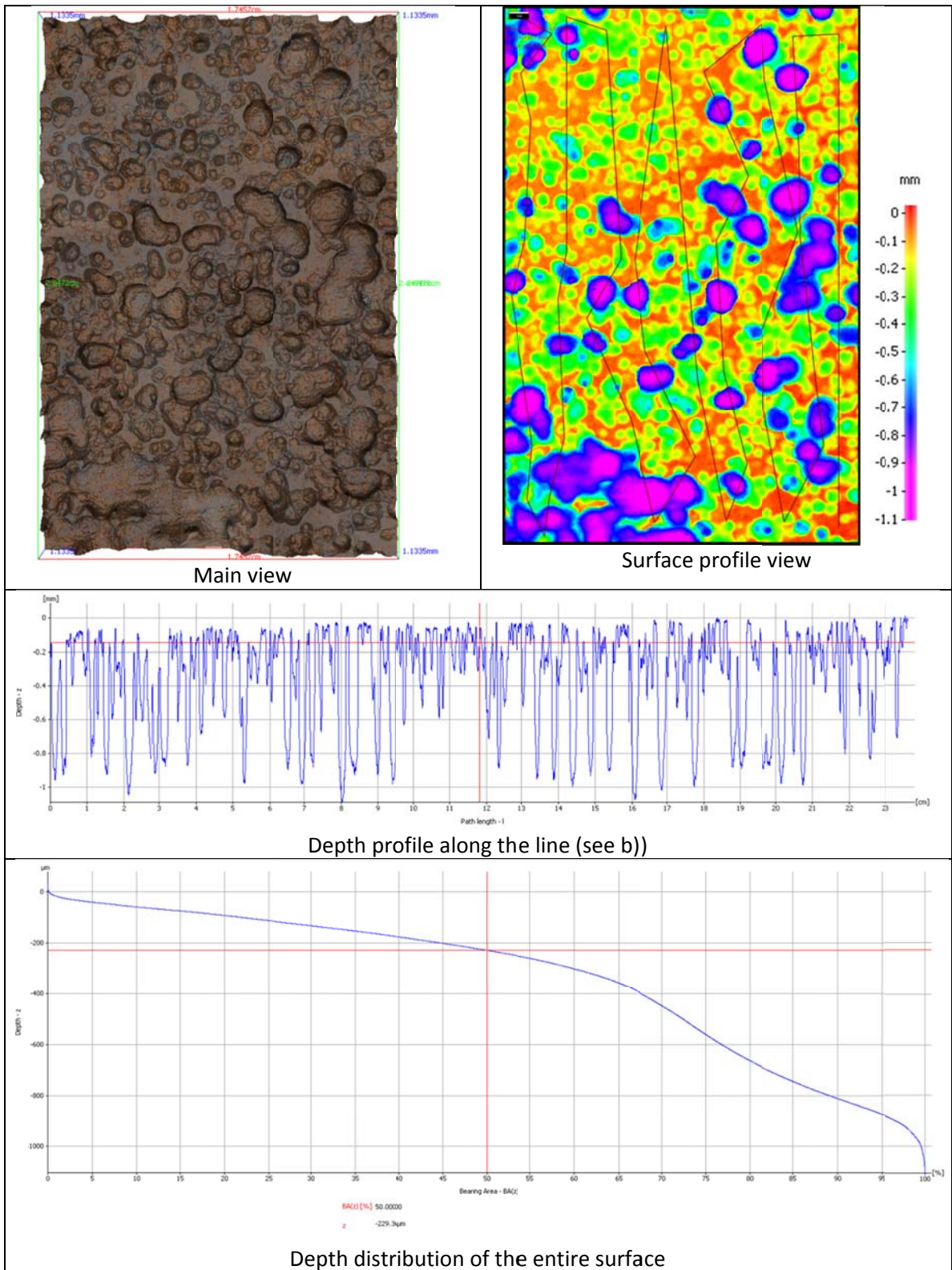


Figure 93: Test #1 – C1018(I) insert – Surface profile analysis  
Upstream section - High condensation (0.76-0.95 mL/m<sup>2</sup>/s)

#### 4.4.2.1.1.3 Corrosion rate analysis

The section of the insert exposed to a low condensation rate showed some pitting corrosion but the pits were fairly isolated. In the middle section exposed to a medium condensation rate, the pitting density increased. However, the pits coalesced in the high condensation rate section which showed severe mesa attack, represented by localized corrosion features with flat bottoms (Figure 94). These corrosion features very much resemble what is observed in real field situations [38], as shown in Figure 12.

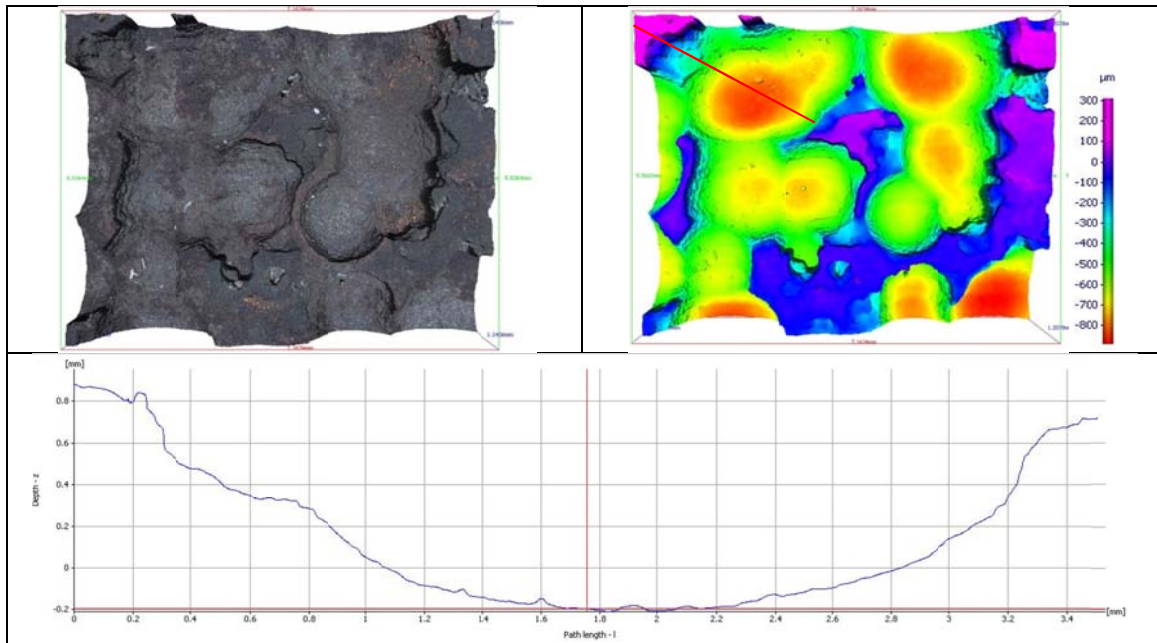


Figure 94: Test #1 - 3D profile of the bare steel surface  
High condensation rate section ( $0.76\text{-}0.95 \text{ ml/m}^2/\text{s}$ )

Feature characteristics could be extracted from the 3D profile analysis. The main results are displayed in Table 12. An effort to collect statistical data of the pit depth distribution is also presented.

Table 12 : Test #1 – Localized corrosion rate analysis

Parameter	Unit	Water condensation rate (mL/m <sup>2</sup> /s)		
		Min 0.14 mL/m <sup>2</sup> /s	Average 0.42 mL/m <sup>2</sup> /s	Max 0.86 mL/m <sup>2</sup> /s
Average localized corrosion rate	mm/year	2.61	5.56	6.24
Max localized corrosion	mm/year	3.48	6.26	6.97
Average feature depth	μm	150	320	359
Max feature depth	μm	200	360	401
Average feature diameter	mm	0.59	0.60	2.23
Arithmetic mean	μm	13.4	23.2	340.0
Standard deviation	μm	36.2	50.6	281.3
Root mean square	μm	38.6	55.6	441.3
Skewness		-8.8	-6.2	-1.6
Kurtosis		93.7	53.1	2.8
Pitting density	cm <sup>-2</sup>	11.1	45.2	70.2
% area affected by localized corrosion	%	6.7	15.2	82.5

The reference plane used for the profile analysis was set to fit the top of the steel surface as much as possible. The following values were systematically computed: the average and maximum feature depth and corresponding localized corrosion rates, the average feature diameter (assuming a cylindrical shape), the pitting density (number of pits per unit area) and the percentage area affected by localized corrosion.

The arithmetic mean  $\mu$  calculates the average depth of features with the top steel surface as a reference, using the following equation:

$$\mu = \frac{1}{n} \sum_{i=1}^n x_i \quad \text{Eq (4-1)}$$

Where:            n: number of values

                      x: depth (μm)

The closer the arithmetic mean is to zero, the lower is the extent of localized corrosion, in terms of depth and number of features.

The standard deviation  $\sigma$  shows how much variation exists from the mean. High standard deviation indicates that the feature depth is spread out over a wide range of values.

$$\sigma = \sqrt{\frac{1}{n} \sum_{i=1}^n (x_i - \mu)^2} \quad \text{Eq (4-2)}$$

The root mean square (RMS) is a representation of the magnitude of the variation in pit depth over the entire surface area and it is calculated as follows:

$$RMS = \sqrt{\frac{1}{n} \sum_{i=1}^n x_i^2} \quad \text{Eq (4-3)}$$

A low RMS number means that the corrosion features are either shallow or very few in numbers. In the case of this study, a higher RMS number is an indication of a higher number of deeper pits.

The skewness and kurtosis factors are used to characterize the shape of a distribution of feature depths over the entire steel surface. The tallest bar on the distribution (Figure 95) always expresses the percentage of surface area at the “zero” or “reference” level (top surface).

The skewness represents the extent to which the distribution leans to the left of this reference plan. Skewness values are consequently negative in this case since the tail of the distribution is almost always longer on the left side. A high absolute value of skewness is obtained when deep isolated pits are present on the metal surface (long and thin left tail). To the other extent, a skewness of zero is obtained when the surface is perfectly symmetrical (for example, in the case of uniform corrosion) and when there is absolutely no pit. The kurtosis is a

representation of the peak characteristics (width of the peak) and tail weight. It is always a positive number that approaches zero as the distribution becomes flatter. For isolated, deep pits, the kurtosis factor will be high. Heavily pitted surfaces, where the distribution tail is thick, will have lower kurtosis factors.

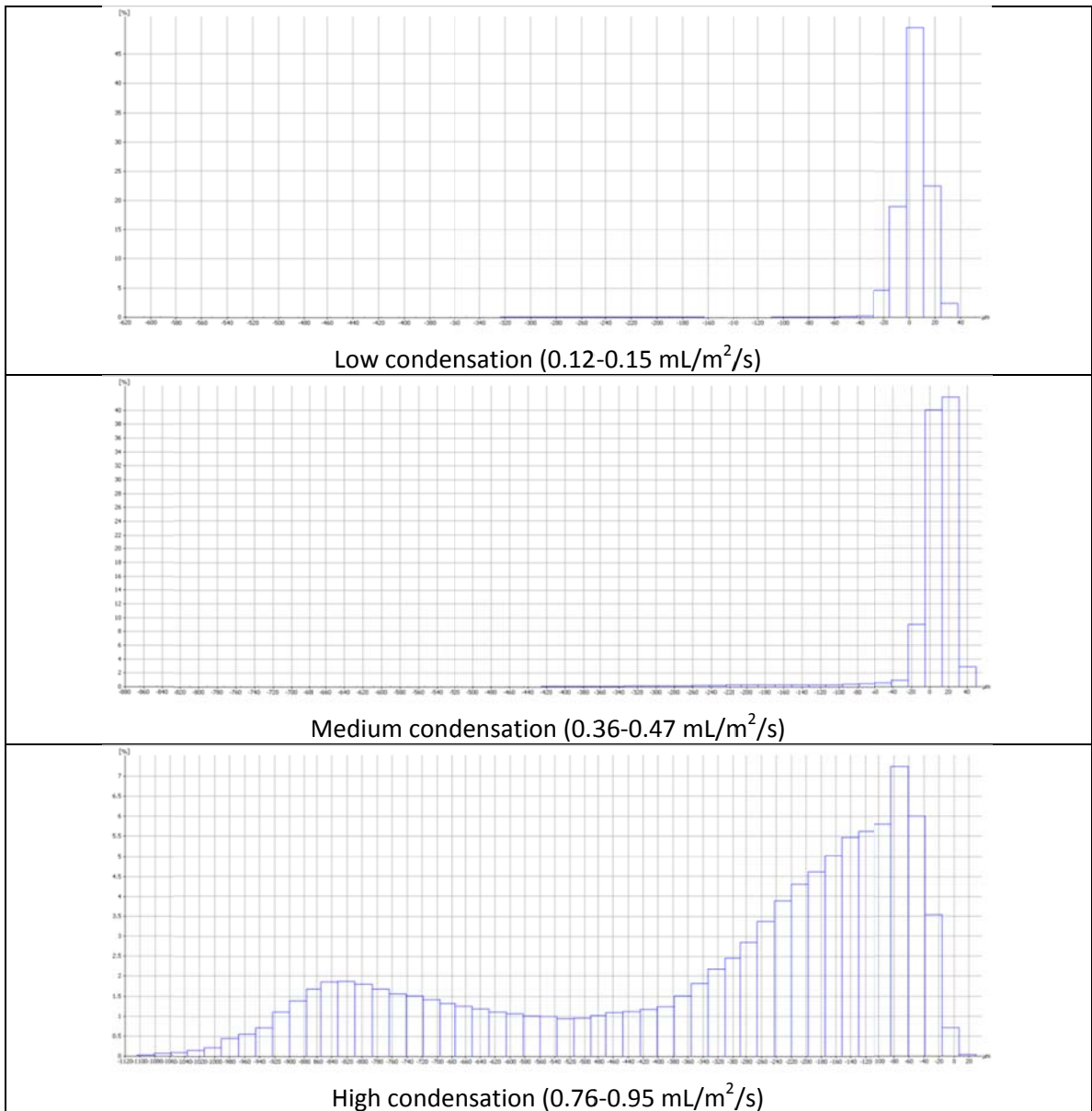


Figure 95: Test #1 - Feature depth distribution over the entire scanned steel surface

The localized corrosion data are presented in Figure 96 and compared to experimental data obtained during the parametric study under the same conditions but for an exposure time of 21 days (Section 4.3.2.4). The “21-day” experimental data were obtained by performing a surface profile scan on weight loss samples. Comparing the data obtained after 21 days and 93 days of exposure, the localized corrosion rates (or more accurately the steel penetration rates) clearly increase with the water condensation rate but also decrease with time.

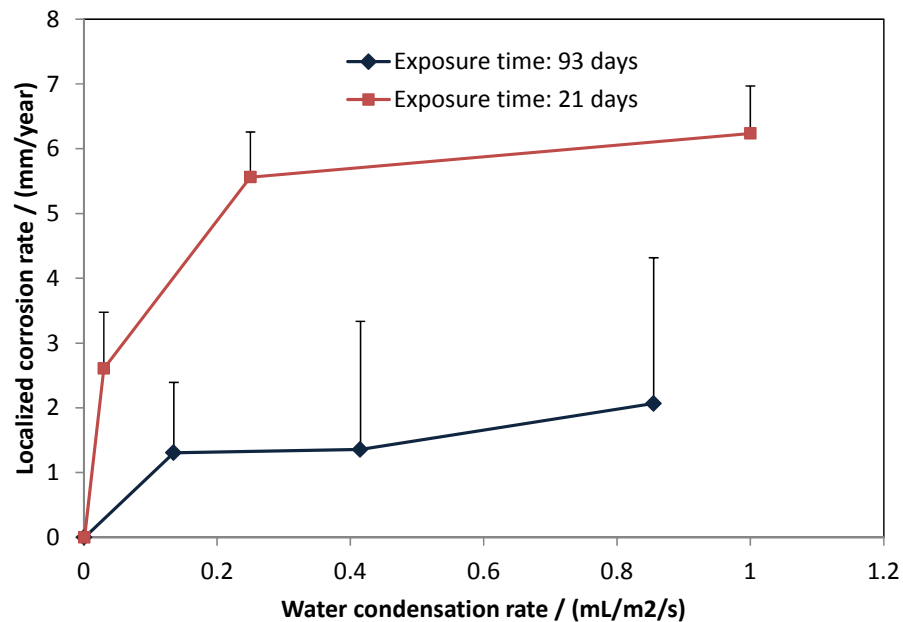


Figure 96: Test #1: Influence of the condensation rate on the localized corrosion rate

Another way to compare the two sets of data is to plot the actual feature depth versus the condensation rate (Figure 97). It is interesting to note that at condensation rates lower than 0.4 mL/m<sup>2</sup>/s, the average feature depth after 21 days and 93 days of exposure is very similar. It could mean that the pit or mesa attack penetration rate significantly slowed down after 21 days

of exposure. At a condensation rate of  $1 \text{ mL/m}^2/\text{s}$ , the localized attack depth measured after 93 days of exposure is almost 50% higher than the one measured after 21 days of testing. The hypothesis here is that TLC may have significantly slowed down at a condensation rate below  $0.4 \text{ mL/m}^2/\text{s}$  while it did not at a condensation rate of  $1 \text{ mL/m}^2/\text{s}$ . This is in some ways consistent with field observations noting the existence of a “threshold” water condensation rate in sweet environments below which TLC is not a lasting issue [37]. The maximum feature depths do show the same trend, although the “threshold” water condensation rate seems to be much lower.

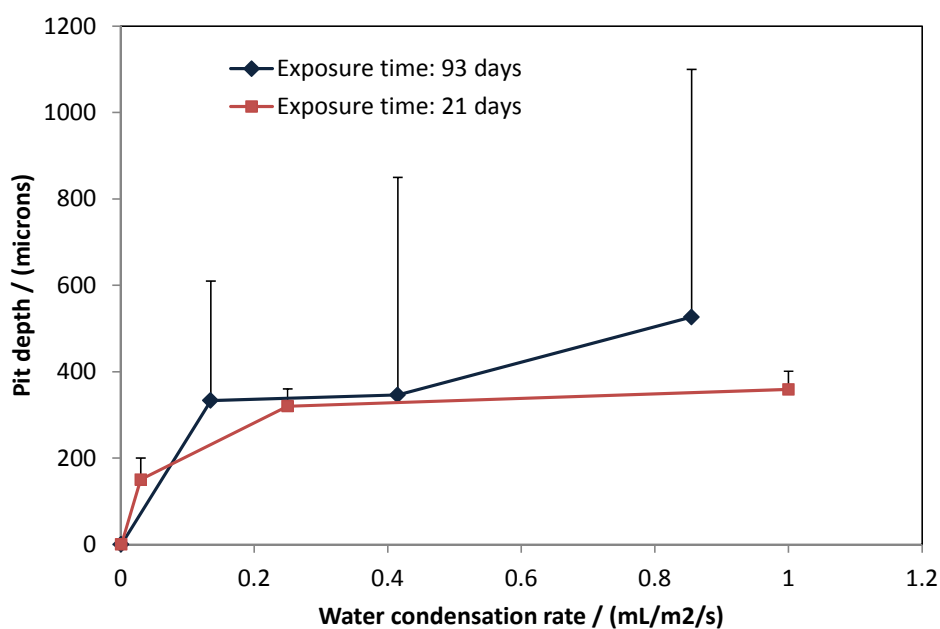


Figure 97: Test #1: Influence of the condensation rate and the exposure time on the pit/mesa depth

The percentage area affected by localized corrosion could also be measured on the steel and the results are displayed in Figure 98 and compared with data obtained for 21 days of exposure.

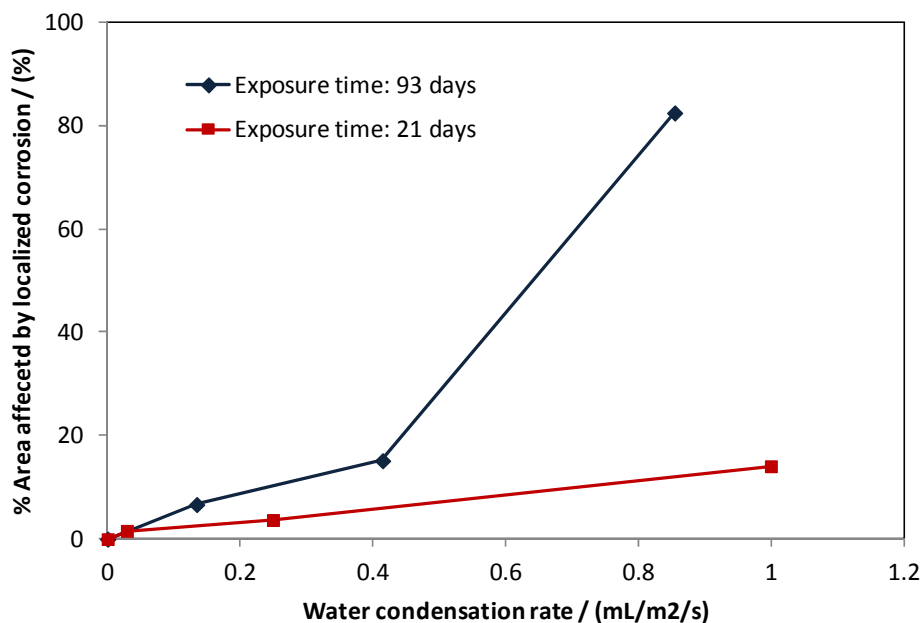


Figure 98: Test #1: Influence of the condensation rate on the percentage of the steel surface area affected by localized corrosion

It is clear that, with time, a higher proportion of the steel surface area is corroded when the water condensation rate is high. This is again in agreement with field observations which seem to show that, although TLC corrosion features depth may not progress at a fixed rate, their numbers do increase with time [42, 46]. As the features grow in number, they coalesce and the steel surface becomes more uniformly attacked. This is clearly demonstrated by the data collected in Table 12, which shows the number of pits per surface area increasing with condensation rate, together with the average feature diameter. The maximum depth of the feature does increase as well, but to a lesser extent.

#### 4.4.2.1.2 TEST #2 - $T_{gas} = 42^{\circ}C$

A second experiment was conducted at a lower temperature (42 instead of 62°C). The primary objective was to investigate the range of test conditions (mainly temperature and water

condensation rate) for which  $\text{FeCO}_3$  formation and localized corrosion would be encountered in a TLC scenario.

#### 4.4.2.1.2.1 Test conditions

The test conditions for Test #2 are shown in Table 13. The main differences from Test #1 are the gas temperature (42 Instead of 62°C) and the range of water condensation rate, since the vapor pressure is lower at 42°C compared of 62°C.

Table 13: Test #2 –Test conditions

Parameter	Value / range
Steel type	X65
Gas temperature	41.5°C
Total pressure	2.6 bars
$p\text{CO}_2$	2.59 bars
Free HAc concentration	0 ppm
Gas velocity	1.8 m/s
pH in bulk liquid phase	4 - 4.8
Section# 1: Low condensation rate (upstream section)	Between 0.09 and 0.11 ml/m <sup>2</sup> /s, $T_{\text{wall}}$ : 35-36 °C
Section# 2: Medium condensation rate (middle section)	Between 0.14 and 0.15 ml/m <sup>2</sup> /s $T_{\text{wall}}$ : 32-33 °C
Section# 3: High condensation rate (Cooled section)	Between 0.22 and 0.23 ml/m <sup>2</sup> /s $T_{\text{wall}}$ : 25-26 °C
Test duration	2.4 months

#### 4.4.2.1.2.2 Surface analysis

##### 4.4.2.1.2.2.1 Overview of the corrosion product layer characteristics

The initial observation of the state of the slab immediately after the test showed that the extent of corrosion seemed higher on the part exposed to higher WCR. More cracks in the corrosion product layers were observed on the cooled section which is usually synonymous with higher corrosion rate (Figure 99). A significant amount of iron oxide (most likely ferric oxide

$\text{Fe}_2\text{O}_3$ ) was also present on the steel surface, although the concentration of  $\text{O}_2$  in the loop was kept under 40 ppb during the test. It is thought that the oxide appeared during the slab removal process, which can take several minutes.

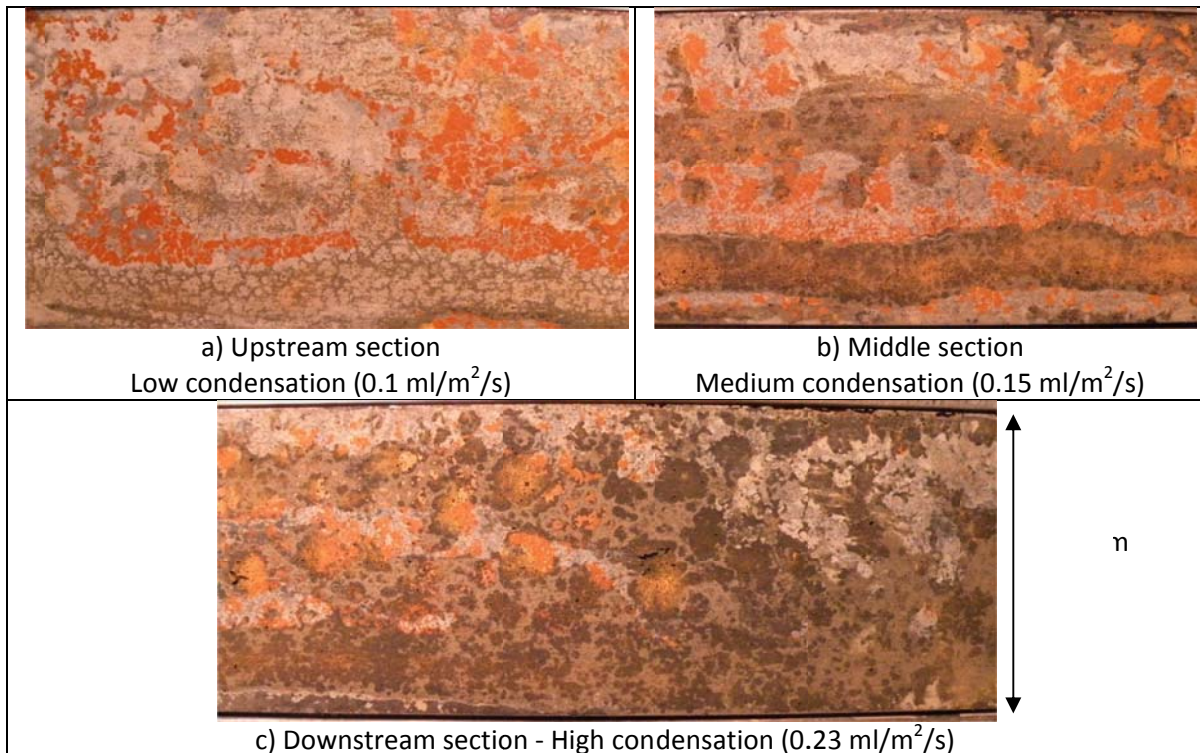


Figure 99: Test #2 - Steel surface before removal of the corrosion product layer  
The flow direction is from left to right

#### 4.4.2.1.2.2.2 SEM/EDS analysis of the corrosion product layer

The SEM/EDX analysis performed on different sections of the insert is shown in Figure 100. There is no major difference caused by the level of cooling. The corrosion product layer is made of a mixture of iron carbonate ( $\text{FeCO}_3$ ), iron carbide ( $\text{Fe}_3\text{C}$ ) and iron oxide (most likely  $\text{Fe}_2\text{O}_3$ ), the later being most probably formed at the end of the test during the steel insert removal procedure. Most of the steel surface was covered with  $\text{FeCO}_3$ , while  $\text{Fe}_3\text{C}$  could be found inside cracks in the  $\text{FeCO}_3$  layer, as is commonly the case in a TLC scenario (Figure 57).

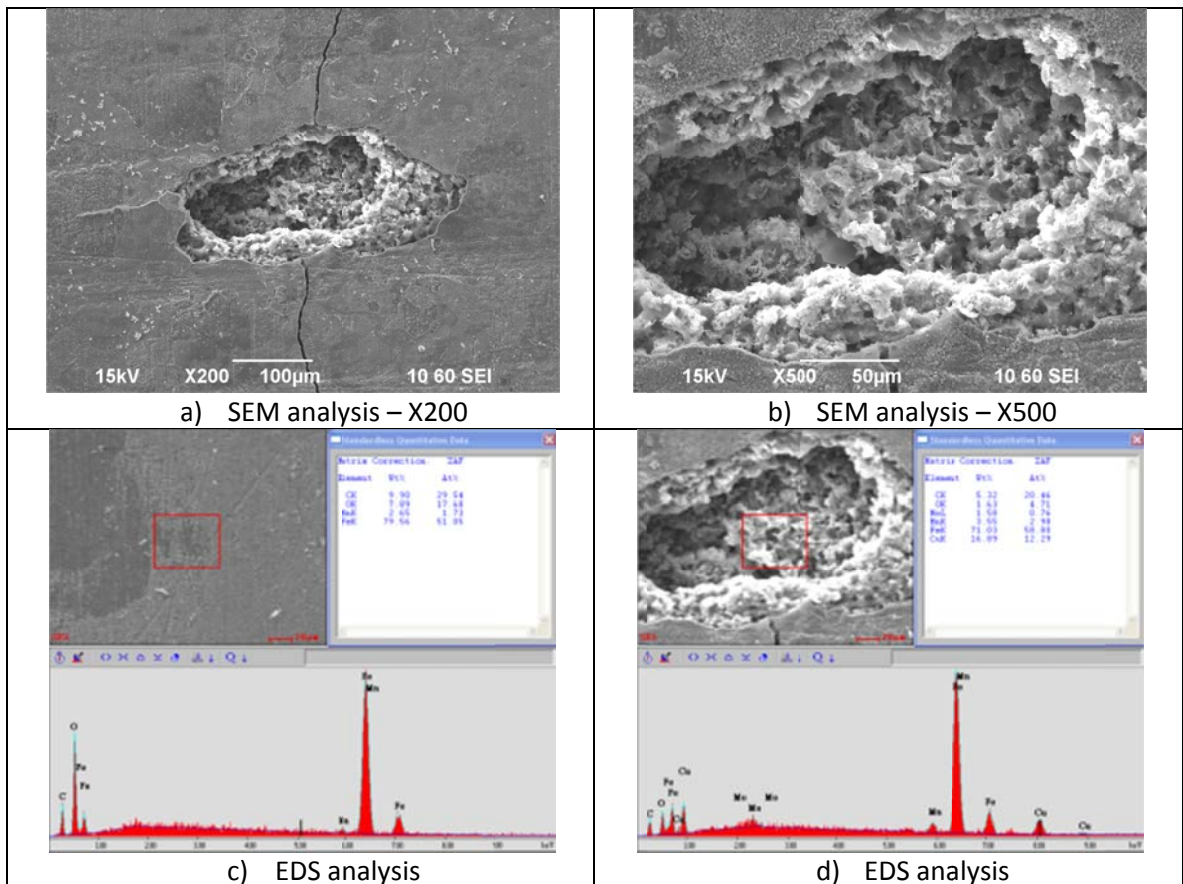


Figure 100: Test #2 – SEM/EDX analysis  
Cooled section - High condensation ( $0.23 \text{ ml/m}^2/\text{s}$ )

#### 4.4.2.1.2.2.3 3D Surface profile analysis of bare steel

The surface of the steel insert, after removal of the corrosion product layer using Clarke's solution (inhibited HCl), is shown in Figure 101. The most striking observation is the extent of localized corrosion (pitting) observed on the cooled section in particular and on the entire slab in general. The cooled section is clearly more affected by pitting corrosion than any other part, as was anticipated. However, the extent of TLC was expected to be less severe at this lower temperature. Previous testing performed with weight loss samples showed no localized

corrosion and a low/moderate uniform corrosion at the top of the line at a gas temperature of 40°C (Section 4.3.2.5).

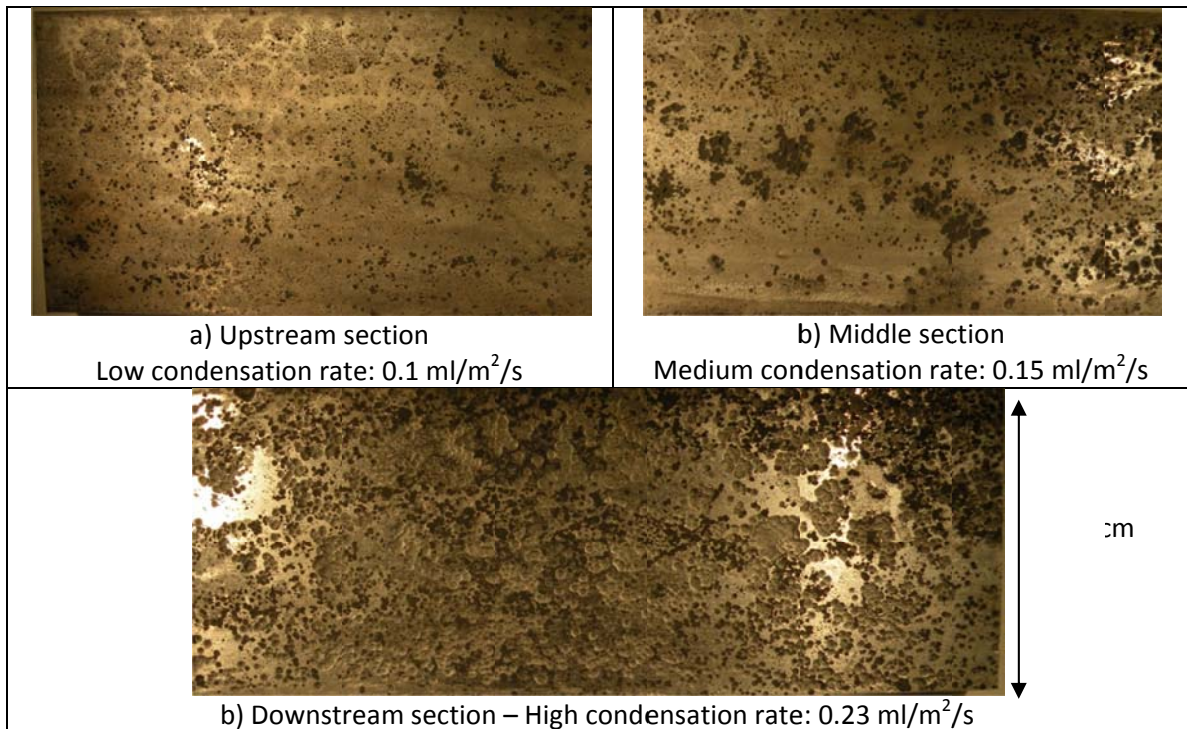


Figure 101: Test #2 – X65 insert - Steel surface before removal of the corrosion product layer  
The flow direction is from left to right

Large areas of the X65 slab were scanned using a 3D surface profilometer, and data on pit depth were collected (Figure 102, Figure 103 and Figure 104). The effect of the condensation rate is clear, as the number of pits and the area affected by localized corrosion rate increases with the condensation rate.

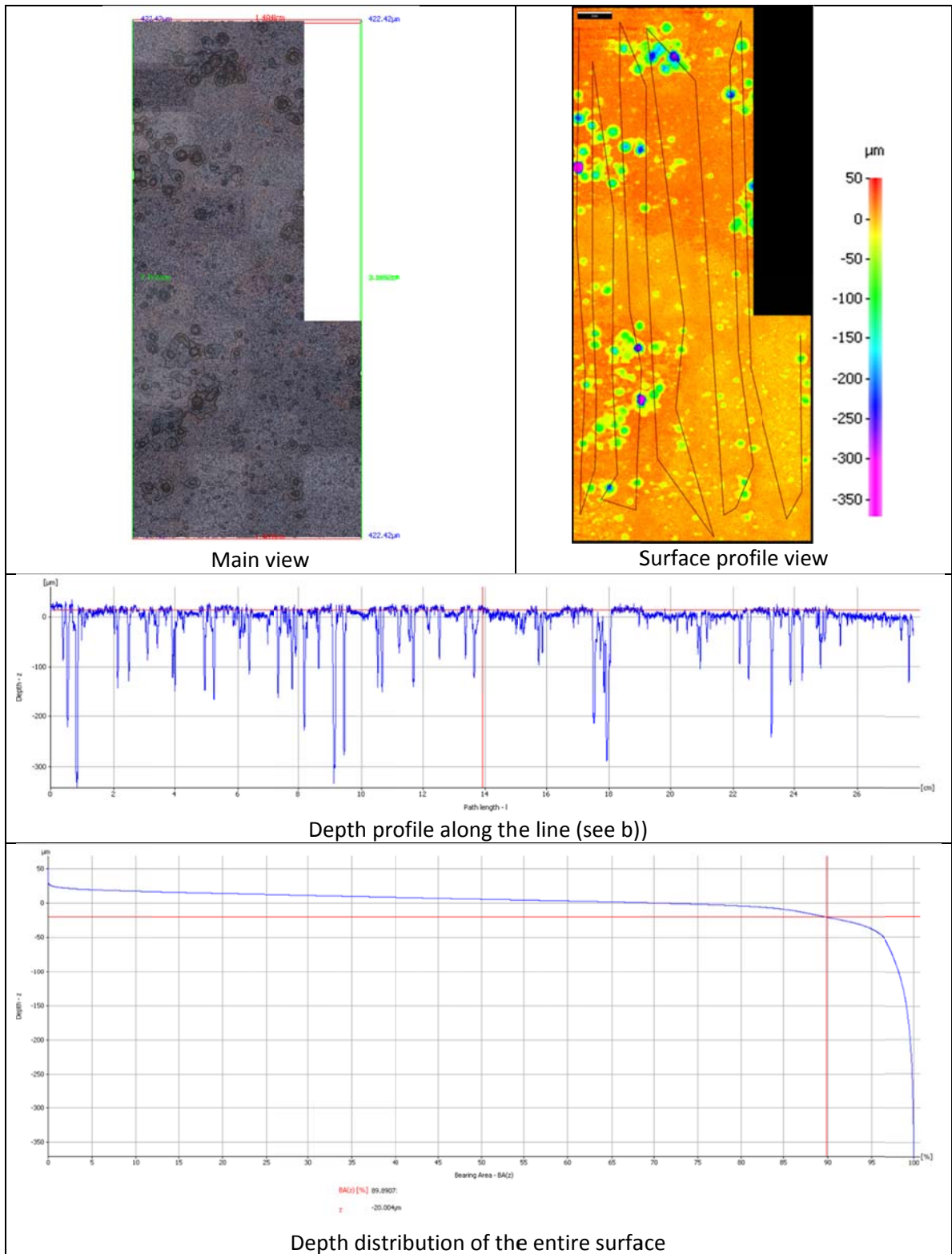


Figure 102: Test #2 – X65 insert – Surface profile analysis  
Upstream section - Low condensation rate: 0.1 ml/m<sup>2</sup>/s

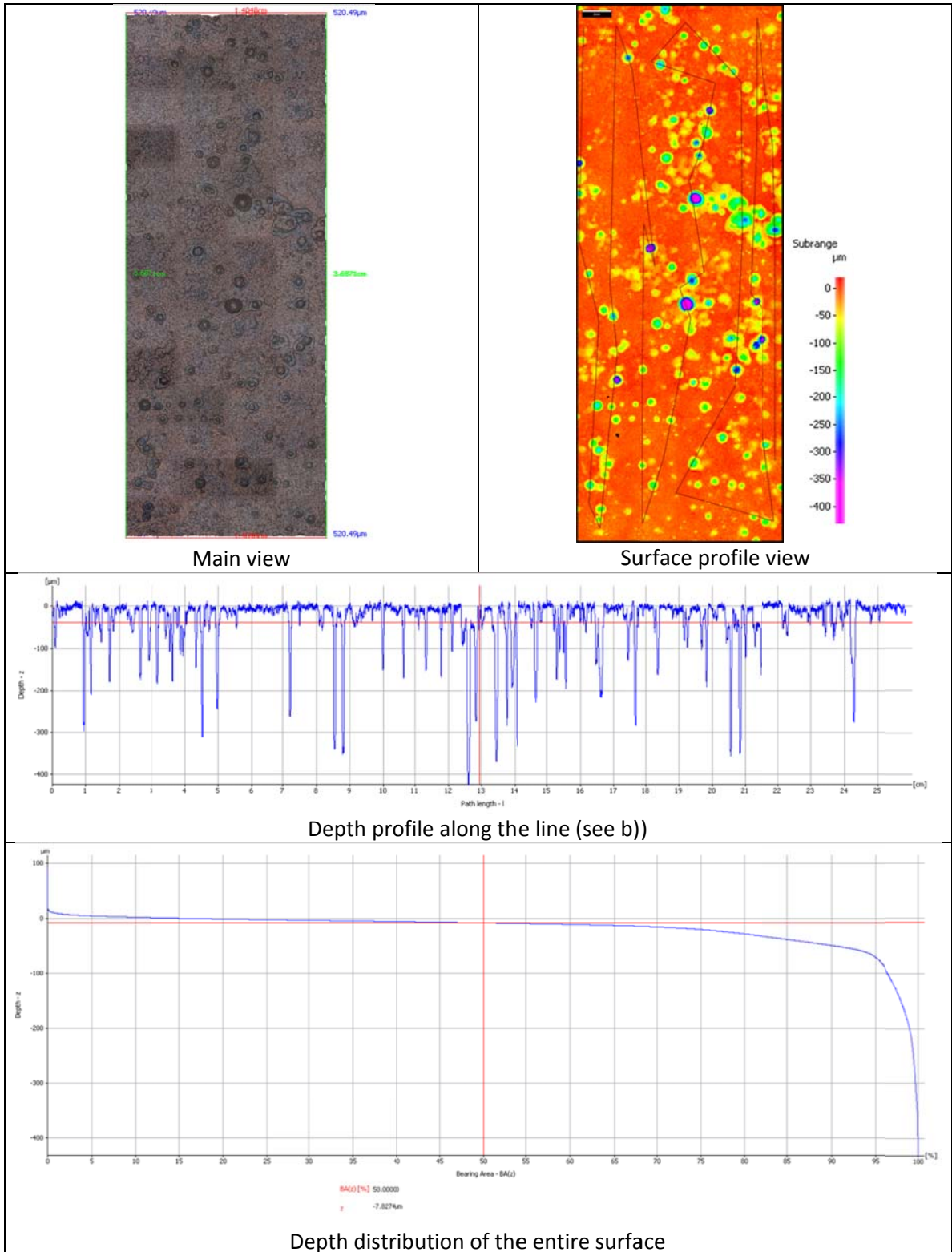


Figure 103: Test #2 – X65 insert – Surface profile analysis  
 Middle section - Medium condensation rate: 0.15 ml/m<sup>2</sup>/s

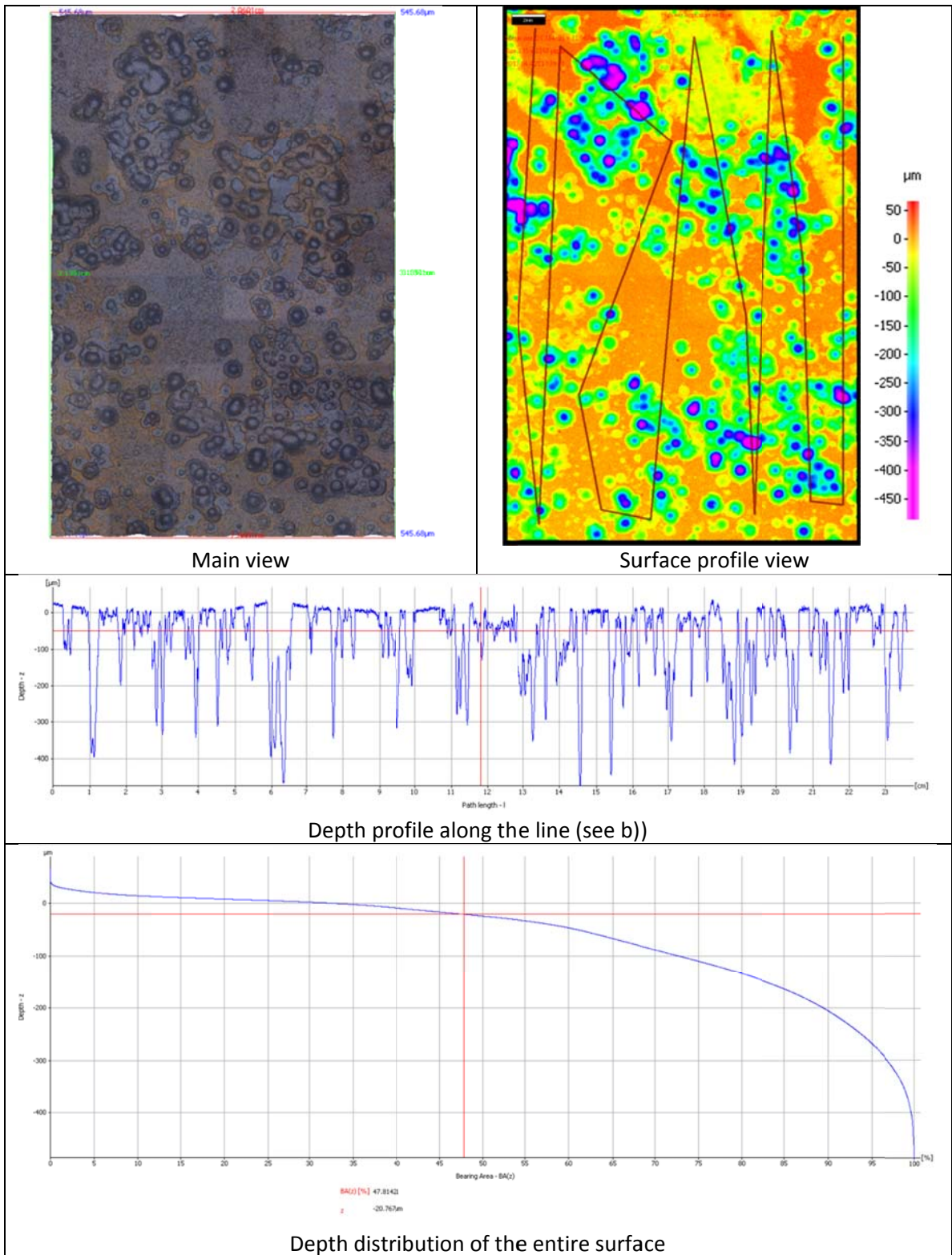


Figure 104: Test #2 – X65 insert – Surface profile analysis  
 Downstream section – High condensation rate: 0.23 ml/m<sup>2</sup>/s

#### 4.4.2.1.2.3 Corrosion rate analysis

As for Test #1, data relevant to the extent of localized corrosion could be extracted from the 3D profile analysis. The main results are displayed in Table 14. The statistical analysis was performed in a systematic manner and the same information was collected.

Table 14 : Test #2 – Localized corrosion rate analysis

Parameter	Unit	Water condensation rate		
		Min 0.11 mL/m <sup>2</sup> /s	Average 0.15 mL/m <sup>2</sup> /s	Max 0.23 mL/m <sup>2</sup> /s
Average localized corrosion rate	mm/year	0.64	0.96	1.13
Max localized corrosion	mm/year	1.72	2.11	2.38
Average feature depth	μm	131.3	195.6	229.4
Max feature depth	μm	350	430	485
Average feature diameter	mm	1.10	1.13	2.26
Arithmetic mean	μm	14.69	20.30	71.34
Standard deviation	μm	24.53	36.98	87.76
Root mean square	μm	28.59	42.183	113.1
Skewness		-5.22	-4.42	-2.14
Kurtosis		41.11	26.57	5.34
Pitting density	cm <sup>-2</sup>	23.9	23.2	43.3
% area affected by localized corrosion	%	29.7	35.7	66.3

The following observations can be made regarding the extent of localized corrosion:

- The influence of the water condensation rate is clear, with increasing feature depth, pitting density, diameter and percentage area affected by localized corrosion at high water condensation rate.
- The trend of skewness and kurtosis factors show once again that pits are isolated under low WCR while they tend to coalesce at higher WCR (Figure 105).

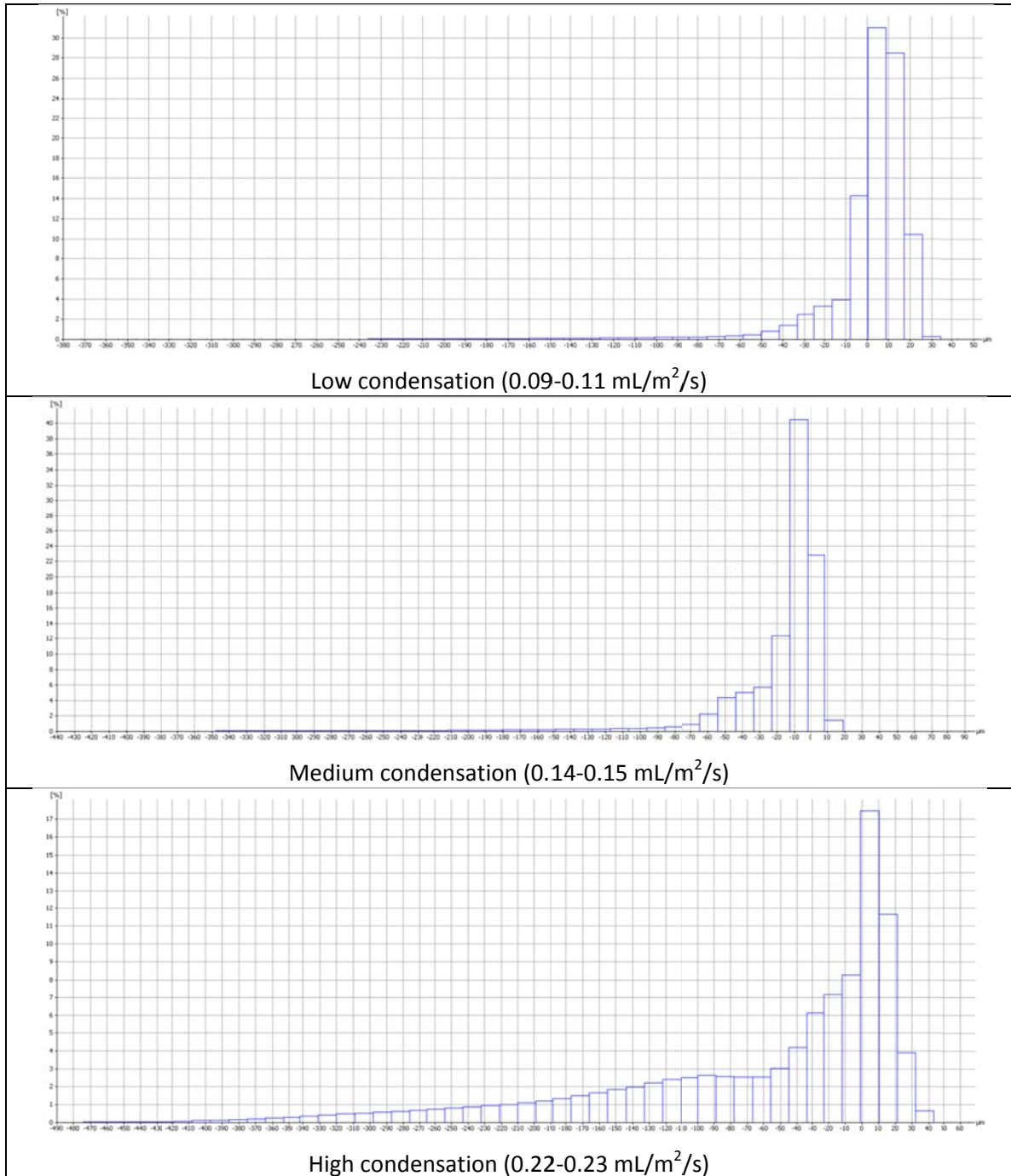


Figure 105: Test #2 - Feature depth distribution over the entire scanned steel surface

Concurrent tests performed with weight loss samples showed a different overall picture: uniform corrosion was experienced on the cooled sample while localized corrosion appeared

only at lower condensation rates (Figure 106). The initiation of localized attack is directly related to the formation of a semi-protective  $\text{FeCO}_3$  layer. With lower steel temperature conditions (due to low gas temperature or/and high WCR), the kinetics of  $\text{FeCO}_3$  precipitation should not favor the formation of such a layer. The  $\text{FeCO}_3$  solubility also increases which renders conditions for super saturation more difficult to achieve. Instead a non-protective iron carbide layer could be expected to form, leading to mostly uniform corrosion. Due to the lower temperature, the kinetics of corrosion reactions should lead to a steady (uniform) but low rate of corrosion. On the other hand, if the WCR is low enough,  $\text{FeCO}_3$  can form at the metal surface even at a low temperature and could lead to localized attack. The results obtained with the weight loss samples corroborate this view: high uniform corrosion on the cooled samples, and localized corrosion on the thermally insulated samples.

This is, however, not corroborated by the “steel insert” experimental results which showed localized corrosion all along the steel surface, with higher penetration rates encountered at higher WCRs. Although the conditions are supposed to be similar on both test sections, it is possible that the cooling conditions experienced by the samples could have been higher than the one applied on the steel insert, leading to a lower steel surface temperature. The “sample” test section is not equipped with embedded thermistors, making accurate measurements of WCR impossible.

At the “medium” WCR ( $0.15 \text{ mL/m}^2/\text{s}$ ), the localized and uniform corrosion rates are quite similar. Under these conditions, it is already not accurate to qualify the corrosion attack as localized, as the entire steel surface corrodes at rates varying within a factor of 2 or 3. At higher WCR ( $0.23 \text{ mL/m}^2/\text{s}$ ), the corrosion attack is clearly uniform.

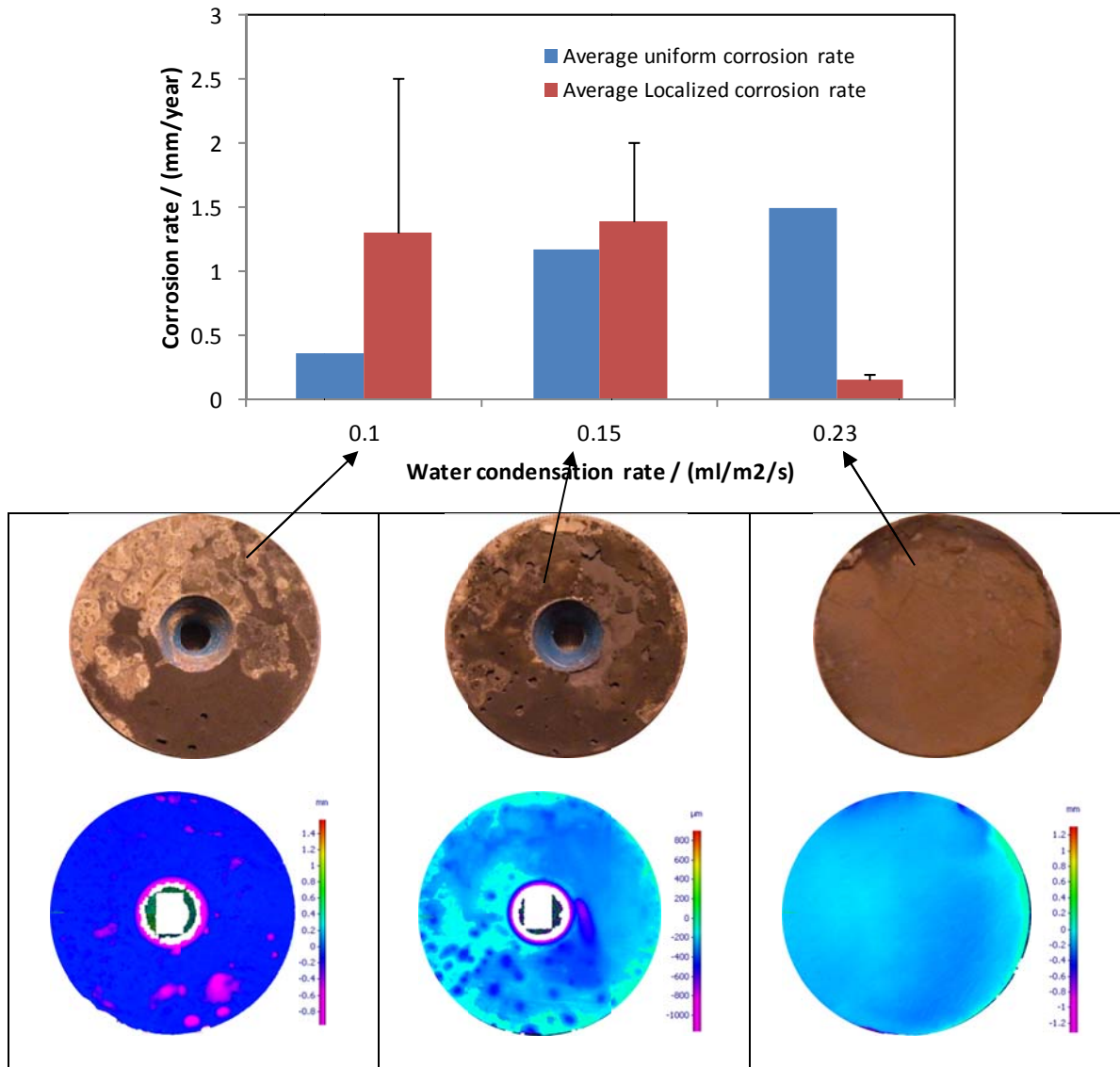


Figure 106: Test #2 - X65 Weight loss sample  
Influence of the condensation rate on the localized and average corrosion rate and pictures of the samples before and after the removal of the corrosion product layer

#### 4.4.2.1.3 TEST #3 - $T_{gas}=25^{\circ}C$

A third experiment was conducted at an even lower temperature (25°C). The expected result was to find mostly uniform corrosion at the high range of WCRs.

##### 4.4.2.1.3.1 Test conditions

The test matrix for the experiments is shown below:

Table 15: Test #3 - Test conditions

Parameter	Value / range
Steel type	X65
Gas temperature	25°C
Total pressure	2.7 bars
pCO <sub>2</sub>	2.7 bars
Free HAc concentration	0 ppm
Gas velocity	3.1 m/s
pH in bulk liquid phase	4 - 4.62
Section# 1: Low condensation rate (upstream section)	0.038 ml/m <sup>2</sup> /s T <sub>wall</sub> : 22.3 °C
Section# 2: Medium condensation rate (middle section)	0.059 ml/m <sup>2</sup> /s T <sub>wall</sub> : 20.7 °C
Section# 3: High condensation rate (Cooled section)	0.101 ml/m <sup>2</sup> /s T <sub>wall</sub> : 17 °C
Test duration	3 months

Instead of regular tap water, refrigerated glycol (set at 5°C) was used a coolant and circulated through the test section cooling coils in order to ensure that the maximum WCR be reached (Figure 107).



Figure 107: Test #3 - MEG Cooling system

#### 4.4.2.1.3.2 Surface analysis

##### 4.4.2.1.3.2.1 Overview of the corrosion product characteristics

Preliminary observation of the state of the insert immediately after the end of the test (before removal of the corrosion product layer) shows that the corrosion product uniformly covers the surface of the steel exposed to low condensation rate (Figure 108). However, a very loose and poorly adherent layer covers the section of the insert exposed to higher WCR ( $0.101 \text{ mL/m}^2/\text{s}$ ). The layer appeared to have formed large flakes, and most of it actually fell off the steel surface as the slab was being prepared for post-processing and analysis. The “bare” steel surface underneath appeared to be uniformly corroded. It is also important to note that, for this experiment, no trace of iron oxide could be seen on the metal surface, which is mostly due to an improvement in the experimental procedures.

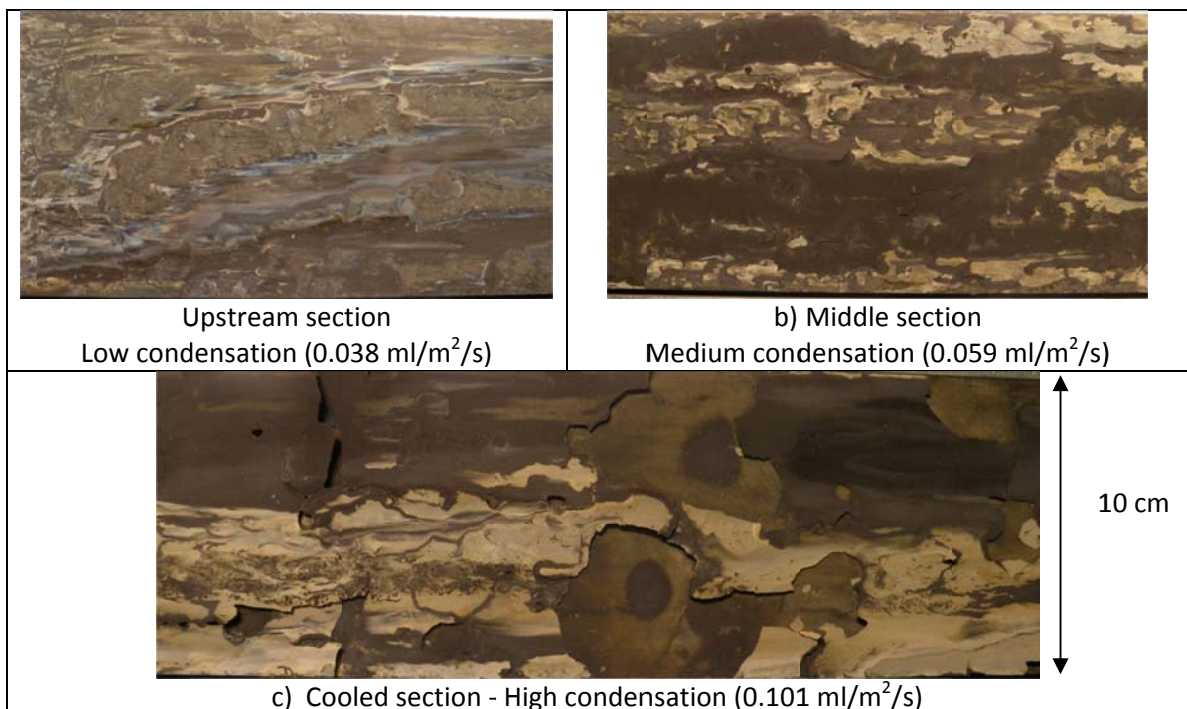


Figure 108: Test #3 - Steel surface before removal of the corrosion product layer  
The flow direction is from left to right

#### 4.4.2.1.3.2.2 SEM/EDS analysis of the corrosion product

As expected, the SEM/EDX analysis identified the corrosion product as  $\text{FeCO}_3$  (Figure 109). As shown in the Pourbaix diagram (Figure 110), and by validation via X-ray diffraction characterization of observed corrosion products [98], no other corrosion product layer could be expected in the range of pH and potential encountered in the study. Iron carbide ( $\text{Fe}_3\text{C}$ ) was observed on some areas of the steel insert but this type of layer is more an indicator of high corrosion rates and exists under any experimental conditions.

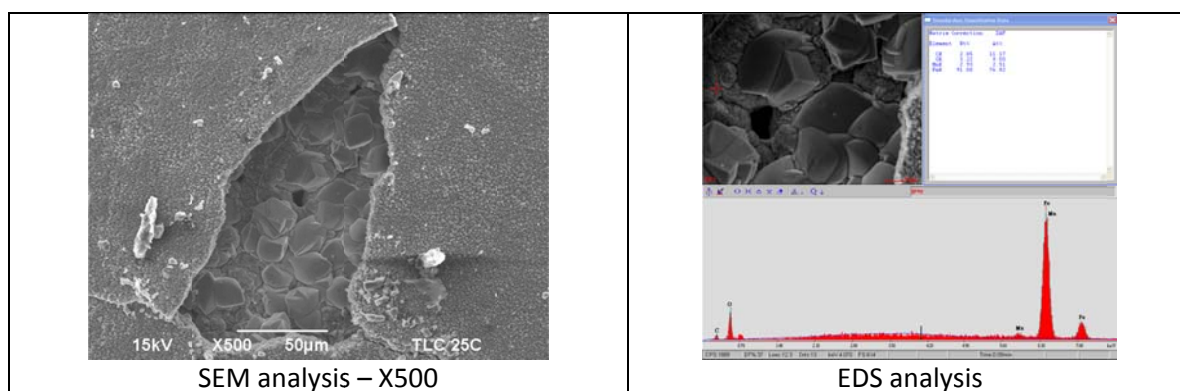


Figure 109: Test #3 – SEM/EDX analysis  
Upstream section - Low condensation ( $0.038 \text{ ml/m}^2/\text{s}$ )

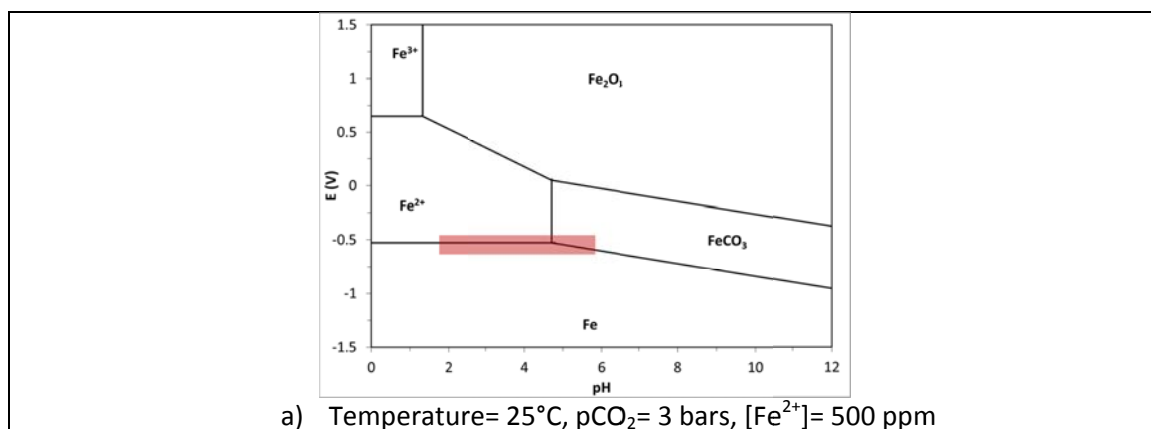


Figure 110: Pourbaix Diagram for  $\text{Fe}/\text{H}_2\text{O}/\text{CO}_2$  system  
Potential vs SHE - Area of interest in highlighted in red

#### 4.4.2.1.3.2.3 3D Surface profile analysis of bare steel

Analysis of the steel surface after the removal of the corrosion product layer showed widespread localized corrosion of the middle section, exposed to a condensation rate of 0.06 mL/m<sup>2</sup>/s. The upstream area, exposed to the lowest water condensation rate, experienced limited localized corrosion. On the other hand -- and contrary to the previous “steel insert” experiments -- no sign of localized corrosion could be found on the area of high WCR.

Large areas of the X65 slab were scanned using a 3D surface profilometer, and data on pit depth were collected (Figure 112, Figure 113 and Figure 114). As found earlier, the extent of localized corrosion clearly increased with the WCR, but only up to a certain limit (between 0.06 and 0.1 mL/m<sup>2</sup>/s in this case). At the highest WCR tested, the steel surface was evenly corroded and no trace of localized corrosion could be found.

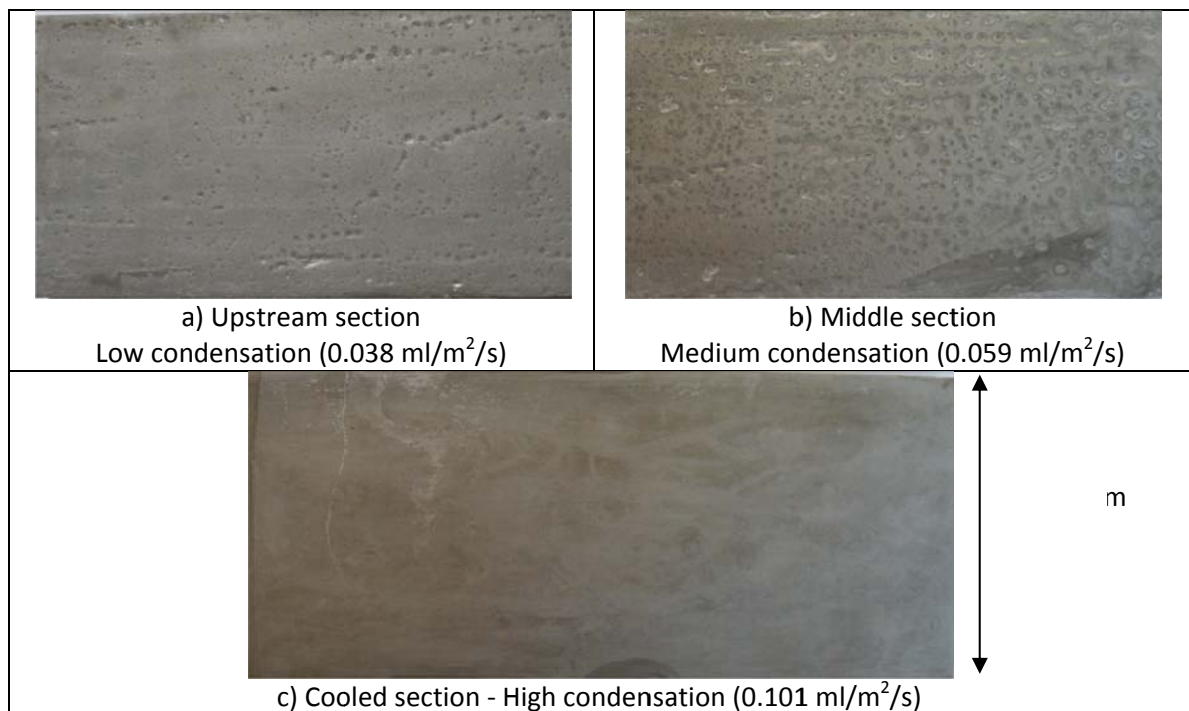


Figure 111: Test #3 - Steel surface before removal of the corrosion product layer  
Upstream section - Low condensation (0.038 ml/m<sup>2</sup>/s)

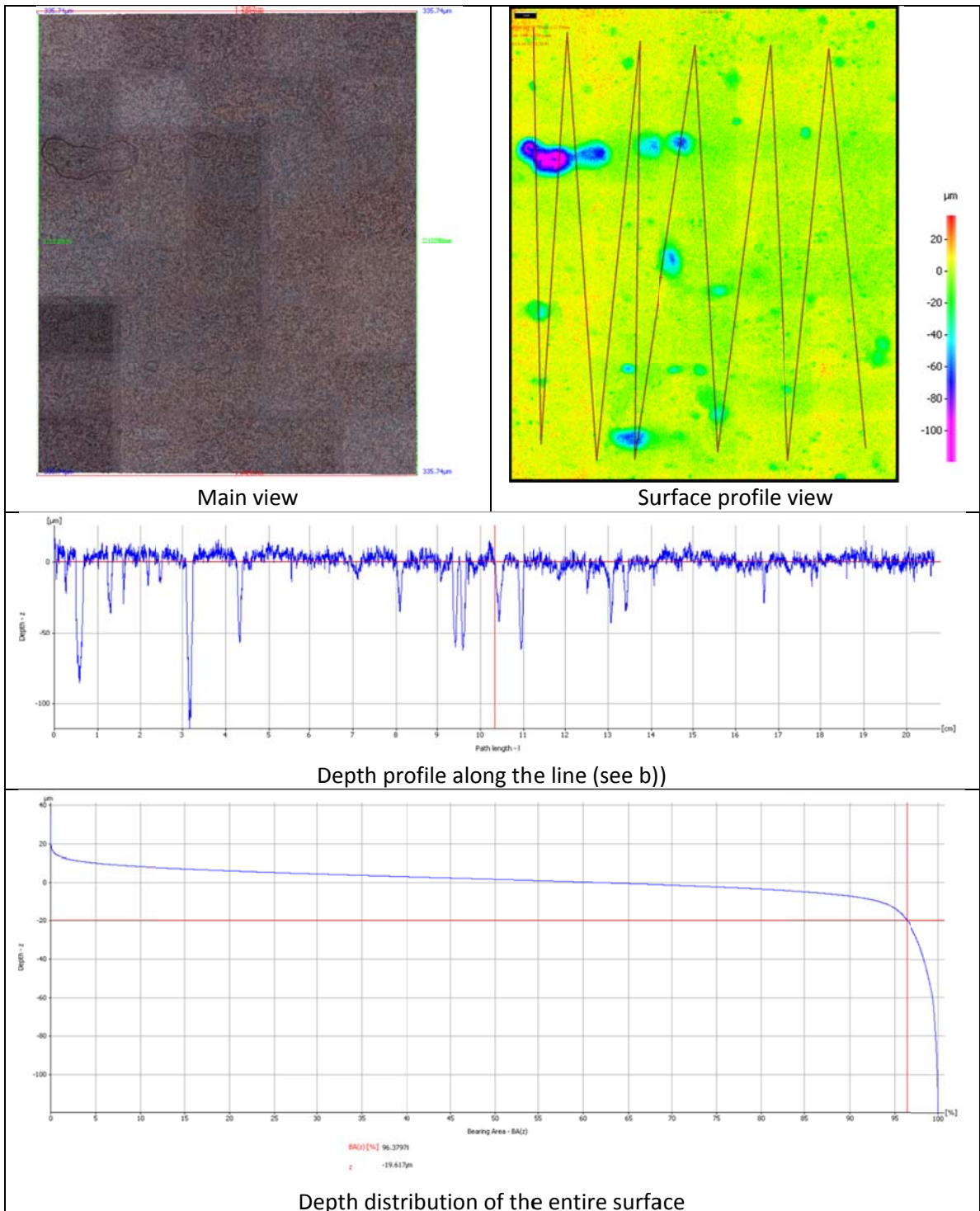


Figure 112: Test #3 – X65 insert – Surface profile analysis  
Upstream section - Low condensation (0.038 ml/m<sup>2</sup>/s)

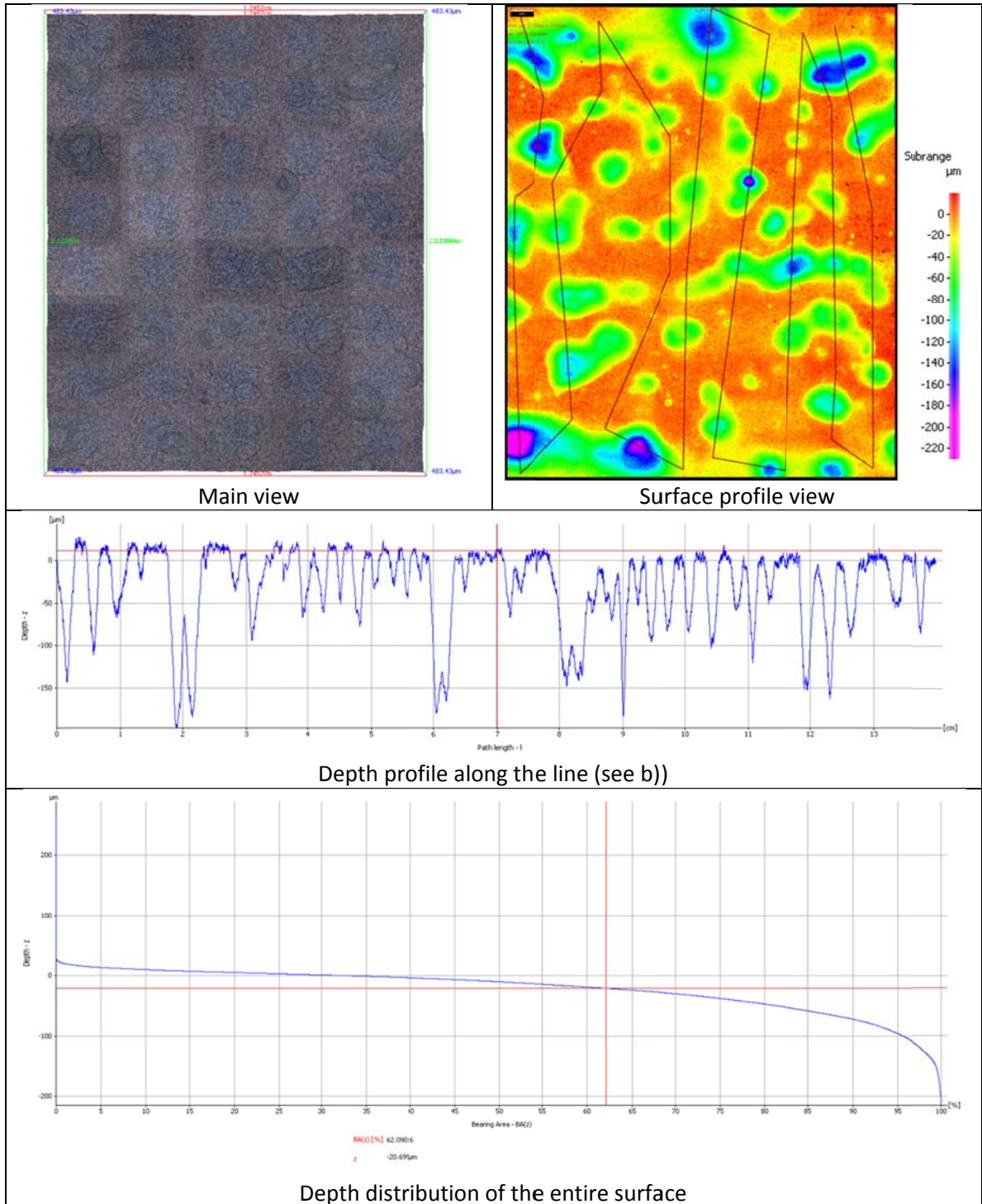


Figure 113: Test #3 – X65 insert – Surface profile analysis  
 Middle section - Medium condensation (0.059 ml/m<sup>2</sup>/s)

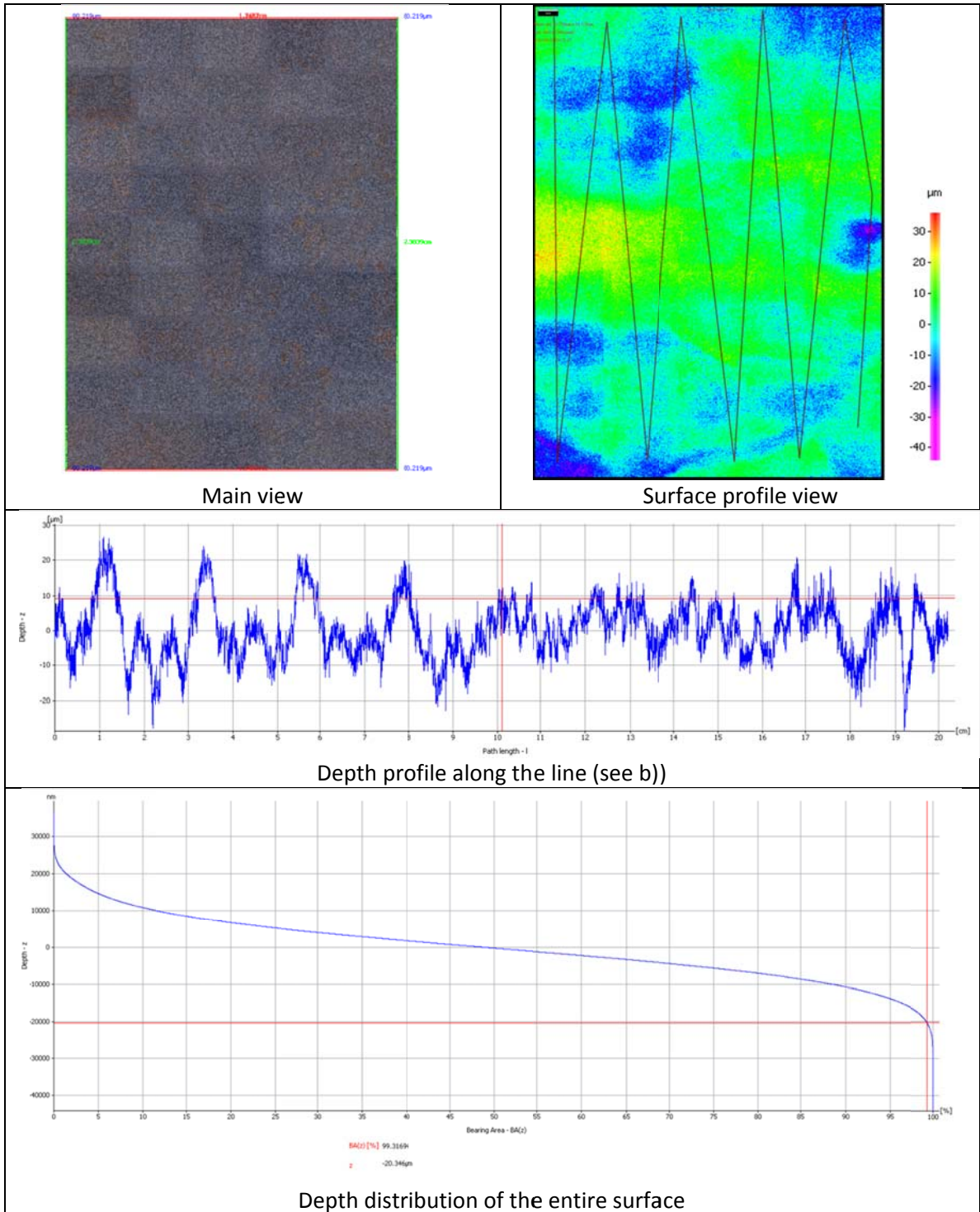


Figure 114: Test #3 – X65 insert – Surface profile analysis  
 Cooled section - High condensation (0.101 ml/m<sup>2</sup>/s)

#### 4.4.2.1.3.3 Corrosion rate analysis

The data collected during the profile analysis of the steel inserts are collected and displayed in Table 16, together with several statistical variables.

Table 16 : Test #3 – Localized corrosion rate analysis

Parameter	Unit	Water condensation rate (mL/m <sup>2</sup> /s)		
		Min 0.038 mL/m <sup>2</sup> /s	Average 0.059 mL/m <sup>2</sup> /s	Max 0.101 mL/m <sup>2</sup> /s
Average localized corrosion rate	mm/year	0.18	0.51	0.11
Max localized corrosion	mm/year	0.47	1.13	0.15
Average feature depth	μm	46.2	103.2	23.3
Max feature depth	μm	120	230	30
Average feature diameter	mm	1.28	2.52	1.74
Arithmetic mean	μm	6.04	29.16	6.65
Standard deviation	μm	8.85	34.42	5.21
Root mean square	μm	10.71	45.11	8.45
Skewness		-4.17	-2.17	0.13
Kurtosis		29.57	5.75	3.11
Pitting density	cm <sup>-2</sup>	8.2	27.3	0.2
% area affected by localized corrosion	%	25.4	64.2	100

The following observations can be made regarding the extent of localized corrosion:

- It is clear that the zone affected by the highest water condensation rate produced little to no localized corrosion. The rest of the X65 insert did suffer from localized corrosion, especially the middle section: extensive pitting was measured, but the pitting rate was relatively low compared to previous tests.
- With WCR values below 0.06 mL/m<sup>2</sup>/s, the trend of skewness and kurtosis factor is coherent with the presence of isolated pits, which tend to coalesce at higher WCR

(Figure 115 a) and b)). However, if the WCR is above a certain threshold value (here between 0.06 and 0.1 mL/m<sup>2</sup>/s), the skewness approaches zero and a positive value of kurtosis factor is calculated -- all signs that the steel surface is evenly corroded and that no localized corrosion is present.

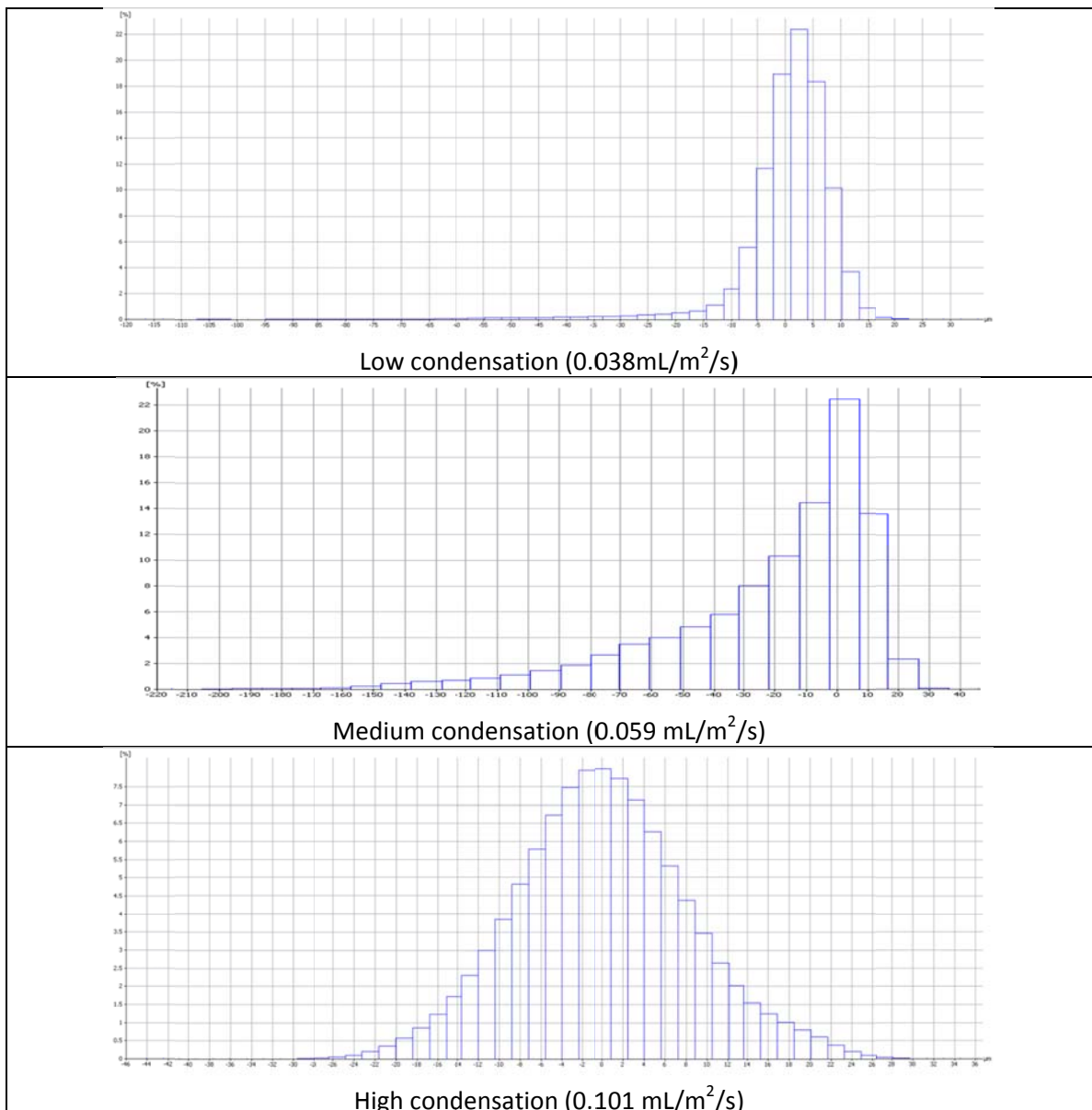


Figure 115: Test #3 - Feature depth distribution over the entire scanned steel surface

The 3D surface profilometer data are plotted with the condensation rate in Figure 116. Localized corrosion is only sustainable in the presence of a semi-protective corrosion product layer (here  $\text{FeCO}_3$ ), provided that this layer is adherent to the metal surface and can provide protection on some part of the steel surface. At high WCR ( $> 0.1 \text{ mL/m}^2/\text{s}$ ), the corrosion product layer does not adhere to the metal surface and the corrosion can consequently only be uniform in nature.

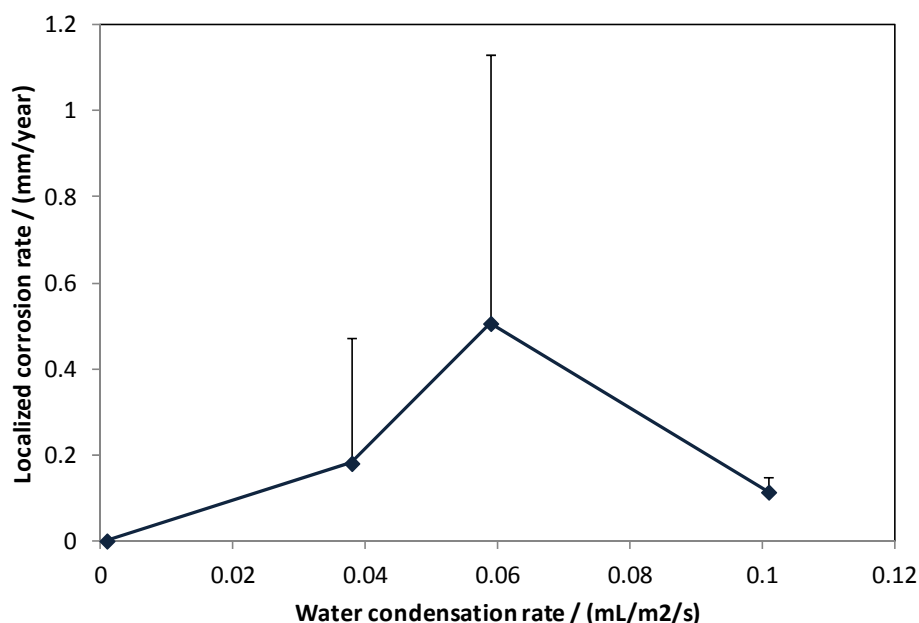


Figure 116: Test #3 - X65 insert - Influence of the condensation rate on the pit/mesa depth

Figure 117 presents the results of the corrosion analysis performed on weight loss samples present in the flow loop under identical conditions to those for the steel insert. The average localized and uniform corrosion rates computed from the surface analysis are shown in Figure 117. This time, the analysis of the weight loss samples and the steel insert yields the same conclusions:

- Where the corrosion product layer adheres to the metal surface (upstream and middle sections), the presence of localized corrosion is evident.
- Where the layer is clearly detached, the corrosion is uniform.

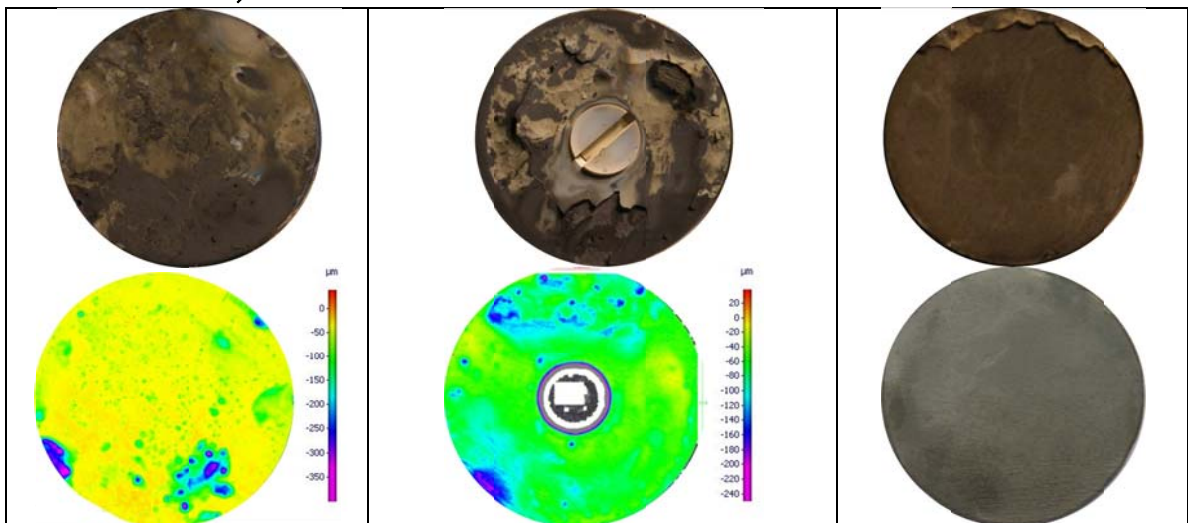
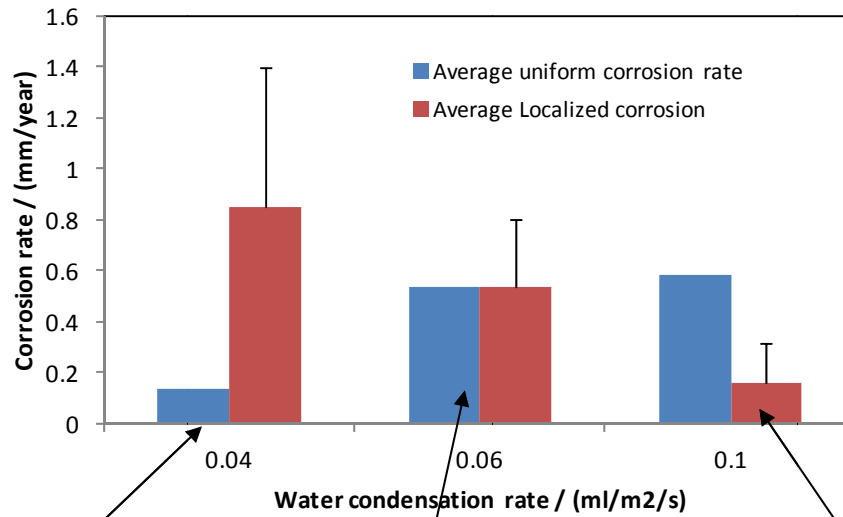


Figure 117: Test #3 - X65 Weight loss sample  
Influence of the condensation rate on the localized and average corrosion rate and pictures of the samples with before the removal of the corrosion product

#### 4.4.2.2 Test #4 - Influence of the presence of acetic acid

A final experiment was performed in order to investigate the effect of a high content of organic acid on TLC, under high gas temperature and high WCR conditions.

##### 4.4.2.2.1.1 Test conditions

The test conditions are presented below, the main difference from the baseline Test #1 being the presence of 1000 ppm of free acetic acid in the main liquid tank. As for the baseline test, the test section was divided into three zones exposed to different cooling rates leading to different WCRs.

Table 17: Test #4 - Test conditions

Parameter	Value / range
Steel type	C1018(III)
Gas temperature	59°C
Total pressure	3bars
pCO <sub>2</sub>	2.7 bars
Free HAc concentration	1000 ppm
Gas velocity	2-3 m/s
Low condensation rate (upstream section)	0.2 mL/m <sup>2</sup> /s - T <sub>wall</sub> :52.7°C
Medium condensation rate (middle section)	0.4 mL/m <sup>2</sup> /s - T <sub>wall</sub> :47.1°C
High condensation rate (Downstream section)	0.7 mL/m <sup>2</sup> /s - T <sub>wall</sub> :35.9°C
Exposure time	93 days

##### 4.4.2.2.1.2 Surface analysis

###### 4.4.2.2.1.2.1 Overview of the corrosion product layer characteristics

Photographs of the C1018(III) insert taken immediately after the end of test are shown in Figure 118. A thin layer of iron oxide covers most of the steel surface. The oxygen level in the loop was measured on several occasions during the test and was always below 10 ppb; it is

believed that the iron oxide (most likely ferric oxide  $\text{Fe}_2\text{O}_3$ ) was formed during the process of removal of the flat slab, which can take several minutes. The same observation was made during the previous tests but to a lower extent. The oxide layer was, however, very thin and superficial; it would flake off very easily, leaving behind a gray layer, expected to be iron carbonate.

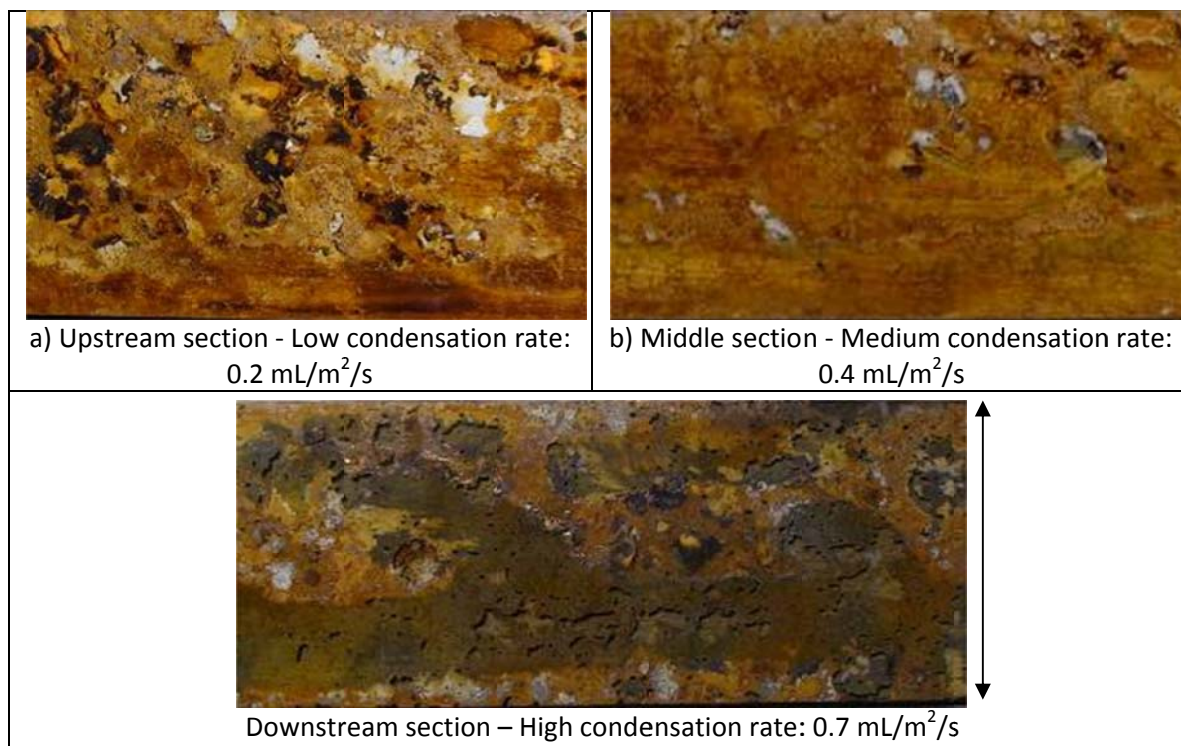


Figure 118: Test #4 - C1018(III) insert - Steel surface before removal of the corrosion product layer -The flow direction is from left to right

#### 4.4.2.2.1.2.2 SEM/EDS analysis of the corrosion product

The SEM/EDX analysis of the corrosion product film was performed on the different sections of the insert (Figure 119).

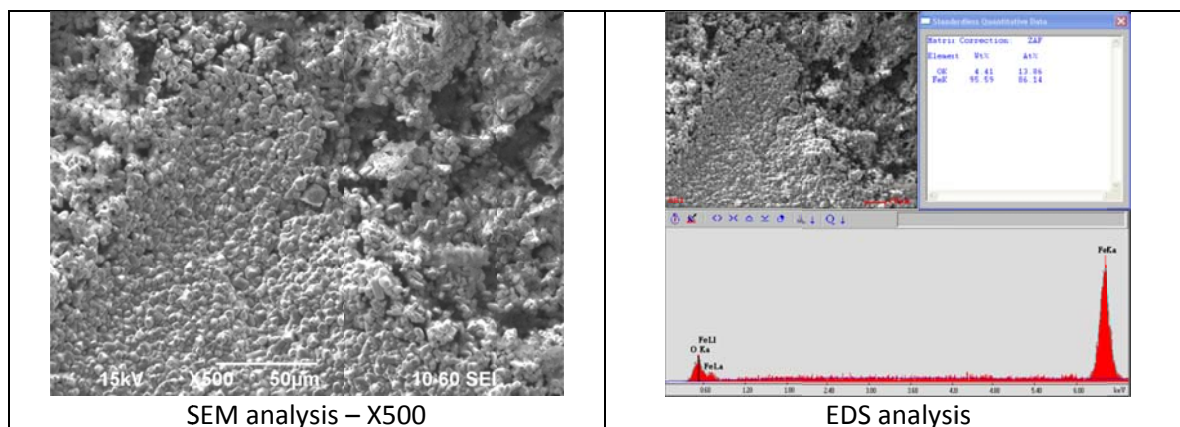


Figure 119: Test #4 – SEM/EDX analysis  
Middle section – Medium condensation ( $0.4 \text{ ml/m}^2/\text{s}$ )

There was no major variation in the film characteristics between the sections exposed to different condensation rates. The corrosion product layer is believed to be a mix of iron oxide (most likely ferric oxide  $\text{Fe}_2\text{O}_3$ ), iron carbonate ( $\text{FeCO}_3$ ) and iron carbide ( $\text{Fe}_3\text{C}$ ).

#### 4.4.2.2.1.2.3 3D Surface profile analysis of bare steel

The surface profile analysis was performed on the steel samples after the removal of the layer (Figure 120). The extent of the corrosion on the downstream section exposed to the highest condensation rate was impressive. The upstream section seemed much less affected, but in all cases pits were measured at similar maximum depths (800 to 1200  $\mu\text{m}$ ). Pits became more numerous as the condensation rate increased and tended to agglomerate together and constitute mesa attack. Large areas of the C1018(III) slab were scanned using a 3D surface profilometer, and data on pit depth were collected (Figure 121, Figure 122 and Figure 123).

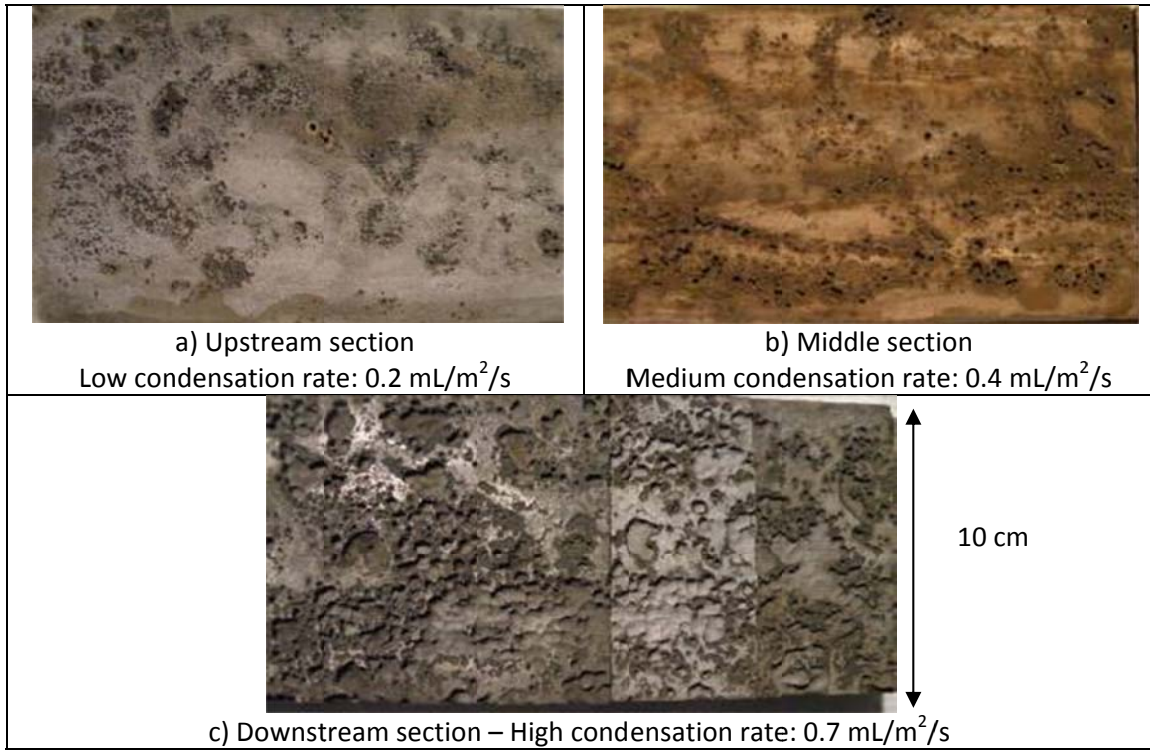


Figure 120: Test #4 - C1018(III) insert - Steel surface before removal of the corrosion product layer - The flow direction is from left to right

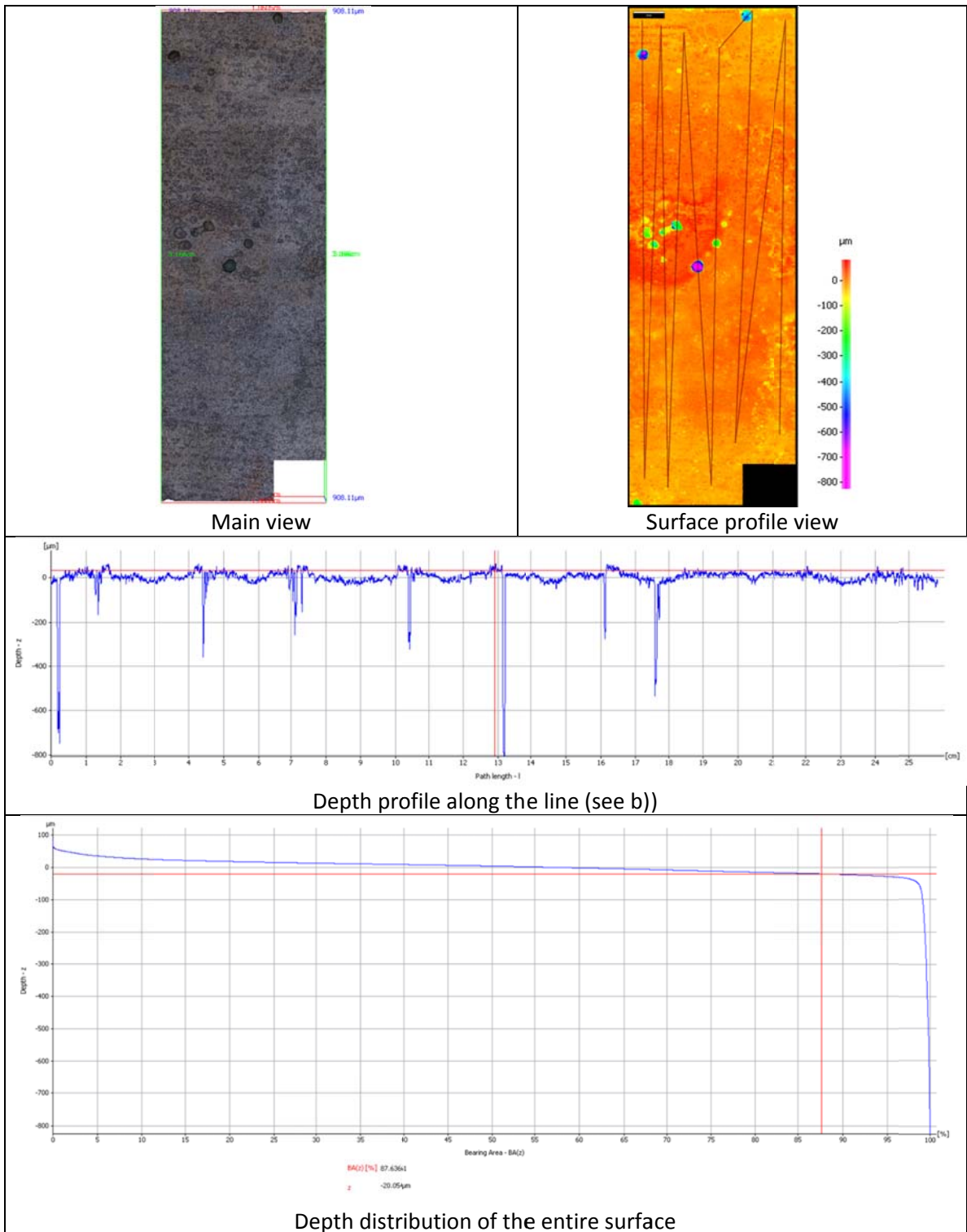


Figure 121: Test #4 – C1018(III) insert – Surface profile analysis  
Upstream section - Low condensation rate: 0.2 mL/m<sup>2</sup>/s

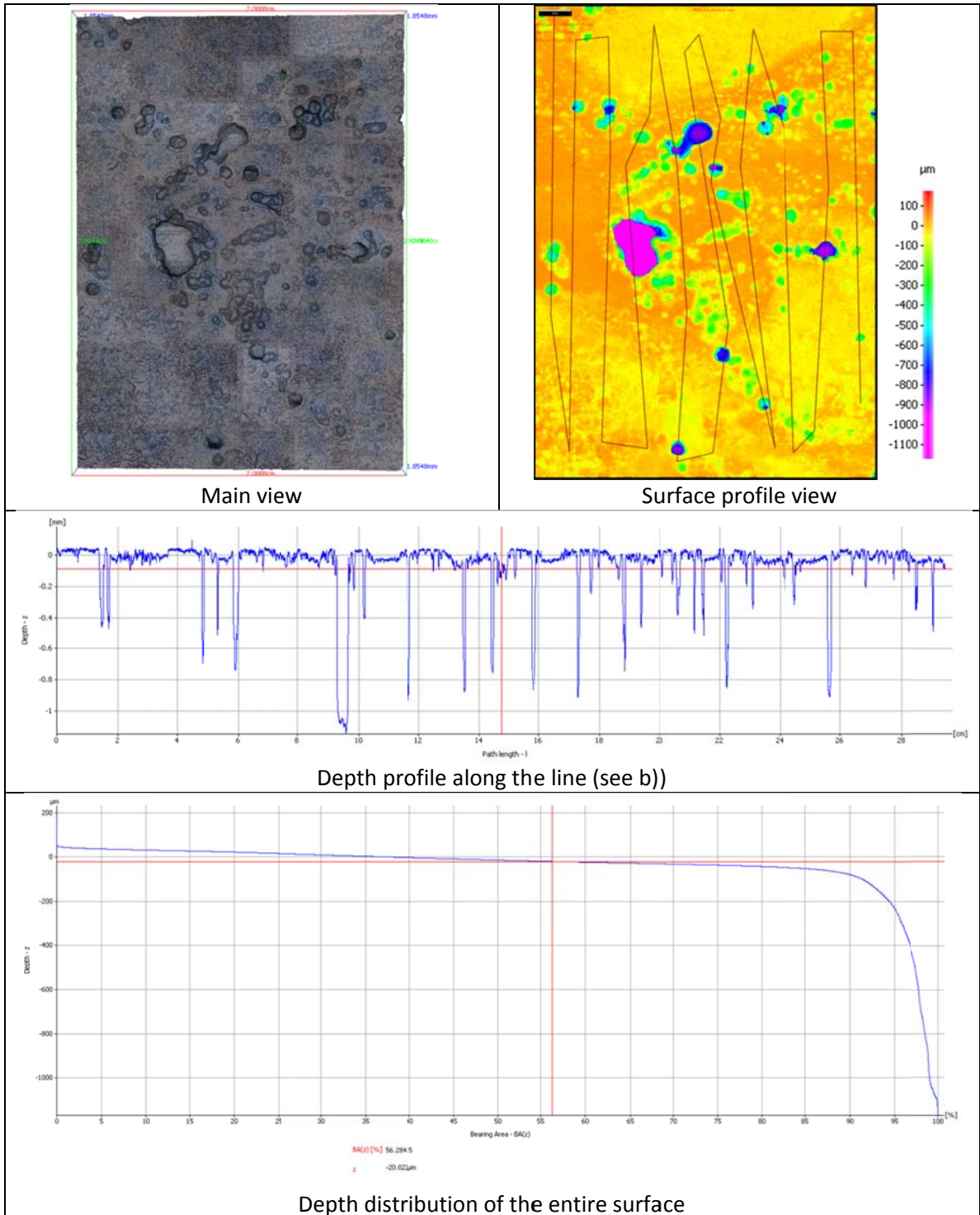


Figure 122: Test #4 – C1018(III) insert – Surface profile analysis  
Middle section - Medium condensation rate: 0.4 mL/m<sup>2</sup>/s

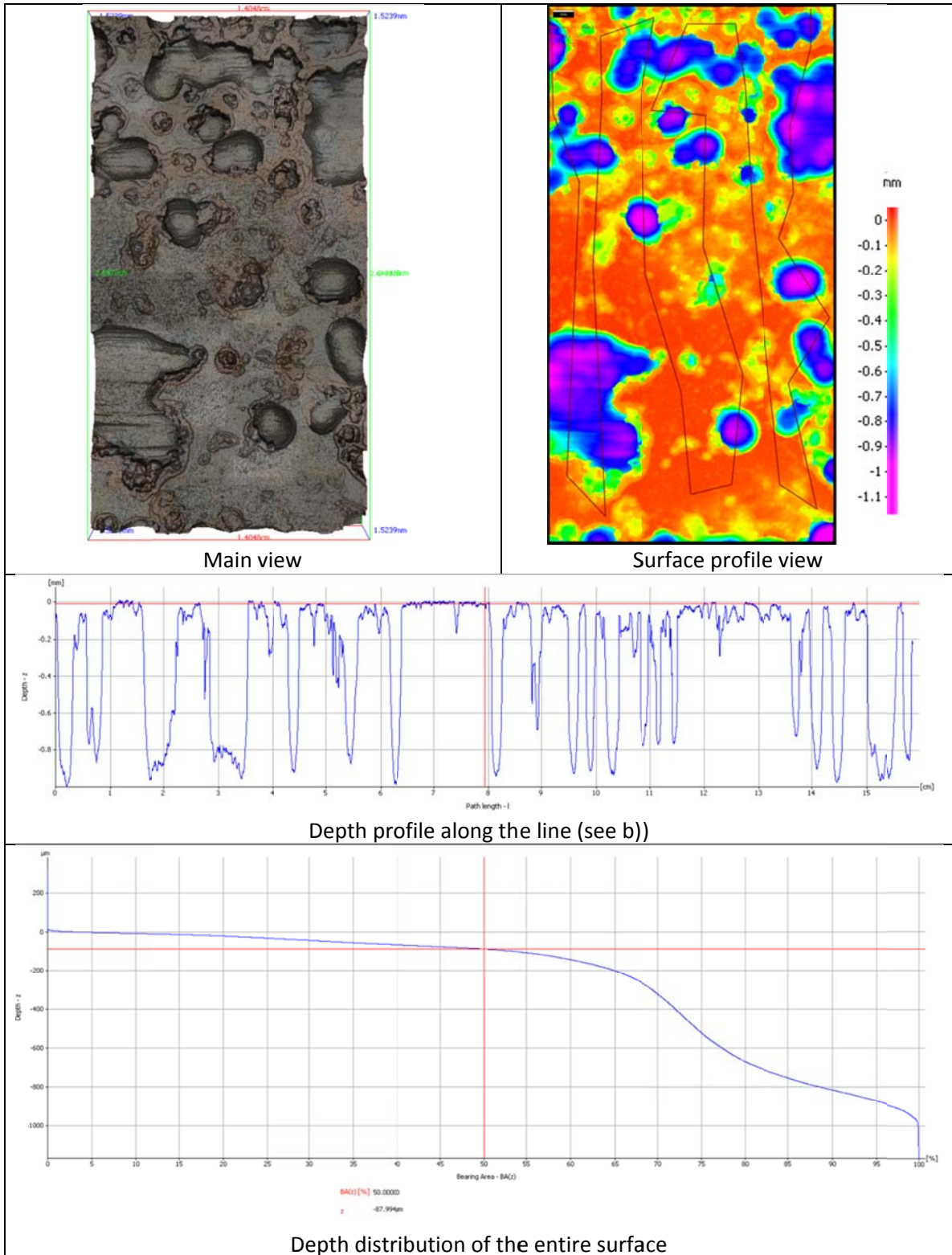


Figure 123: Test #4 – C1018(III) insert – Surface profile analysis  
 Downstream section – High condensation rate: 0.7 mL/m<sup>2</sup>/s

#### 4.4.2.2.1.3 Corrosion rate analysis

The 3D surface analysis data are displayed in Table 18. They include, as previously, statistical parameters qualifying the features relating to depth distribution.

Table 18 : Test #4 – Localized corrosion rate analysis

Parameter	Unit	Water condensation rate (mL/m <sup>2</sup> /s)		
		Min 0.2 mL/m <sup>2</sup> /s	Average 0.4 mL/m <sup>2</sup> /s	Max 0.7 mL/m <sup>2</sup> /s
Average localized corrosion rate	mm/year	1.56	2.09	2.99
Max localized corrosion	mm/year	3.24	4.55	4.58
Average feature depth	μm	396.8	532.8	762.2
Max feature depth	μm	825	1160	1167
Average feature diameter	mm	0.64	1.46	3.18
Arithmetic mean	μm	18.54	59.92	264.41
Standard deviation	μm	37.26	141.56	313.86
Root mean square	μm	41.62	153.72	410.39
Skewness		-10.17	-5.14	-1.85
Kurtosis		148.62	30.53	3.61
Pitting density	cm <sup>-2</sup>	4.90	12.36	16.12
% area affected by localized corrosion	%	6.15	20.86	72.13

The following observations can be made regarding the extent of localized corrosion:

- As in Test# 1, the influence of the WCR is clear. Feature depth, pitting density, diameter and percentage of the area affected by localized corrosion increase with WCR.
- At high WCR, corrosion features are large and form mesa-type attack (large pits with flat bottoms). The metal surface is so extensively corroded than the corrosion attack could be labeled uniform.

- The trend of skewness and kurtosis factor show that pits are isolated under low WCR while they tend to coalesce at higher WCR (Figure 124).

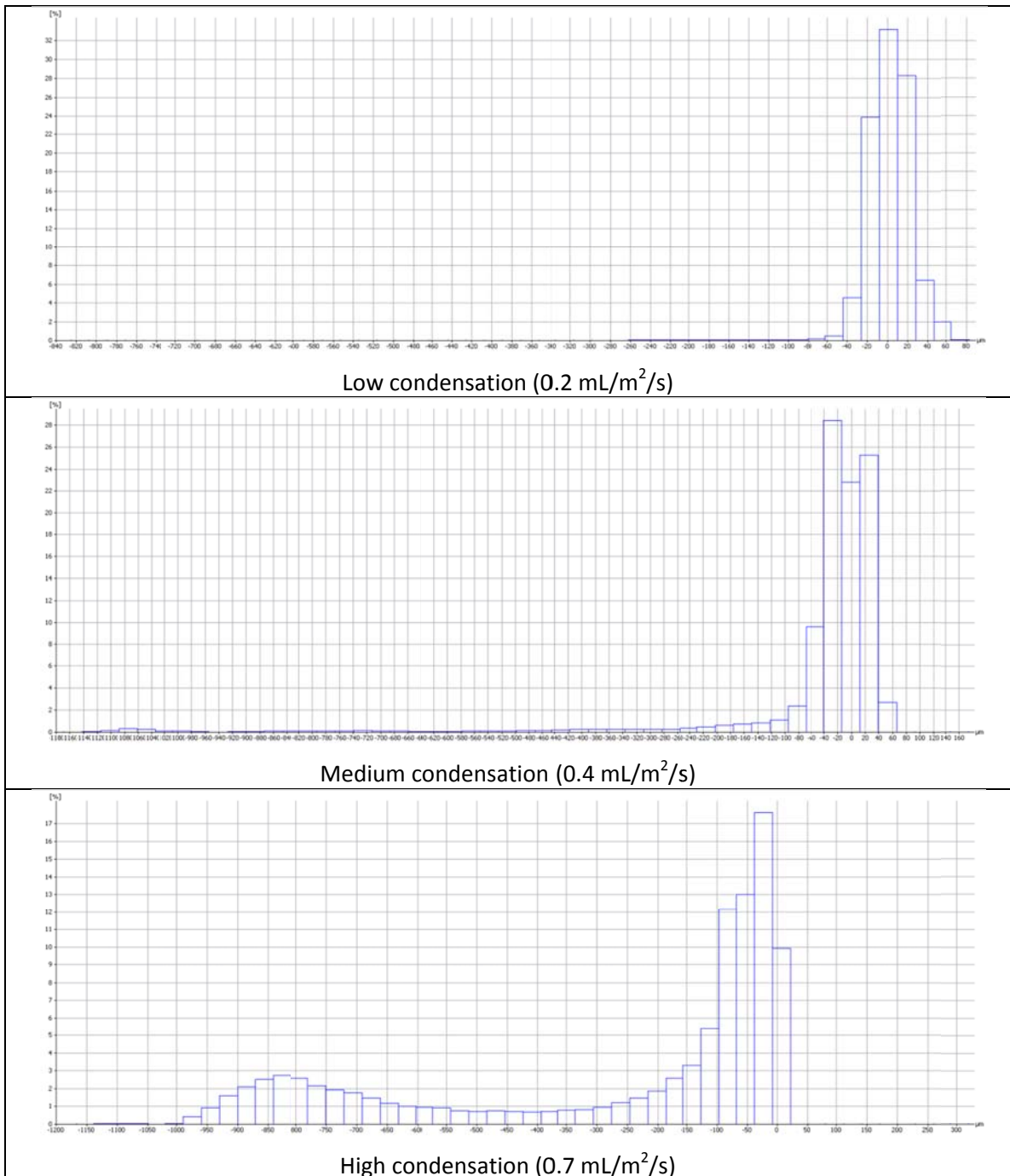


Figure 124: Test #4 - Feature depth distribution over the entire scanned steel surface

Figure 125 shows the comparison between the pit depths results obtained for the short term experiments performed with weight loss samples in similar conditions. As for Test #1, the localized corrosion rates (or more precisely the steel penetration rates) are about four times lower after 99 days of exposure as compared to 21 days of exposure. The presence of acetic acid does not modify the overall trend although the feature depth is significantly higher, as shown in the next section.

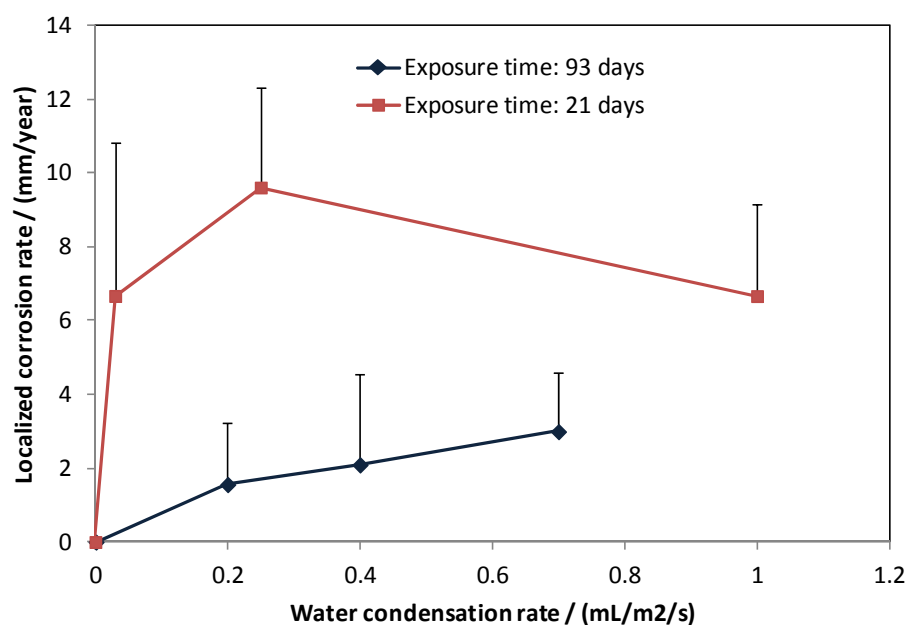


Figure 125: Test #4 - Comparison between short and long term experiments  
Influence of the condensation rate on the pit/mesa depth

#### 4.4.3 Summary

This section presents a summary of the experimental results obtained with the “flat slab” test section as well as some main comments of the effect of the WCR, the gas temperature and the presence of acetic acid on the extent of localized corrosion at the top of the line.

- **Proof of concept**

The “flat slab” test section, equipped with a steel insert, was successful in simulating TLC without obvious edge effects and in capturing the effect of the condensation rate. Localized corrosion could be very clearly observed on the steel surface and correlated to the WCR. On the cooled section, pits still seemed to be growing in depth with time and also forming large clusters with mesa attack characteristics. These observations are in agreement with field observation of TLC.

- **Influence of the presence of acetic acid**

The presence of 1000 ppm of undissociated acetic acid did not completely change the picture as compared with the baseline test (Figure 126).

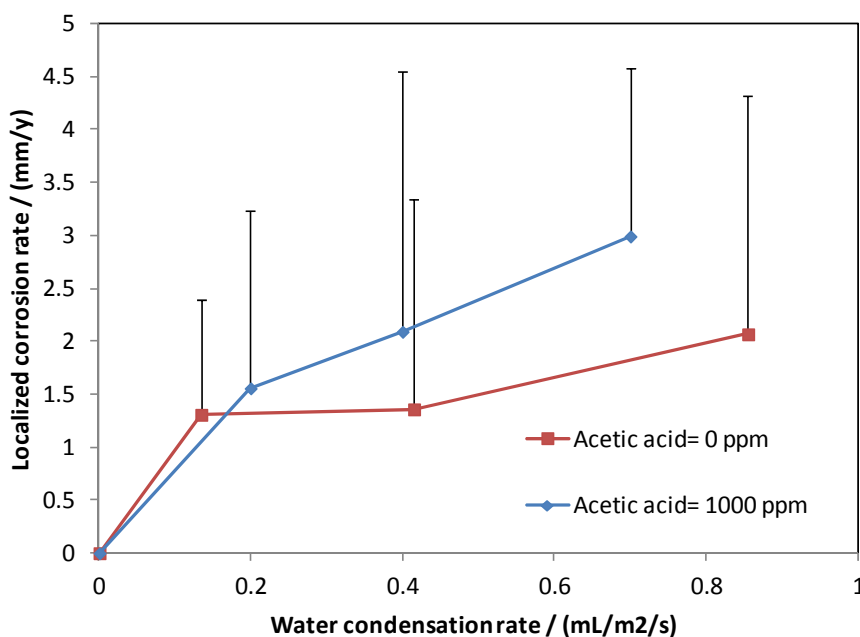


Figure 126: Influence of the acetic acid concentration and condensation rate

However, the extent of the corrosion attack was more severe due to the presence of the acetic acid. This is expected since the presence of an additional acid in solution decreases the pH

of the condensed water, acts as a buffer (with related acetate) with regard to hydrogen ions and increases the solubility of  $\text{FeCO}_3$ . Average and maximum pits depths are also consequently higher in the presence of organic acid.

Statistical parameters are consistent with a wide variation in corrosion feature depth, especially at high WCR (Figure 127 b)) and the presence of deep but isolated pits at lower WCR ((Figure 127 f)). The main effect of the presence of acetic acid is seen at high WCR on the average feature diameter and the percentage area of the steel surface affected by localized corrosion ((Figure 127 c) and e)). Since the solution is more aggressive, pits seem to cluster more easily and mesa type attack is more wide spread. The decrease in pitting density with acetic acid ((Figure 127 d)) is due to the increase in feature size.

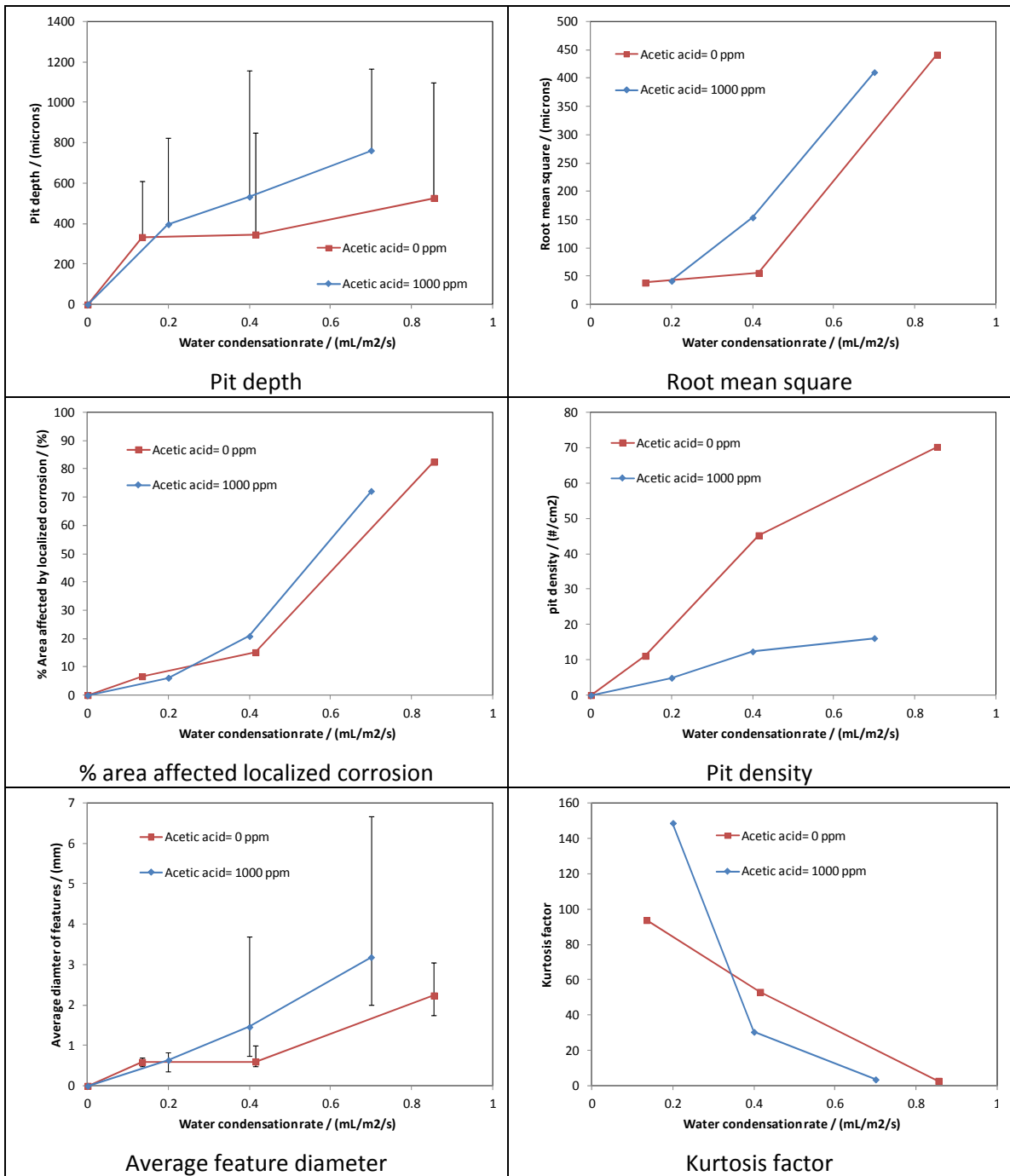


Figure 127: Influence of the acetic acid concentration and the water condensation rate  
 Summary of results

- **Effect of temperature**

This section presents a comparison of the experimental results obtained at different gas temperature (62, 42 and 25°C). The tests were performed without acetic acid.

Figure 128 shows the effect of the water condensation on the localized corrosion rates for several experiments performed at gas temperatures varying from 25 to 62°C. The water condensation rate depends on the gradient of temperature between the outside environment (steel surface) and the bulk gas. Consequently, the effect of water condensation and steel surface or gas temperature cannot be treated separately. The following comments are made:

- Low water condensation rate is often associated with high steel surface temperature (small gradient of temperature) and leads to the formation of an adherent and protective  $\text{FeCO}_3$  layer. At very low gas temperature, kinetics of  $\text{FeCO}_3$  formation are not favored, but super saturation is still easily reached due to the relatively low rate for condensed water renewal.  $\text{FeCO}_3$  can precipitate and pits can initiate but do not seem to progress with time.
- High water condensation rate is often associated with lower steel surface temperature (larger gradient of temperature). Two sub-cases are then identified:
  - If a partially adherent/protective  $\text{FeCO}_3$  layer forms (due to moderate steel temperature), localized corrosion is initiated and can be very severe.
  - If the steel temperature is too low to form an adherent corrosion product layer, localized corrosion cannot be initiated and the corrosion is uniform.
- At lower gas temperature, high WCRs are difficult to achieve, as the water vapor pressure is lower. However, for a fixed WCR, the average and maximum localized corrosion rates are only marginally higher at higher temperature.

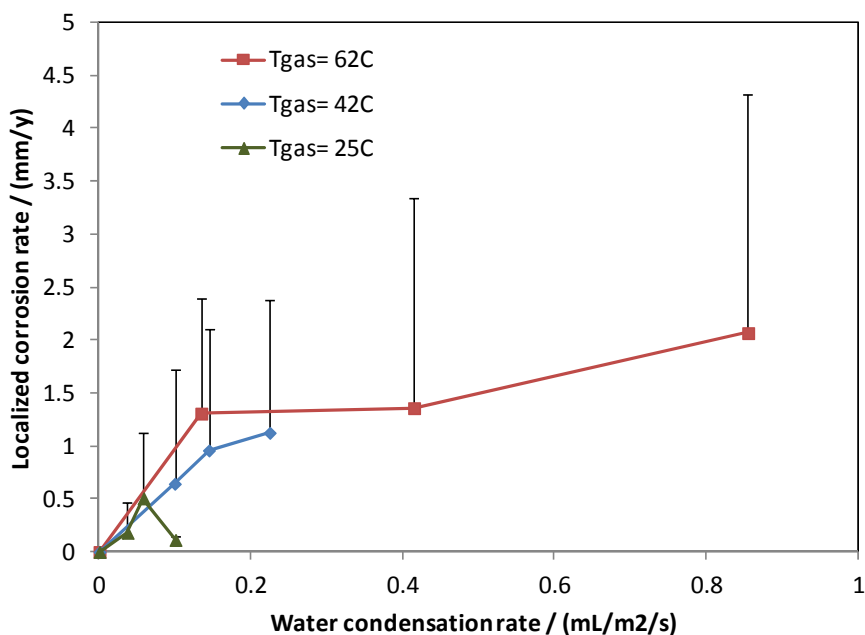


Figure 128: Effect of the gas temperature and the WCR on the localized corrosion rate

The main influence of the gas temperature is seen in the percentage area affected by localized corrosion, which increases very rapidly with WCR at lower temperature (Figure 129 c)). The corrosion attack switches from localized to uniform over a small variation of WCR. This is reflected by an increase in  $\text{FeCO}_3$  solubility at low temperature and the difficulty to form an adherent and protective corrosion product layer.

The maximum feature diameter is similar in all conditions tested but the features will be correspondingly deeper at higher temperature (Figure 129 a) and e)).

There is also a logically greater variation in the feature depth distribution at higher temperature (Figure 129 d)) since the features are often deeper and more isolated than at lower temperature.

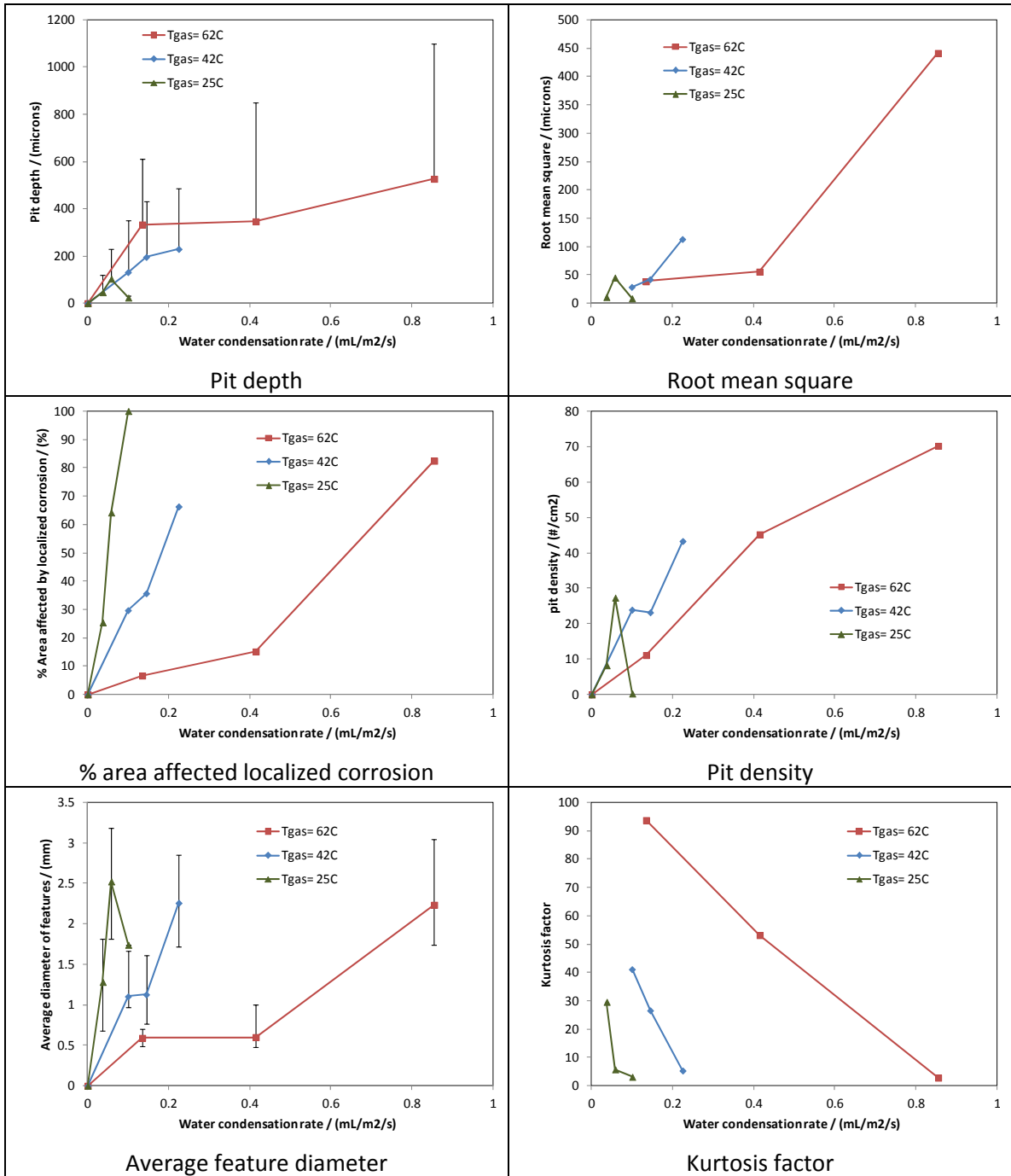


Figure 129: Influence of the gas temperature and the water condensation rate  
 Summary of results

## CHAPTER 5 DIRECT OBSERVATION OF THE CONDENSATION PROCESS

### 5.1 Objective

The objective of this section is to discuss the implementation of various methods and to qualitatively and quantitatively characterize the interaction between condensation pattern and corrosion attack. More specifically, this constitutes an investigation of the interaction between the presence of droplets of condensed water and the extent of the corrosion attack. The hypothesis is that, in dropwise condensation mode, the droplet will always tend to form at specific locations on the steel surface (broken corrosion product film or location with higher surface roughness). These locations would suffer from high condensed water renewal rate and lead, inevitably, to severe localized corrosion.

### 5.2 Indirect indication of the presence of droplets of condensed water

Although the parametric study produced valuable information about the mechanisms of TLC, it was flawed in the sense that the specific design of the test section was not ideally suited to capture the effect of the condensation rate. As shown in Figure 33, edge effects between the flat sample and the curved pipe wall lead to artificial accumulation of water on the sample surface. The influence of the rate of droplet renewal was masked by this effect. However, this situation is very representative of what would happen when a droplet is “trapped” and at the same time constantly renewed with freshly condensed water. Figure 130 shows a few examples of these cases where indications of the presence of droplets are very clear. Areas of the sample surface affected by the accumulation of condensed water show evident signs of severe corrosion:

- $\text{FeCO}_3$  either heavily cracked or no existent, and evidence of  $\text{Fe}_3\text{C}$
- Steel surface under the corrosion layer product layer uniformly corroded at a high rate

This situation is often intensified by the presence of large concentrations of acetic acid or by high WCRs. It is interesting to note that in some cases, localized corrosion was clearly present on the rest of the sample surface, even though there was no sign of significant water accumulation (Figure 77).

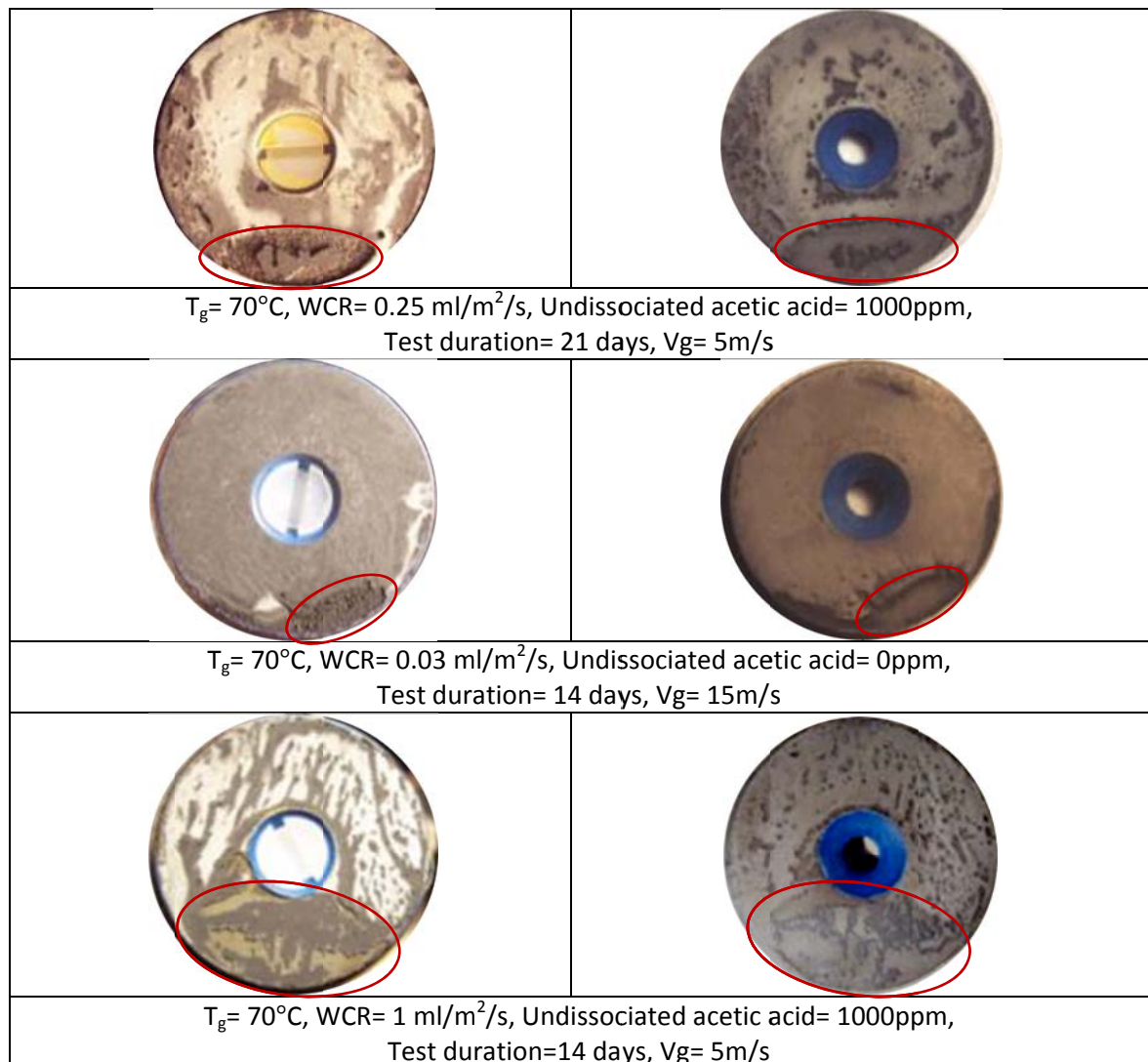


Figure 130: Indication of the presence of droplets or of the artificial accumulation of condensed water (edge effect) at the same location on the surface of a sample  
 Droplets of condensed water can be trapped on the side the flat sample since it cannot be perfectly flushed with the curved pipe surface  
 (X65 samples before (left) and after (right) removal of the FeCO<sub>3</sub> layer)

The pitting rate, however, was always similar to the corrosion rate measured on the areas exposed to high water accumulation. This means that the severity of the corrosion attack, in terms of steel penetration rate, may be more governed by the corrosiveness of the environment rather than the presence *per se* of large condensed water droplets.

### 5.3 Experimental setup

A novel high-pressure, high-temperature video camera was acquired for this study in order to enable direct observation of the condensation and the corrosion processes (Figure 131).



Figure 131: In-situ video camera for live observation of corrosion phenomena

The video camera was especially designed to be mounted on the TLC test section, using one of the bottom ports. Live visual observation of the corresponding top port was consequently rendered possible (Figure 132).

This tool was essential in obtaining direct observation of the condensation process. Under conditions of low gas velocity or low pressure, the droplets of condensed liquid that form on the steel surface grow by condensation and then eventually reach their maximum size and undergo detachment from the metal surface due to gravity forces. This represents the stagnant droplet condensation mode. However, if the drag force is high enough (high gas velocity and gas pressure), the droplets may start to slide on the steel surface before they reach their critical size. This is called the sliding droplet condensation mode [83].



Figure 132: Test section equipped with video camera (left) – Observation of the condensation process on a weight loss sample (right)

These observations are important since the corrosion process happening at the top of the line is directly affected by the condensation mode.

A number of experiments were performed in the newly developed flat slab test section in order to capture the interaction between the condensation process and the extent of the corrosion attack. The high temperature in-situ video camera was used to observe the condensation process. Only relatively low water condensation rates could be tested, as higher rates would lead the camera lens to be constantly obstructed by water.

A number of experiments were conducted, but the followings section only presents the most relevant results related to three cases:

- Example A: Observation of the condensation process on a weight loss sample (Low WCR).
- Example B: Observation of the condensation process on a weight loss sample (medium WCR).
- Example C: Simulation of an artificial water trap on a steel insert.

#### 5.4 Example A: In-situ observation of the condensation process

A “typical” TLC experiment, lasting 43 days, was performed in the TLC flow loop. The experimental conditions were as follows:  $P_T$ : 4.4 bars,  $p_{CO_2}$ : 4.2 bars, gas temperature: 62°C, water condensation rate: 0.05 mL/m<sup>2</sup>/s, undissociated acetic acid: 1000 ppm, gas velocity: 2 m/s. The X65 weight loss sample was inserted into the “flat slab” test section (Figure 35) at the beginning of the experiment once the test conditions were stable. 1000 ppm of total acetic acid was introduced into the loop two hours before the insertion of the weight loss samples. Pictures and video clips of the condensation process happening on the exposed sample were taken every 2-3 days.

Figure 133 shows random pictures of the weight loss sample taken over the entire duration of the experiment.

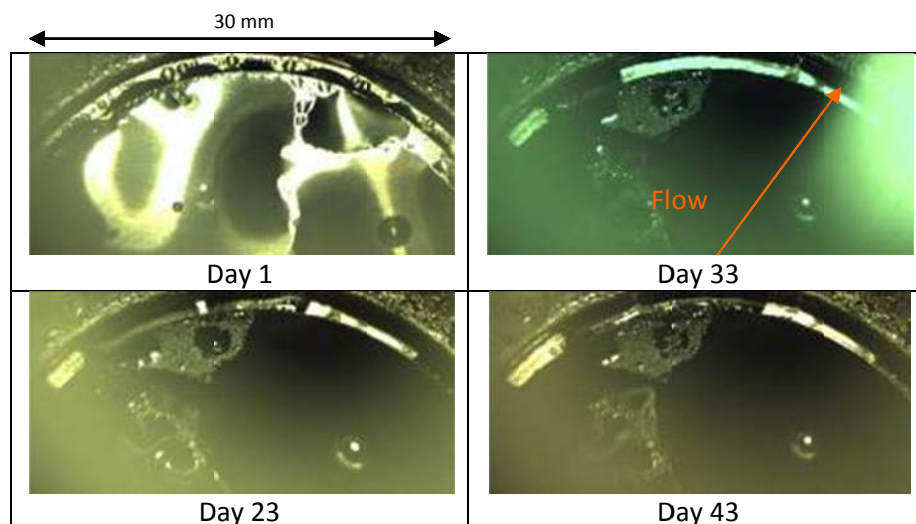


Figure 133: Localized corrosion test – Condensation process  
A droplet of condensed water forms always at the same location

Due to technical limitations, only the upper part of the sample can be seen. Small droplets initially formed on the freshly polished surface of the sample, which eventually coalesced together and wetted the surface uniformly. After a few days of testing, a single large droplet could be seen on the right side of the picture. The rest of the surface was either covered with smaller droplets or with a thinner film, while some part of the sample did not appear to be wetted at all. The condensation is a heterogeneous process strongly influenced by nucleation sites such as non-uniformity in the corrosion product scale. The droplet still seemed to always form at the same location on the steel surface, as shown in Figure 133.

The large droplet went through the typical cycle of growth and fall, as can be seen in Figure 134. Another droplet would always replace it at the exact same location on the steel surface. The maximum droplet radius measured around 8 mm and the duration of the cycle “growth/removal” could reach 20 to 60 minutes.

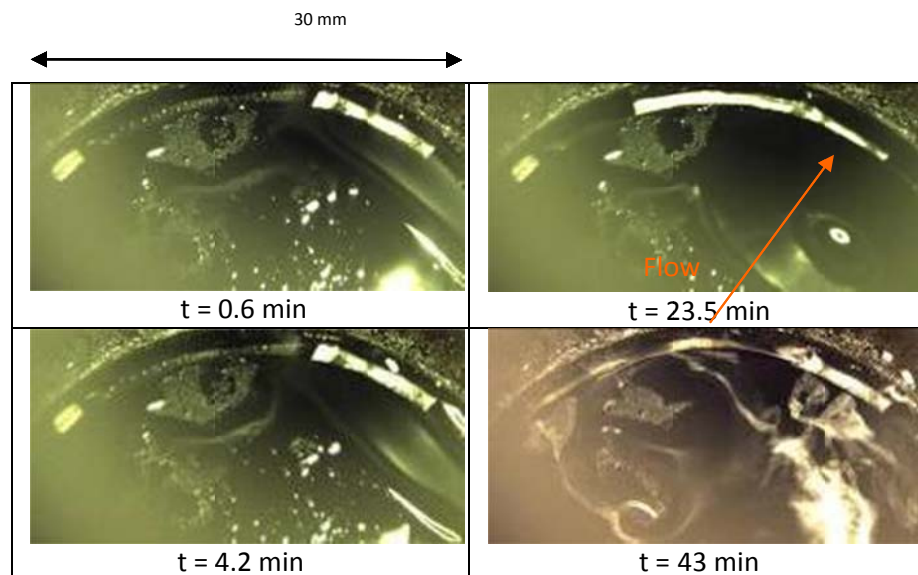


Figure 134: Localized corrosion test – Condensation process – Falling droplet cycle

The sample was recovered at the end of the experiment and the corrosion product layer was identified as  $\text{FeCO}_3$  through EDS analysis. On the area covered by the droplet, the crystals showed sharp edges and formed a dense layer (see Figure 135).

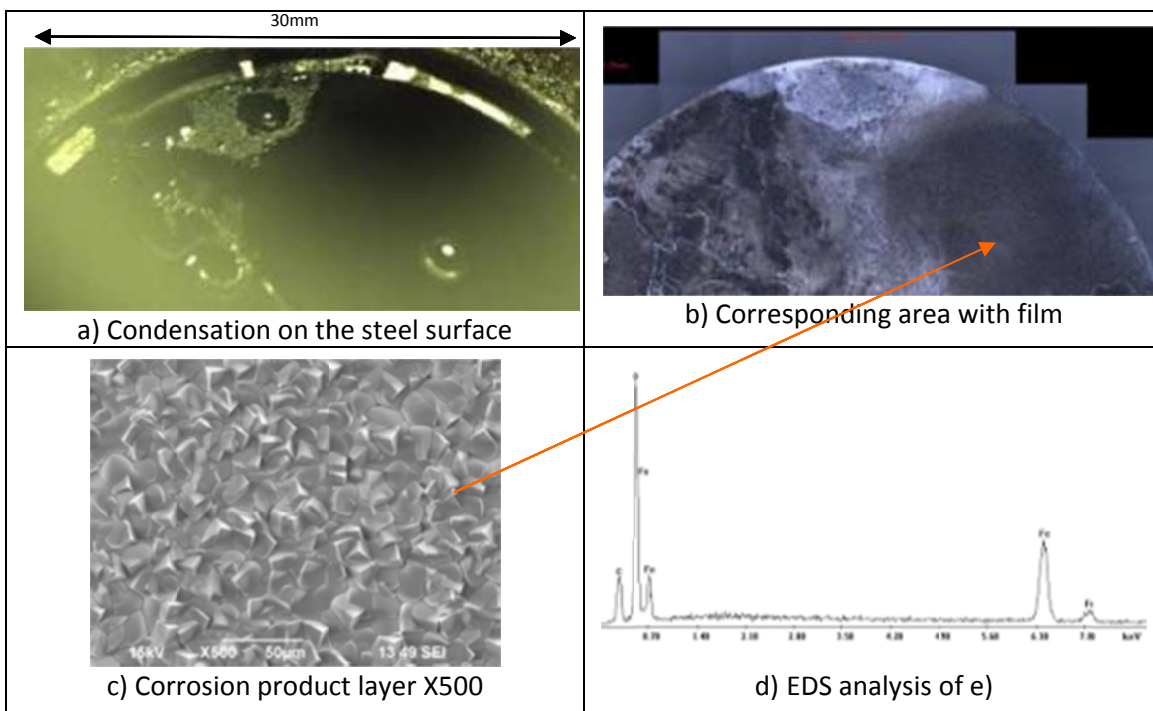


Figure 135: Surface analysis of the surface wetted by the droplet

Once the layer was removed, some evidence of localized corrosion could be seen with pits as deep as  $220\ \mu\text{m}$ . This corresponded to an average pitting rate over the 43 days of testing of around  $1.8\ \text{mm/year}$ , which is 9 times higher than the uniform corrosion rate, measured at around  $0.2\ \text{mm/year}$ . However, the particular section of the sample, which was continuously monitored and where a large droplet was continuously present, did not show any clear evidence of localized corrosion (Figure 136). The maximum localized corrosion rate (if any) was measured at around  $0.7\ \text{mm/year}$  which is only 3.5 times higher than the uniform corrosion rate and does not constitute localized corrosion since the localized corrosion rate needs to be at least 5 times

higher than the uniform corrosion rate to be classified as such. No clear link could be made between the location of the droplet and the extent of the corrosion attack. This could be due to the relatively low water condensation rate in this test (WCR:  $0.05 \text{ mL/m}^2/\text{s}$ ).

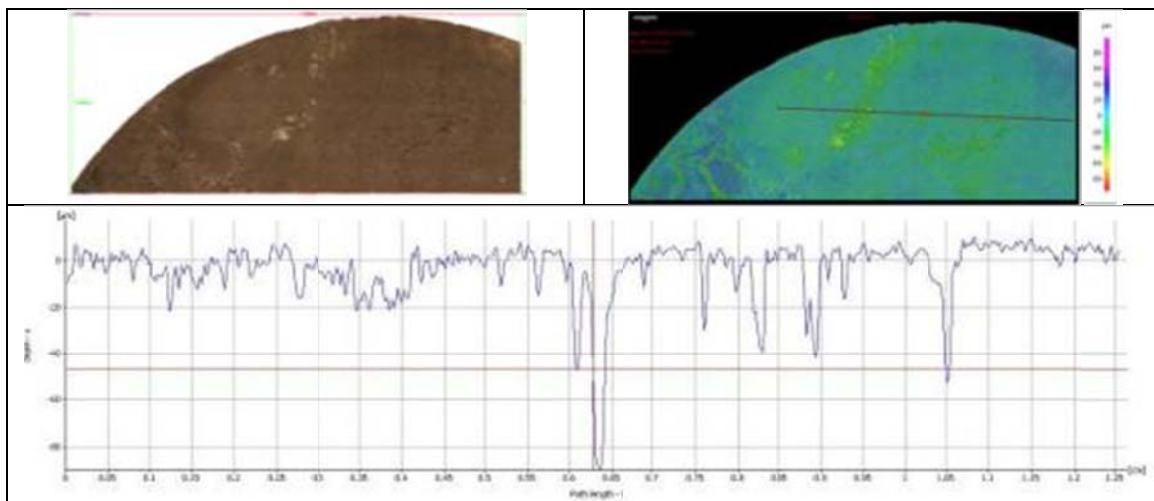


Figure 136: Surface profile of the surface wetted by the droplet  
Weight loss samples after the removal of the corrosion product layer

### 5.5 Example B: In-situ observation of the condensation process

Another experiment was performed concurrently with Test #4 (Section 4.4.2.2). The experimental conditions were as follows:  $P_T$ : 4 bars,  $p\text{CO}_2$ : 2.7 bars, Gas temperature:  $59^\circ\text{C}$ , Water condensation rate:  $0.2 \text{ mL/m}^2/\text{s}$ , undissociated acetic acid: 1000 ppm, gas velocity: 4 m/s. Figure 137 presents photographs of the steel sample at different points in time during the experiment. They show that the condensation regime on the steel sample was stagnant droplet condensation and that a large droplet was always present on the steel surface more or less at the same location on the sample.

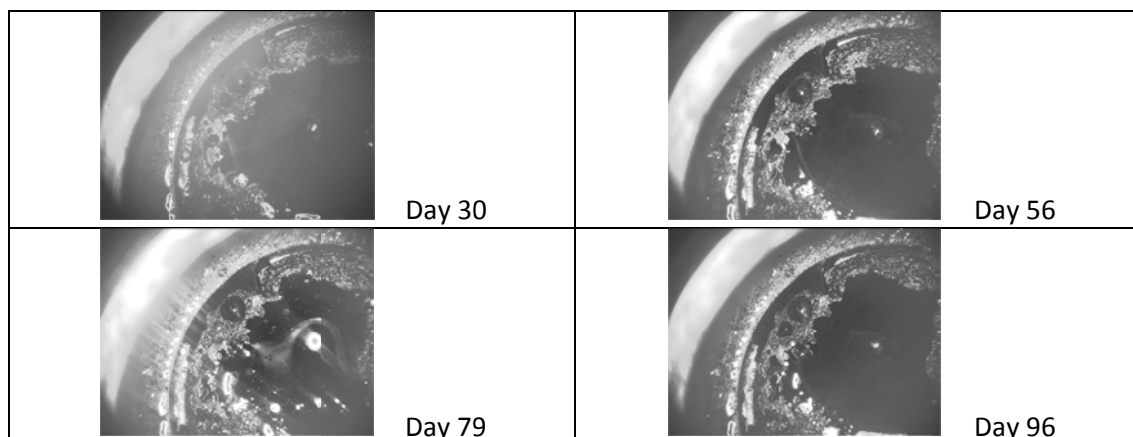


Figure 137: X65 WL sample – Observation of the condensation process

Figure 138 shows the relative position of this droplet with regard to the localized corrosion analyzed after the end of the experiment. It seems that pits are located in a more or less random fashion with regard to the morphology of the water droplet. The extent of corrosion on the edges of the droplet, where the fresh corrosive condensed liquid is more quickly renewed, was not more severe than on the rest of the steel surface. It is also interesting to note that, even after the removal of the corrosion product layer using inhibited acid, the pits are still surrounded by a dark ring of what is believed to be remaining  $\text{FeCO}_3$ . Although the rest of the steel surface is easily cleaned, the corrosion product layer next to the pit seems to be much denser.

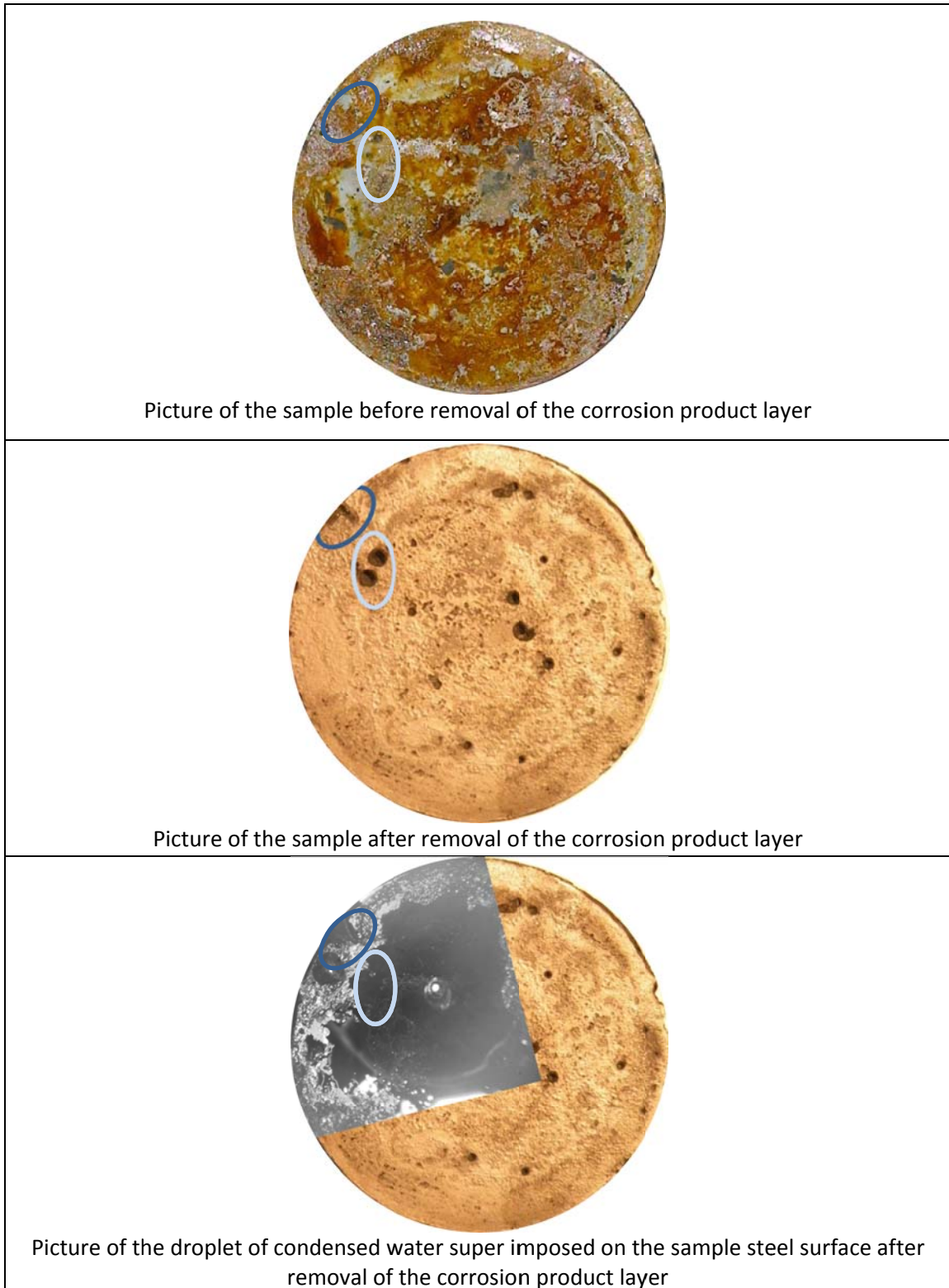


Figure 138: X65 WL sample – Exposure time 99 days

## 5.6 Artificial water trap

Another attempt to link condensation and corrosion process was made during the long term Test #4 ((Section 4.4.2.2). The small indentations (1.7 mm deep) were drilled on the upstream and downstream sections of the slab in order to develop artificial local areas where the condensed water would be trapped (Figure 139). The local WCRs were expected to be higher due to the lower steel thickness. However, the difference in WCR was neglected as most of the temperature drop happens at the gas/liquid interface and not through the liquid or the steel. The conditions are listed in Table 17 ( $P_T$ : 3 bars,  $pCO_2$ : 2.7 bars, gas temperature: 59°C, undissociated acetic acid: 1000 ppm, gas velocity: 4 m/s). The water condensation rates were set at 0.2 and 0.7 ml/m<sup>2</sup>/s at the location of the two artificial traps, respectively.

Surface profile scans of the indentations were performed before the beginning of the tests (using molds) in order to document a reference depth.

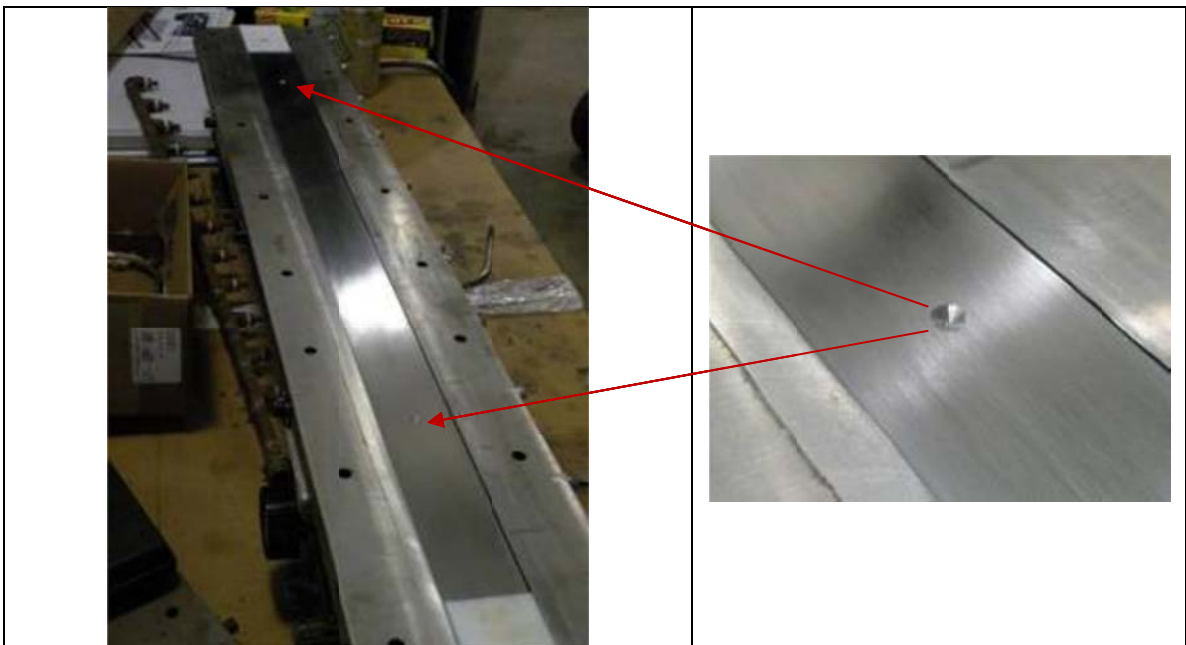


Figure 139 : Test #4 – Artificial indentations created on the steel insert before the beginning of the test.

Surface profile scans were also run after the end of the test and after the removal of the corrosion product layer (Figure 140). No real difference in the extent of the corrosion attack could be seen between the artificial indentation and the surrounding area. The area exposed to a lower condensation rate suffered from the growth of small isolated pits. The area exposed to the highest condensation rate experienced extensive pitting, but the localized corrosion did not seem to be aggravated inside the artificial indentation.

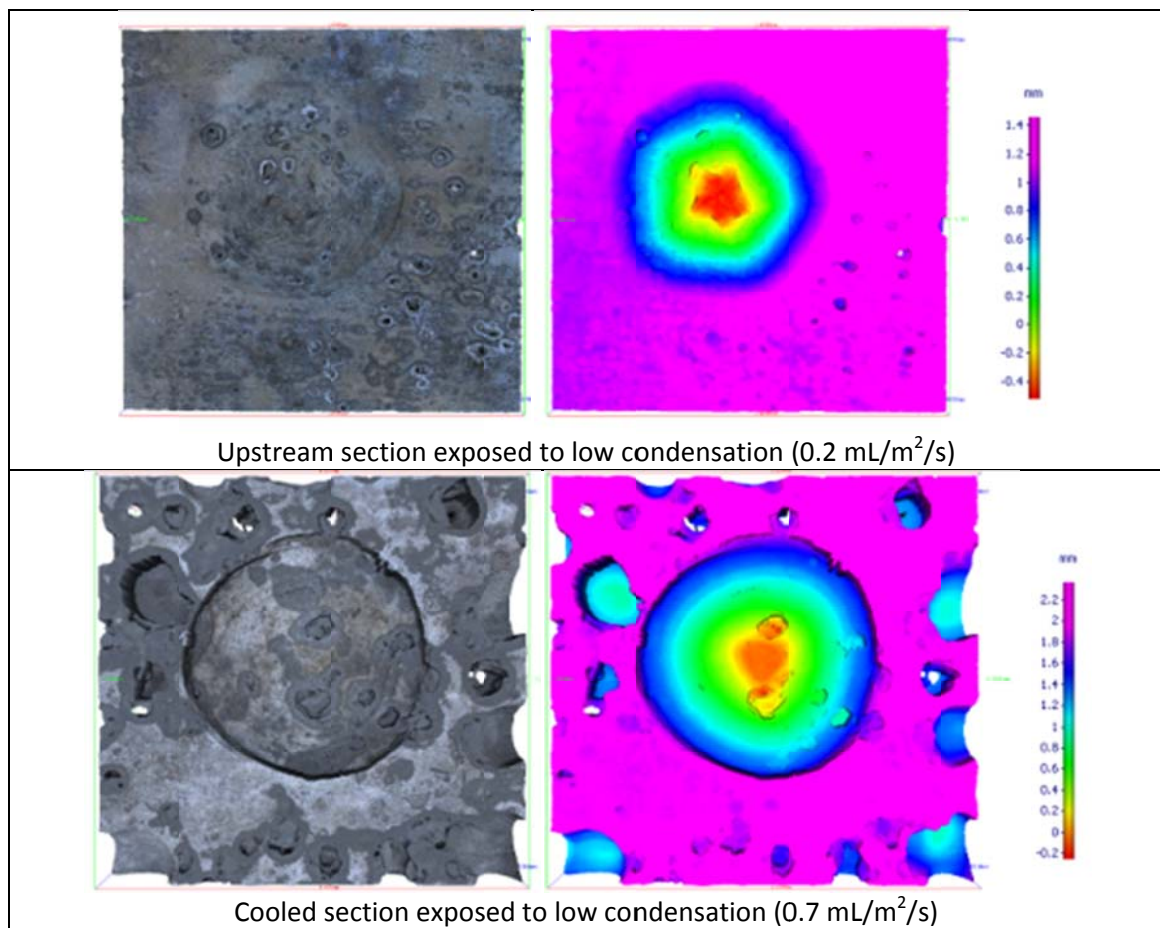


Figure 140: Test #4 - C1018(III) insert – Morphology of the artificial indentation after the end of the experiment

Table 19 shows the evolution of the depth of the artificial indentation with time on both upstream and downstream sections. It appears that the indentation located on the section exposed to the low condensation rate did not grow at all. On the downstream cooled section (corresponding to a WCR of  $0.7 \text{ mL/m}^2/\text{s}$ ), the depth of the indentation increased by  $184 \text{ }\mu\text{m}$ , but that corresponds also to a somewhat lower corrosion rate ( $0.68 \text{ mm/year}$ ) than on the surrounding areas ( $3.63 \text{ mm/year}$ ).

There was, therefore, no preferential corrosion inside the artificial indentations.

Table 19: Test #4 - Corrosion analysis on the artificial holes

	Initial depth	Final depth	Pit growth	Pit growth rate	Average pit depth on section	Average corrosion rate on section
	$\mu\text{m}$	$\mu\text{m}$	$\mu\text{m}$	$\text{mm/year}$	$\mu\text{m}$	$\text{mm/year}$
Upstream section Low condensation rate	1842	1856	14	0.05	681	2.51
Downstream section High condensation rate	2193	2377	184	0.68	983	3.63

## 5.7 Summary

It is clear from the experiments performed that, once the initial nucleation/growth/coalescence cycle is completed, larger droplets always seem to form at the same location on the steel surface. Once they reach their maximum size, they leave the location (either by falling or sliding along the pipe), leaving a thin liquid layer behind, where condensed water then accumulates preferentially. The steel surface between large droplets is usually wetted by a thin continuous liquid film.

However, the presence or absence of a large droplet on the steel surface cannot be correlated directly to the extent of corrosion occurring underneath:

- In case of high water condensation rate, severe localized corrosion happens everywhere on the steel surface, irrespective of where the large droplets are. Underneath the droplet, the corrosion features are larger but seem to progress at the same rate as anywhere else on the steel surface.
- In case of low condensation rate, isolated pitting could still be observed on the steel surface but no correlation with the presence of a large droplet could be validated.
- Artificial “water traps” do not promote higher localized corrosion.
- The extent of corrosion is controlled by the rate of water condensation and the overall aggressiveness of the environment (CO<sub>2</sub>, acetic acid).

## CHAPTER 6 CHARACTERISTICS OF LOCALIZED FEATURES AT THE TOP OF THE LINE

## 6.1 Objective

The objective of this chapter is to study the very peculiar morphology of typical localized TLC features in order to gain insight into how localized corrosion is initiated and how it progresses.

## 6.2 Methodology

A flow loop experiment was performed with the intent of collecting information about localized corrosion characteristics. The experiment was performed using the flat slab equipped with corrosion probe ports (Figure 36). The test conditions (Table 10) were selected for their aggressiveness, in order to ensure that large localized features would be created.

Table 20: TLC feature characteristics study - Test conditions

Parameters	Value
Steel type	X65
Tg (°C)	70
Total pressure (bar)	4.3
pCO <sub>2</sub> (bar)	4
pH <sub>2</sub> S (bar)	0
Water condensation rate (mL/m <sup>2</sup> /s)	0.4-0.6
Undissociated HAc (ppm)	0
Gas velocity (m/s)	2.5
Corrosion measurement	Weight loss sample
Exposure time (days)	21

The same procedure presented in Section 3.3 was followed, although the focus of this experiment was not to measure the actual corrosion rate but more to preserve steel samples for further SEM, EDS and XRD analysis.

General observations on the morphology of localized corrosion features are made based on the results of this experiment, but other comments are derived from experience gathered throughout the course of the present study.

### 6.3 Analysis of localized feature characteristics

#### 6.3.1 Overall view

After the end of the experiment, the weight loss samples were visually inspected and the typical grey corrosion product layer was present on the metal surface. The surface coverage was largely uniform but breakdown of the corrosion product layer could also be seen, and be indicative of potential localized corrosion (Figure 141).



Figure 141: Weight loss sample at the end of the test

XRD analysis (Figure 142) clearly identified  $\text{FeCO}_3$  as the sole component of the corrosion product layer present on the metal surface. No iron oxide could be detected, either by visual observation of the sample surface or by XRD analysis.

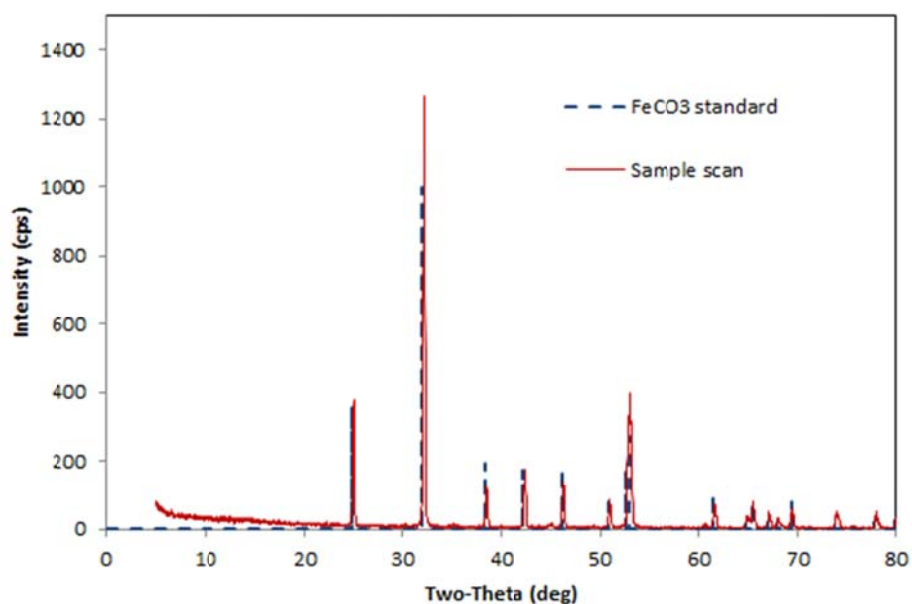


Figure 142: XRD analysis identifying the presence of  $\text{FeCO}_3$

### 6.3.2 SEM analysis of the corrosion product layer

The SEM analysis focused on several of the breakdown features and provided general information on the composition of the layer and morphology of the pits. Some common characteristics of these breakdown features are as follows:

- The top layer of the corrosion product is comprised of tightly packed crystals of  $\text{FeCO}_3$ . The size of the crystals varies between 10 and 20  $\mu\text{m}$  (Figure 143 c) and e)).
- Several large breakdown features in the corrosion product layer are encountered. In almost all of the cases, a more amorphous phase, identified as  $\text{Fe}_3\text{C}$ , is present inside these breakdown features (Figure 143 d) and f)).

- After removal of the corrosion product layer, using inhibited acid [74], large localized corrosion features are visible and can be clearly correlated with the location of the  $\text{FeCO}_3$  breakdown.

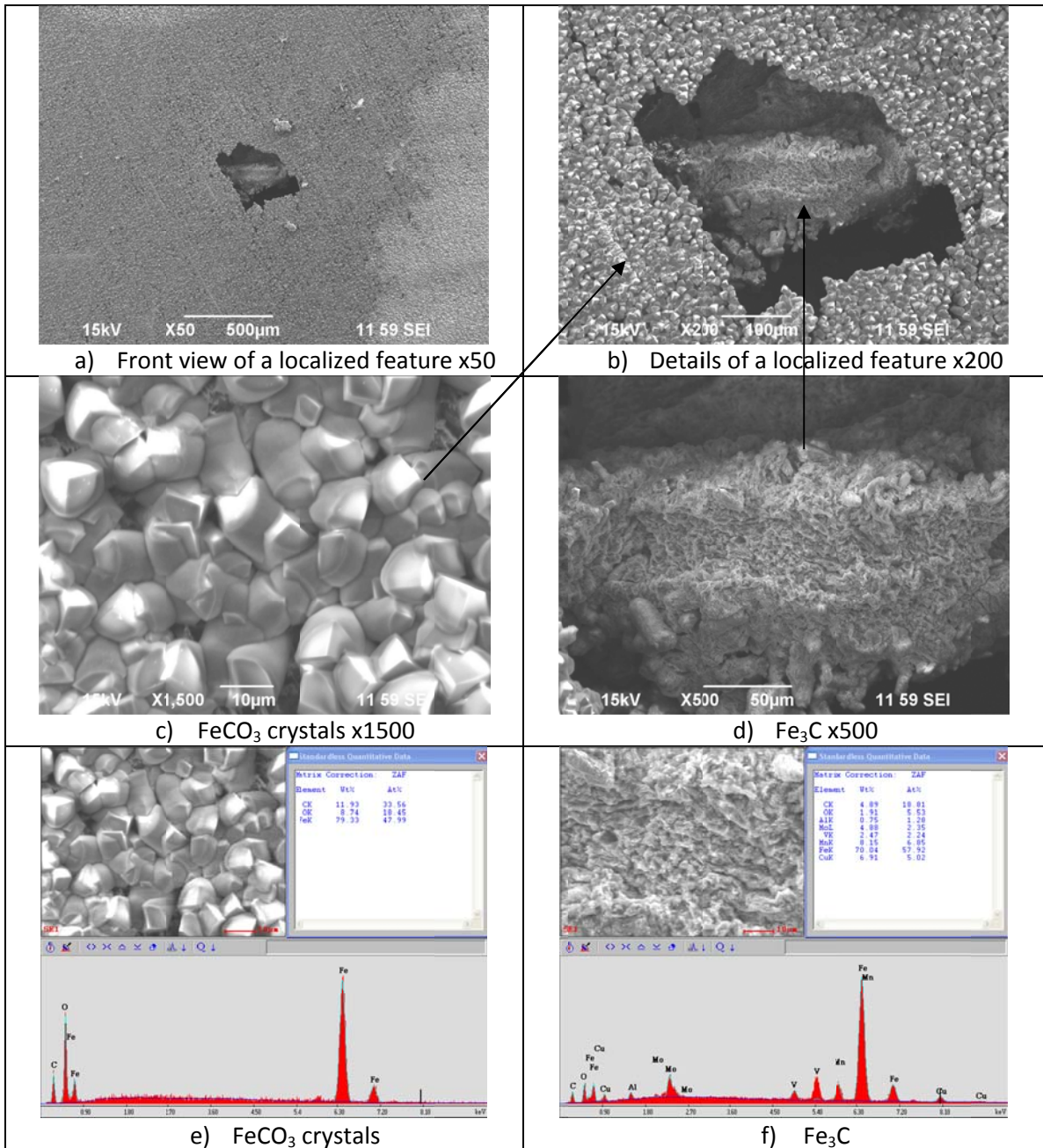


Figure 143: EDS analysis of the corrosion product layer and associated breakdowns

### 6.3.3 Cross sectional analysis

The sample was mounted in epoxy and cut in order to perform a cross sectional analysis of one of these breakdown features. The results are shown in Figure 144 to Figure 147. Once again, several common characteristics are notable:

- A 20 to 70 $\mu\text{m}$  thick  $\text{FeCO}_3$  layer can clearly be seen on both sides of the localized feature, which can itself reach a depth close to 400  $\mu\text{m}$  (Figure 144 a) and b)).
- The features can be quite wide and relatively flat bottomed. The actual pit can be much larger than the layer breakdown would show.
- The pit is relatively empty. Often, the remainder of the  $\text{FeCO}_3$  layer can be seen “hanging” on top of the pit, although there is nothing to support it.

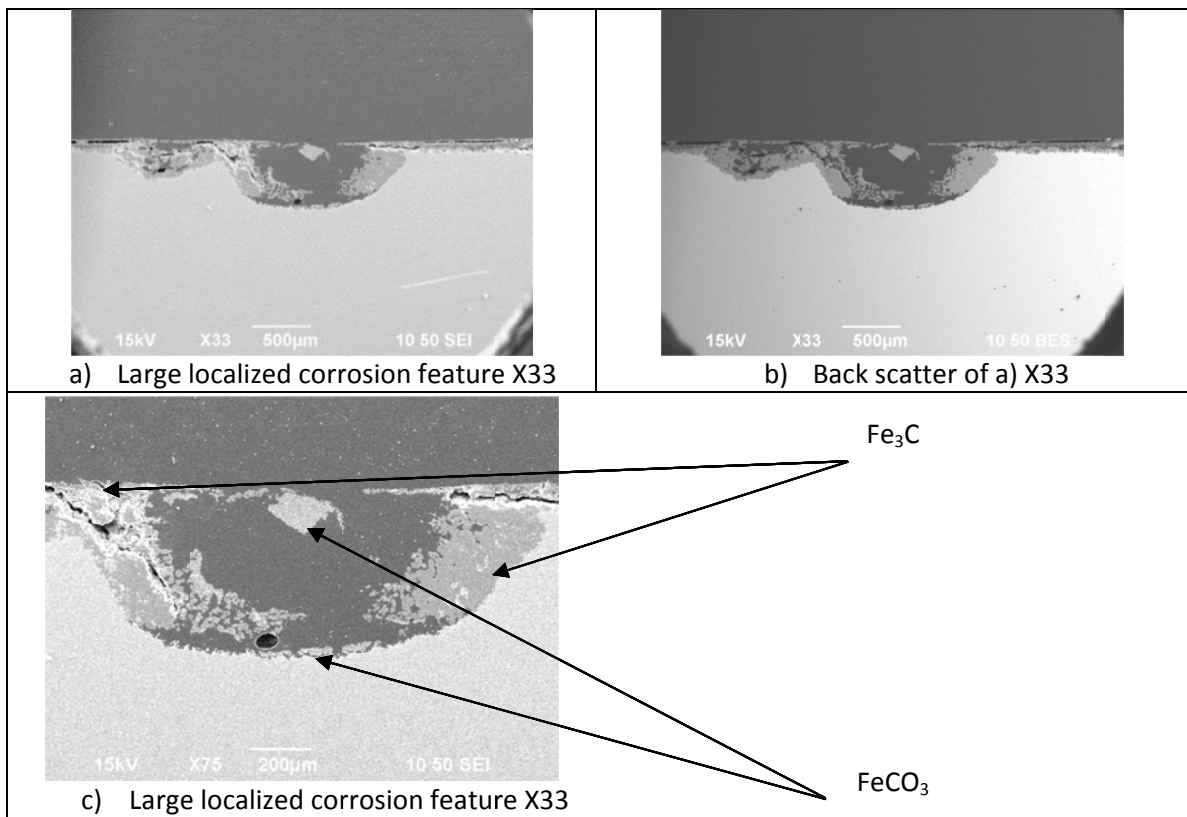


Figure 144: Cross section analysis – Morphology of large localized features

- Large amount of  $\text{FeCO}_3$  crystals are encountered on the side walls of the pits (Figure 145).  $\text{FeCO}_3$  seems to precipitate preferentially on already formed  $\text{FeCO}_3$  crystals, rather than on the bare steel surface. This is especially true if the corrosion rate is high and the undermining effect considerable.

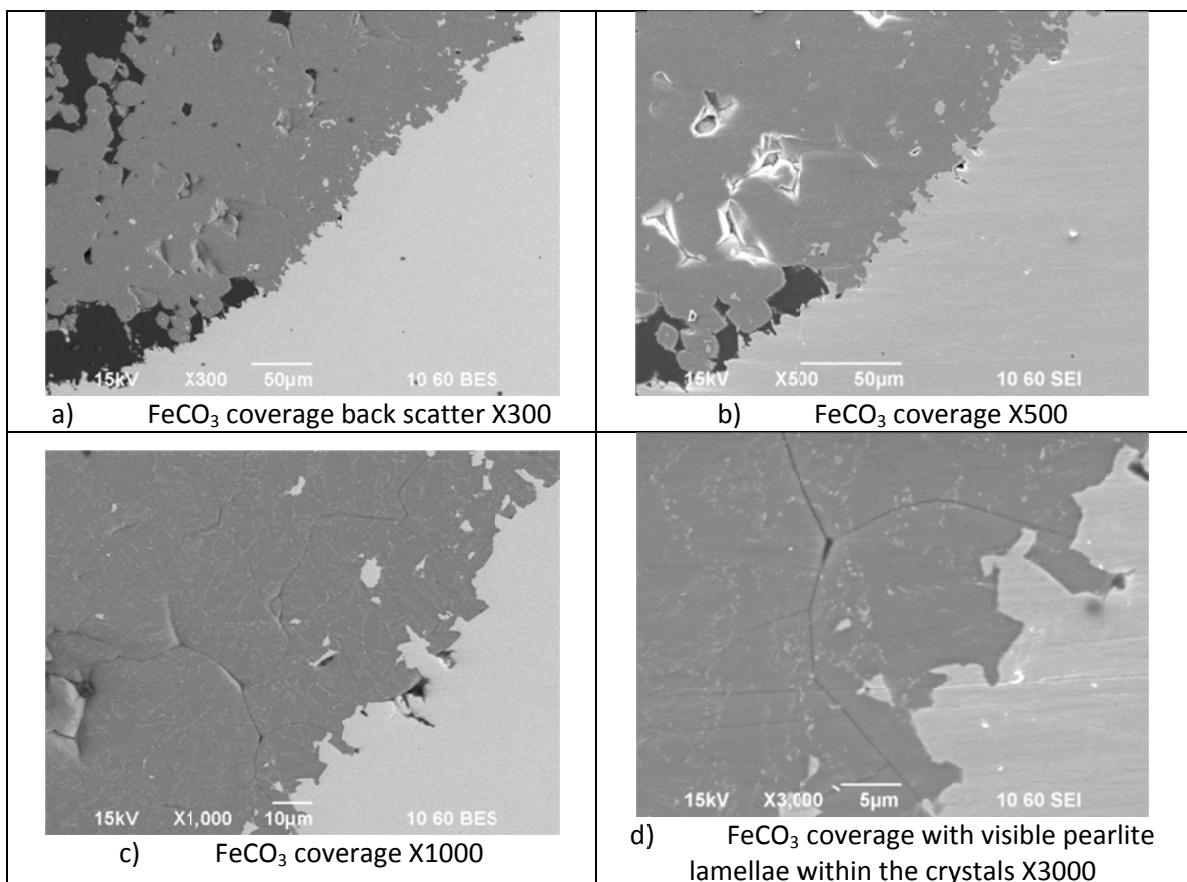


Figure 145: Cross section analysis –  $\text{FeCO}_3$  coverage on the side of the localized feature

- On the areas well-covered by  $\text{FeCO}_3$ , the crystals can be tightly packed and form an effective mass transfer barrier. Pearlite lamellae can be seen superimposed onto the  $\text{FeCO}_3$  crystal network (Figure 145 d)).

- $\text{Fe}_3\text{C}$  is identified at the bottom or at the center of the pit. This is not an indication that the pH inside the pit is acidic. It is, rather, an indication that  $\text{FeCO}_3$  did not precipitate at that specific location (Figure 146).

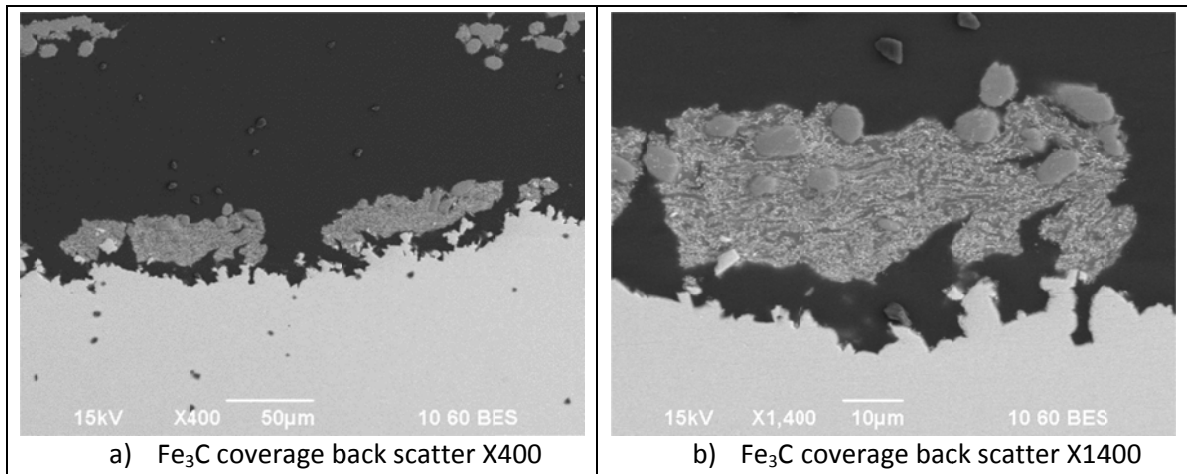


Figure 146: Cross section analysis –  $\text{Fe}_3\text{C}$  coverage on the side of the localized feature

- A line EDS performed at the steel/ $\text{FeCO}_3$  interface could not confirm the presence of an iron oxide layer (Figure 147), contrary to what has been proposed elsewhere [122, 123].

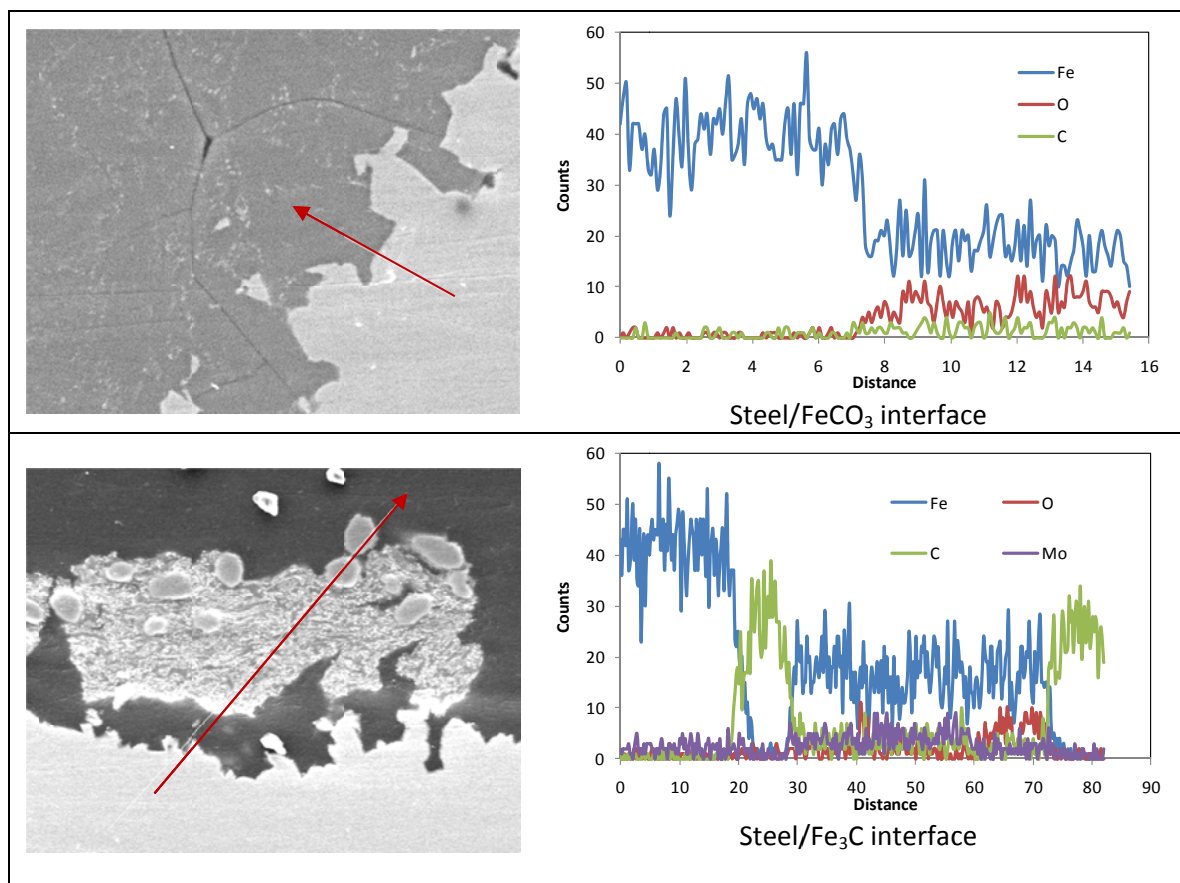


Figure 147: Cross section analysis - EDS Line scan (along the red line)

#### 6.4 General comments on properties of the $\text{FeCO}_3$ layer

##### 6.4.1 Initiation of localized corrosion

In most of the TLC experiments performed, a very dense and tightly packed  $\text{FeCO}_3$  layer would form on the metal surface and provide effective protection against corrosion. However, numerous breakdowns in the otherwise protective layer could be seen after long term exposure to the corrosive environment.

No localized corrosion was ever observed on the steel samples after short term exposure. However, there were signs that the  $\text{FeCO}_3$  was not completely uniform on the entire metal surface (Figure 148). The non-uniformity in the  $\text{FeCO}_3$  coverage is mostly due to the rate

of water renewal on the steel surface, which constantly brings new, aggressive condensed water and alters the chemistry. Although pitting corrosion does not happen to any measureable extent on short term exposure, non-uniformity in the  $\text{FeCO}_3$  coverage is visible and could lead later on to the initiation of localized corrosion.

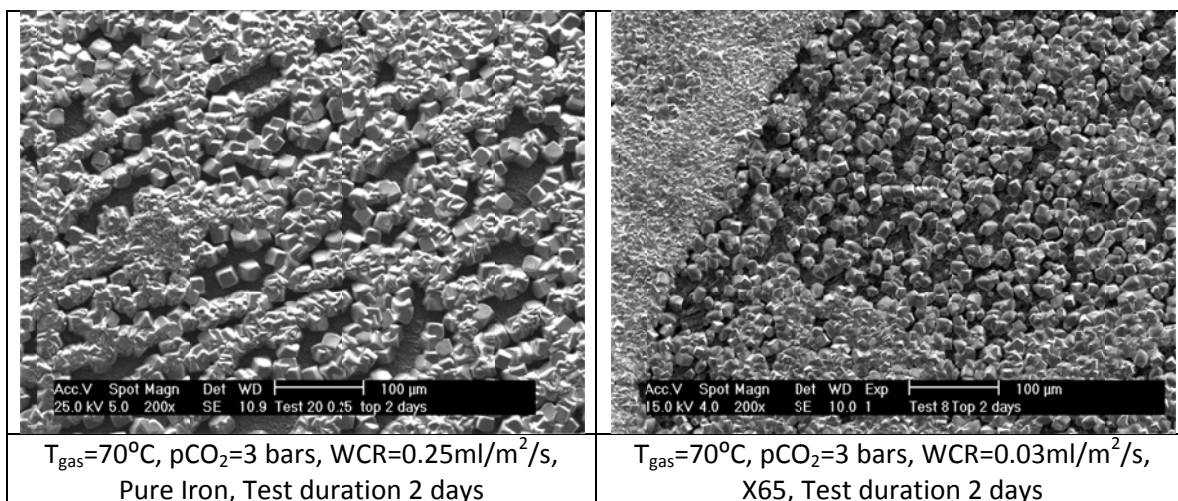


Figure 148: Localized corrosion initiation  
 $\text{FeCO}_3$  layer initial coverage after 2 days of exposure

#### 6.4.2 Localized corrosion growth

Figure 149 shows the 3D surface profile performed before and after the removal of the corrosion product layer (Figure 149 a) and b), respectively). This experiment was performed over a 21-day period. Although breakdowns of the layer could clearly be seen, areas affected by high localized corrosion rates covered a much higher percentage of the surface. This shows that localized corrosion grew in depth but also underneath the corrosion product layer. This undermining effect could lead to the collapse of large portions of the  $\text{FeCO}_3$  layer (Figure 150).

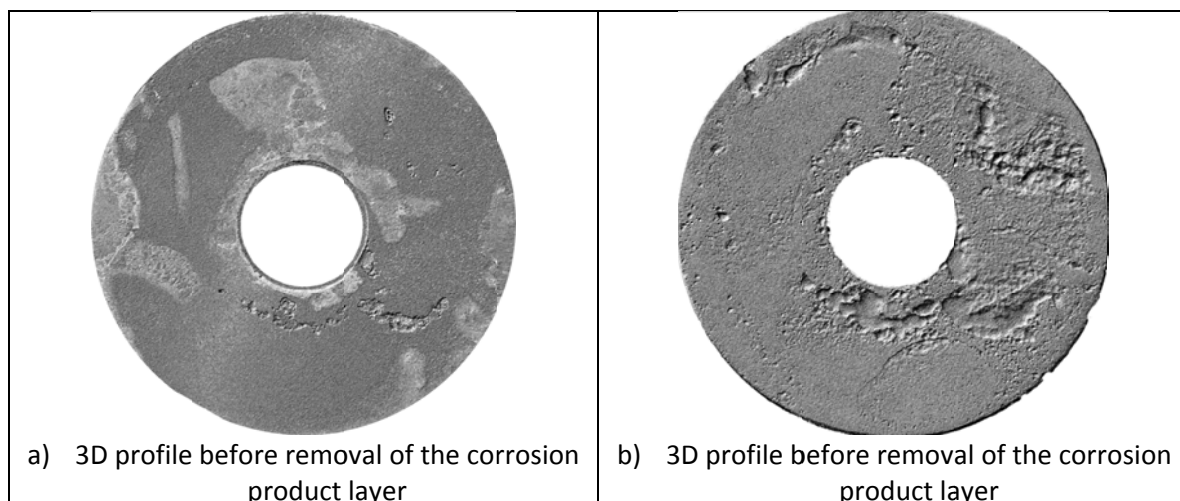


Figure 149: Localized corrosion features growth underneath  $\text{FeCO}_3$  layer  
 $T=70^\circ\text{C}$ , WL X65, HAC=0 ppm, WCR=  $1 \text{ mL/m}^2/\text{s}$ , Exposure time= 21 days

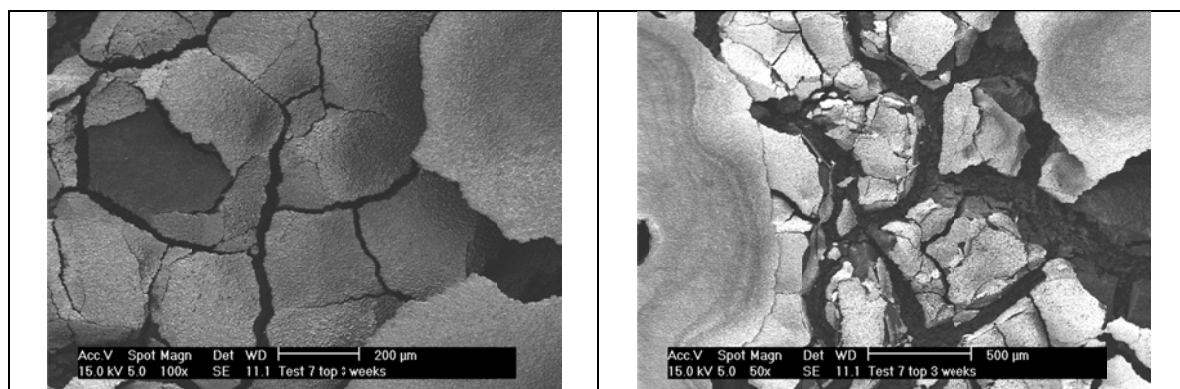


Figure 150:  $\text{FeCO}_3$  top layer collapsing  
 $T=70^\circ\text{C}$ , WL X65, HAC=1000 ppm, WCR=  $1 \text{ ml/m}^2/\text{s}$ , Exposure time= 21 days

#### 6.4.3 Localized corrosion termination/sustainability

Figure 151 presents a cross section of a TLC localized feature, whose bottom part seems to be well covered by a  $\text{FeCO}_3$  layer, and therefore protected against further corrosion. This shows that not all of the TLC features remain “active” throughout the exposure to the corrosive environment. The reason behind such behavior is unclear but could be due to mass transfer limitation which would make  $\text{FeCO}_3$  precipitation more likely at the bottom of deep and narrow localized features, while other shallower pits would continue to grow.

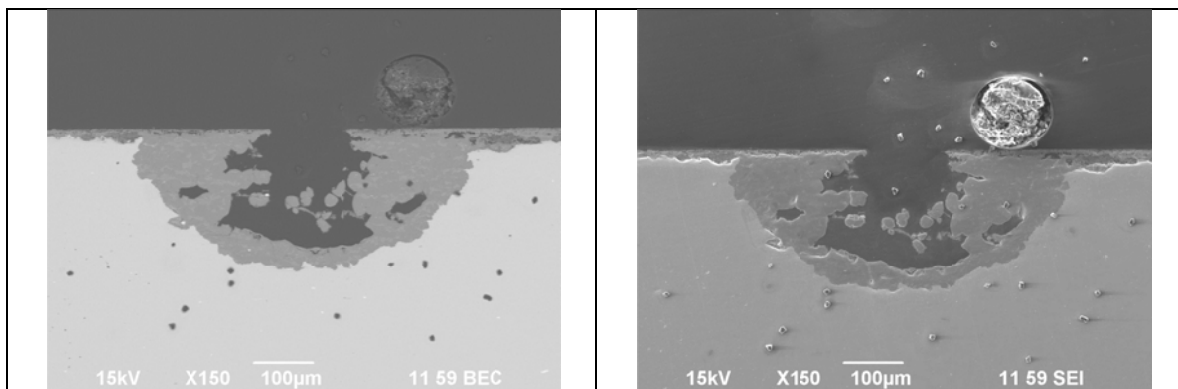


Figure 151:  $\text{FeCO}_3$  layer regaining coverage on the metal surface  
 $T=70^\circ\text{C}$ , WL X65, HAC=1000 ppm, WCR=  $1 \text{ ml/m}^2/\text{s}$ , Exposure time= 21 days

## 6.5 Summary

TLC localized features can be wide and relatively flat bottomed. The actual pit can be significantly larger than the corresponding  $\text{FeCO}_3$  layer breakdown that could be seen on top of it before the removal of the layer. The pits are relatively empty, and layers of  $\text{FeCO}_3$  can be seen “hanging” on top of the pit although there is little to mechanically support it. Large amounts of  $\text{FeCO}_3$  crystals are encountered on the side walls of the pits while the bottom part is bare steel.  $\text{FeCO}_3$  grows preferentially on already formed  $\text{FeCO}_3$  crystals, rather than on the steel surface. Large pieces of  $\text{Fe}_3\text{C}$  are identified at the bottom or at the center of the pit. This is not an indication that the pH inside the pit is acidic. It is, rather, an indication that  $\text{FeCO}_3$  did not precipitate at that specific location.

## CHAPTER 7 DESCRIPTIVE MODEL OF LOCALIZED CORROSION AT THE TOP OF THE LINE

## 7.1 Objective

Based on the experimental data, a new modeling approach for the prediction of the localized attack in a top of the line corrosion scenario is proposed.

## 7.2 Literature review

A full description of the literature review related to the modeling of the condensation and corrosion processes is shown in Appendix B. The latest developments related to the understanding of the localized corrosion mechanism in sweet environment, albeit not pertaining to TLC, are also presented.

## 7.2.1 Water condensation rate (WCR) prediction

## 7.2.1.1 Average WCR calculations considering water dropout

The way most commercial flow assurance software predicts a WCR is by calculating the overall heat loss over a small section of pipe, creating a temperature gradient profile, and then calculating how much water drops out from the vapor over this section of pipe. The saturation level of water carried in the gas phase is specifically modeled; any reduction in its vapor pressure is presumed to be due to water condensing out of the system on the upper pipe wall.

Only the upper half of the pipe area is considered for the water condensation rate calculations. The equation below is only valid for small sections of pipes:

$$WCR = m_{gas} \frac{M_{water}}{M_{gas}} \frac{2}{AL} \left( \frac{P_{vap}^{in} - P_{vap}^{out}}{P_{Total}} \right) \quad \text{Eq (7-1)}$$

With WCR: Water condensation rate [kg/m<sup>2</sup>/s]

$m_{gas}$ : Gas mass flow rate [kg/s]

$M_{gas}$  and  $M_{water}$ : Molecular weight of gas phase and of water [kg/mol]

$P_{\text{vap}}^{\text{in}}$  and  $P_{\text{vap}}^{\text{out}}$ : Vapor pressure at the inlet and outlet of the pipe section [bar]

$A/2$ : Half of pipe perimeter [m]

$L$ : Pipe length of the section considered [m]

The water that drops out is assumed to be the total amount of condensed water, but the pipeline is a dynamic system and the gas phase cools more rapidly than the bulk liquid. Therefore, while some water vapor condenses at the cold steel surface, some liquid water should also evaporate at the warmer bulk liquid interface. The overall rate of water accumulation that the above method calculates is actually the water condensed from the vapor minus the water that evaporates from the bulk liquid. This approach does not separate the two, and, consequently, can under-predict the actual water condensation rate happening locally at the top of the pipe.

#### 7.2.1.2 *Local WCR calculations considering dropwise condensation theory*

The phenomenon of dropwise condensation (as opposed to filmwise condensation) has been studied extensively over the past sixty years. It can be described in terms of a four-stage scenario [99]: nucleation, growth, coalescence and removal. It is now commonly accepted that nucleation is an essential feature of dropwise condensation and that the existence of a thin film of liquid between the droplets is not necessary [100]. An excellent review paper summarizing the early findings in terms of mechanism and modeling was published by Rose [101] in 2002. Rose has published several papers on the subject of dropwise condensation [102-104] over the past thirty years. As dropwise condensation is a random process, the common approach is to calculate the heat flux through a single droplet and to integrate the expression over an average distribution of drop sizes:

$$Q = \int_{r_{\min}}^{r_{\max}} q(r)N(r)dr \quad \text{Eq (7-2)}$$

With: Q: Total heat flux (W/m<sup>2</sup>)

q(r): Heat flux through an individual droplet of radius r (W/m<sup>2</sup>)

N(r)dr: Number of drops per area with radius between r and r+dr (m<sup>-2</sup>)

r<sub>max</sub> and r<sub>min</sub>: maximum and minimum radii of droplet (m)

The total heat flux includes the heat transfer due to the phase change and the presence of non-condensable gas. It has been reported that the main resistance for heat transfer comes from the presence of non-condensable gas [105-107]. The relationship between total heat flux and condensation rate can be stated in the following way [83]:

$$Q = Q_g + Q_c = h_g \times (T_b^g - T_i^g) + WCR \times H_{fg} \quad \text{Eq (7-3)}$$

with: Q: Total heat flux (W/m<sup>2</sup>)

Q<sub>g</sub>: Heat flux through the gas boundary layer (W/m<sup>2</sup>)

Q<sub>c</sub>: Latent heat flux released by the phase change (W/m<sup>2</sup>)

h<sub>g</sub>: Heat transfer coefficient in the gas boundary layer (W/m<sup>2</sup>/K)

(T<sub>b</sub><sup>g</sup> - T<sub>i</sub><sup>g</sup>): Temperature difference between bulk and vap/liq interface (K)

WCR: Water condensation rate (kg/m<sup>2</sup>/s)

H<sub>fg</sub>: Latent heat of evaporation/condensation (J/kg)

A full description of the methodology developed for the heat transfer derivation in dropwise condensation is presented in APPENDIX D.

In 2007, Zhang [83] adapted the dropwise condensation theory to a pipeline situation in which the presence of droplets of condensed water was clearly identified (top of the line corrosion). It is important to mention that dropwise condensation is believed to happen at the

11 to 1 o'clock position in the pipeline while the remainder of the surface is more likely to be subject to filmwise condensation. Zhang added a mass balance of the water in order to calculate the condensation rate:

$$WCR = \rho_g \beta_g \times (x_b^g - x_i^g) = \rho_g \beta_g \times \frac{M_w}{P_T M_g} (P_{sat}(T_b^g) - P_{sat}(T_i^g)) \quad \text{Eq (7-4)}$$

With: WCR: Water condensation rate (kg/m<sup>2</sup>/s)

$\beta_g$ : Mass transfer coefficient in the gas boundary layer (m/s)

$x_b^g$ : Mass fraction of water vapor in the bulk gas flow (kg<sub>v</sub>/kg<sub>g</sub>)

$x_i^g$ : Mass fraction of water vapor at the gas-liquid interface (kg<sub>v</sub>/kg<sub>g</sub>)

$\rho_g$ : Density of gas (kg<sub>g</sub>/m<sup>3</sup>)

$M_w$  and  $M_g$ : Molecular weight of the water and the gas mixture (g/mol)

$P_T$ : Total pressure (Pa)

$P_{sat}$ : Saturation pressure as a function of temperature (Pa)

Zhang also improved the calculation of the maximum droplet radius by performing a force balance on a single droplet. He could then calculate the condensation rate by solving the equations above using an iterative method. This new approach is also able to take into account the effect of non-condensable gas. A mechanistic corrosion model described in the following section was then adapted by Zhang to the condensation scenario in order to predict the corrosion rate.

In summary, the dropwise condensation approach calculates a local WCR, while the water dropout approach (Section 7.2.1.1) calculates an overall water accumulation rate (or a net water condensation rate). The dropwise condensation approach likewise only considers the water that condenses from the vapor phase. Since the calculations are made locally at the

surface of the pipe, the evaporation of water from the bulk is not taken into account. This is why dropwise condensation can calculate greater WCRs than the water dropout approach.

A significant difference between the two approaches should only exist when there is a considerable amount of produced water in the pipe. The heat carried in the water is much larger than in the gas and it will prevent the fluid from rapidly cooling, acting as a constant source of water vapor. If there is little liquid water produced in the line, the fluid will cool down rapidly and the influence of evaporation will be reduced.

### *7.2.2 Corrosion mechanisms under dewing conditions*

Some sections of this chapter are taken directly or slightly adapted from one of the author's publications [47].

#### *7.2.2.1 Empirical and semi empirical modeling of top of the line corrosion*

The first attempt to model TLC was made twenty years ago by Olsen et al. [64]. They found that the competition between the corrosion and the condensation rates controlled the  $\text{FeCO}_3$  saturation level and, consequently, the extent of the corrosion attack. At high temperature (70°C) and low condensation rate, a dense and protective  $\text{FeCO}_3$  is favored to form rapidly. At high condensation rate, the saturation in  $\text{FeCO}_3$  is more difficult to obtain due to the rate of fresh water renewal.

DeWaard et al. [108] proposed the first modeling approach to TLC based on his widely used full pipe flow empirical equation. DeWaard introduced a correcting factor  $F_{\text{cond}}=0.1$  in order to adapt his model to condensation conditions for condensation rates below an experimentally determined critical rate of 0.25 mL/m<sup>2</sup>/s. The correlation proposed by DeWaard gives an extremely conservative prediction. It is listed below:

$$CR = F_{Cond} \times 10^{\left(\frac{5.8 - \frac{1710}{T_K} + 0.67 \times \log(p_{CO_2})}{1}\right)} \quad \text{Eq (7-5)}$$

With  $p_{CO_2}$ : Partial pressure of  $CO_2$  (bar)

$T_K$ : Temperature (K)

$F_{cond}$ : 0.1

CR: Corrosion rate (mm/year)

In 2000, a new model was proposed by Pots et al. [60] which aimed at taking into account the competition between the scale formation rate linked to the iron dissolution and the condensation rate. The so called “supersaturation model” is based on the calculation of the concentration of iron at saturation under film-forming conditions. The corrosion rate CR, calculated using the formula below, is equated with the precipitation rate PR, calculated using an equation developed by Van Hunnik et al. [109]. The concentration of  $Fe^{2+}$  which is present on both sides of the equations (Eq (7-6) and Eq (7-7)) is calculated and re-inserted in the corrosion rate equation.

$$CR = \frac{M_{Fe} \times 10^6 \times 24 \times 3600 \times 365}{\rho_{Carbonsteel}} \times [Fe^{2+}]_{supersat} \times \frac{WCR}{\rho_w} \quad \text{Eq (7-6)}$$

With CR: Corrosion rate (mm/y)

WCR: Water condensation rate ( $g/m^2/s$ )

$\rho_w$ : Water density ( $g/m^3$ )

$[Fe^{2+}]_{supersat}$ : Iron concentration at  $FeCO_3$  saturation (mol/L)

$M_{Fe}$ : Iron molecular weight (55.847 g/mol)

$\rho_{carbonsteel}$ : Density of a typical carbon steel ( $7860000 g/m^3$ )

$$PR = A_p \times e^{\frac{-E_a}{RT}} \times K_{sp} \times (s-1) \left(1 - \frac{1}{s}\right) \quad \text{and} \quad s = \frac{[Fe^{2+}] \times [CO_3^{2-}]}{K_{sp}} \quad \text{Eq (7-7)}$$

With PR: Precipitation rate converted in mol/m<sup>2</sup>/s

A<sub>p</sub>: Constant

E<sub>a</sub>: Activation energy (KJ/mol)

R: Ideal gas constant (J/K/mol)

T: Temperature (K)

s: FeCO<sub>3</sub> saturation

K<sub>sp</sub>: FeCO<sub>3</sub> solubility product (mol<sup>2</sup>/m<sup>2</sup>)

A complete chemistry analysis, including the electro-neutrality equation, the dissociation equations and the CO<sub>2</sub> solubility, also needed to be implemented. Pots et al. [60] emphasized the importance of correctly evaluating the condensation rate in order to accurately predict the corrosion rate. However, no clear guidelines on how to calculate it are provided.

More recently, in 2007, Nyborg et al. [110] developed a new empirical equation for TLC prediction through experimental work. It is based on the concept that TLC is limited by the amount of iron which can be dissolved in the thin film of condensing water. According to Nyborg, the TLC rate can be modeled as proportional to the water condensation rate, the iron carbonate solubility and a supersaturation factor. The empirical equation is displayed below and is valid only for low acetic acid content (<0.001 Mol/L), low to medium carbon dioxide partial pressure (<3 bars) and no H<sub>2</sub>S:

$$CR = 0.004 \times WCR \times [Fe^{2+}] \times (12.5 - 0.09 \times T) \quad \text{Eq (7-8)}$$

With CR: Corrosion rate (mm/y)

WCR: Water condensation rate (g/m<sup>2</sup>/s),

[Fe<sup>2+</sup>]: Solubility of iron ions (ppm<sub>w</sub>)

T: Temperature (°C)

Nyborg notes that the solubility of iron ion is a function of temperature, total pressure, CO<sub>2</sub> partial pressure and glycol concentration, and calculates this with an in-house pH and solubility program. Although no detail is provided on how the condensation rate is calculated, Nyborg stresses the importance of predicting an accurate condensation rate, as it will have a much more pronounced effect on TLC than, for example, the CO<sub>2</sub> partial pressure

#### 7.2.2.2 *Mechanistic modeling of top of the line corrosion*

As detailed below, a fair amount of research and modeling work has been done on TLC. It should be noted that these works pertain almost exclusively to sweet (CO<sub>2</sub> dominated) TLC and that no serious attempt to model sour (H<sub>2</sub>S dominated) TLC has been performed to date.

In 2002, Vitse et al. [75-77] completed a thorough experimental and theoretical study on TLC due to carbon dioxide. Condensation and corrosion experiments were conducted in a large scale 4" ID flow loop. Vitse developed two models and adapted them to a top of the line scenario: a mechanistic film-wise condensation model based on Nusselt theory and a semi-empirical corrosion model. The condensation model has a sound mechanistic approach and is based on the assumption that a continuous film of liquid covers the steel surface at the top of the line (film-wise condensation). Vitse acknowledges that, while this approach is valid to estimate the condensation rate on the side of the pipe, it is not ideal to cover the condensation process happening at the top (11 to 1 o'clock position), which is drop-wise. It has also been reported by other authors that the condensation process in TLC is drop-wise condensation [37]. Nevertheless, the corrosion model constituted a considerable breakthrough in the understanding of the mechanisms involved in TLC. Once the value of the condensation rate was

obtained (see the previous chapter), Vitse conducted a  $\text{Fe}^{2+}$  flux balance in a controlled volume, taking into account the fluxes of  $\text{Fe}^{2+}$  created by corrosion, removed by  $\text{FeCO}_3$  precipitation and transported by condensed water film convection. A schematic representation of this approach is presented in Figure 152.

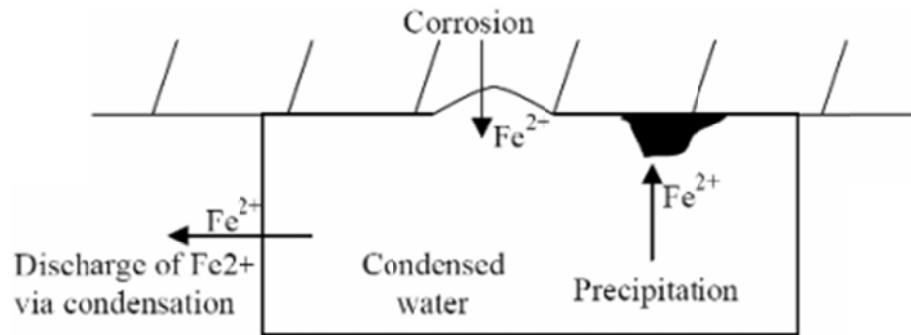


Figure 152: Transport, source and sink of  $\text{Fe}^{2+}$  under a thin film of condensed water during TLC (Reproduced from [75] - © NACE international 2003)

The equation used in the  $\text{Fe}^{2+}$  flux balance is displayed below:

$$\frac{d[\text{Fe}^{2+}]}{dt} = \frac{1}{\delta} \times [\text{CR} - \text{PR} - \text{WCR} \times [\text{Fe}^{2+}]] \quad \text{Eq (7-9)}$$

With  $\text{Fe}^{2+}$ : Concentration of iron ion ( $\text{mol}/\text{m}^3$ )

t: Time (s)

CR: Corrosion rate ( $\text{mol}/\text{m}^3/\text{s}$ )

PR: Precipitation rate ( $\text{mol}/\text{m}^3/\text{s}$ )

WCR: Water condensation rate ( $\text{m}^3/\text{m}^2/\text{s}$ )

$\delta$ : Liquid film thickness (m)

The liquid film thickness is assumed to be constant and is not linked to the condensation rate. Vitse calculated it with the following equation:

$$\delta = \left( \frac{\sigma}{g \times (\rho_l - \rho_g)} \right)^{0.5} \quad \text{Eq (7-10)}$$

With  $g$ : Gravitational acceleration ( $\text{m/s}^2$ )

$\sigma$ : Surface tension ( $\text{N/m}$ )

$\rho_l$  and  $\rho_g$ : Liquid and gas density respectively ( $\text{kg/m}^3$ )

The corrosion rate is first calculated using the electrochemical model developed by Nestic et al. in 1996 [25]. This mechanistic model takes into account the chemistry of the liquid (*i.e.* pH,  $\text{CO}_2$  solubility, etc) and the electrochemical reactions but does not cover the influence of the  $\text{FeCO}_3$  layer formation. The computational procedure gives the change in pH as the iron concentration increases, and the corresponding corrosion rate is calculated, allowing the prediction of the new concentration of iron ion at the next time step. The iteration continues until no further change in the iron ion concentration is computed. Vitse modified his corrosion equation in order to include the influence of corrosion product film on the corrosion rate once the saturation in  $\text{FeCO}_3$  is reached. It was done by introducing an empirical correcting factor  $K$  which would represent the covering effect of the  $\text{FeCO}_3$  film, underneath which no corrosion would occur. This factor was determined experimentally but was correlated with the scaling tendency (ratio of corrosion and precipitation rate).

$$\frac{d[\text{Fe}^{2+}]}{dt} = \frac{1}{\delta} \times [K \times CR - (1 - K) \times PR - WCR \times [\text{Fe}^{2+}]] \quad \text{Eq (7-11)}$$

With  $\text{Fe}^{2+}$ : Concentration of iron ion ( $\text{mol/m}^3$ )

T: Time (s)

CR: Corrosion rate ( $\text{mol}/\text{m}^3/\text{s}$ )

PR: Precipitation rate ( $\text{mol}/\text{m}^3/\text{s}$ )

WCR: Water condensation rate ( $\text{m}^3/\text{m}^2/\text{s}$ )

$\delta$ : Liquid film thickness (m)

K: Covering factor

The iteration procedure described above was used again until no significant change in  $\text{Fe}^{2+}$  concentration could be calculated. Vitse's method gave insight into how to model TLC phenomena and it constitutes a considerable improvement in the understanding of TLC without being a fully mechanistic corrosion model.

In 2007, Zhang et al. [83] published the first fully mechanistic approach on TLC modeling. The model covers the three main processes involved in top of the line corrosion phenomena: dropwise condensation, chemistry in the condensed water and corrosion at the steel surface. Since the condensation approach is drop-wise, the model is valid only for the 11-1 o'clock position in a pipeline. The condensation model is based on the heat and mass transfer theory and the approach is described in more detail in the previous chapter. The chemistry of the condensed liquid is established through standard chemical and thermodynamic equations [9]. The corrosion model is adapted from the mechanistic  $\text{CO}_2$  corrosion approach developed by Nordsveen et al. [26] and Nestic et al. [111-112]. Zhang stated that, from a statistical point of view, every point on the metal surface has the same probability of being covered by liquid droplets and, consequently, the entire surface is subject to uniform corrosion. This simplifies the mathematical approach from a three-dimensional situation (semi-hemispherical droplet) to a one-dimensional situation (liquid layer), as shown in Figure 153.

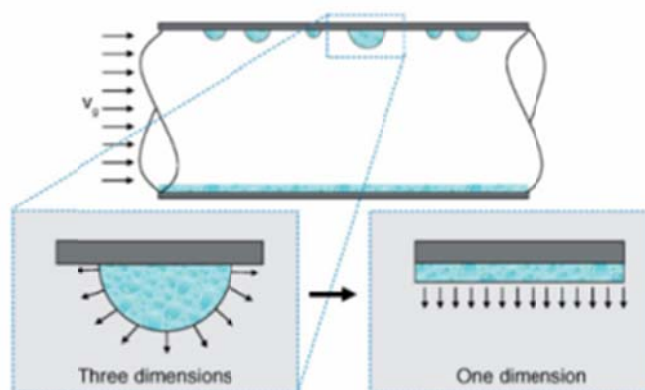


Figure 153: The simplification from a 3D (droplet) to 1D (liquid film) approach reproduced from (Reproduced from [83] - © NACE international 2007)

In Zhang's approach, the droplet growth is simulated by an increase in the liquid film with time until it reaches a calculated maximum size where the droplet disappears (falls or slides). The calculation then restarts with a minimum film thickness (corresponding to the minimum droplet size), and the cycle is carried out until the corrosion process reaches a steady state. The corrosion module includes chemical reactions (dissociation, dissolution and precipitation), transport of species to and away from the metal surface, and the electrochemical reactions at the metal surface. The main equations used are summarized below and constitute a set of non-linear coupled differential equations.

The expression for transport of species in the presence of chemical reactions, which is valid both for the liquid in the droplet and the porous film, can be described using the species conservation equation. Zhang simplifies the equation by assuming no convection (stagnant droplet) and by considering the effect of migration to be insignificant. The overall species conservation equation in the droplet becomes:

$$\frac{\partial \varepsilon C_i}{\partial t} = D_i \frac{\partial^2 (\kappa C_i)}{\partial x^2} + \varepsilon R_i \quad \text{Eq (7-12)}$$

With  $C_i$ : concentration of species  $i$  (mol/L),  
 $\varepsilon$ : volumetric porosity of the film, equal to 1 outside the corrosion layer,  
 $\kappa$ : Surface permeability of the film, equal to 1 outside the corrosion layer,  
 $D_i$ : Molecular diffusion of species  $i$  ( $m^2/s$ ),  
 $R_i$ : source or sink of species  $i$  (mol/L/s),  
 $t$ : time (s),  
 $x$ : spatial coordinate (m).

The porosity  $\varepsilon$  is calculated through a mass balance conducted on  $FeCO_3$  and by using the Van Hunnik equation [109] for  $FeCO_3$  dissolution/precipitation rate:

$$\frac{\partial \varepsilon}{\partial t} = - \frac{M_{FeCO_3}}{\rho_{FeCO_3}} R_{FeCO_3} \quad \text{Eq (7-13)}$$

With  $M_{FeCO_3}$ : Iron carbonate molecular weight (kg/mol)  
 $\rho_{FeCO_3}$ : Iron carbonate density ( $k/m^3$ )  
 $R_{FeCO_3}$ : Iron carbonate precipitation rate (mol/ $m^3/s$ )

The flux of species participating in the corrosion reactions is calculated with the following equation:

$$N_j = - \frac{i_j}{n_j F} \quad \text{Eq (7-14)}$$

With  $i_j$ : current density for species  $j$  ( $A/m^2$ )  
 $n_j$ : number of electrons exchanged for species  $j$   
 $F$ : faraday number (A.s/mol)  
 $N_j$ : Flux of species  $j$  (mol/ $m^2/s$ )

The current density of each corrosive species can be expressed as a function of the potential at the metal surface:

$$i = \pm i_0 \cdot 10^{\pm \frac{E - E_{rev}}{b}} \quad \text{Eq (7-15)}$$

With  $i_0$ : exchange current density,

$E_{rev}$ : reversible potential,

$b$ : tafel slope.

Zhang stated that the growth of the droplet is simulated by controlling the position of the vapor/liquid interface (vapor/liquid boundary layer) as shown in Figure 154.

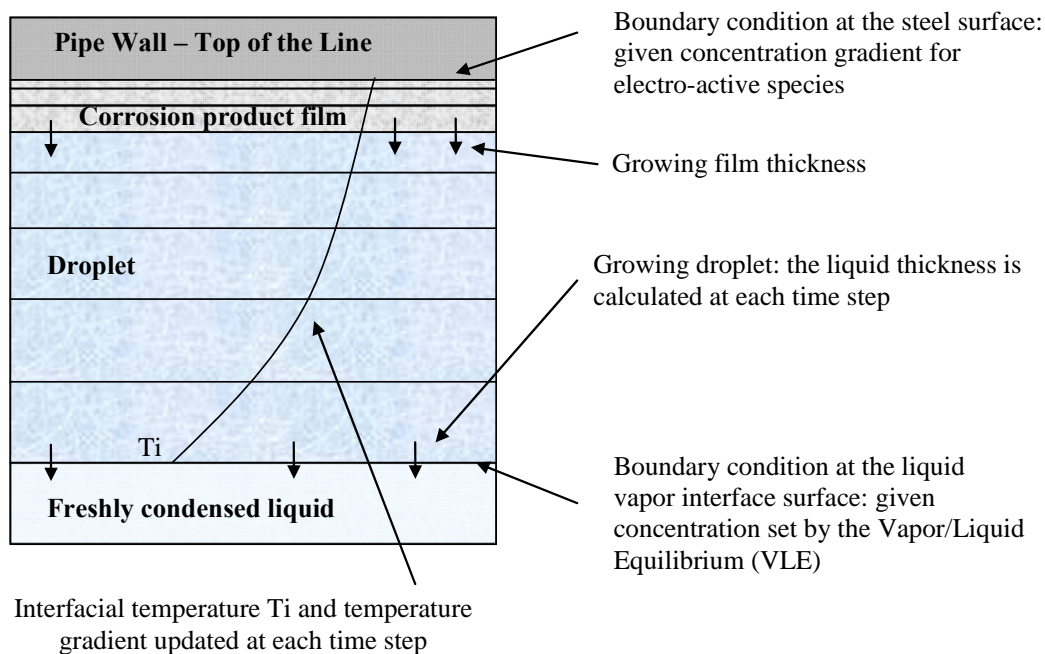


Figure 154: Schematic of the corrosion calculations in a growing droplet

Zhang's approach represents the most advanced attempt to model the mechanisms involved in TLC to date. It takes into account the most important parameters in CO<sub>2</sub> TLC: condensation rate, gas temperature, CO<sub>2</sub> partial pressure and acetic acid concentration.

Remita et al. [113] also extended the work proposed by Vitse et al. [77] and developed a model for CO<sub>2</sub> corrosion under a thin liquid film. It follows a mechanistic approach for the chemical and electrochemical side of the phenomena but assumes a homogeneous composition within the film. Like Vitse, Remita introduces a covering factor  $\theta$  in order to take into account the effect of FeCO<sub>3</sub> film formation, this factor being difficult to obtain.

Finally, overall guidelines on sweet and sour TLC prediction were proposed by Asher et al. in 2011 [114]. The importance of modeling the chemistry and the physics of the corrosion process was stressed. The corrosion model is based on the concept that, at steady state, the corrosion flux (flux of iron ions away from the surface) is equal to the FeCO<sub>3</sub> precipitation flux (*i.e.*, flux of iron ions required to form the corrosion product layer). No specifics were given on the algorithm or equations used.

#### 7.2.2.3 *Modeling of localized corrosion*

Even though great progress has been made over the years in the understanding of the TLC mechanisms, none of the models thus far tackle the occurrence and prediction of localized corrosion in TLC.

The top of the line is not the only situation where localized corrosion is encountered. Actually, a lot of research has already been undertaken on the study of mesa attack in single phase flow (a situation related to the bottom of the line). One of the first experimental studies on mesa attack [116] was conducted in 1998. The initiation and growth of the local attack on carbon steel was monitored with a video camera. It was found that a prerequisite of any local

attack is a formation of a partially protective  $\text{FeCO}_3$  scale. Corrosion would initiate underneath the porous layer and create small pits. The effect of flow was also found to be important in removing the damaged corrosion product film, as described in the schematic below. The pits would grow together and form larger mesa type features. The corrosion continues both laterally and in depth as long as no protective scale is re-formed at the bottom of the mesa attack.

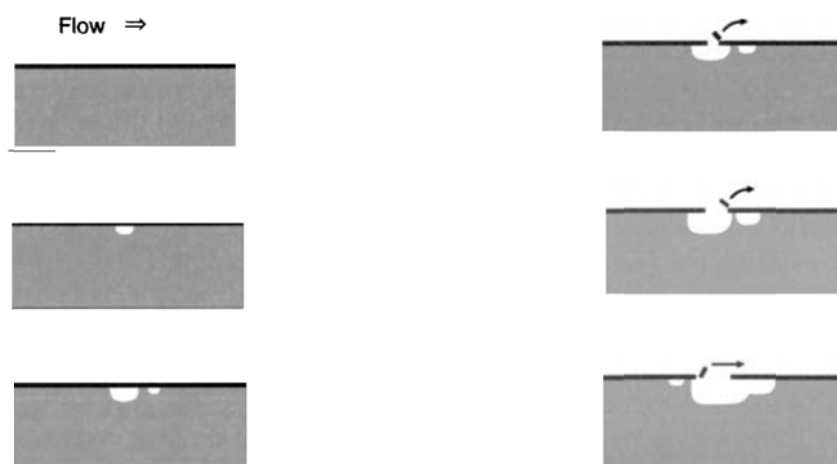


Figure 155: Mechanism for initiation and growth of mesa attack  
(Reproduced from [116] - © NACE international 1998)

The possibility of a galvanic affect between the bottom of the mesa attack feature (film-free) and the surrounding area covered with  $\text{FeCO}_3$  was also introduced. The induced difference in potential could accelerate the corrosion rate of the exposed steel.

In 1999, Schmitt et al. [117] completed a study focused on the effect of flow on localized attack growth. It was found that the wall shear stresses induced by the flow were an order of magnitude too low to cause breakdown of the corrosion product. Schmitt also stated that the conductivity of  $\text{FeCO}_3$  was too low to constitute a viable site for the cathodic reaction. This

means that the cathodic and the anodic reaction sites should both be located at the active surface of the mesa attack and that galvanic coupling should be unlikely.

Another strong advance in the understanding of CO<sub>2</sub> localized corrosion was achieved by Sun and Netic in 2000 [118]. A series of flow loop experiments performed at different partial pressures of CO<sub>2</sub> and pH was used to identify a zone where localized corrosion occurrence and propagation was most likely. Once again, the presence of a partially protective FeCO<sub>3</sub> was crucial, as under film-free or fully protective film conditions, no localized corrosion was observed (Figure 156). The scaling tendency (ratio of precipitation and corrosion rate) was introduced to quantify the likelihood of localized corrosion occurrence. The precipitation rate was directly derived for the FeCO<sub>3</sub> saturation level in the bulk phase, which could also be used to evaluate the protectiveness of the scale.

no film	partially protective film	fully protective film
High uniform attack	Low/high uniform attack	Low uniform attack
No localized attack	Localized attack	No localized attack

Figure 156: Mechanism for initiation and growth of mesa attack  
(Reproduced from [118] - © NACE international 2004)

Another major contribution in the understanding of localized corrosion was proposed by Han et al. in 2008 [119-122]. Using a novel experimental setup artificially simulating a pit, Han could actually measure the difference in potential between the film-covered surface and the film-free site of the bottom of the pit. He could also link the localized corrosion growth with a saturation level between 0.5 and 2, as Sun et al. [118] did. More importantly, Han stipulated that the pH of the solution trapped between the corrosion product layer and the steel was

actually much higher than the pH in the bulk, leading to the formation of thin iron oxide ( $\text{Fe}_3\text{O}_4$ ) film. This layer could provide an explanation for the significant increase in potential of the film-covered “passive” surface and the establishment of a galvanic cell with the active site of the pit. However, the existence of the iron oxide film has been debated, as attempts by several authors to identify the oxide layer were inconclusive at best [121, 123].

In 2008, Amri [85, 86], performed similar experiments in an effort to relate pit growth and environmental conditions, especially in the presence of acetic acid. It was found that the growth of the pit was related to the depletion of the acetic acid concentration inside the pit. It was also stated that the growth should stop once the pit reaches a certain depth. Many of the observations made by the author were typical of a TLC scenario and were put forward to explain TLC stabilization. Consequently, this study constituted the first attempt to adapt the localized corrosion process to top of the line corrosion.

One of the objectives of this research work is to develop a mechanistic model for the prediction of localized corrosion in a TLC scenario. This model is based on previous modeling works mentioned in the literature review and on the knowledge acquired throughout the experimental test matrices. The approaches and assumptions selected so far are discussed in the section below.

### 7.3 Descriptive model of localized TLC

#### 7.3.1 *Summary of experimental observations*

The experience gathered through the different experiments performed on this topic highlight the following general comments on the characteristics of localized corrosion in  $\text{CO}_2$ -dominated TLC:

- Three main “modes” of corrosion are observed in  $\text{CO}_2$ -dominated TLC:

1. Little to no corrosion, neither uniform nor localized, is encountered due to the presence of a protective  $\text{FeCO}_3$  layer on the entire steel surface area.

This case is often observed if the environment is not very aggressive (mainly low WCR and acetic acid content but also low  $\text{CO}_2$  partial pressure) and if the steel temperature is high.

2. Localized corrosion, with varying rates, occurs on the steel surface, which is only partially covered with protective  $\text{FeCO}_3$ .

This case is encountered at moderate and high WCRs and in the presence of acetic acid. The steel can have a 15-25°C temperature difference with the gas. Pitting rates can reach several mm/year, depending mainly on the steel temperature, and the bottom of the pit is often “ $\text{FeCO}_3$  free”.

3. Uniform corrosion, affecting the entire steel surface area, can also be observed.

This case occurs at very low steel temperature (or/and very high WCR). Some type of non-protective, non-adherent  $\text{FeCO}_3$  layer can form. The steel corrodes uniformly but at a low rate due to the low steel temperature.

- There is no significant correlation between the mere presence of a droplet and the extent of corrosion. Although droplets of condensed water always form at the same location on the steel surface, no localized corrosion was observed in a number of cases. The steady supply of freshly condensed liquid (*i.e.*, corrosive liquid) seems to be the main parameter responsible for the loss of protectiveness of the  $\text{FeCO}_3$  layer.
- The occurrence of localized corrosion is linked to the presence of a semi-protective corrosion product layer. Pits observed are usually surrounded by areas that are not corroded and covered with very dense and tightly packed  $\text{FeCO}_3$  crystals. As the corrosion

process develops, pits grow laterally and in depth, undermining the  $\text{FeCO}_3$  layer. Isolated pits tend to coalesce and form large localized corrosion features.

### 7.3.2 Model basis

The corrosion features observed in the field can be so large than the corrosion process is often referred to as a “**localized uniform corrosion**” instead of as purely “**localized corrosion**”. In the first case, the corrosion mechanism is driven by the corrosiveness of the solution and therefore by the process of water condensation. In the second case, it is driven by a difference of potential between bare steel and steel covered with corrosion product film. These two scenarios are discussed briefly below.

1. **Localized corrosion - Galvanic corrosion approach:** this mechanism involves a damaged “protective” film and a difference in potential between the exposed steel and the surrounding area covered by the corrosion product. The ensuing galvanic effect is the driving force for the corrosion attack. The mechanism developed by Han [120, 122] identified the presence of a thin iron oxide ( $\text{Fe}_3\text{O}_4$ ) film between the  $\text{FeCO}_3$  layer and metal surface, establishing a galvanic cell with the active site of the pit. The existence of this oxide layer has been debated and the potential difference could simply be due to the presence of  $\text{FeCO}_3$  [123]. Several attempts were made in order to confirm the presence of this “layer” on the  $\text{FeCO}_3$ -covered area and its absence at the bottom of the pit with TLC steel samples (Figure 157). They were performed by cutting a thin slice of material at the steel/ $\text{FeCO}_3$  interface of a cross section with a Focused Ion Beam (FIB) followed by analysis of the element distribution with a Transmission Electron Microscope (TEM). However, these attempts were not successful due to technical difficulties related to the large thickness of the  $\text{FeCO}_3$  layer and the size of localized features typical for TLC. Simple line EDS scans

performed on cross sections for this study (Figure 147) did not reveal the presence of an iron oxide layer, although the instrument would not be accurate enough to detect changes on a nanometer scale.

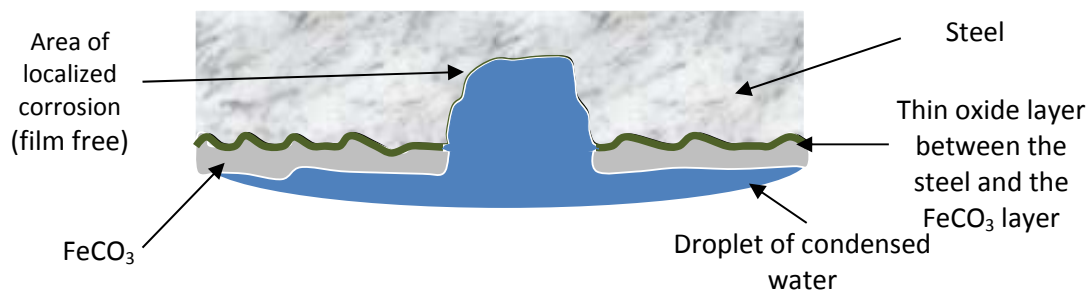


Figure 157: Schematic representation of the galvanic corrosion approach

In addition, this approach cannot be applied to the top of the line corrosion for the main reason that the electrolyte is not sufficiently conductive to “carry” the current at any significant level [124]. The condensed water is comprised of relatively low concentrations of  $\text{HCO}_3^-$ ,  $\text{CO}_3^{2-}$  and  $\text{OH}^-$  ions, which are set by the chemistry of a  $\text{CO}_2$  buffer.  $\text{Fe}^{2+}$  ions are indeed released due to the corrosion process but are also consumed by the formation of  $\text{FeCO}_3$ . The maximum concentration of  $\text{Fe}^{2+}$  is controlled by the saturation in  $\text{FeCO}_3$  and cannot reach more than 200-400 ppm of “free”  $\text{Fe}^{2+}$  ions in solution depending on the temperature. Examples of the maximum concentration of  $\text{Fe}^{2+}$  ions, which can be present at  $\text{FeCO}_3$  saturation, are shown in Figure 158 and Figure 159 at two different steel temperatures (25 and 70°C). Any galvanic effect is consequently disregarded in the modeling approach.

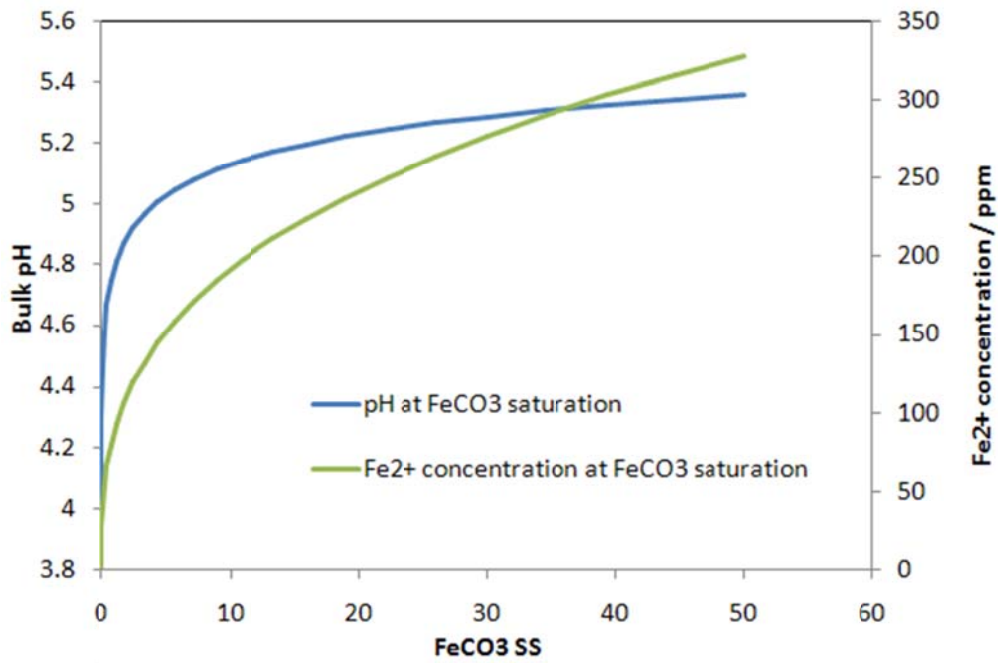


Figure 158: Fe<sup>2+</sup> concentration and pH at different FeCO<sub>3</sub> saturation levels and different temperature - T=25°C, pCO<sub>2</sub>=3 bars

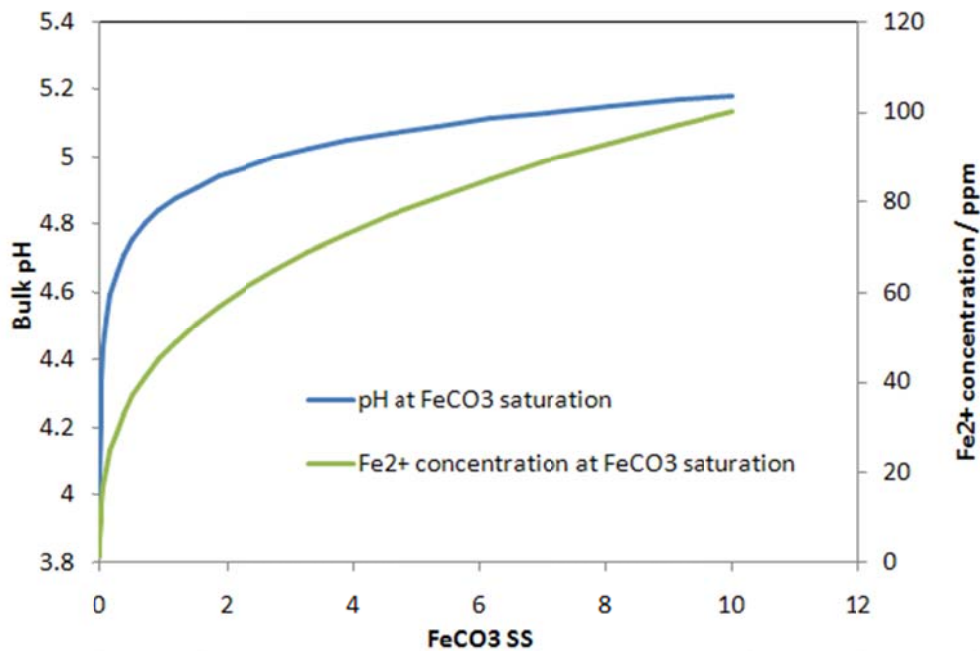


Figure 159: Fe<sup>2+</sup> concentration and pH at different FeCO<sub>3</sub> saturation levels and different temperature - T=70°C, pCO<sub>2</sub>=3 bars

2. **Localized uniform corrosion - condensation approach:** The corrosion is initiated by the condensation of water vapor: the rates are high at the beginning of the process and decrease as the pH of the condensed water increases. Conditions are met rapidly in order to saturate the aqueous phase with regard to  $\text{FeCO}_3$  and a layer forms on the steel surface. The rate of droplet renewal then affects the  $\text{FeCO}_3$  saturation, which can lead to different degrees (rates, surface coverage) of localized corrosion. It is possible that the effective condensation rate is “artificially” increased by defects in the  $\text{FeCO}_3$  layer (and consequent capillary effects), where condensed water accumulates preferentially. However, it is not believed that this could greatly affect the localized corrosion rates, as discussed in CHAPTER 5. This scenario is presented in the schematic below.

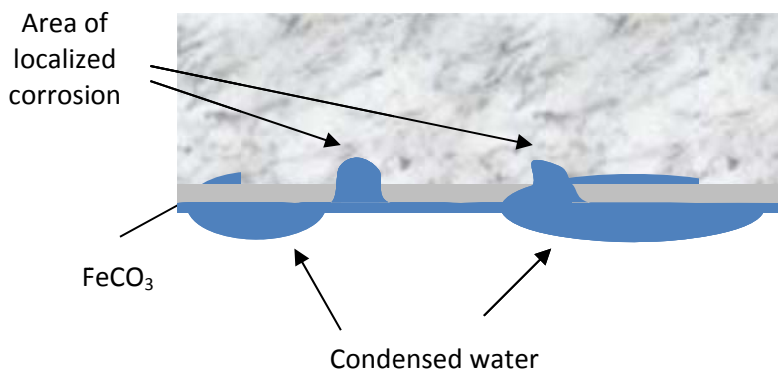


Figure 160: Schematic representation of the localized condensation approach

Experimental work clearly shows that the presence of large droplets of condensed water does not affect the corrosion process as long as the rate of condensation is low. If the environment is aggressive (high WCR, high HAC), localized corrosion is observed randomly on the wetted metal surface. Locally higher water condensation rates can theoretically be achieved

in specific places on the metal surface but this scenario is not required to lead to high levels of localized corrosion.

### 7.3.3 Model overall narrative

The following narrative is then proposed to explain the initiation and propagation of localized corrosion in a sweet TLC environment. It is inspired by an approach originally proposed by Olsen [64].

1. The first drop of water condensing on the steel leads to uniform corrosion on the metal surface. The corrosiveness of the water slowly reduces with time as  $\text{Fe}^{2+}$  ions accumulate in solution leading to an increase in pH.  $\text{Fe}_3\text{C}$  is left behind as the product of the ferrite phase dissolution.
2. If  $\text{FeCO}_3$  saturation is never reached (due to low steel temperature, high organic acid content and/or high condensation rate), the corrosion is uniform and the rate is constant, controlled by the corrosion reaction kinetics.
3. If the  $\text{FeCO}_3$  saturation level reaches one (or a slightly supersaturated level),  $\text{FeCO}_3$  crystals begin to precipitate and the uniform corrosion further decreases due to limitations in mass transfer through the corrosion product layer. Higher condensation rates increase the time needed to reach saturation and the steel is consequently exposed to the corrosive environment for a longer time.
4. Since the uniform corrosion rate is now low and fresh water is constantly added, the bulk liquid phase can become slightly under-saturated, leading part of the layer to re-dissolve. The steel surface can become segregated between areas well-protected by the  $\text{FeCO}_3$  layer and areas suffering from “bare steel” corrosion.

5. The chemistry in the condensed liquid cannot change with time (or can only oscillate around the  $SS_{\text{FeCO}_3}$  level), as the excess  $\text{Fe}^{2+}$  ions should rapidly either be consumed to form more  $\text{FeCO}_3$  or be diluted by the constant flux of condensed water. Consequently, the corrosion rate, or more accurately the flux of  $\text{Fe}^{2+}$  ions in  $\text{mol/m}^2/\text{s}$ , becomes constant, controlled by the  $\text{FeCO}_3$  saturation.
6. Unless the  $\text{Fe}^{2+}$  solubility is very high (due to low steel temperature, high organic acid content and/or high condensation rate), the corrosion rate corresponding to a chemistry “at  $\text{FeCO}_3$  saturation” is sustainable only on part of the steel surface – hence becoming localized in nature.
7. Active corrosion occurs preferentially in areas where the  $\text{FeCO}_3$  layer is damaged or on steel.  $\text{FeCO}_3$  precipitation also happens preferentially on sites already covered with  $\text{FeCO}_3$  crystals. The balance of the flux of  $\text{Fe}^{2+}$  ions (from corrosion and dilution in the condensed water) controls how much of the steel surface can corrode actively and prevent any dissolution of the already formed  $\text{FeCO}_3$ . It also controls whether the localized corrosion will propagate or cease.

#### 7.3.4 Localized TLC model development

This section presents the details of the model of “uniform localized corrosion” developed to describe the process of localized corrosion in sweet TLC environments. The model narrative was implemented in a Visual Basic for Application format and linked to the FREECORP platform which is described in APPENDIX E.

The model is based on the following assumptions:

- The maximum level of  $\text{FeCO}_3$  saturation inside the droplet cannot exceed a value of 10.

- This means that the droplet pH and  $\text{Fe}^{2+}$  concentration also have maximum “saturation” values set by the  $SS_{\text{FeCO}_3}$ .
- In theory,  $SS_{\text{FeCO}_3}$  cannot exceed one as  $\text{FeCO}_3$  should precipitate. However, practical laboratory experience shows that super-saturation values of 5-10 are often sustainable, especially at high temperature [125]. However, higher levels of super-saturation can be maintained at lower temperatures.
- As a consequence, the bare steel corrosion rate, corresponding to this specific environment, is constant once the chemistry inside the droplet is stable.
- On the  $\text{FeCO}_3$ -covered steel surface, where the corrosion rate is assumed to be zero, the active localized corrosion site experiences active corrosion. The electrochemical FREECORP model [126] is used to calculate the corrosion on these “ $\text{FeCO}_3$ -free” areas.
- The droplet is assumed to be homogenous. This assumption is valid except close to the metal surface and at the liquid/vapor interface. The corrosion model FREECORP incorporates the gradient of concentration at the metal surface through the use of the mass transfer coefficient [126].
- The different chemical reactions involved in the  $\text{CO}_2/\text{H}_2\text{O}/\text{CH}_3\text{COOH}$  system considered are listed in Section 1.3 ( $\text{H}_2\text{S}$  is not considered in this section):

#### 7.3.4.1 Step 1 – Initial uniform corrosion

The first droplets of condensed water form at the steel surface due to the gradient of temperature between the steel and the vapor phase. The vapor condenses, forming small droplets, which rapidly coalesce to form larger droplets. The entire surface is wetted either by a thin film or by large droplets.

The chemistry of freshly condensed water is very aggressive and the steel corrodes uniformly at a high rate initially. The release of  $Fe^{2+}$  ions in solution leads to an increase in pH and a consequent decrease in corrosion. The dilution effect due to the continuous water condensation retards the rise in  $Fe^{2+}$  concentration. In theory, if the WCR is high enough, it could prevent any significant buildup of the  $Fe^{2+}$  concentration, but this is not practically observed (except at low temperature).

Figure 161 represents the evolution of pH,  $SS_{FeCO_3}$  and corrosion rate during this initial step. The FREECORP corrosion rate responds to the change in bulk droplet pH but also to the rise in  $Fe^{2+}$  concentration and the formation of a not yet protective  $FeCO_3$  on the entire steel surface.

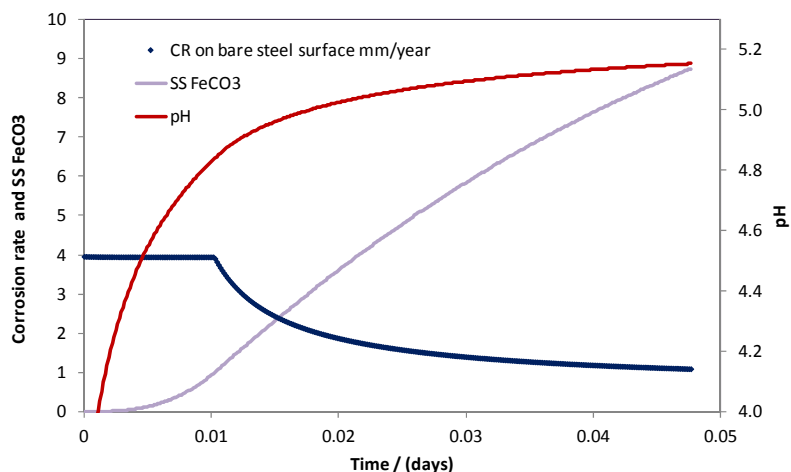


Figure 161: Initial steps of uniform corrosion on “film-free” steel surface  
 $T_{steel}=35^{\circ}C$ ,  $WCR=1\text{ ml/m}^2/s$ ,  $pCO_2=3\text{ bars}$ ,  $SS_{FeCO_3}\text{ max}=10$   
 100% of the steel surface is corroded uniformly – No localized corrosion

A mole balance is performed on the  $Fe^{2+}$  ion concentration in order to represent the evolution of the system:

$$\frac{d[Fe^{2+}]}{dt} = \frac{1}{\delta} \times [CR_{BareSteel} - WCR \times [Fe^{2+}]] \quad \text{Eq (7-16)}$$

With:  $Fe^{2+}$ : Concentration of iron ion ( $mol/m^3$ )

$d[Fe^{2+}]$ : Small change in  $Fe^{2+}$  concentration around the saturation value ( $mol/m^3$ ).

t: Time (s)

$CR_{Bare\ Steel}$ : Corrosion rate calculated by Freecorp ( $mol/m^2/s$ )

WCR: Water condensation rate ( $m^3/m^2/s$ )

$\delta$ : Liquid film thickness, assumed constant at 0.01 (m)

The actual volume of the condensed water film has no impact on the determination of sustainability of localized corrosion. Consequently, the thickness of the liquid film is set at a fixed value.

#### 7.3.4.2 Step 2 – Formation and breakdown of the $FeCO_3$ layer

Once the  $FeCO_3$  super saturation reaches the value of 10, the concentration of  $Fe^{2+}$  cannot rise any further and any additional  $Fe^{2+}$  ions released in solution precipitate as  $FeCO_3$  as it cannot exist as “free” solution. A distinction is made here between the “free  $Fe^{2+}$  ions” (which can exist freely in solution) and the “excess  $Fe^{2+}$  at saturation” (which should immediately precipitate). It is understood that the reaction kinetics play an important role and that the transition cannot be as sudden as proposed.

The  $FeCO_3$  layer forms at the metal surface, initially uniformly since the droplet chemistry is assumed to be uniform. This is verified by experimental evidence which shows a rather uniform  $FeCO_3$  layer covering the entire metal surface of a steel sample exposed to TLC for a short duration (1-2 days).

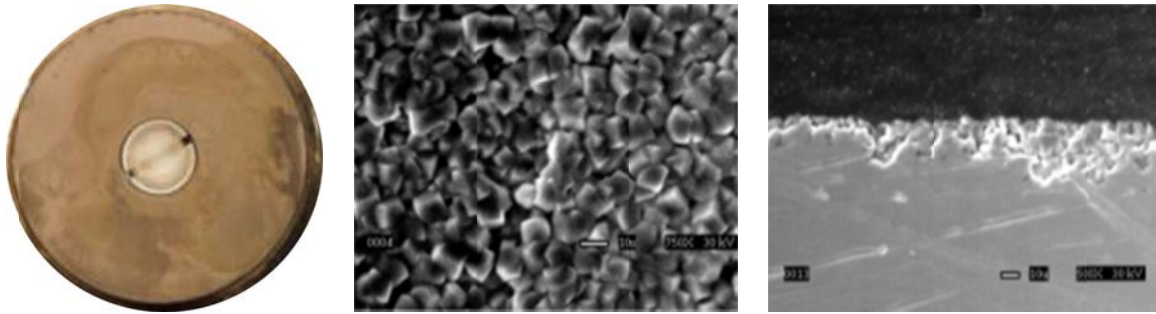


Figure 162: Formation of a uniform FeCO<sub>3</sub> layer after short term exposure  
 T<sub>gas</sub>=70°C, WCR=0.25 ml/m<sup>2</sup>/s, pCO<sub>2</sub>=8 bars, Undissociated HAc=0 ppm  
 Exposure time: 2 days – No Localized corrosion

As the FeCO<sub>3</sub> forms on the metal surface, a mass transfer barrier is created, which decreases the corrosion rate and consequently the flux of Fe<sup>2+</sup> ions in solution. The water condensation is not affected by the FeCO<sub>3</sub> layer formation, diluting the Fe<sup>2+</sup> concentration and decreasing the SS<sub>FeCO<sub>3</sub></sub>, which could reach an under-saturated level. The assumption here is that the newly formed FeCO<sub>3</sub> starts dissolving back into solution in order to maintain the FeCO<sub>3</sub> saturation. The dissolution of FeCO<sub>3</sub> may not be uniform on the steel surface and some areas would expose the bare steel while others would remain covered, as shown in the drawing below.

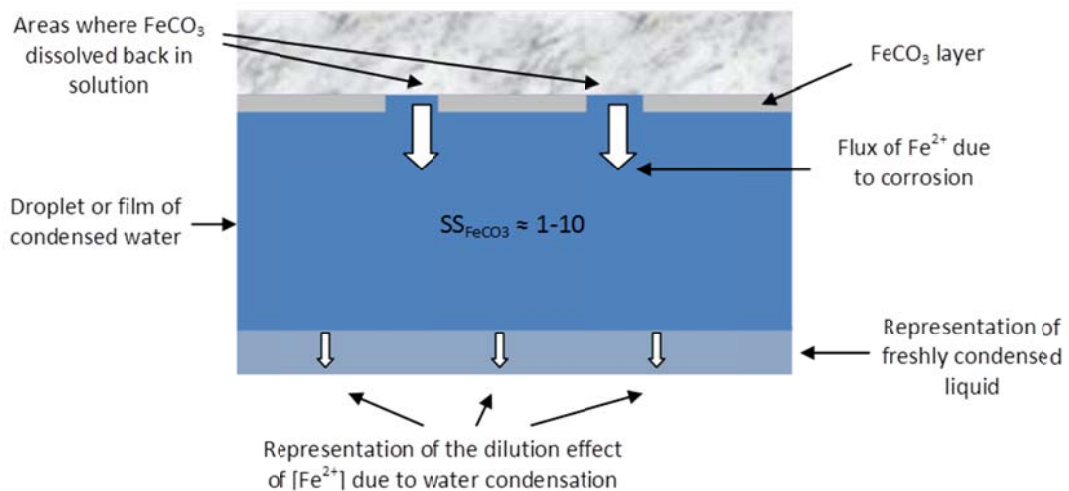


Figure 163: Schematic representation of the initiation step of localized corrosion at the top of the line

The mole balance on the  $Fe^{2+}$  concentration becomes, with the maximum surface area affected by localized  $A_{Localized}$  corrosion being an unknown variable:

$$\frac{d[Fe^{2+}]}{dt} = \frac{1}{\delta} \times \left[ \frac{A_{Localized}}{A_{Total}} \times CR_{BareSteel} - WCR \times [Fe^{2+}] \right] \quad \text{Eq (7-17)}$$

with  $A_{Localized}$ : Area not protected by  $FeCO_3$  (bare steel) ( $m^2$ )

$A_{Total}$ : Area wetted by droplet ( $m^2$ )

The  $FeCO_3$  precipitation rate should also be taken into account as a sink of  $Fe^{2+}$  ions. It is calculated using the equation developed by Sun [27]:

$$PR = e^{\frac{B-E_A}{RT}} \times K_{sp} \times (s-1) \quad \text{and} \quad s = \frac{[Fe^{2+}] \times [CO_3^{2-}]}{K_{sp,FeCO_3}} \quad \text{Eq (7-18)}$$

with PR: Precipitation rate converted in  $mol/m^2/s$

B: Constant (28.2)

$E_A$ : Activation Energy (64850 J/mol)

R: Ideal gas law (J/K/mol)

s:  $FeCO_3$  saturation

The choice of the expression of the equilibrium constant governing the iron carbonate precipitation/dissolution ( $K_{sp, FeCO_3}$ ) is also important, as many empirical equations exist. Recent work proposed by Sun [27] suggests using the equation presented in Section 1.5.

Taking into account the precipitation rate, the mole balance on the  $Fe^{2+}$  concentration becomes:

$$\frac{d[Fe^{2+}]}{dt} = \frac{1}{\delta} \times \left[ \frac{A_{Localized}}{A_{Total}} \times CR_{BareSteel} - \left(1 - \frac{A_{Localized}}{A_{Total}}\right) \times PR - WCR \times [Fe^{2+}] \right] \quad \text{Eq (7-19)}$$

with PR: Precipitation rate ( $mol/m^2/s$ )

Since the  $\text{FeCO}_3$  supersaturation is never allowed to exceed 10, the  $\text{FeCO}_3$  precipitation rate term has very little influence on the overall balanced equation.

Whether or not the localized corrosion will initiate is the topic of the next section.

#### 7.3.4.3 Step 3 – Determination of the sustainability of localized corrosion

Once the  $\text{FeCO}_3$  saturation reaches the value of 10, it is not permitted by the model to go further since it is assumed that any excess  $\text{Fe}^{2+}$  ions will be used for  $\text{FeCO}_3$  precipitation. At that point, the chemistry in the condensed water reaches its “saturation level” and the pH and the  $\text{Fe}^{2+}$  concentration become constant, as is the flux of  $\text{Fe}^{2+}$  generated by corrosion and the flux of  $\text{Fe}^{2+}$  “consumed” by precipitation.

Any buildup of  $\text{Fe}^{2+}$  concentration above the saturation value translates into overwhelming  $\text{FeCO}_3$  precipitation and the impossibility of sustained localized corrosion. If the  $\text{Fe}^{2+}$  concentration oscillates around the saturation value, localized corrosion is possible.

The steady state version of Equation Eq (7-19) can be used as the criterion to determine how much of the steel surface area can sustain localized corrosion (bare steel corrosion) under the conditions simulated:

$$\frac{A_{Localized}}{A_{Total}} \times CR_{BareSteel} - \left(1 - \frac{A_{Localized}}{A_{Total}}\right) \times PR = WCR \times [Fe^{2+}]_{Saturation} \quad \text{Eq (7-20)}$$

$$A_{Localized} = \frac{A_{Total} \cdot (WCR \times [Fe^{2+}]_{Saturation} + PR)}{CR_{BareSteel} - PR} \quad \text{Eq (7-21)}$$

The percentage of surface area affected by localized corrosion is set as an input and the model predicts if localized corrosion is sustainable in this condition. In Figure 164, the percentage area affected by localized corrosion is set at 50% ( $A_{Localized}/A_{Total}=50\%$ ). The

concentration of  $\text{Fe}^{2+}$  ions released in solution clearly exceeds the "saturation" concentration.

This is a sign that localized corrosion cannot be sustained on 50% of the surface area.

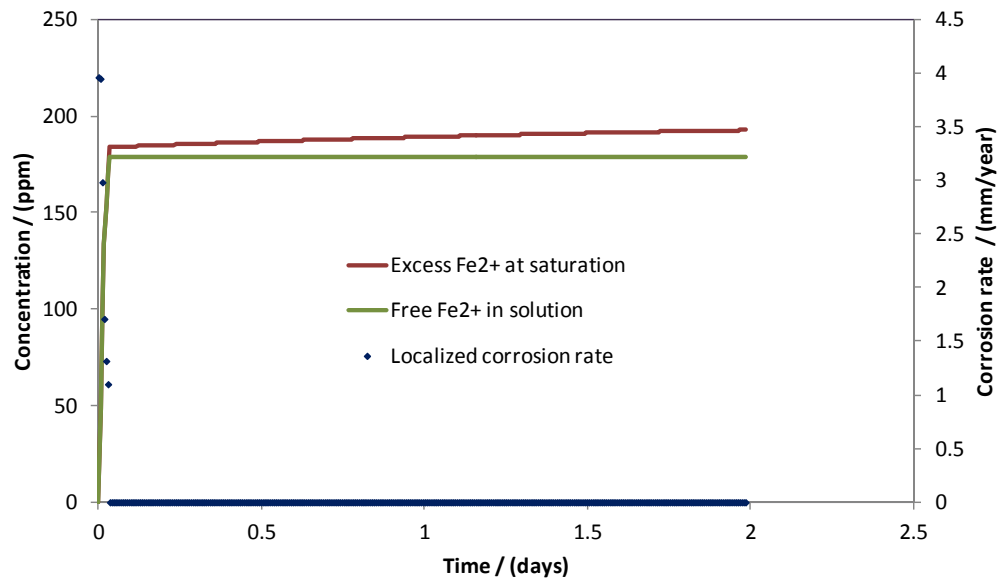


Figure 164: Unsustainable localized corrosion  
 $T_{\text{steel}}=35^{\circ}\text{C}$ ,  $\text{WCR}=0.05 \text{ ml/m}^2/\text{s}$ ,  $\text{pCO}_2=3 \text{ bars}$ ,  $\text{SS}_{\text{FeCO}_3} \text{ max}=10$ ,  $A_{\text{Localized}}=4\%$   
 Localized corrosion cannot not be sustained on 50% of the surface area

Figure 165 to Figure 167 present examples on how the model calculates the likelihood of localized corrosion based on environmental conditions.

- If less than 5% of the surface area remains "film-free" and actively corroded ( $A_{\text{Localized}}/A_{\text{Total}} < 5\%$ ), then it is likely that the localized corrosion will be unsustainable (Figure 165). This is the case at very low WCRs. Because the WCR is never zero, the flux of  $\text{Fe}^{2+}$  ions coming from the steel cannot be zero, since the  $\text{FeCO}_3$  saturation level has to be maintained.

- If  $A_{\text{Localized}}/A_{\text{Total}} > 5\%$ , sustainable localized corrosion is likely (Figure 166). In the experiments performed for this study, this situation was clearly encountered at high WCR and high steel temperature (above  $0.4 \text{ mL/m}^2/\text{s}$  and  $30^\circ\text{C}$ , respectively).
- If 100% of the surface area can corrode ( $A_{\text{Localized}}=A_{\text{Total}}$ ), then the corrosion is purely uniform (Figure 167). This is mostly the case at very low steel temperature, which is often associated with very high WCR and low fluid temperature.

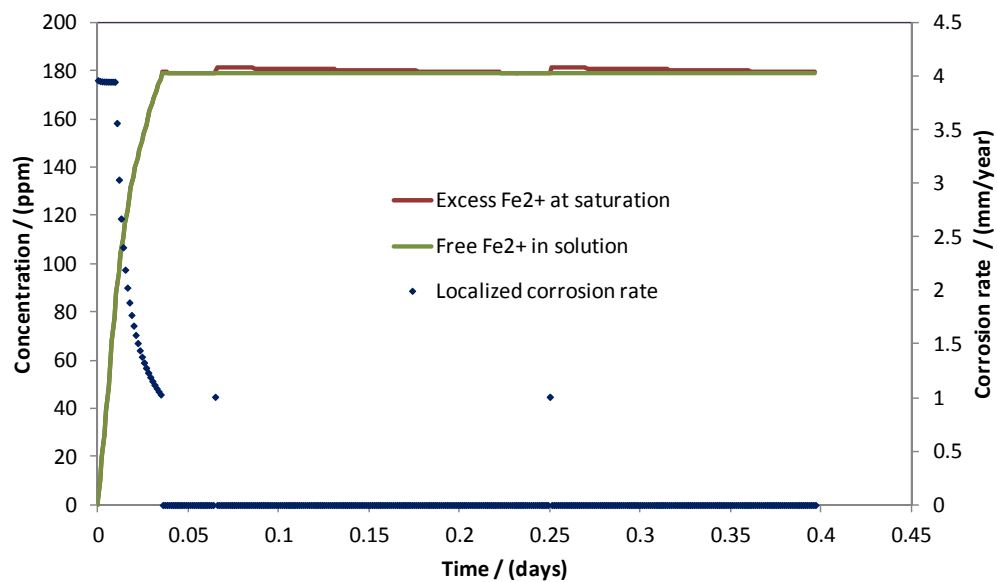


Figure 165: Unsustainable localized corrosion

$T_{\text{steel}}=35^\circ\text{C}$ ,  $\text{WCR}=0.05 \text{ ml/m}^2/\text{s}$ ,  $p\text{CO}_2=3 \text{ bars}$ ,  $\text{SS}_{\text{FeCO}_3} \text{ max}=10$ ,  $A_{\text{Localized}}=3\%$   
 3% of the steel surface can sustain localized corrosion at rate of 1 mm/year

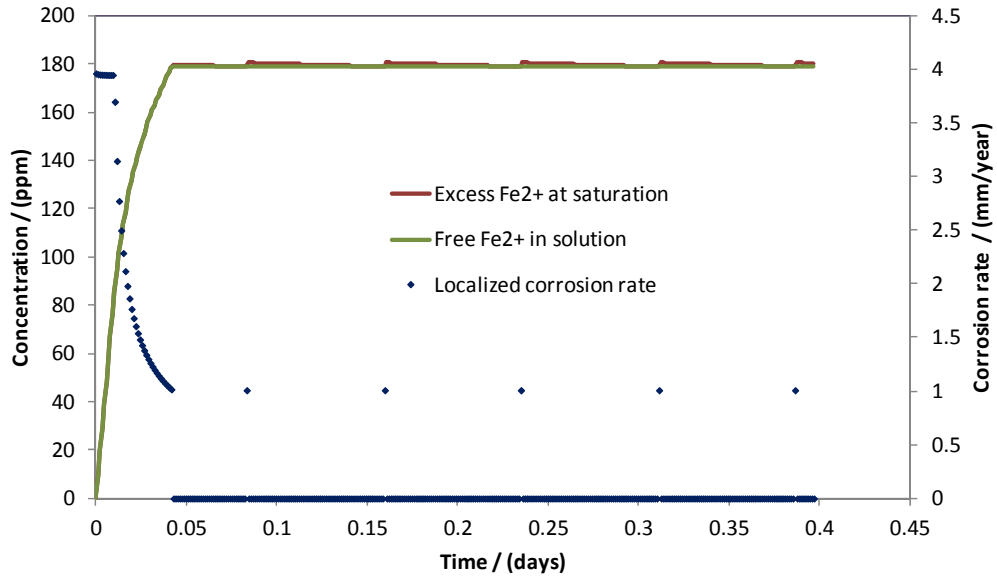


Figure 166: Sustainable localized corrosion  
 $T_{\text{steel}}=35^{\circ}\text{C}$ ,  $\text{WCR}=0.5 \text{ ml/m}^2/\text{s}$ ,  $p\text{CO}_2=3 \text{ bars}$ ,  $\text{SS}_{\text{FeCO}_3} \text{ max}=10$ ,  $A_{\text{Localized}}=35\%$   
 35% of the steel surface can be corroded locally at a rate of 1 mm/year

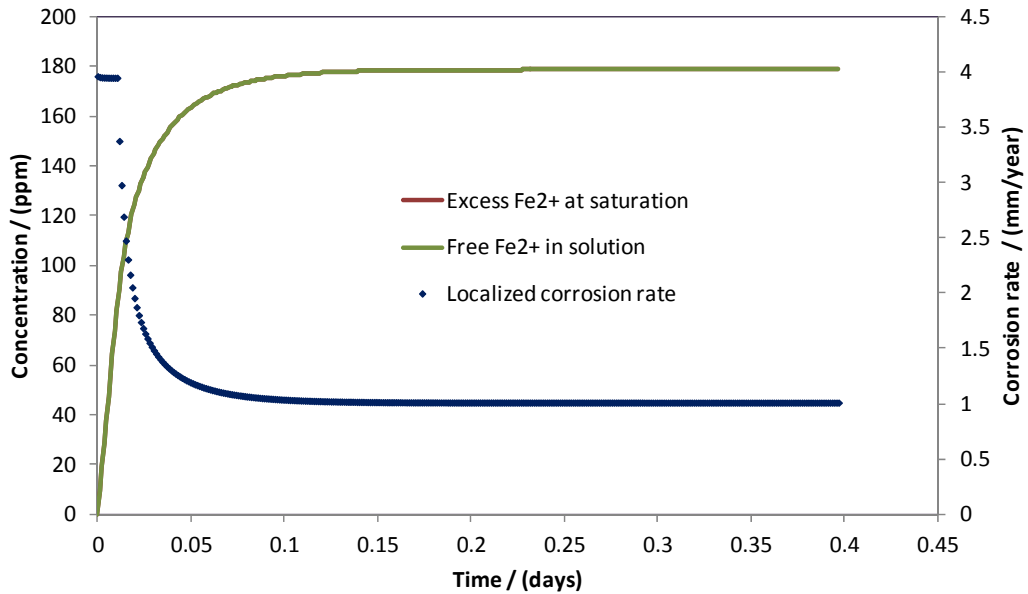


Figure 167: Sustainable uniform corrosion  
 $T_{\text{steel}}=35^{\circ}\text{C}$ ,  $\text{WCR}=1.4 \text{ ml/m}^2/\text{s}$ ,  $p\text{CO}_2=3 \text{ bars}$ ,  $\text{SS}_{\text{FeCO}_3} \text{ max}=10$ ,  $A_{\text{Localized}}=100\%$   
 100% of the steel surface can sustain a corrosion of 1 mm/year

#### 7.3.4.4 Step 4 – Localized corrosion propagation

The pit initially propagates in depth as the immediate surroundings are covered by protective  $\text{FeCO}_3$ . However, it is expected that, as the localized process goes on, the corrosion will also progress laterally, underneath the already existing  $\text{FeCO}_3$  layer. Although the overall flux of  $\text{Fe}^{2+}$  ions should remain constant in order to maintain the  $\text{FeCO}_3$  saturation level, the steel wall thickness loss rate will effectively decrease with time. Limitation in mass transfer may also become significant depending on the overall morphology of the pit:

- Deep narrow pits would not be sustainable in this scenario.
- Large mesa-type features are more likely to be encountered.

#### 7.3.5 Model validation

The conditions of the experiments performed in Section 4.4 were used to validate the model. Figure 168 presents the comparison between localized corrosion rates predicted by the model and those measured during the experiments. The range of corrosion rate is in good agreement, with lower gas temperatures generally leading to lower corrosion rates and higher acetic acid content leading to higher corrosion rates. However, at a given gas temperature, the model predicts lower corrosion rates as the steel temperature decreases (*i.e.* when the WCR is increasing), which is contradictory to laboratory experience. The dependency of the FREECORP model on temperature is not in question here. The discrepancy most likely comes from simplifications made for the model regarding localized feature morphologies. In this approach, corrosion rates are equated to steel penetration rates. Mass transfer limitations encountered for narrow pits (often associated with low WCR and steel higher temperature) should limit the steel penetration rate. This limitation should disappear when most of the steel surface is affected by localized corrosion.

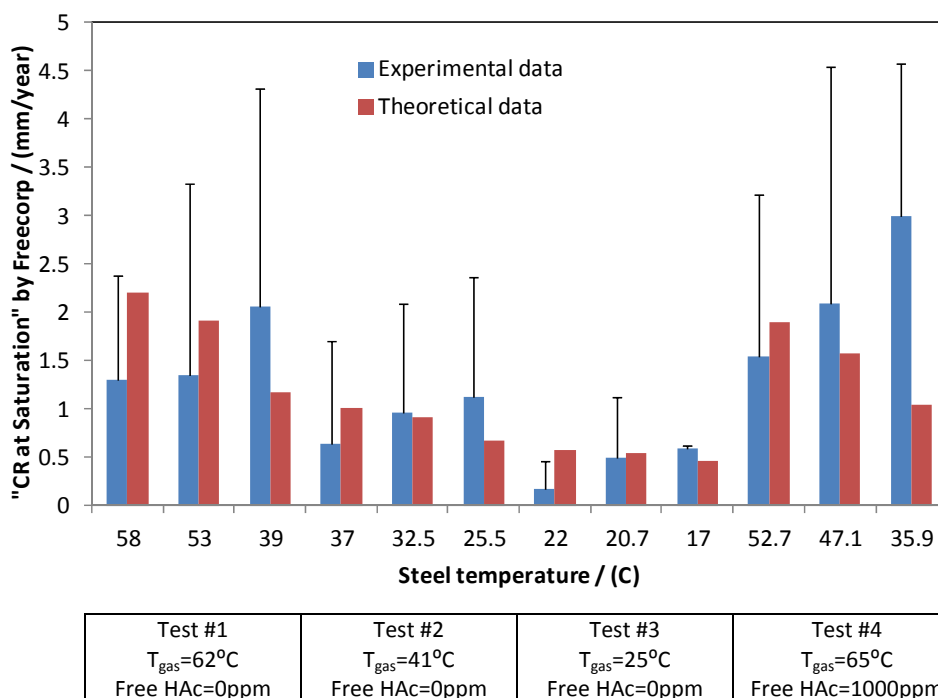
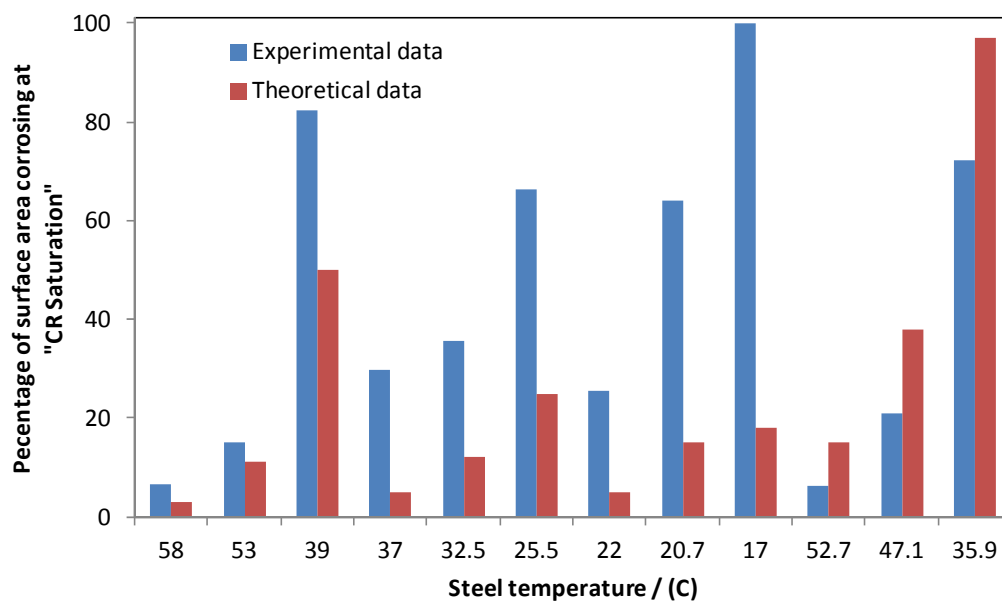


Figure 168: Model validation / Comparison between experimental data and model predictions  
 $SS_{\text{FeCO}_3} \text{ max}=10$

Figure 169 presents the comparison in terms of percentage area affected by localized corrosion between predictions and experiments. At a maximum  $\text{FeCO}_3$  supersaturation of 10, there is quite good agreement at high gas temperatures (Tests #1 and #4 with  $T_{\text{gas}}=60^{\circ}\text{C}$ ). However, the agreement is not as good at lower gas temperatures (Tests #2 and #3, with  $T_{\text{gas}}=42$  and  $25^{\circ}\text{C}$ , respectively). This discrepancy most likely comes from the assumption made about the maximum  $\text{FeCO}_3$  supersaturation level that can be effectively sustained. While a number of experimental data validate the  $SS_{\text{FeCO}_3}$  maximum value of 10 at high temperatures [125], published data obtained at lower temperatures are scarcer. However, it is fully expected that the  $SS_{\text{FeCO}_3}$  maximum value should be higher as the temperature decreases, following the trend of  $\text{FeCO}_3$  solubility. Figure 170 presents simulation results obtained with different levels of

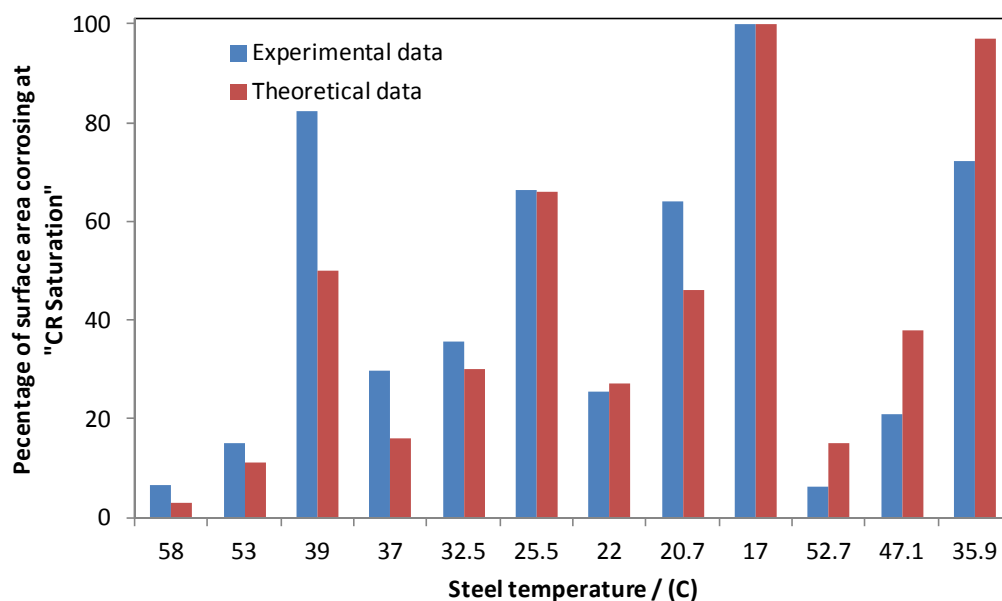
$SS_{FeCO_3}$  maximum value:  $SS_{FeCO_3} \text{ max}=10$  at  $T_{gas}=60^\circ\text{C}$ ;  $SS_{FeCO_3} \text{ max}=26$  at  $T_{gas}=42^\circ\text{C}$ ; and  $SS_{FeCO_3} \text{ max}=53$  at  $T_{gas}=25^\circ\text{C}$ . Here the agreement with experimental data is much better.



Test #1 $T_{gas}=62^\circ\text{C}$ Free HAc=0ppm	Test #2 $T_{gas}=41^\circ\text{C}$ Free HAc=0ppm	Test #3 $T_{gas}=25^\circ\text{C}$ Free HAc=0ppm	Test #4 $T_{gas}=65^\circ\text{C}$ Free HAc=1000ppm
--	--	--	---

Figure 169: Model validation / Comparison between experimental data and model predictions

$SS_{FeCO_3} \text{ max}=10$



Test #1 $T_{\text{gas}}=62^{\circ}\text{C}$ Free HAc=0ppm	Test #2 $T_{\text{gas}}=41^{\circ}\text{C}$ Free HAc=0ppm	Test #3 $T_{\text{gas}}=25^{\circ}\text{C}$ Free HAc=0ppm	Test #4 $T_{\text{gas}}=65^{\circ}\text{C}$ Free HAc=1000ppm
---	---	---	--

Figure 170: Model validation / Comparison between experimental data and model predictions  
 $SS_{\text{FeCO}_3} \text{ max}=10$  at  $T_{\text{gas}}=60^{\circ}\text{C}$ ,  $SS_{\text{FeCO}_3} \text{ max}=26$  at  $T_{\text{gas}}=42^{\circ}\text{C}$  and  $SS_{\text{FeCO}_3} \text{ max}=53$  at  $T_{\text{gas}}=25^{\circ}\text{C}$

### 7.3.6 Model context and limitations

As mentioned earlier, the present model is inspired from an approach originally developed by Olsen [64], the main concept being that the  $\text{FeCO}_3$  layer needs to be challenged in some way in order to enable the initiation of localized corrosion. In the case of TLC, the main challenging “agent” is the renewal of freshly condensed water (*i.e.* the water condensation rate) which requires active corrosion of the steel in order to maintain saturation in  $\text{FeCO}_3$ . Several modeling approaches, specific to TLC, have been proposed by Pots et al. [60], Nyborg et al. [110], Vitse et al. [75-77] or Zhang et al. [83]. They all include the effect of the water condensation rate and can predict with more or less accuracy the overall wall thickness loss of the pipeline. However, these modeling efforts are all uniform corrosion in nature and do not consider the

occurrence of localized corrosion in the TLC, which is quite unfortunate since TLC is inherently a localized corrosion process. The present model aims at covering this gap by proposing an explanation on how localized corrosion is initiated and grows with time. Overall, the corrosion occurring at the bottom of active localized features is still uniform in nature as the steel surface is bare of any corrosion product. Consequently, the different TLC prediction models proposed by other authors are not unvalidated by the present model, which only attempt to address the occurrence of localized corrosion.

There are a number of limitations that need to be considered in this localized TLC model:

- The model is highly dependent on the accuracy of the corrosion rate prediction at  $\text{FeCO}_3$  saturation (*i.e.* FREECORP model). Although the most widely accepted equation for  $\text{FeCO}_3$  precipitation rate and  $\text{FeCO}_3$  solubility are used, the approach selected in FREECORP to incorporate the effect of  $\text{FeCO}_3$  layer is still mostly empirical.
- The model does not consider specific morphologies of the localized features (for example, narrow or wide pits). In this sense, the model does not predict a steady state localized wall thickness loss rate (*i.e.* steel penetration rate), as mass transfer limitations could widely affect the results, especially if pits are narrow.
- Surface pH values are reported to be one or two units higher at the steel surface than in the bulk droplet [121]. This should create a considerable driving force for  $\text{FeCO}_3$  precipitation on the bare steel surface. However, this was not experimentally observed at the surface of active localized corrosion features. The kinetics of  $\text{FeCO}_3$  precipitation versus steel dissolution could provide some explanation.

## 7.4 Summary

A modeling approach, based on the observations made during the experimental part of the work, was proposed for the prediction of the localized attack in a top of the line corrosion scenario. A mechanism for the prediction of the onset and propagation of localized corrosion is proposed. The concept of  $\text{FeCO}_3$  saturation level is used as a key parameter in order to qualify the corrosiveness of the condensed water, while the water condensation rate and the steel temperature are defined as controlling to which degree (*i.e.*, the percentage area affected by localized corrosion) the localized attack is sustainable.

The model narrative is represented in Figure 171.

no film		partially protective film		fully protective film	
High uniform attack No localized attack		Low/high uniform attack Localized attack		Low uniform attack No localized attack	
100% = $A_{Loc}$		50% < $A_{Loc}$ < 100%		50% < $A_{Loc}$ < 5%	
					
No or non adherent layer (Very low steel temperature) – Uniform corrosion		High WCR, high HAC, Moderate steel temperature, Uniform localized Corrosion Sustainable TLC		Medium WCR, Sustainable TLC	
				Very low WCR, any temperature No sustainable severe TLC	

Figure 171: Narrative of localized TLC - (Adapted from [118] - © NACE international 2004)

## CHAPTER 8 CONCLUSIONS AND RECOMMENDATIONS FOR FUTURE DEVELOPMENT

A number of large scale flow loop experiments were performed in order to investigate the effect of different influencing parameters on top of the line corrosion (both uniform and localized rates). This helped improve the understanding and build a narrative on how TLC occurs in sweet and sour environments.

A new experimental setup (carbon steel inserts in flat slab) was also developed to improve the quality of the experimental data. The new set of experiments was successful in simulating TLC without obvious edge effects and in capturing the effect of the condensation rate. Localized corrosion could be very clearly observed on the steel surface and correlated to the condensation rate and the gas temperature.

- Pitting/mesa corrosion is strongly related to the level of condensation applied to the steel section.
- On the thermally insulated areas, localized corrosion is marginally observed but does not grow with time after the first months of exposure.
- On the cooled section, pits still seem to be growing in depth with time and also form clusters.
- In the presence of undissociated acetic acid, the extent of the corrosion attack was much more severe compared to previous results obtained without acetic acid. Especially, the condensation rate did not seem to have a strong effect on the maximum depth of the corrosion features.

Despite several attempts, the presence or absence of a large droplet on the steel surface could not be correlated directly to the extent of corrosion occurring underneath. It was

therefore concluded that the corrosion is controlled only by the rate of water condensation and the overall aggressiveness of the environment (CO<sub>2</sub>, acetic acid).

A modeling approach was proposed for the prediction of the localized attack in a top of the line corrosion scenario. The method is based on the observation made during the experimental part of the work and presents a mechanism for the prediction of the onset and propagation of localized corrosion. The FeCO<sub>3</sub> saturation level plays a key role in defining the overall corrosiveness of the condensed water. The condensation rate controls the degree to which localized attack is sustainable.

The following points present a few recommendations on how this work could be extended:

- Further study on the mechanisms of sour TLC is warranted. Especially of interest are the correlation between the types of iron sulfide polymorphs that can form corrosion product layers in relation to the extent of corrosion and the range of conditions where iron sulfide and iron carbonate can both form at the metal surface.
- The chemistry of H<sub>2</sub>O/H<sub>2</sub>S/CO<sub>2</sub> systems should also be studied further, with a focus on condensed water scenarios (*i.e.*, weak electrolyte).
- Being able to measure the chemistry of the condensed water (pH, Fe<sup>2+</sup> ions concentration), as the corrosion is occurring, would also be of great benefit, both in sour and sweet systems. This would help further validate the model of localized corrosion proposed in this work.
- The two dimensional modeling of the chemistry and the corrosion inside a pit would be useful both in a CO<sub>2</sub> dominated TLC scenario and for CO<sub>2</sub> corrosion in general. The specific geometry would have to be taken into account together with associated mass

transfer limitations. This could also be extended to sour environments when the knowledge is mature.

## REFERENCES

1. H. Matsubara, K. Naito, "Effect of liquid viscosity on flow patterns of gas-liquid two-phase flow in a horizontal pipe", *International Journal of Multiphase Flow*, Vol. 37(10), pp. 1277-1281., 2011.
2. L.M. Mine-Thomson, "Theoretical hydrodynamics", MacMillan Co., New York, 1960
3. Y. Taitel, A.E. Dukler, "A model for predicting flow regime transitions in horizontal and near horizontal gas-liquid flow", *AIChE Journal*, Vol. 22(1), pp. 47-55, 1976.
4. N. Jauseau, "Droplets transport in gas pipelines", TLC Advisory Board meeting, Presentation, Ohio Univ., Athens, OH, 2011.
5. M. Singer, B. Brown, A. Camacho, S. Nestic, "Combined effect of CO<sub>2</sub>, H<sub>2</sub>S and acetic acid on bottom of the line corrosion", *Corrosion*, vol.67, no. 1, pp.1-16, 2011.
6. J. A. Dougherty, "A review of the effect of organic acids on CO<sub>2</sub> corrosion", In *Proc. Corrosion*, Houston, TX, 2004, paper. 4376.
7. M. Bonis, M. Girgis, K. Goerz, R. MacDonald, "Weight loss corrosion with H<sub>2</sub>S: using past operations for designing future facilities", In *Proc. Corrosion*, Houston, TX, 2006, paper. 6122.
8. S. Smith, M. Joosten, "Corrosion of carbon steel by H<sub>2</sub>S in CO<sub>2</sub> containing environments", In *Proc. Corrosion*, Houston. TX, 2006, paper. 6115.
9. D. Hinkson, M. Singer, Z. Zhang and S. Nestic, "A study of the chemical composition and corrosiveness of the condensate in top of the line corrosion", in *Proc. Corrosion*, New Orleans, LA, 2008, paper. 8466.
10. M. Abdou, A. Carnegie, S.G. George, M. O'Keefe, R. Bhavani, W. Wei, X. ChengGang, "Finding value in formation water", *Oilfield Review*, vol.23, no. 1, pp.24-35, 2011.

11. K. George, S. Wang, S. Netic, C. de Waard, "Modeling of CO<sub>2</sub> corrosion of mild steel at high pressures of CO<sub>2</sub> and in presence of acetic acid", In *Proc. Corrosion*, Las Vegas, NV, 2004, paper no. 4623.
12. J.L. Crolet, N. Thevenot, A. Dugstad, "Role of free acetic acid on the CO<sub>2</sub> corrosion of steel" In *Proc. Corrosion*, Houston, TX, 1999, paper. 24.
13. A. Dugstad, "The importance of FeCO<sub>3</sub> Supersaturation on the CO<sub>2</sub> Corrosion of Carbon Steel", In *Proc. Corrosion*, Houston, TX, 1992, paper. 14.
14. O. Nafday, S. Netic, "Iron carbonate film scale formation and CO<sub>2</sub> corrosion the presence of acetic acid", In *Proc. Corrosion*, Houston, TX, 2005, paper. 5295.
15. C. De Waard, U. Lotz, "Prediction of CO<sub>2</sub> corrosion of carbon steel", In *Proc. Corrosion*, Houston, TX, 1993, paper. 69.
16. M. Matos, C. Canhoto, M. Bento, M. Geraldo, "Simultaneous evaluation of the dissociated and undissociated acid concentrations by square wave voltammetry using microelectrodes", *Journal of Electro-analytical Chemistry*, vol. 647, pp. 144-149, 2010.
17. B. Hedges, L. McVeigh, "The role of acetate in CO<sub>2</sub> corrosion: the double whammy", In *Proc. Corrosion*, Houston, TX, 1999, paper. 21.
18. Y. Garsany, D. Pletcher, B. Hedges, "The role of acetate in CO<sub>2</sub> corrosion of carbon steel: has the chemistry been forgotten? ", In *Proc. Corrosion*, Denver, CO, 2002, paper. 2273.
19. T. Tran, B. Brown, S. Netic, B. Tribollet, "Investigation of the mechanism for acetic acid corrosion of mild steel", In *Proc. Corrosion*, Orlando, FL, 2013, paper. 2487.
20. E. Remita, B. Tribollet, E. Sutter, V. Vivier, F. Ropital, J. Kittel, "Hydrogen evolution in aqueous solutions containing dissolved CO<sub>2</sub>: Quantitative contribution of the buffering effect", *Corrosion Science*, vol. 50, pp. 1433-1440, 2008.

21. D. Rickard, G. W. Luther, "Chemistry of iron sulfides," *Chem. Rev.*, vol. 107, pp. 514-562, 2007.
22. Y. Zheng, B. Brown, S. Netic, "Electrochemical study and modeling of H<sub>2</sub>S corrosion of mild steel", In *Proc. Corrosion*, Orlando, FL, 2013, paper 2406.
23. Y. Sun, K. George, S. Netic, "The effect of Cl<sup>-</sup> and acetic acid on localized CO<sub>2</sub> Corrosion in wet gas flow", In *Proc. Corrosion*, Houston, TX, 2003, paper. 3327.
24. K. George, S. Netic, C. de Ward, "Electrochemical investigation and modeling of carbon dioxide corrosion on carbon steel in the presence of acetic acid", In *Proc. Corrosion*, Houston, TX, 2004, paper. 4379.
25. S. Netic, J. Postlethwaite, S. Olsen, "An electrochemical model for prediction of corrosion of mild steel in aqueous carbon dioxide solutions", *Corrosion*, vol.52, no.4, pp.280-294, 1996.
26. N. Nordsveen, S. Netic, R. Nyborg and A. Stangeland, "A Mechanistic Model for Carbon Dioxide Corrosion of Mild Steel in the Presence of Protective Iron Carbonate Films - Part 1: Theory and verification", *Corrosion*, vol. 59, no. 5, pp. 443-456, 2003.
27. W. Sun, "Kinetics of iron carbonate and iron sulfide scale formation in CO<sub>2</sub>/H<sub>2</sub>S corrosion", PhD dissertation, Ohio University, Chemical and Bio-molecular Engineering Department, 2006.
28. J. Greenberg, M. Tomson, "Precipitation and dissolution kinetics and equilibria of aqueous ferrous carbonate vs. temperature", *Appl. Geochem.*, vol.7, pp.185-190, 1992.
29. C. A. R. Silva, X. Liu, F. J. Millero, "Solubility of siderite (FeCO<sub>3</sub>) in NaCl solutions", *J. Sol. Chem.*, vol.31, pp.97-108, 2002.
30. W. Sun, S. Netic, D. Young, R. Woollam, "Equilibrium Expressions Related to the Solubility of the Sour Corrosion Product Mackinawite", *Ind. Eng. Chem. Res.*, vol.47, pp.1738-1742, 2008.
31. D. Rickard, G.W. Luther, "Chemistry of iron sulfides", *Chem. Rev.*, vol.107, pp.514-562, 2007.

32. J. Vera, S. Kapusta, N. Hackerman, "Localized corrosion of iron in alkaline sulfide solutions. Iron sulfide formation and the breakdown of passivity", *Journal of the Electrochemical Society*, vol.133, no.3, pp.461, 1986.
33. O. M. Suleimenov and R. E. Krupp, "Solubility of hydrogen sulfide in pure water and in NaCl solutions, from 20 to 320°C and at saturation pressures", *Geochimica et Cosmochimica Acta*, vol.58, pp.2433-2444, 1994.
34. O. M. Suleimenov and T. M. Seward, "A spectrophotometric study of hydrogen sulfide ionization in aqueous solutions to 350°C", *Geochimica et Cosmochimica Acta*, vol.61, pp.5187-5198, 1997.
35. L. G. Benning, R. T. Wilkin, H. L. Barnes, "Reaction pathways in the Fe-S below 100°C", *Chemical Geology*, vol.167, pp.25-51, 2000.
36. Y. Gunaltun, D. Supriyataman and A. Jumakludin, "Top of the line corrosion in multiphase gas line. A case history", in *Proc. Corrosion*, Houston, TX, 1999, paper no. 36.
37. Y. Gunaltun and D. Larrey, "Correlation of cases of top of the line corrosion with calculated water condensation rates", in *Proc. Corrosion*, Houston, TX, 2000, paper. 71.
38. Y. Gunaltun, R. Piccardino and D. Vinazza, "Interpretation of MFL and UT inspection results in case of top of line corrosion", in *Proc. Corrosion*, Houston, TX, 2006, paper. 6170.
39. G. Bouriot, "Top of line corrosion cases at Total E&P Netherlands", in *Proc. 2<sup>nd</sup> TOL Corrosion conference*, Bangkok, 2009.
40. D. Hinkson, G. Peck, "Field assessment and verification of organic acid speciation for corrosion risk assessment", in *Proc. Corrosion*, San Antonio, TX, 2010, paper. 10100.
41. J.R. Piccardino, M. Stuvik, Y. Gunaltun and T. Pornthep, "Internal inspection of wet gas line subject to top of line corrosion", in *Proc. Corrosion*, Houston, TX, 2004, paper. 4354.

42. M. Thammachart, Y. Gunaltun and S. Punpruk, "The use of inspection results for the evaluation of batch treatment efficiency and the remaining life of the pipelines subjected to top of line corrosion", in *Proc. Corrosion*, New Orleans, LA, 2008, paper. 8471.
43. Y. Gunaltun, L. Payne, "A new technique for the control of top of line corrosion: TLCC-PIG", in *Proc. Corrosion*, Houston, TX, 2003, paper. 3344.
44. U. Kaewpradap, M. Singer, S. Nestic, S. Punpruk, "Top of the line corrosion – Comparison of model predictions with field data", in *Proc. Corrosion*, New Orleans, LA, 2012, paper no. 1449.
45. U. Kaewpradap, "The Developed Mehtodology in Comparing Top of the Line Model Prediction with Field Data", Master's Thesis, Ohio University, Chemical and Bio-molecular Engineering Department, 2012.
46. Y. Gunaltun, S. Punpruk, M. Thammachart, T. Pornthep, "Worst-case TLC: Cold spot corrosion", in *Proc. Corrosion*, San Antonio, TX, 2010, paper. 10097.
47. Y. Gunaltun, M. Thammachart, M. Singer, S. Nestic, S. Punpruk, U. Kaewpradap, "Progress in the prediction of top of the line corrosion and challenges to predict corrosion rates measured in gas pipeline", in *Proc. Corrosion*, San Antonio, TX, 2010, paper. 10093.
48. M. Singer, Top of the line corrosion in sour environments – Study of the controlling parameters", In *Proc. International Corrosion Congress*, Perth, 2011, paper. 80.
49. R. Paillassa, M. Dieumegard and M. Estevoyer, "Corrosion control in the gathering system at Lacq sour gas field", in *proc. 2<sup>nd</sup> Intl. Congress of Metallic Corrosion NACE*, New York, 1963, pp. 410-417.
50. D.F. Ho-Chung-Qui, A.I. Williamson and P. Eng, "Corrosion experiences and inhibition practices in wet sour gathering systems", in *Proc. Corrosion*, San Fransisco, CA, 1987, paper. 46.

51. N.N. Bich, K.E. Szklarz, "Crossfield Corrosion Experience", In *Proc. Corrosion*, Saint Louis, IL, 1988, paper. 196.
52. M. Edwards and B. Cramer, "Top of the line corrosion –Diagnostic, root cause analysis and treatment", in *Proc. Corrosion*, Houston, TX, 2000, paper. 72.
53. M. Joosten, D. Owens, A. Hobbins, H. Sun, M. Achour, D. Lanktree, "Top-of-line corrosion – A field failure", In *Proc. EuroCorr*, Moscow, Russia, 2010, paper. 9524.
54. M. Bonis, "Form sweet to sour TLC: what's different?", in *Proc. 2<sup>nd</sup> TOL Corrosion conference*, Bangkok, 2009.
55. S. Punpruk, M.Thammachart, Y. Gunaltun, "Field testing of volatile corrosion inhibitors and batch treatment efficiency by cooled probe", in *Proc. Corrosion*, San Antonio, TX, 2010, paper. 10096.
56. Y. Gunaltun, T.E. Pou, M. Singer, C. Duret, S. Espitalier, "Laboratory testing of volatile corrosion inhibitors", In *Proc. Corrosion*, San Antonio, TX, 2010, paper. 10095.
57. M. Thammachart, "Corrosion mitigation for pipeline failure due to top of the line corrosion", in *Proc. 3<sup>rd</sup> TOL Corrosion conference*, Bangkok, 2012.
58. Y. Gunaltun, "Design with high TLC risk", in *Proc. 3<sup>rd</sup> TOL Corrosion conference*, Bangkok, 2012.
59. B.F.M. Pots, T. Bos, R. Henkes, "Evaluation of CRA requirements to control top of line corrosion at warm gas pipeline tie-in", in *Proc. 3<sup>rd</sup> TOL Corrosion conference*, Bangkok, 2012.
60. B.F.M. Pots, E.L.J.A. Hendriksen, "CO<sub>2</sub> corrosion under scaling conditions – The special case of top-of-the-line corrosion in wet gas pipelines", in *Proc. Corrosion*, Houston, TX, 2000, paper. 31.

61. M. Cough, I. Salim, R. Saberon, M.H. Asraf., "Design and development of inhibitors for TOL corrosion control", in *Proc. 3<sup>rd</sup> TOL Corrosion conference*, Bangkok, 2012.
62. M.C. Oehler, S.I Bailey, R. Gubner, "Comparison of top of the line corrosion test methods for generic volatile inhibitor compounds", in *Proc. 3<sup>rd</sup> TOL Corrosion conference*, Bangkok, 2012.
63. T. Pojtanabuntoeng, M. Singer, S. Nestic, "Water/Hydrocarbon co-condensation and the influence on top-of-the-line corrosion", In *Proc. Corrosion*, Houston, TX, 2011, paper. 11330.
64. S. Olsen, A. Dugstad, "Corrosion under dewing conditions", in *Proc. Corrosion*, Houston, TX, 1991, paper. 472.
65. L. Zhang, J. Yang, M. Lu, "Effect of pressure on wet H<sub>2</sub>S/CO<sub>2</sub> corrosion of pipeline steel", In *Proc. Corrosion*, Atlanta, GA, 2009, paper. 9565.
66. H. Qin, L. Xu, W. Chang, M. Lu, L. Zhang, "Top of the line corrosion under low temperature and high condensation rate conditions", in *Proc. Corrosion*, Houston, TX, 2011, paper. 11328.
67. V. Jovancicevic, S. Ramachandran, K. Cattanach, I. Ahmed, " TLC control by volatile corrosion inhibitors in sweet gas systems", in *Proc. 3<sup>rd</sup> TOL Corrosion conference*, Bangkok, 2012.
68. T. Andersen, A.M.K. Halvorsen, A. Valle and G. Kojen, "The influence of condensation rate and acetic acid concentration on TOL corrosion in multiphase pipelines", in *Proc. Corrosion*, Nashville, TN, 2007, paper. 7312.
69. R. Nyborg, A. Dugstad and T. Martin," Top of line corrosion with high CO<sub>2</sub> and traces of H<sub>2</sub>S", in *Proc. Corrosion*, Atlanta, GA, 2009, paper. 9283.
70. M. Singer, S. Nestic and Y. Gunaltun, "Top of the line corrosion in presence of acetic acid and carbon dioxide", in *Proc. Corrosion*, Houston, TX, 2004, paper. 4377.
71. M. Singer, D. Hinkson, Z. Zhang, H. Wang and S. Nestic, "CO<sub>2</sub> top of the line corrosion in presence of acetic acid - a parametric study", in *Proc. Corrosion*, Atlanta, GA, 2009, paper. 9292.

72. M. Singer, A. Camacho, B. Brown and S. Nestic, "Sour top of the line corrosion in the presence of acetic acid", in *Proc. Corrosion*, San Antonio, TX, 2010, paper. 10101.
73. B. Brown, A. Schubert, "The design and development of a large-scale multiphase flow loop for the study of corrosion in sour gas environments," In *Proc. Corrosion*, Houston, TX, 2002, paper. 02502.
74. ASTM G1-03, "Standard practice for preparing, cleaning and evaluating corrosion test specimens", ASTM, Philadelphia, PA, pp.17-23, 2009.
75. F. Vitse, Y. Gunaltun, D. Larrey de Torreben and P. Duchet-Suchaux, "Mechanistic model for the prediction of top-of-the-line corrosion risk", in *Proc. Corrosion*, Houston, TX, 2003, paper. 3633.
76. F. Vitse, K. Alam, Y. Gunaltun, D. Larrey de Torreben D. and P. Duchet-Suchaux, "Semi-empirical model for prediction of the top-of-the-line corrosion risk", in *Proc. Corrosion*, Houston, TX, 2002, paper. 2245.
77. F. Vitse, "Experimental and theoretical study of the phenomena of corrosion by carbon dioxide under dewing conditions at the top of a horizontal pipeline in presence of a non-condensable gas", PhD dissertation, Russ College of Eng., Dept. of Chem. Eng., Ohio Univ., Athens, OH, 2002.
78. C. Mendez, M. Singer, A. Camacho, S. Hernandez and S. Nestic, "Effect of acetic acid, pH and MEG on CO<sub>2</sub> top of the line corrosion", in *Proc. Corrosion*, Houston, TX, 2005, paper. 5278.
79. A.M.K. Halvorsen, T. Andersen, E. Halvorsen, G. Kojen and J. Skar, "The relationship between internal corrosion control method, scale formation, and MEG handling of a multiphase carbon steel carrying wet gas with CO<sub>2</sub> and acetic acid", in *Proc. Corrosion*, Nashville, TN, 2007, paper. 7313.

80. R. Nyborg and A. Dugstad, "Top of the line corrosion and water condensation rates in wet gas pipelines", in *Proc. Corrosion*, Nashville, TN, 2007, paper. 7555.
81. J.L. Crolet, M. Bonis, "The role of acetate ions in CO<sub>2</sub> corrosion of carbon steel", in *Proc. Corrosion*, Houston, TX, 1983, paper. 160.
82. P. Okafor and S. Nestic, "Effect of acetic acid CO<sub>2</sub> corrosion of carbon steel in vapor-water two-phase horizontal flow", *Chem. Eng. Comm.*, vol. 194, pp.141–157, 2007.
83. Z. Zhang, D. Hinkson, M. Singer, H. Wang and S. Nestic, "A mechanistic model for Top of the line corrosion", *Corrosion*, vol. 63, no. 11, pp. 1051-1062, Nov. 2007.
84. A. Rotimi, R.A. Ojifinni, C. Li, "A parametric study of sweet top of the line corrosion in wet gas pipelines", in *Proc. Corrosion*, Houston, TX, 2011, paper. 11331.
85. J. Amri, E. Gulbrandsen and R.P. Nogueira, "The effect of acetic acid on the pit propagation in CO<sub>2</sub> corrosion of carbon steel", *Electrochemistry Communications*, vol. 10, pp. 200–203, 2008.
86. J. Amri, E. Gulbrandsen and R.P. Nogueira, "Effect of acetic acid on propagation and stifling of localized attacks in CO<sub>2</sub> corrosion of carbon steel", in *Proc. Corrosion*, Atlanta, GA, 2009, paper. 9284.
87. A. Valdes, R. Case, M. Ramirez, A. Ruiz, "The effect of small amounts of H<sub>2</sub>S on CO<sub>2</sub> corrosion of carbon steel", In *Proc. Corrosion*, Houston, TX, 1998, paper. 22.
88. J. Kvarekval, "The influence of small amounts of H<sub>2</sub>S on CO<sub>2</sub> corrosion of iron and carbon steel", Eurocorr 97, Trondheim, Norway.
89. B. Brown, K.L. Lee, S. Nestic, "Corrosion in multiphase flow containing small amounts of H<sub>2</sub>S", In *Proc. Corrosion*, Houston, TX, 2003, paper. 3341.
90. B. Brown, S. Reddy Parakala, S. Nestic, "CO<sub>2</sub> corrosion in presence of trace amounts of H<sub>2</sub>S", In *Proc. Corrosion*, Houston, TX, 2004, paper. 4736.

91. W. Sun, S. Netic, "A mechanistic model for uniform hydrogen sulfide/carbon dioxide corrosion of mild steel", *Corrosion*, Vol.65, No.5, pp.291-307, 2009.
92. B. Pots, R. John, I. Rippon, "Improvements on de-Waard Milliams corrosion prediction and applications to corrosion management", In *Proc. Corrosion*, Houston, TX, 2002, paper. 2235.
93. S. Smith, "Discussion of the history and relevance of the CO<sub>2</sub>/H<sub>2</sub>S ratio", In *Proc. Corrosion*, Houston, TX, 2011, paper. 11065.
94. S. Smith, J.L. Pacheco, "Prediction of Corrosion in Slightly Sour Environments", In *Proc. Corrosion*, Houston, TX, 2002, paper. 2241.
95. A. Camacho, "CO<sub>2</sub> top of the line corrosion in presence of H<sub>2</sub>S ", Master's thesis, Ohio University, Chemical and Bio-molecular Engineering Department, 2006.
96. A. Camacho, M. Singer, B. Brown and S. Netic., "Top of the Line Corrosion in H<sub>2</sub>S/CO<sub>2</sub> Environments", in *Proc. Corrosion*, New Orleans, LA, 2008, paper. 8470.
97. D. Pugh, S. Asher, J. Cai, W. Sisak, J. Pacheco, F. Ibrahim and E. Wright, "Top-of-line corrosion mechanisms for sour wet gas pipelines", in *Proc. Corrosion*, Atlanta, GA, 2009, paper. 9285.
98. T. Tanupabrunsun, B. Brown, D. Young, and S. Netic, "Construction and verification of Pourbaix diagram for CO<sub>2</sub> corrosion of mild steel valid up to 250°C," in *Proc. Corrosion*, Salt Lake City, UT, 2012, paper.1418.
99. P. Meakin, "Dropwise condensation: the droplet growth and coalescence of fluid droplets", *Physica Scripta*, vol. T44, pp. 31-41, Feb. 1992.
100. J.W. Rose, "On the mechanism of dropwise condensation", *International Journal of Heat and Mass Transfer*, vol. 10, pp. 755-762, 1967.
101. J.W. Rose, "Dropwise condensation theory and experiment: a review", *Journal of Power and Energy*, vol. 216, pp. 115-128, 2002.

102. J.W. Rose, "Dropwise condensation theory", *International Journal of Heat and Mass Transfer*, vol. 24, pp. 191-194, 1981.
103. J.W. Rose, "On interphase matter transfer, the condensation coefficient and dropwise condensation", in *Proc. of the Royal Society of London, Series A, Math. and Phys. Sci.*, vol. 411, No. 1841, pp. 305-311, June 1987.
104. J.W. Rose, "Some aspects of condensation heat transfer theory", *International Communication in Heat and Mass Transfer*, vol. 15, pp. 449-473, 1988.
105. D.W. Tanner, C.J. Potter, D. Pope and D. West, "Heat transfer in dropwise condensation – Part1 & 2", *International Journal of Heat and Mass Transfer*, vol. 8, pp. 419-426 & 426-436, 1965.
106. C.Y. Wang and C.J. Tu, "Effect of non-condensable gas on laminar film condensation in a vertical tube", *International Journal of Heat and Mass Transfer*, vol. 31, no. 11, 2339-2345, 1988.
107. S. Wang and Y. Utaka, "Effect of non-condensable gas mass fraction on condensation heat transfer for water-ethanol vapor mixture", *JSME International Journal, Series B*, vol. 47, no. 2, pp. 162-167, 2004.
108. C. DeWaard, U. Lotz and D.E. Milliams, "Predictive model for CO<sub>2</sub> corrosion engineering in wet natural wet gas pipelines", *Corrosion*, vol. 47, no. 12, pp. 976-985, 1991.
109. E.W.J. Van Hunnik, B.F.M. Pots, E.L.J.A.Hendriksen, "The formation of protective FeCO<sub>3</sub> corrosion product layers in CO<sub>2</sub> corrosion", in *Proc. Corrosion*, Houston, TX, 1996, paper. 6.
110. R. Nyborg, A. Dugstad, "Top of the line corrosion and water condensation rates in wet gas pipelines", in *Proc. Corrosion*, Nashville, TN, 2007, paper. 7555.
111. S. Nestic, N. Nordsveen, R. Nyborg and A. Stangeland, "A Mechanistic Model for Carbon Dioxide Corrosion of Mild Steel in the Presence of Protective Iron Carbonate Films - Part 2: A numerical experiment", *Corrosion*, vol. 59, no. 6, pp. 489-497, 2003.

112. S. Nestic, N. Nordsveen, R. Nyborg and A. Stangeland, "A Mechanistic Model for Carbon Dioxide Corrosion of Mild Steel in the Presence of Protective Iron Carbonate Films - Part 3: Film growth model", *Corrosion*, vol. 59, no. 7, pp. 616-628, 2003.
113. E. Remita, B. Tribollet, B. Sutter, F. Ropital, X. Longaygue, J. Kittel, C. Tavel-Condard and N. Desamaise, "A kinetic model for CO<sub>2</sub> corrosion in confined aqueous environments", *Journal of the Electrochemical Society*, vol. 155, no. 1, pp. C41-C45, 2008.
114. S.L. Asher, W. Sun, R.A. Ojifinni, S. Ling, C. Li, J.L. Pacheco and J.L. Nelson, "Top of the line corrosion modeling in wet gas pipelines", in *Proc. 18<sup>th</sup> International Corrosion Congress*, Perth, Australia, 2011, paper. 303.
115. W. Sun and S. Nestic, "A mechanistic model of H<sub>2</sub>S corrosion of mild steel", in *Proc. Corrosion*, Nashville, TN, 2007, paper. 7655.
116. R. Nyborg, "Initiation and growth of mesa corrosion attack during CO<sub>2</sub> corrosion of carbon steel", in *Proc. Corrosion*, Houston, TX, 1998, paper. 48.
117. G. Schmitt, M. Mueller, M. Papenfuss and E. Strobel-Effertz, "Understanding localized CO<sub>2</sub> corrosion of carbon steel from physical properties of iron carbonate scales", in *Proc. Corrosion*, Houston, TX, 1999, paper. 38.
118. Y. Sun and S. Nestic, "A parametric study and modeling on localized CO<sub>2</sub> corrosion in horizontal wet gas flow", in *Proc. Corrosion*, Houston, TX, 2004, paper. 4380.
119. J. Han, Y. Yang, B. Brown and S. Nestic, "Electrochemical investigation of localized CO<sub>2</sub> corrosion on mild steel", in *Proc. Corrosion*, Nashville, TN, 2007, paper. 7323.
120. J. Han, Y. Yang, S. Nestic and B. Brown, "Role of passivation and galvanic effects in localized CO<sub>2</sub> corrosion of mild steel", in *Proc. Corrosion*, New Orleans, LA, 2008, paper. 8332.

121. J. Han, "Galvanic mechanism of localized corrosion for mild steel in carbon dioxide environments", PhD dissertation, Russ College of Eng., Dept. of Chem. Eng., Ohio Univ., Athens, OH, 2009.
122. J. Han, D. Young, H. Colijn, A. Tripathi and S. Nestic, "Chemistry and structure of the passive film on mild steel in CO<sub>2</sub> corrosion environments", *Ind. Eng. Chem. Res.*, vol. 48, pp. 6296–6302, 2009.
123. W. Li, "Investigation of pseudo-passive layer formation in CO<sub>2</sub> corrosion", Master's thesis, Russ College of Eng., Dept. of Chem. Eng., Ohio Univ., Athens, OH, 2011.
124. H. Li, "A mechanistic model for CO<sub>2</sub> localized corrosion of carbon steel", PhD Dissertation, Russ College of Eng., Dept. of Chem. Eng., Ohio Univ., Athens, OH, 2011.
125. Y. Yang, "Removal mechanisms of protective iron carbonate layer in flowing solutions", PhD Dissertation, Russ College of Eng., Dept. of Chem. Eng., Ohio Univ., Athens, OH, 2012.
126. S. Nestic, H. Li, D. Sormaz and J. Huang, "A free open source mechanistic model for prediction of mild steel corrosion", in *Proc. 17<sup>th</sup> International Corrosion Congress*, 2009, paper. 2659.
127. D. J. Zigrang, N.D. Sylvester, "A review of explicit friction factor equations", *Transactions of ASME, Journal of Energy Resources Technology*, Vol. 107, pp. 280–283, 1985.
128. A. Baker, K. Nilsen, A. Gabb, "Pressure loss, liquid-holdup calculations developed", *Oil & Gas Journal*, 55-59, 1988.
129. O. Shoham, Y. Taitel, "Stratified turbulent-turbulent gas liquid flow in horizontal and inclined pipes", *AIChE J.*, 30, pp. 377-385, 1984.
130. H. Jeffreys, "On the formation of water waves by wind", *Proc. R. Soc. A* 107, 189–201, 1925.

131. N. Andritsos, C. Tzotsi, T.J. Hanratty, "Interfacial shear stress in wavy stratified gas-liquid two-phase flow", In *Proc. 5<sup>th</sup> European Thermal-Sciences Conference*, The Netherlands, 2008.
132. J.E. Ramirez, M. Singer, "Evaluation of steel microstructure effect on CO<sub>2</sub> corrosion", Internal note, EWI, Ohio University, 2010.
133. C. Graham and P. Griffith, "Drop size distribution and heat transfer in dropwise condensation", *International Journal of Heat and Mass Transfer*, vol. 16, pp. 337-346, 1973.
134. M. Abu-Orabi, "Modeling of heat transfer in dropwise condensation", *International Journal of Heat and Mass Transfer*, vol. 41, pp. 81-87, 1998.
135. B.M. Burnside and H.A. Hadi, "Digital computer simulation of dropwise condensation from equilibrium droplet to detectable size", *International Journal of Heat and Mass Transfer*, vol. 42, pp. 3137-3146, 1999.
136. S. Verumi, K.J. Kim, "An experimental and theoretical study on the concept of dropwise condensation", *International Journal of Heat and Mass Transfer*, vol. 49, pp. 649-657, 2006.
137. J.R. Maa, "Drop size distribution and heat flux of dropwise condensation", *The Chemical Engineering Journal*, vol. 16, pp. 171-176, 1978.
138. N. Fatica and D.L. Katz, "Dropwise condensation", *Chemical Engineering Progress*, vol. 45, no. 11, pp. 661-674, 1949.
139. E.J. Le Fevre and J.W. Rose, "A theory of heat transfer by dropwise condensation", in *Proc. Third Int. Heat Transfer Conf. AIChE*, 1966, vol. 2, pp. 362.
140. J.W. Rose and L.R. Glicksman, "Dropwise condensation – The distribution of drop sizes", *International Journal of Heat and Mass Transfer*, vol. 16, pp. 411-425, 1973.

141. Y.T. Wu, C.X. Yang and X.G. Yuan, "Drop distribution and numerical simulation of dropwise condensation heat transfer", *International Journal of Heat and Mass Transfer*, vol. 44, pp. 4455-4464, 2001.
142. C. Graham and P. Griffith, "Drop size distribution and heat transfer in dropwise condensation", *International Journal of Heat and Mass Transfer*, vol. 16, pp. 337-346, 1973.
143. C. Yamali and H. Merte, "A theory of dropwise condensation at large subcooling including the effect of the sweeping", *Heat and Mass Transfer*, vol. 38, pp. 191-202, 2002.

## APPENDIX A MOMENTUM BALANCE FOR FLOW REGIME PREDICTION

### A.1 Momentum balance and determination of liquid holdup

In stratified flow, liquid flows at the bottom of the line while gas flows concurrently at the top. As in the cross section of a pipeline drawn in Figure 163, part of the volume is occupied by the liquid, whereas the gas fills the remainder.

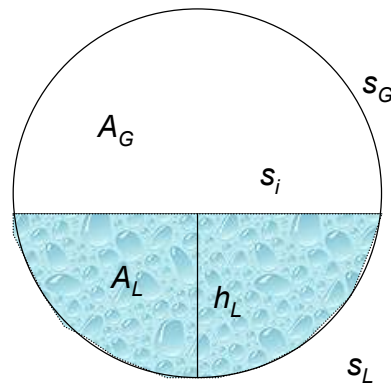


Figure 172: Schematic of the cross section of a pipe in gas-liquid two-phase flow ( $A_G$ : area covered by gas,  $A_L$ : area covered by liquid,  $S_G$ : wetted length of the gas phase,  $S_L$ : wetted length of the liquid phase,  $S_i$ : the boundary length at gas-liquid interface,  $h_L$ : liquid holdup)

Momentum balance equations were established on both phases according to Taitel [3].

$$-A_L \left( \frac{dP}{dx} \right) - \tau_{WL} S_L + \tau_i S_i + \rho_L A_L g \sin \alpha = 0 \quad \text{Eq (A-1)}$$

$$-A_G \left( \frac{dP}{dx} \right) - \tau_{WG} S_G + \tau_i S_i + \rho_G A_G g \sin \alpha = 0 \quad \text{Eq (A-2)}$$

where:

$\tau$ : Shear stress at the interface of liquid-wall ( $\tau_{WL}$ ), gas-liquid ( $\tau_i$ ), and wall-gas ( $\tau_{WG}$ ),

[Pa]

$\alpha$ : Angle between the pipe and the horizontal (positive for downward flow), [°]

$A$ : Area of the different phases in a cross section, [m<sup>2</sup>]

$S$ : Wetted length of different phases, [m]

$\rho_L$ :	Liquid density, [kg/m <sup>3</sup> ]
$\mu_L$ :	Liquid viscosity, [Pa s]
$\rho_G$ :	Gas density, [kg/m <sup>3</sup> ]
$\mu_G$ :	Gas viscosity, [Pa s]
$g$ :	Gravity, [m/s <sup>2</sup> ]
$D$ :	Pipe diameter, [m]

Pressure drop is the same for these two equations. Substituting one equation for another one, the liquid holdup  $h_L$  can be evaluated through the liquid and gas cross section areas  $A_L$  and  $A_G$ .

$$\tau_{WG} \frac{S_G}{A_G} - \tau_{WL} \frac{S_L}{A_L} + \tau_i S_i \left( \frac{1}{A_L} + \frac{1}{A_G} \right) + (\rho_L - \rho_G) g \sin \alpha = 0 \quad \text{Eq (A-3)}$$

From the basic definition in flow dynamics, the conventional equation of the shear stress on the gas side of a gas-liquid interface is:

$$\tau_i = f_i \frac{\rho_G \cdot (U_G - U_L) \cdot |U_G - U_L|}{2} \quad \text{Eq (A-4)}$$

where:

$f_i$ :	Interfacial friction factor at the gas side
$U_G$ :	Actual gas velocity, m/s
$U_L$ :	Actual liquid velocity, m/s

Similarly, equations of the interfacial shear stress between gas and pipe wall and between liquid and pipe wall are given, respectively:

$$\tau_G = f_G \frac{\rho_G U_G^2}{2}$$

$$\tau_L = f_L \frac{\rho_L U_L^2}{2}$$

where:

$f_G$ : Gas/wall friction factor

$f_L$ : Liquid/wall friction factor

Usually, friction factors can be calculated through:

$$f_L = C_L \left( \frac{\rho_L D_L U_L}{\mu_L} \right)^{-n}$$

$$f_G = C_G \left( \frac{\rho_G D_G U_G}{\mu_G} \right)^{-m}$$

where:

$C_L$ : Constant (= 0.046 for turbulent flow or = 16 for laminar flow)

$C_G$ : Constant (= 0.046 for turbulent flow or = 16 for laminar flow)

$m$ : Constant (= 0.2 for turbulent flow or = 1 for laminar flow)

$n$ : Constant (= 0.2 for turbulent flow or = 1 for laminar flow)

$D_L$ : Liquid hydraulic diameter, m

$D_G$ : Gas hydraulic diameter, m

More specifically, the determination of these friction factors was refined when appropriate depending on the Reynolds number. The approach developed by Zingrang [127] was used to determine the friction factor (Fanning rather than Darcy-Weisbach friction factor). The modifications are listed below:

For a gas or liquid Reynolds number below 2000:

$$f = \frac{16}{\text{Re}}$$

Eq (A-5)

- For  $2000 < (Re_G \text{ or } Re_L) < 2500$ :

$$f = \text{Max} \left[ \frac{16}{\text{Re}}, 4 \cdot \left( -2 \cdot \log \left( \frac{\varepsilon}{3.7 \cdot D} - \frac{4.518}{\text{Re}} \cdot \log \left( \left( \frac{\varepsilon}{3.7 \cdot D} \right)^{1.11} + \frac{6.9}{\text{Re}} \right) \right) \right)^{-2} \right] \quad \text{Eq (A-6)}$$

where:

$\varepsilon$ : Steel porosity, m

- For  $(Re_G \text{ or } Re_L) > 2500$ :

$$f = 4 \cdot \left( -2 \cdot \log \left( \frac{\varepsilon}{3.7 \cdot D} - \frac{4.518}{\text{Re}} \cdot \log \left( \left( \frac{\varepsilon}{3.7 \cdot D} \right)^{1.11} + \frac{6.9}{\text{Re}} \right) \right) \right)^{-2} \quad \text{Eq (A-7)}$$

The determination of the interfacial friction factor  $f_{iG}$  was developed based on an approach proposed by Baker [128] and Shoham [129], as follows:

- For internal pipe diameter  $> 5''$

$$f_i = 4 \cdot \left( -2 \cdot \log \left( \frac{\varepsilon_I}{3.7 \cdot D} - \frac{4.518}{\text{Re}_G} \cdot \log \left( \left( \frac{\varepsilon_I}{3.7 \cdot D} \right)^{1.11} + \frac{6.9}{\text{Re}_G} \right) \right) \right)^{-2} \quad \text{Eq (A-8)}$$

$$\text{If } \left( \frac{\rho_G}{\rho_L} \right) \times \left( \frac{\mu_G \cdot U_L}{\sigma_{GL}} \right)^2 \leq 0.005 \text{ then } \varepsilon_I = \frac{34 \cdot \sigma_{GL}}{\rho_G \cdot U_L^2}$$

$$\text{If } \left( \frac{\rho_G}{\rho_L} \right) \times \left( \frac{\mu_G \cdot U_L}{\sigma_{GL}} \right)^2 > 0.005 \text{ then}$$

$$\varepsilon_I = \frac{170 \cdot \sigma_{GL} \cdot \left( \left( \frac{\rho_G}{\rho_L} \right) \times \left( \frac{\mu_G \cdot U_L}{\sigma_{GL}} \right)^2 \right)^{0.3}}{\rho_G \cdot U_L^2}$$

where:

$\sigma_{GL}$ : Gas liquid surface tension, N/m

However,  $\varepsilon = \text{Max}(\varepsilon, \varepsilon_i)$  and if  $\varepsilon_i > 0.25$  then  $\varepsilon_i = 0.25 h_L$ .

- For internal pipe diameter  $< 5''$

$$f_i = 0.0142 \quad \text{Eq (A-9)}$$

Substituting all of the corresponding parameters into the momentum balance, the liquid

holdup can be determined by evaluating the geometrical parameters as follows:

$$A_G = \frac{D^2}{4} \left( \pi - \cos^{-1} \left( 1 - \frac{2h_L}{D} \right) \right) + \left( 1 - \frac{2h_L}{D} \right) \cdot \left( 1 - \left( 1 - \frac{2h_L}{D} \right)^2 \right)^{0.5} \quad \text{Eq (A-10)}$$

$$A_L = A - A_G \quad \text{Eq (A-11)}$$

$$S_G = D \cdot \left( \pi - \cos^{-1} \left( 1 - \frac{2h_L}{D} \right) \right) \quad \text{Eq (A-12)}$$

$$S_L = S - S_G \quad \text{Eq (A-13)}$$

$$S_i = D \cdot \left( 1 - \left( 1 - \frac{2h_L}{D} \right)^2 \right)^{0.5} \quad \text{Eq (A-14)}$$

## A.2 Transition between stratified and non-stratified

As mentioned earlier, the most widely accepted mechanism for the transition between stratified and slug/annular flow is the wave-mixing mechanism developed by Milne-Thomson [2] and Taitel [3].

The transition criterion is developed through an analysis of the hydrodynamic characteristics of the gas-liquid interface in the presence of unstable waves. According to Milne-Thomson's analysis, transition from stratified flow to intermittent/annular flow will happen when waves can grow:

$$U_G > \left[ 1 - \frac{h_L}{D} \right] \times \left[ \frac{g(\rho_L - \rho_G) \cdot \cos(\alpha) \cdot A_G}{\rho_G \cdot \frac{dA_L}{dh_L}} \right]^{1/2} \quad \text{Eq (A-15)}$$

with:

$$A_G = \frac{D^2}{4} \left[ \pi - \cos^{-1} \left( 1 - \frac{2h_L}{D} \right) + \left( 1 - \frac{2h_L}{D} \right) \cdot \sqrt{\left( 1 - \left( 1 - \frac{2h_L}{D} \right)^2 \right)} \right] \quad \text{Eq (A-16)}$$

$$\frac{dA_L}{dh_L} = D \cdot \sqrt{\left(1 - \left(1 - \frac{2h_L}{D}\right)^2\right)} \quad \text{Eq (A-17)}$$

where:

$U_G$ : Gas velocity, m/s

$g$ : Gravity, m/s<sup>2</sup>

$\rho_G$ : Density of the gas, kg/m<sup>3</sup>

$\rho_L$ : Density of the liquid, kg/m<sup>3</sup>

$h_L$ : Liquid height in pipe (liquid holdup), m

$\alpha$ : angle between the pipe and the horizontal (positive for downward flow), °

$D$ : Pipe diameter, m

$A_G$ : area covered by gas, m<sup>2</sup>

### A.3 Transition between stratified-smooth and stratified-wavy

The stratified flow regime can be divided into two subdivisions: stratified-smooth and stratified-wavy. At the transition between these two types of stratified flow, the gas flow increases and starts forming waves but is still low enough that it does not lead to significant wave growth (*i.e.*, the waves do not reach the top of the pipe). The waves are initiated when the gas/liquid interfacial shear stress can overcome viscous dissipation, holding the liquid phase stable and smooth [3].

According to the criterion developed in Taitel's work [3] (based on earlier work from Jeffreys [130]), the transition from stratified-smooth to stratified-wavy occurs when the gas velocity exceeds:

$$U_G \geq \left[ \frac{4v_L \cdot g(\rho_L - \rho_G) \cdot \cos(\alpha)}{s \cdot \rho_G \cdot U_L} \right]^{1/2} \quad \text{Eq (A-18)}$$

with:

- $U_L$ : Liquid velocity, m/s
- $s$ : Sheltering coefficient (set at 0.06) [131]
- $\nu_L$ : Liquid kinetic viscosity,  $m^2/s$

## APPENDIX B SIMULATION OF FLOW DISTURBANCE CREATED BY TEST SECTION GEOMETRY

### B.1 Introduction

Some concerns have been raised about the experimental errors induced by using flat samples in a 4" ID pipe. Unwanted artificial edge effects appeared in previous experiments, consequently affecting the results obtained at the top of the line.

As a remedy, it was proposed to use a 4" ID carbon steel spool piece in the loop. However, even if the edge effects were eliminated, the wall curvature corresponding to a 4" ID pipe is still completely different from a 20" or 30" ID pipe typically found in the field. The wall curvature is a very important parameter in TLC as it greatly influences the condensation regime. On a curved surface (corresponding to a 4"), droplets tend to slide easily on the sides of the pipe. On flatter surface (corresponding to 30" ID pipe), droplets can grow and remain attached to the pipe wall for a much longer time.

Therefore, it was proposed to design a test section that would at once remove the edge effects and also simulate a 30" pipe curvature at the top of the line. The top part of 4" ID stainless steel pipe could be cut over a 1.5 – 2 meters length (see Figure 173) and replaced by a flat stainless steel block (called slab). The difference of pipe curvature between 4" and 30" is so large (see Figure 174) that it would be satisfactory to use a completely flat carbon steel block in a 4" ID pipe. This way, the sample preparation would be also much easier, as there would be no need to polish a curved sample.



Figure 173: 4" ID stainless steel pipe with top part removed

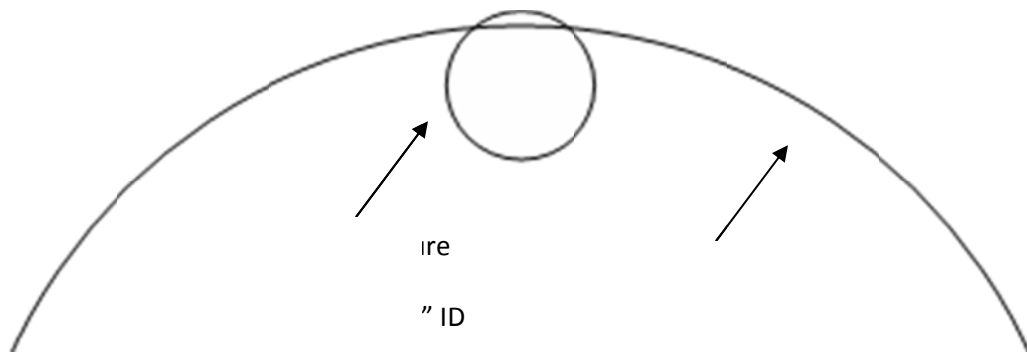


Figure 174: Difference in pipe curvature between 4" and a 30" ID pipes

Standard corrosion ports are drilled in the stainless steel piece to allow for the introduction of weight loss or other corrosion measurement methods. This design is very similar to a regular test section, the only difference being that the top part of the pipe is perfectly flat. This way, the edge effects on the carbon steel samples would be avoided (as there is no difference of curvature). Representations of the stainless steel section are shown in Figure 175, Figure 176 and Figure 177.



Figure 175: Schematic representation of the Flat Stainless steel Section

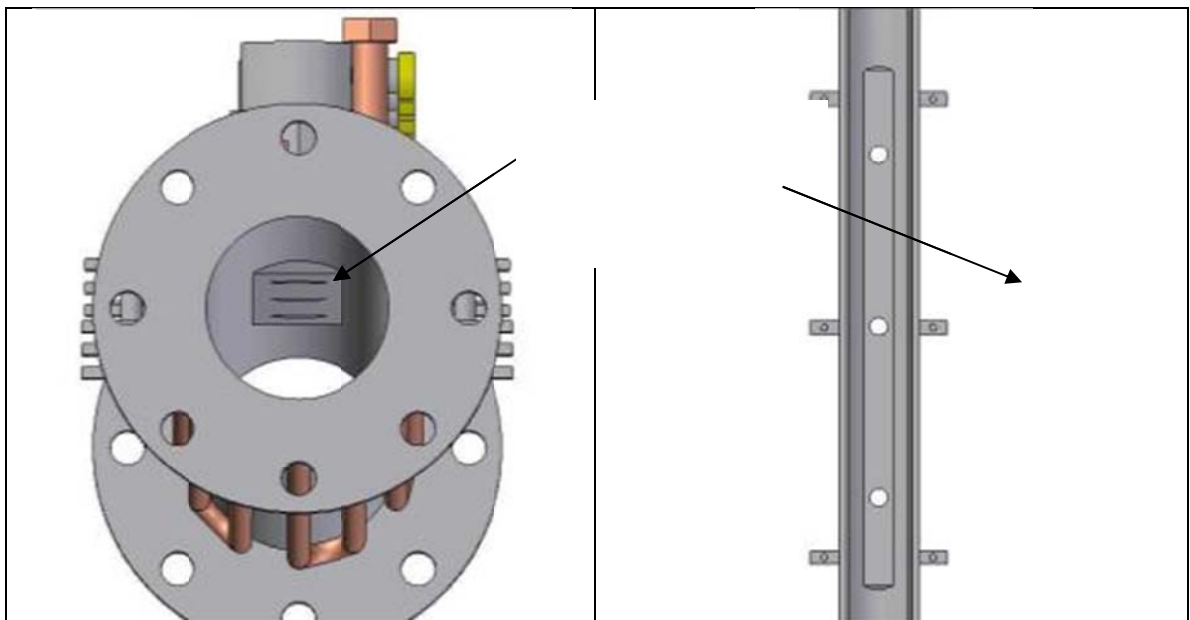


Figure 176: Frontal and cross sectional view of the Flat Stainless steel Section FSS

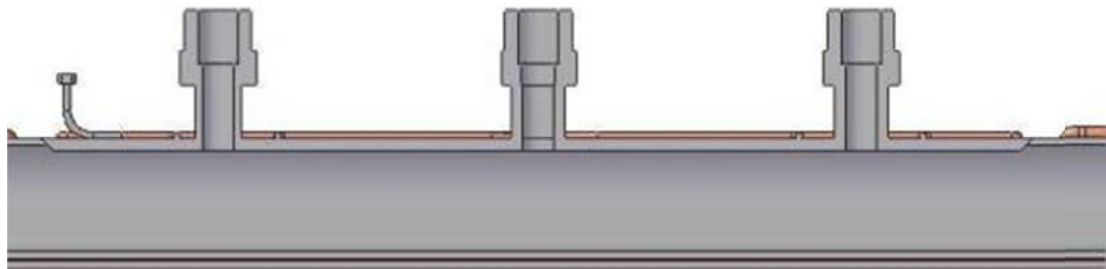


Figure 177: Cross section representation of the stainless steel section

This design was used to build the test section, a photograph of which is shown in Figure 178. The next figure shows the inside of the pipe in the flow direction. The leading edge of the slab, which has an angle of  $45^\circ$ , is clearly visible.



Figure 178: Picture of the actual stainless steel section

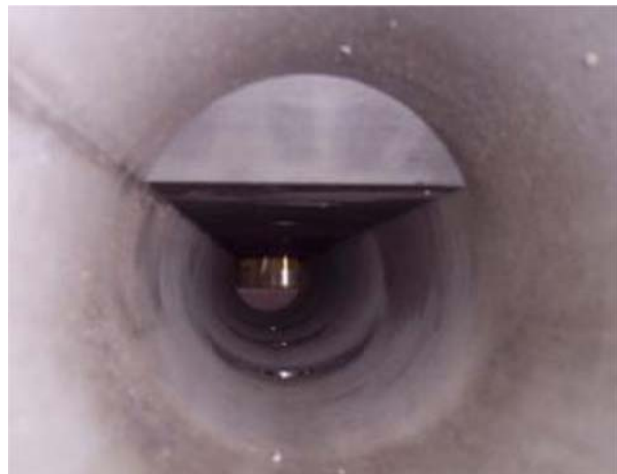


Figure 179: Inside of the pipe – View of the leading edge of the slab

## B.2 Objectives

It is understood that the flow velocity in the “slab” section will be higher than in the regular 4" ID pipe. It can be calculated and controlled. However, some concerns were raised as

to whether the flow disturbance caused by the edge of the slab would lead to a non-fully developed flow under the slab itself. This could lead to unrepresentative flow conditions in the area closed to the corrosion ports. Consequently, corrosion results would be difficult to analyze, because they could be affected by the peculiar flow instability.

The objective of this work is to simulate the flow conditions in this stainless steel section and to evaluate the extent of the disturbance caused by the presence of the slab. This work is done using the CAD software Fluent and Gambit.

The system is simulated in a 3D approach. Several gas velocities are tested while the flow regime remains highly turbulent in all cases.

### B.3 Problem simulation (mesh creation)

The pipe is created using the software Gambit.

A schematic of the mesh is shown Figure 180. The upstream section is shorter than the downstream section since, as will be seen later, most of the flow disturbance occurs downstream of the slab.

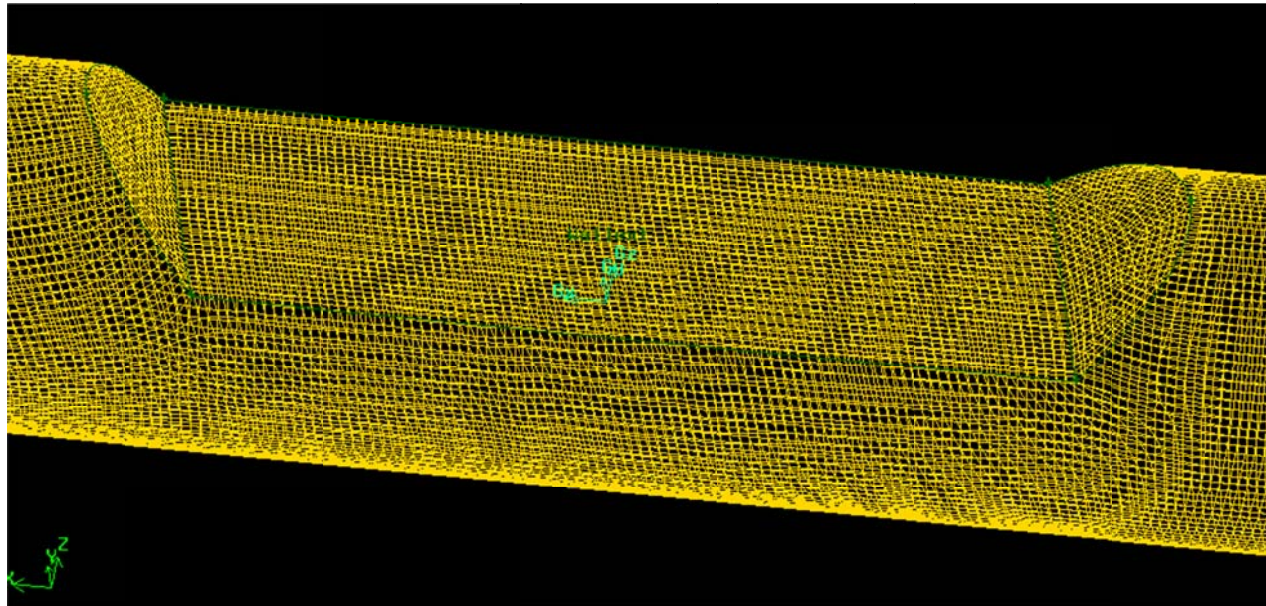
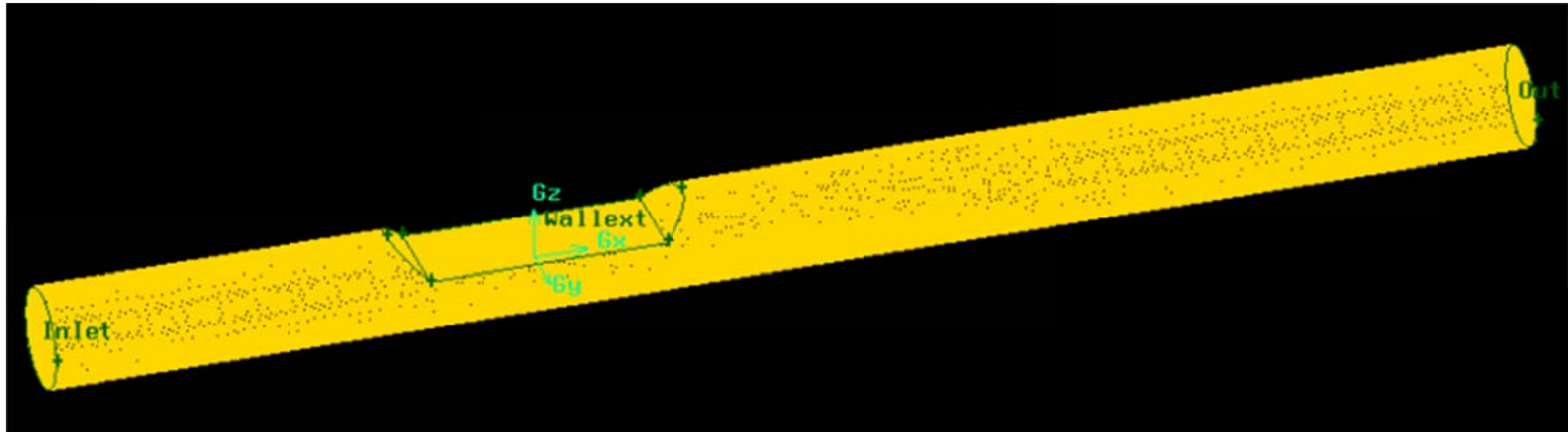


Figure 180: 3D approach – Mesh of slab (entire view and close-up on the slab)

#### B.4 Simulation results

The meshes created with Gambit are first scaled to the real dimension of the problem. CO<sub>2</sub> was selected as the carrying gas and the total pressure was set at 3 bars. The standard k-epsilon model was selected to model the turbulence. The total pressure was set at 3 bars (experimental test conditions). The numerical method used to solve the Navier Stokes equation was fully implicit.

The graphs shown below represent the profiles of velocity (or turbulence) once a steady state has been reached. Two types of information are displayed in the following graphs:

- The velocity magnitude. This is the sum of the absolute values of the x, y, z velocities. In the case of this study, it is very similar to the x- velocity.
- The turbulence intensity. This is the ratio between the root mean square of the turbulent velocity fluctuations and the mean velocity. This value gives an indication of the level of the turbulence based on the calculation of the turbulent energy.

The simulations were carried out for 5 and 10 m/s.

A typical 3D simulation enables the user to create a flow map of the entire volume considered (in the case, the test section). An example of the type of results displayed is shown in Figure 181. However, the portion of interest is located along the slab section on a longitudinal cross section area (inside the pipe). It is therefore necessary to create imaginary planes of view in order to study the “inside” of the pipe. The views selected are shown in Figure 182 and Figure 183.

It is also important to note that the black areas sometime observed on the flow maps are most likely due to some graphical representation issues more than convergence instability of the calculations. In fact, the mesh created with Gambit is “checked” by Fluent, and any error

would be located early in the simulation. It is then believed that these black dots are due to some limitations of the graphic capabilities of the computer.

The area of interest is the longitudinal cross section plane taken in the middle of the slab. The results of the simulation for a gas velocity of 5 m/s are displayed in Figure 184 and Figure 185. The results, associated with a gas velocity of 10 m/s, are shown in Figure 186 and Figure 187.

It is clear that the flow is strongly disturbed by the presence of the slab. Under the slab section, the gas velocity is locally increased by 30 to 50%, which is as expected. However, the flow seems well established under the slab, meaning that there is no peculiar flow line observed. Most of the disturbance actually appears downstream of the slab. The two leading edges of the test section do highly affect the flow which, in return, will influence the corrosion process. Apart from these edges, the horizontal portion of the slab does not seem affected by peculiar flow lines or unexpectedly high level of turbulence.

The two simulations performed with the two gas velocities show very similar results. At higher velocity, the turbulence fluctuation is carried out on a longer portion of the pipe.

However, even if common characteristics are observed, there are also fundamental differences. It seems that the presence of the slab has, in general, a less dramatic effect on the flow conditions. The gas velocity under the slab is at most only 30% greater compared to the inlet velocity. The turbulence induced by the presence of the slab is also reduced, even if it remains high close to the leading edges of the slab.

Overall, the flow seems well established under the slab, meaning that there is no peculiar flow line observed. Most of the disturbance actually appears downstream of the slab.

The two simulations performed with the two gas velocities show very similar results. At higher velocity, the turbulence fluctuation is carried out on a longer portion of the pipe.

#### B.5 Conclusions

The presence of the slab section inside a regular 4" ID pipe does induce a strong change in the flow conditions. The gas velocity increases locally by at least 30%, but the phenomenon is completely expected and can be predicted and controlled.

There are no obvious local flow disturbances under the slab section that may cause peculiar corrosion conditions. The flow is rapidly established and, apart from the two leading edges of the slab, the level of turbulence is relatively constant at the locations where the corrosion measurements are taken. It is recommended, however, to consider coating the leading edges of the slab with Teflon. Even if they are valid, the severe corrosion issues expected in these locations do not represent the phenomenon being reproduced (top of the line corrosion).

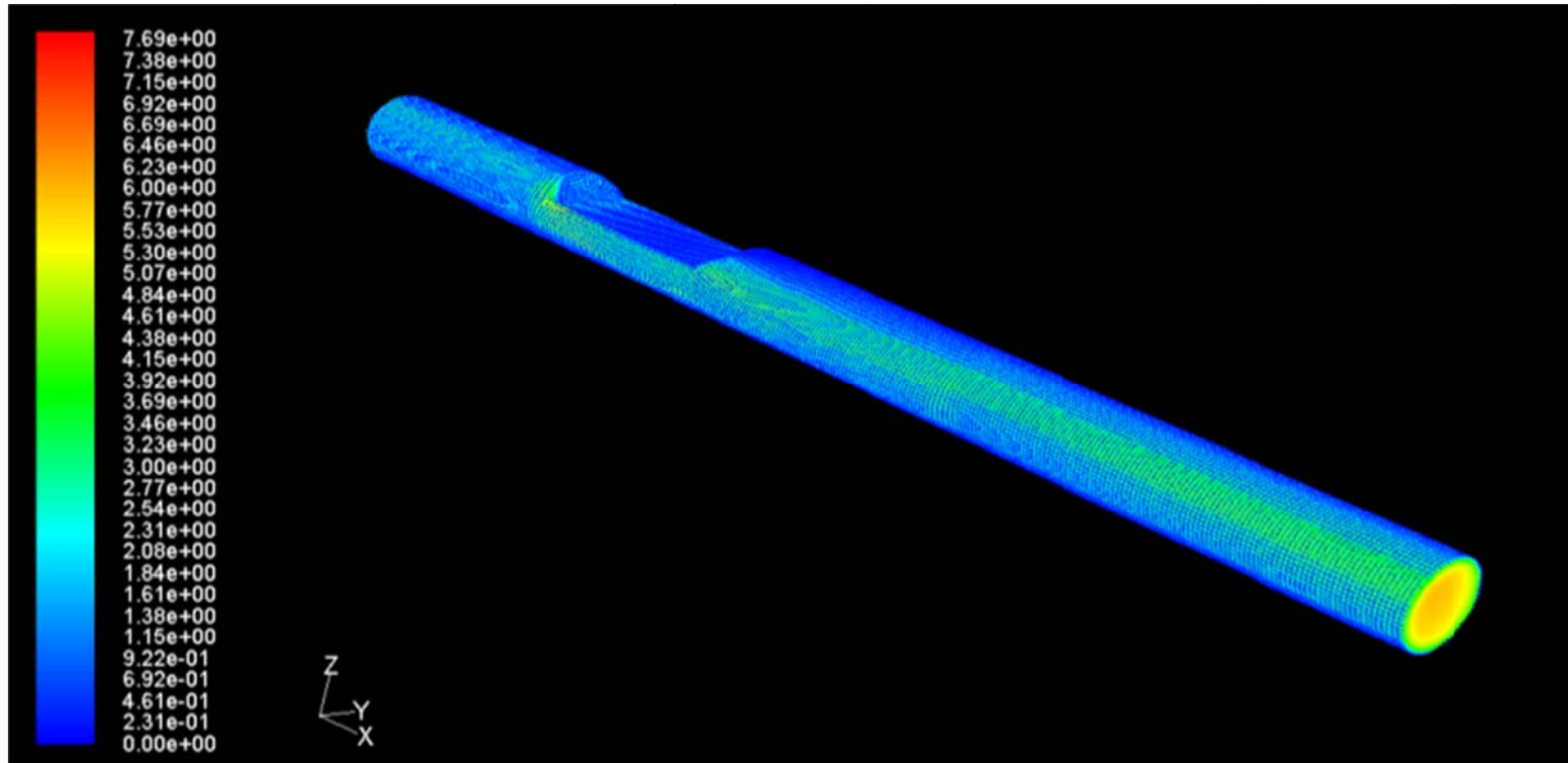


Figure 181: 3D approach – Velocity magnitude in m/s (mostly velocity I the direction of the flow) –  $V_G$ : 5 m/s  
Selection of view planes

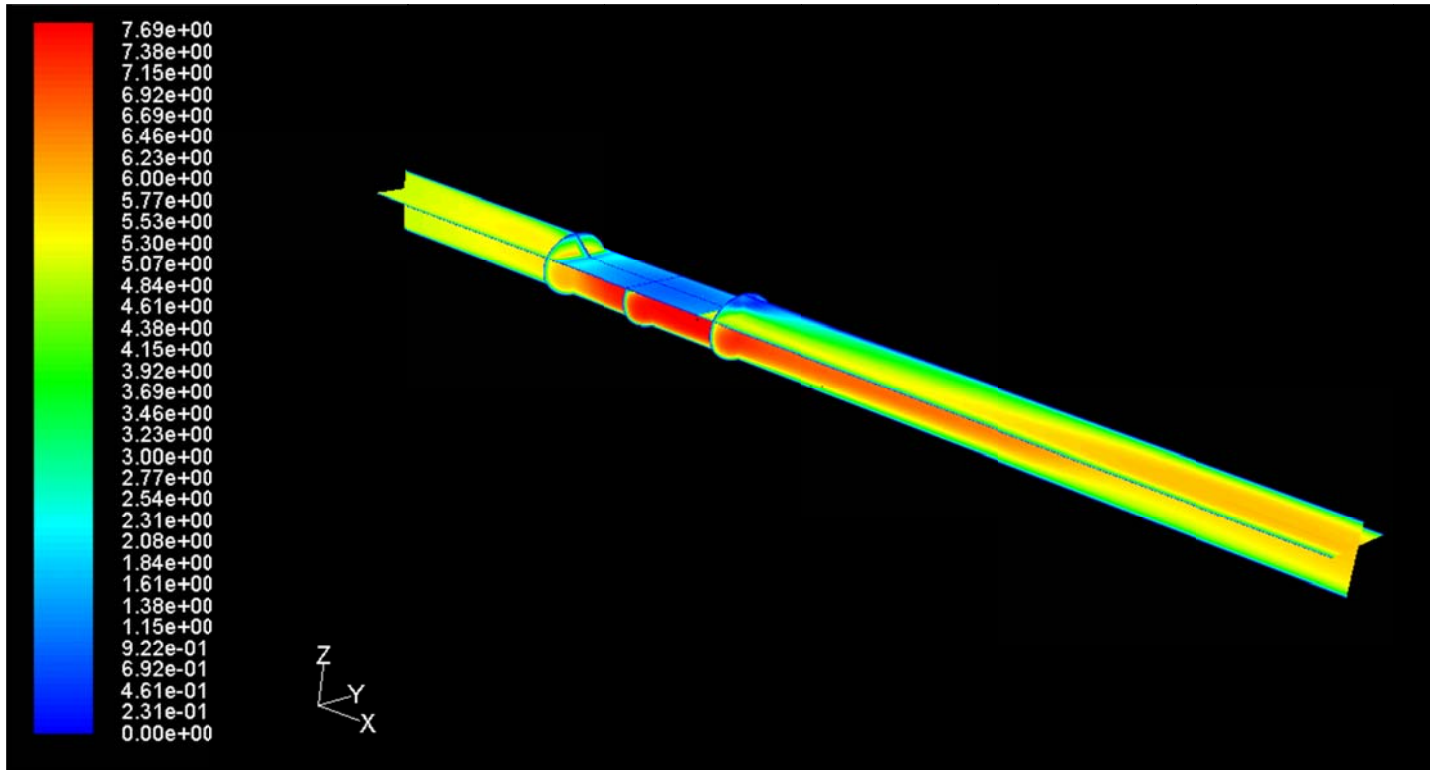


Figure 182: 3D approach – Velocity magnitude in m/s (mostly velocity I the direction of the flow) –  $V_G$ : 5 m/s  
Selection of view planes

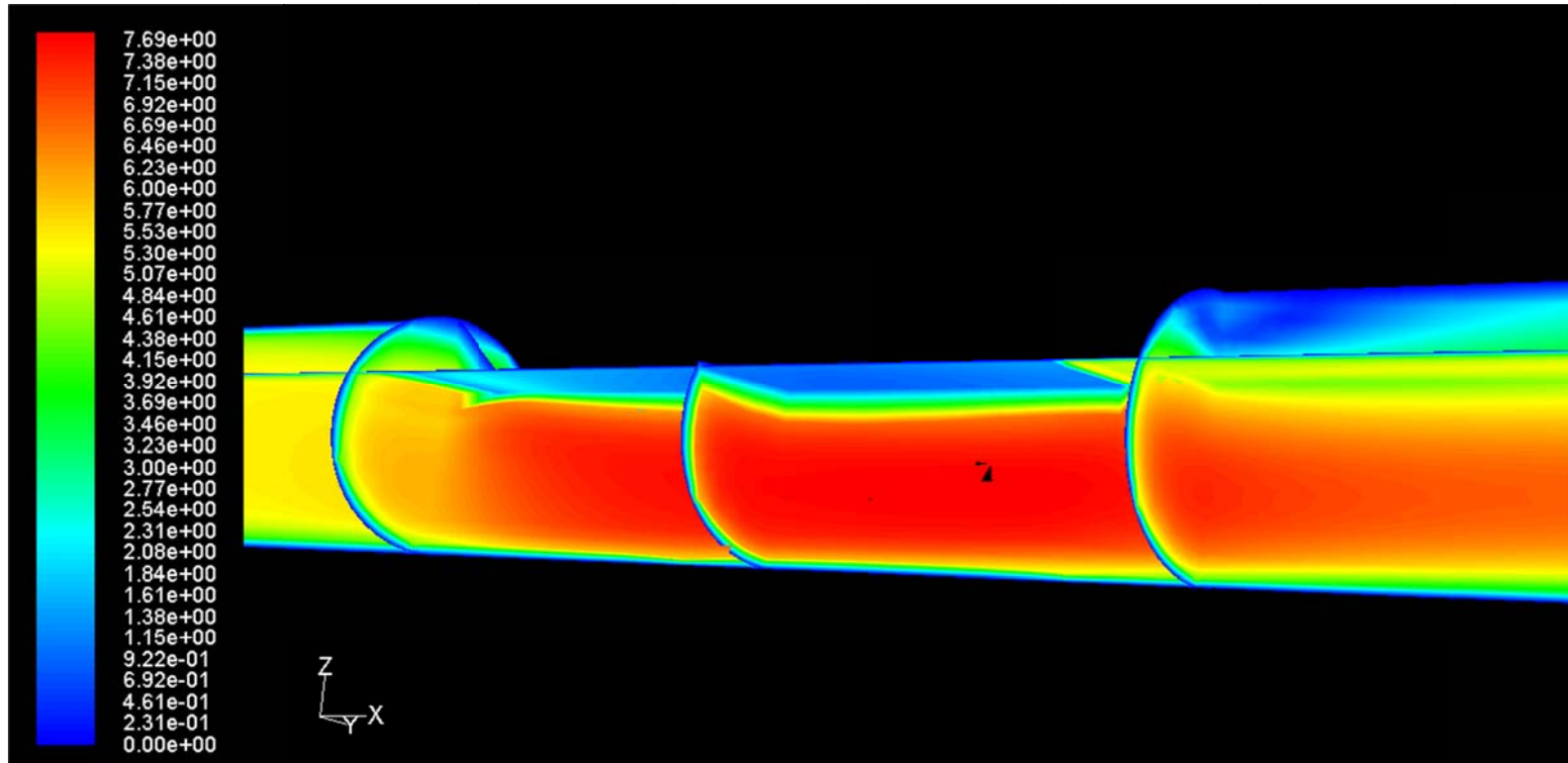


Figure 183: 3D approach – Velocity magnitude in m/s (mostly velocity I the direction of the flow) –  $V_G$ : 5 m/s  
 Selection of view planes – Details on the slab section

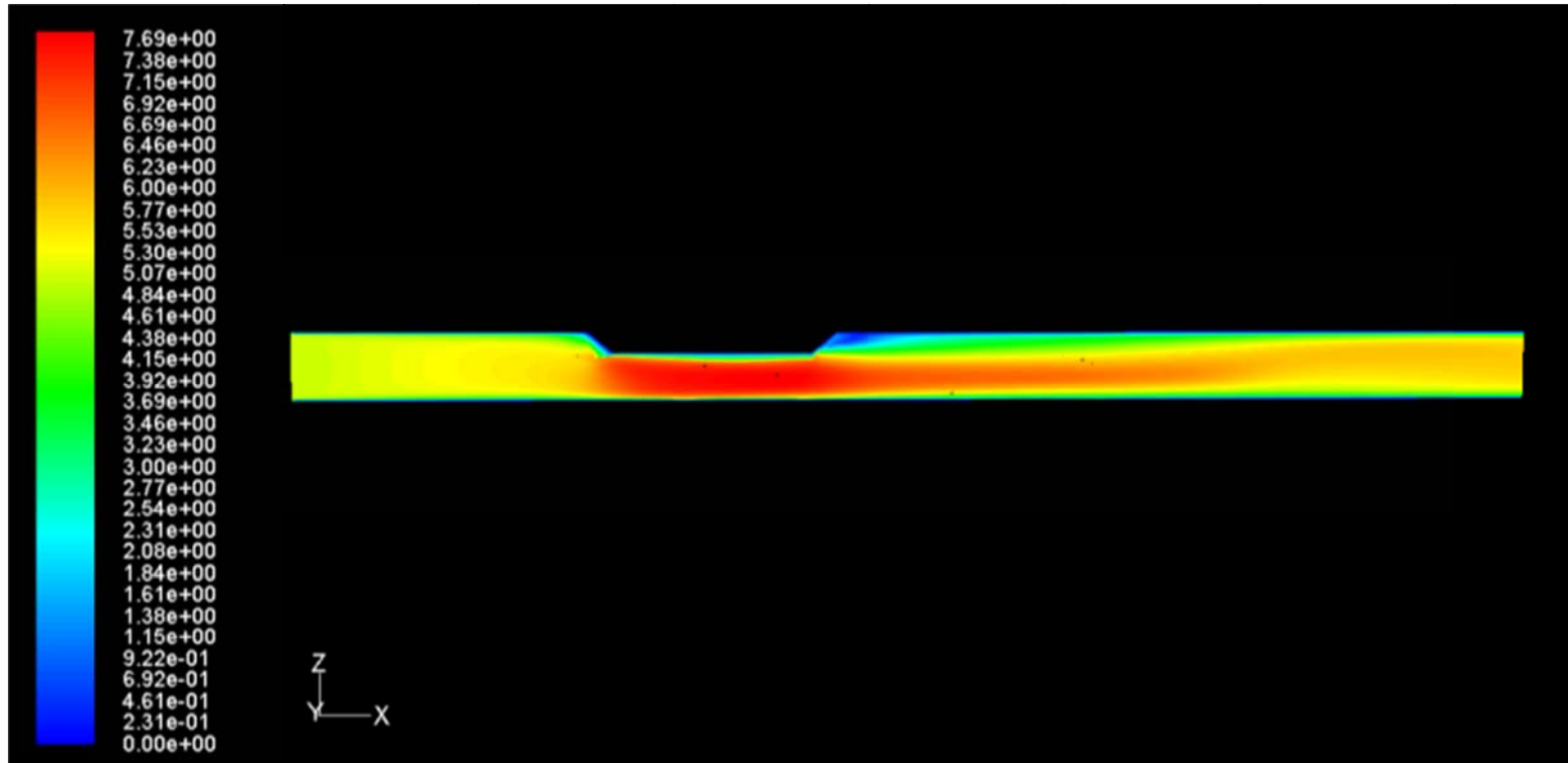


Figure 184: 3D approach – Velocity magnitude in m/s (mostly velocity in the direction of the flow) –  $V_G$ : 5 m/s  
Longitudinal plane - The flow direction is from left to right

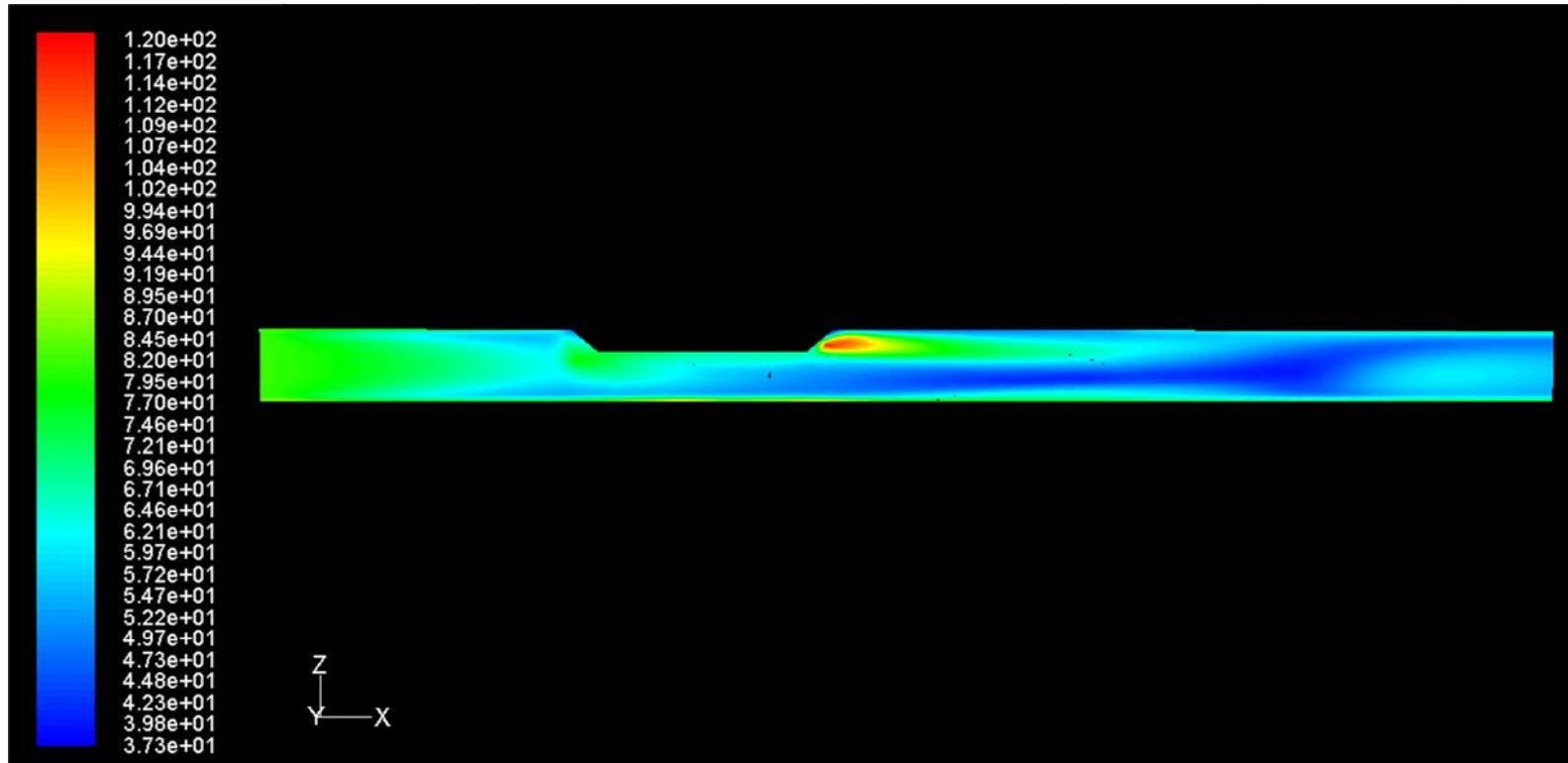


Figure 185: 3D approach – Turbulence intensity (non dimensional ratio of velocities) –  $V_G$ : 5 m/s  
Longitudinal plane - The flow direction is from left to right

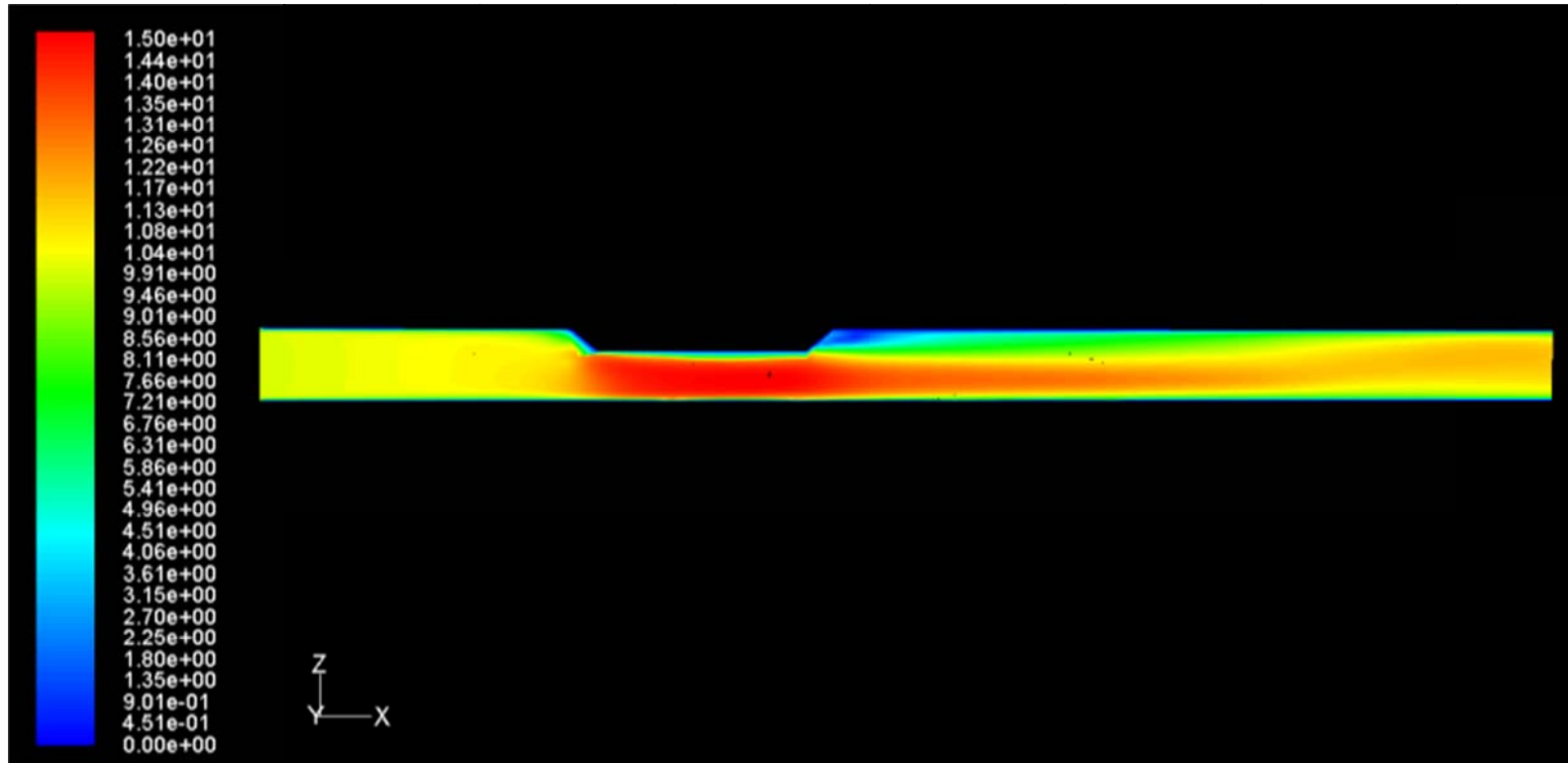


Figure 186: 3D approach – Velocity magnitude in m/s (mostly velocity  $\parallel$  the direction of the flow) –  $V_G$ : 10 m/s  
Longitudinal plane - The flow direction is from left to right

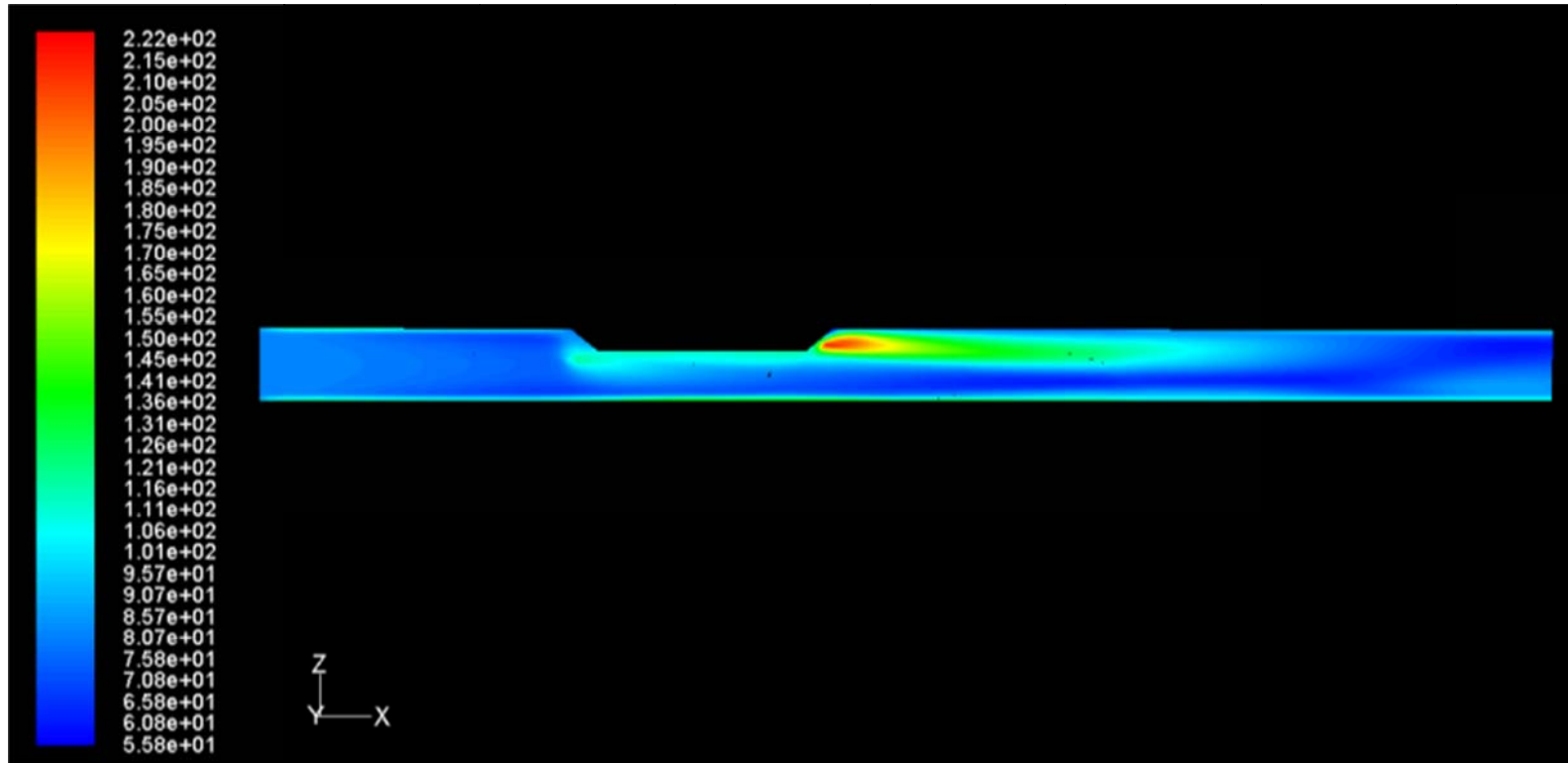


Figure 187: 3D approach – Turbulence intensity (non dimensional ratio of velocities) –  $V_G$ : 10 m/s  
Longitudinal plane - The flow direction is from left to right

## APPENDIX C CONSIDERATIONS ON STEEL MICROSTRUCTURE CHARACTERISTICS

The following section is extracted from an internal report completed in collaboration with Dr Jose E. Ramirez from the Edison Welding institute [132].

### C.1 Objectives

The long term experiments presented in section 4.4.2 were performed using carbon steel inserts made of C1018 and X65. The two inserts made of C1018 came from suppliers (they are labeled C1018(I) and C1018(III)), while the X65 inserts were extruded from a single 20" ID pipe spool. The chemical composition analysis is presented in Table 3 and Table 4. The C1018 steels showed very similar composition within the specification of C1018. The X65 was also within specification.

The three steel samples (C1018(I), C1018(III) and X65) were exposed to a CO<sub>2</sub>-containing gas environment for a period of 3 months to evaluate their corrosion behavior. The experimental conditions are summarized in Table 10. The main objective of this work was to investigate if the differences in steel microstructure could significantly influence the long-term corrosion behavior and consequently affect the results analysis.

### C.2 Methodology

After exposure, the corrosion products covering the steel surface were removed by treating the corroded surface with inhibited acid (Clarke's solution: solution of HCl, antimony trioxide, stannous chloride) in accordance with the ASTM G1-03 [74]. The analysis conducted with these samples included evaluation of the general appearance of corrosion attack, and analysis of the microstructure of the steel samples. For each of the three steel samples, a section of the slab corresponding with the zone exposed to the highest condensation rate was selected for microstructure analysis. The steel samples were mounted and polished using 320-

to 800-grit papers and 0.05 $\mu$ m colloidal silica. After that, the samples were etched with 2% nital solution (2% volume nitric acid and 98% volume alcohol) to prepare them for microstructural analysis. Only the surface analyses performed in Tests #1, #2 and #4 are considered in this section, as the steel grade used for Test #2 and Test #3 is identical (X65).

### C.3 Results analysis

#### C.3.1 General Appearance of Corrosion Attack

The appearance of the corrosion attack was different in each sample in terms of the pitting density and size. In Test #1 ( $T_{\text{gas}}=62^{\circ}\text{C}$ , no acetic acid), the corroded surface presented a high density of medium size pits. In Test #2 ( $T_{\text{gas}}=42^{\circ}\text{C}$ , no acetic acid), the overall corrosion attack was lower in intensity due to the lower temperature, but numerous pits could still be clearly observed on the metal surface. The corrosion attack in Test #4 ( $T_{\text{gas}}=59^{\circ}\text{C}$ , 1000ppm of acetic acid) was more severe as compared to the other two samples; it presented less density of pits but much larger pits as compare to the Baseline Test #1. In some areas of Test #4 samples the pitting attack is so severe that it resembles gross general corrosion attack.

#### C.3.2 Microstructural Analysis of Steel Samples

The general microstructure observed in the steel samples of Test #1, Test #2 and Test #4 are shown in Figure 188 to Figure 190. As mentioned earlier, all three samples present a ferritic-pearlitic microstructure, consisting of a mixture of ferrite (white constituent) and pearlite colonies (black constituent). However, the steel samples present differences in microstructure as related to the volume fraction, colony site and colony density of the pearlite constituent. The steel sample from Test #2 (X65) contains the lowest-volume fraction of pearlite out of the three samples. Additionally, fewer pearlite colonies are present in this sample, and they are also smaller as compared to the other two steel samples. The volume fraction of pearlite and the

pearlite colony size in the sample from Test #4 (C1018(III)) seem to be larger than those in the sample from Test #1 (C1018(I)).

In order to identify micro-structural features that may be associated with the nucleation of the pitting attack in the steel samples, the area close to the bottom of a shallow pit was examined at a magnification of 500X in each of the 3 steel samples and is shown in Figure 188 to Figure 190. At this high magnification, the difference in volume fraction, density and colony size of the pearlite between the steel samples is confirmed. However, no specific microstructural feature or preferential attack of either phase -- ferrite or pearlite -- was observed in any of the steel samples. The sheer size of the corrosion features, which can easily reach 400-800  $\mu\text{m}$  in depth or width, is more than one order of magnitude larger than the ferrite and pearlite colonies. Under these conditions, the steel microstructure could have an effect on the initiation of localized corrosion, at the early stage of the experiments. However, any effect that may exist would completely disappear with time, especially under long-term exposure.

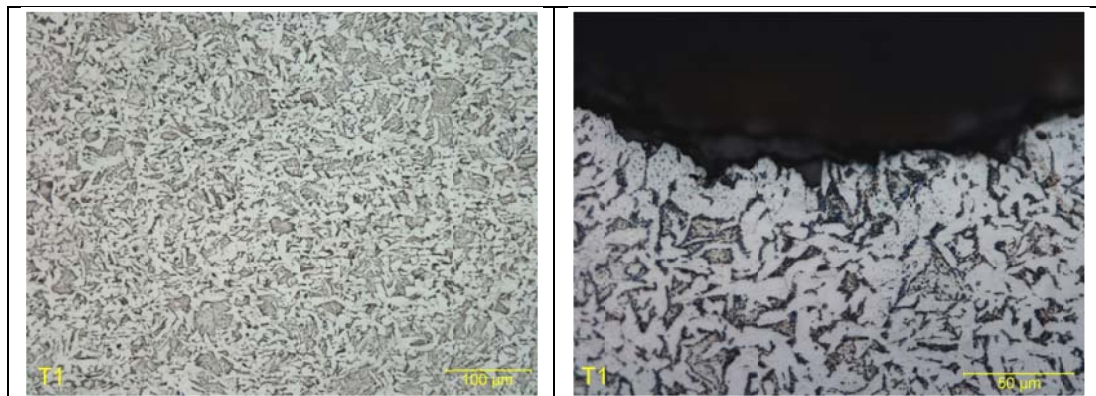


Figure 188: Optical analysis - General microstructure and general appearance of corrosion attack at the bottom of a shallow pit observed in steel sample from Baseline Test #1 (C1018(I))

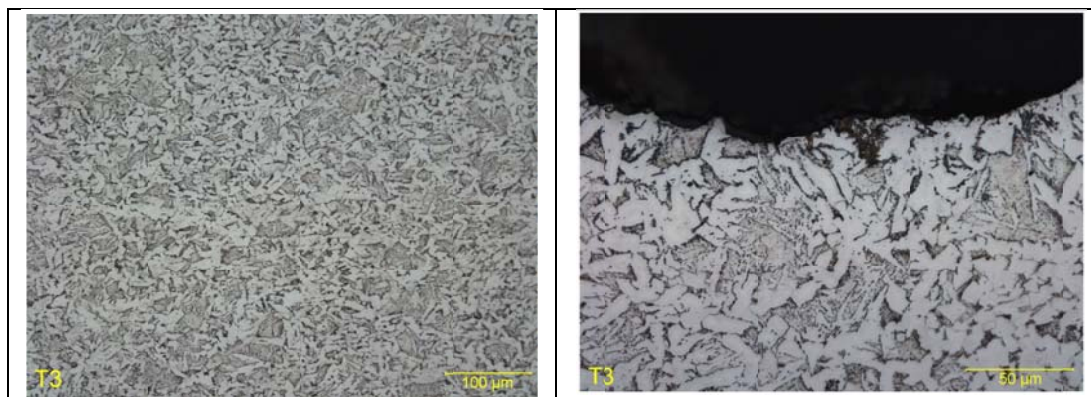


Figure 189: Optical analysis - General microstructure and general appearance of corrosion attack at the bottom of a shallow pit observed in steel sample from Test #4 (C1018(III))

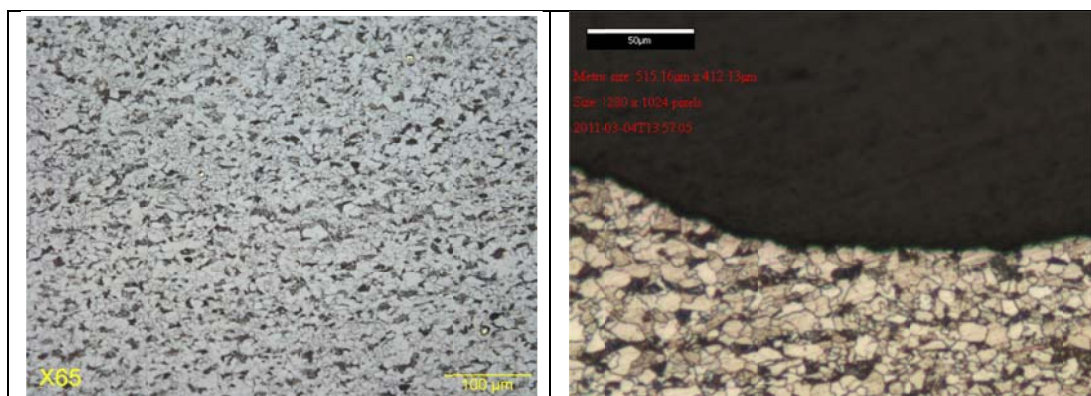


Figure 190: Optical analysis - General microstructure and general appearance of corrosion attack at the bottom of a shallow pit observed in steel sample from Test #2 (X65)

#### C.4 Summary

In order to identify micro-structural features that may be associated with the nucleation of the pitting attack in the steel samples, the area close to the bottom of a shallow pit was examined at a magnification of 500X and higher (with optical microscope and SEM) in each of the 3 steel samples. The difference in volume fraction, density and colony size of the pearlite between the steel samples is confirmed. However, no specific microstructural feature or preferential attack of either phase -- ferrite or pearlite -- was observed in any of the steel samples.

## APPENDIX D HEAT BALANCE DERIVATION FOR DROPWISE CONDENSATION

The phenomenon of dropwise condensation has been studied extensively over the past sixty years. It can be described in terms of a four-stage scenario [99]: nucleation, growth, coalescence and removal. It is commonly accepted that that nucleation is an essential feature of dropwise condensation and that the existence of a thin film of liquid between the droplets is not necessary [100]. An excellent review paper summarizing the early findings in terms of mechanism and modeling was published by Rose [101] in 2002. Rose has published several papers on the subject of dropwise condensation [102-104] over the past thirty years. As dropwise condensation is a random process, the common approach is to calculate the heat flux through a single droplet and to integrate the expression over an average distribution of drop sizes:

$$Q = \int_{r_{\min}}^{r_{\max}} q(r)N(r)dr \quad \text{Eq (D-1)}$$

With: Q: Total heat flux (W/m<sup>2</sup>)

q(r): Heat flux through an individual droplet of radius r (W/m<sup>2</sup>)

N(r)dr: Number of drops per area with radius between r and r+dr (m<sup>-2</sup>)

r<sub>max</sub> and r<sub>min</sub>: maximum and minimum radii of droplet (m)

The total heat flux includes the heat transfer due to the phase change and the presence of non-condensable gas. It has been reported that the main resistance for heat transfer comes from the presence of non-condensable gas [105-107]. The relationship between total heat flux and condensation rate can be stated in the following way [83]:

$$Q = Q_g + Q_c = h_g \times (T_b^g - T_i^g) + WCR \times H_{fg} \quad \text{Eq (D-2)}$$

with: Q: Total heat flux ( $\text{W}/\text{m}^2$ )

$Q_g$ : Heat flux through the gas boundary layer ( $\text{W}/\text{m}^2$ )

$Q_c$ : Latent heat flux released by the phase change ( $\text{W}/\text{m}^2$ )

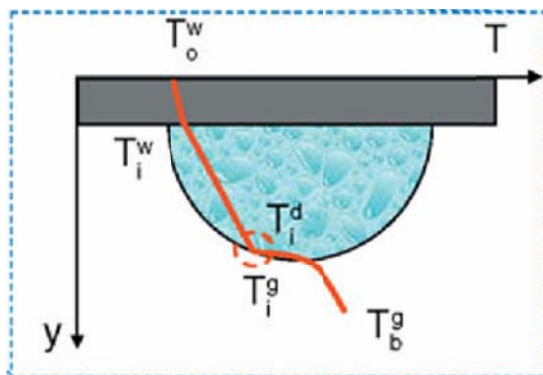
$h_g$ : Heat transfer coefficient in the gas boundary layer ( $\text{W}/\text{m}^2/\text{K}$ )

$(T_b^g - T_i^g)$ : Temperature difference between bulk and vap/liq interface (K)

WCR: Water condensation rate ( $\text{kg}/\text{m}^2/\text{s}$ )

$H_{fg}$ : Latent heat of evaporation/condensation ( $\text{J}/\text{kg}$ )

The heat transfer theory applied to dropwise condensation is well understood and has been described and applied by many authors [133-136]. The approach involves the calculation of the heat resistances caused by the presence of non-condensable gas, the curvature of the droplet, the vapor/liquid interface, the liquid thickness and the promoter surface itself. Assuming that the shape of the drop is hemispherical, a basic representation of the scenario is shown in the picture below:



( $T_o^w$ : outer promoter temperature;  $T_i^w$ : inner promoter temperature;  $T_i^d$ : interfacial temperature in the liquid side;  $T_i^g$ : interfacial temperature in the gas side;  $T_b^g$ : bulk gas temperature)

Figure 191: Temperature gradient for a single droplet (Reproduced from [83] - © NACE international 2007)

The difference in temperature between the vapor and the condensing surface can be expressed as:

$$\Delta T = \Delta T_c + \Delta T_i + \Delta T_d + \Delta T_w \quad \text{Eq (D-3)}$$

With  $\Delta T$ : Total temperature difference  $(T_i^g - T_o^w)$  (K)

$\Delta T_c$ : Temperature drop due to droplet curvature (K)

$\Delta T_i$ : Temperature drop at the vapor/liquid interface  $(T_i^g - T_i^d)$  (K)

$\Delta T_d$ : Temperature drop in the liquid layer  $(T_i^d - T_i^w)$  (K)

$\Delta T_w$ : Temperature drop in the promoter layer  $(T_i^w - T_o^w)$  (K)

The different temperature drops are calculated this way:

- Temperature drop due to droplet curvature [134]

$$\Delta T_c = \frac{2T_i^g \sigma}{H_{fg} r \rho_w} \quad \text{Eq (D-4)}$$

With  $r$ : radius of the droplet (m)

$\sigma$ : vapor-liquid surface tension (N/m)

$\rho_w$ : water density (kg/m<sup>3</sup>)

- Temperature drop due to vapor/liquid interface [137]

$$\Delta T_i = \frac{q}{2\pi r^2 h_i} \quad \text{Eq (D-5)}$$

With  $h_i$ : Heat transfer coefficient at the droplet interface (W/m<sup>2</sup>/K)

- Temperature drop through the liquid droplet [138]

$$\Delta T_d = \frac{q \times r}{4\pi r^2 k_c} \quad \text{Eq (D-6)}$$

With  $k_c$ : Water thermal conductivity (W/m/K)

- Temperature drop through the promoter layer [134]

$$\Delta T_w = \frac{q \times L_p}{4\pi r^2 k_p} \quad \text{Eq (D-7)}$$

With  $k_p$ : Promoter thermal conductivity (W/m/K)

$L_p$ : Thickness of the promoter layer (m)

Finally, the heat flux through a single droplet can be expressed by combining all of the equations above:

$$q(r) = \frac{T_i^g \left( 1 - \frac{2\sigma}{H_{fg} r \rho_w} \right) - T_o^w}{\frac{r}{4\pi r^2 k_c} + \frac{1}{2\pi r^2 h_i} + \frac{L_p}{4\pi r^2 k_p}} \quad \text{Eq (D-8)}$$

With  $q(r)$ : Heat flux through an individual droplet of radius  $r$  (W/m<sup>2</sup>)

The accepted dropsize distribution is derived from an expression developed by Le Fevre [139] in 1966 and is commonly used by many authors [101, 102, 140, 141] in the following form:

$$N(r)dr = \frac{1}{3 \times \pi \times r^2 \times r_{\max}} \times \left( \frac{r}{r_{\max}} \right)^{\frac{2}{3}} dr \quad \text{Eq (D-9)}$$

With  $N(r)dr$ : number of drops per area with radius between  $r$  and  $r+dr$  (m<sup>-2</sup>)

$r$ : Radius of the droplet

$r_{\max}$ : the maximum droplet radius, m

The final equation becomes:

$$h_g \times (T_b^g - T_i^g) + WCR \times H_{fg} = \int_{r_{\min}}^{r_{\max}} \frac{T_i^g \left( 1 - \frac{2\sigma}{H_{fg} r \rho_w} \right) - T_o^w}{\frac{r}{4\pi r^2 k_c} + \frac{1}{2\pi r^2 h_i} + \frac{L_p}{4\pi r^2 k_p}} \times \frac{1}{3\pi r^2 r_{\max}} \left( \frac{r}{r_{\max}} \right)^{\frac{2}{3}} dr \quad \text{Eq (D-10)}$$

The expressions of the size of the smallest viable (thermodynamically) droplet is [142]:

$$r_{\min} = \frac{2T_s \sigma}{H_{fg} \rho_w \Delta T} \quad \text{Eq (D-11)}$$

With:  $T_s$ : Saturation temperature (K)

The maximum droplet size based on a dimensional analysis is expressed as [102]:

$$r_{\max} = K \times \left( \frac{\sigma}{\rho_w g} \right)^{0.5} \quad \text{Eq (D-12)}$$

With:  $K$ : Experimentally defined constant close to unity

$g$ : Gravitational acceleration ( $\text{m/s}^2$ )

## APPENDIX E DESCRIPTION OF THE FREECORP MODEL

This chapter presents a summary of the modeling approach developed by Nescic for the FREECORP software [126]. More details can be found in the original publication. Being freely available online, the aim of this software is to provide the corrosion community with a sound mechanistic model for prediction of CO<sub>2</sub> and H<sub>2</sub>S internal corrosion of carbon steel pipelines. Although FREECORP is capable of predicting corrosion rates in complex environments, this appendix focuses on the CO<sub>2</sub>/HAc electrochemical model developed from three main sources [24], [115], [25].

- Chemical and electrochemical reactions

The chemical and electrochemical reactions involved in H<sub>2</sub>O/CO<sub>2</sub>/HAc system are already presented in Sections 1.3, 1.4 and 1.5. These reactions are consequently not repeated here.

- Numerical calculation for CO<sub>2</sub>/HAc corrosion

The equation enabling the calculation of the corrosion rate is obtained using the total current density of the anodic or cathodic reactions:

$$CR = \frac{i_a M_{w,Fe}}{\rho_{Fe} nF} \quad \text{Eq (E-1)}$$

With:  $CR$ : corrosion rate (unit conversion factors are needed for appropriate unit);

$i_a$ : anodic current density, [A/m<sup>2</sup>];

$M_{w,Fe}$ : atomic mass of iron, [kg/mol];

$\rho_{Fe}$ : density of iron, [kg/m<sup>3</sup>];

$n$ : number of moles of electrons involved in iron oxidation, [2 mol<sub>e</sub>/mol];

$F$ : Faraday's constant.

The current density for the only oxidation reaction considered (iron oxidation) is expressed as follows:

$$i_{a,Fe} = i_{o,Fe} \times 10^{\frac{E_{corr} - E_{rev,Fe}}{b_{Fe}}} \quad \text{Eq (E-2)}$$

With:  $i_{a,Fe}$ : current density of iron oxidation, [A/m<sup>2</sup>];

$i_{o,Fe}$ : exchange current density of iron oxidation, [A/m<sup>2</sup>];

$E$ : corrosion potential, [V];

$E_{rev,Fe}$ : reversible potential of iron oxidation, [V];

$b_{Fe}$ : Tafel slope of iron oxidation, [V].

The total current density is expressed by using the charge transfer and limiting current density for each cathodic reaction,

$$\frac{1}{i_c} = \frac{1}{i_{ct}} + \frac{1}{i_{lim}} \quad \text{Eq (E-3)}$$

With:  $i_c$ : current density of any cathodic reaction, [A/m<sup>2</sup>];

$i_{ct}$ : component of charge transfer current density, [A/m<sup>2</sup>];

$i_{lim}$ : component of limiting current density, [A/m<sup>2</sup>];

The concentrations of species at the metal surface are, in general, different from the ones in the bulk solution, as some species are consumed and other produced by the chemical

and, especially, electrochemical reactions. Species travel due to the subsequent concentration gradients at different speeds, governed by their respective diffusion coefficient and by the overall turbulence level of the liquid flow. FREECORP takes into account this important phenomenon by considering a mass transfer coefficient in the expression of the limiting current.

The charge transfer current density of the cathodic reactions is calculated as follows,

$$i_{ct} = i_o \times 10^{\frac{E_{rev} - E_{corr}}{b}} \cdot \eta_{FeCO_3} \quad \text{Eq (E-4)}$$

With:  $i_o$ : exchange current density of cathodic reactions, A/m<sup>2</sup>;

$E_{rev}$ : reversible potential of cathodic reactions, V;

$b$ : Tafel slope of cathodic reactions, V;

$\eta_{FeCO_3}$ : scale factors due to formation of FeCO<sub>3</sub>.

The limiting current density of the cathodic reactions (except for the H<sub>2</sub>CO<sub>3</sub> reduction, which is chemical reaction limited [126]) are expressed as follows:

$$i_{lim}^d = \eta_{FeCO_3} \cdot k_m F c_j \quad \text{Eq (E-5)}$$

With,  $k_m$ : mass transfer coefficient of corrosive species, m/s;

$c_j$ : bulk concentration of corrosive species, mol/m<sup>3</sup>;

The effect of iron carbonate is simulated using an empirical relationship in the form of the scale factors  $\eta_{FeCO_3}$  to enhance the accuracy of predictions. These scale factors were developed based on experimental data and are defined as follows:

$$\eta_{FeCO_3} = (SS_{FeCO_3})^{-0.7} \text{ with } SS_{FeCO_3} = \frac{c_{Fe^{2+}} \times c_{CO_3^{2-}}}{K_{SPFeCO_3}} \quad \text{Eq (E-6)}$$

With:  $c_{Fe^{2+}}$ : concentration of  $Fe^{2+}$  in bulk solution, mol/L;

$c_{CO_3^{2-}}$ : concentration of  $CO_3^{2-}$  in bulk solution, mol/L;

$SS_{FeCO_3}$ : saturation level in  $FeCO_3$ , -;

$K_{SPFeCO_3}$ : Solubility product in  $FeCO_3$ , mol/L.

Solving the charge balance below enables the calculation of the corrosion potential, and consequently the corrosion rate:

$$\sum_1^{n_a} i_a = \sum_1^{n_c} i_c \quad \text{Eq (E-7)}$$

With:  $i_a, i_c$ : anodic and cathodic current density, respectively, A/m<sup>2</sup>;

$n_a, n_c$ : total numbers of anodic and cathodic reactions, respectively.



**OHIO**  
UNIVERSITY

Thesis and Dissertation Services